New Therapeutic Perspectives for Rare Disorders: Targeting the Endolysosomal and Autophagy Pathways

---

Dissertation

zur

Erlangung der naturwissenschaftlichen Doktorwürde
(Dr. sc. nat.)

vorgelegt der

Mathematisch-naturwissenschaftlichen Fakultät

der

Universität Zürich

von

Marine Berquez

aus

Frankreich

Promotionskommission

Prof. Dr. Olivier Devuyst (Vorsitz)

Prof. Dr. Andrew Hall

Prof. Dr. Matthias Baumgartner

Prof. Dr. Uyen Huynh-Do

Dr. Alessandro Luciani

Zürich, 2020

Table of Contents

Summary

The endolysosome and autophagy–mediated quality control systems maintain the homeostasis and physiology of epithelial cells lining the kidney tubules. Defects in the autophagy-endolysosome degradation system leads to kidney tubule dysfunction and chronic kidney disease. The mechanisms linking endolysosomal dysfunction and tubular cell damage remain unknown, slowing down the development of novel therapies. Studies of inherited kidney diseases, through the use of *in vitro* and *in vivo* genetically-modified model organisms, help to decipher the pathways that regulate the endolysosomal system in kidney tubule cells. In turn, novel pathogenic cascades can help to design targeted treatments. Drug repurposing, which identifies new uses for already approved drugs, offers crucial advantages compared to the development of new compounds, for instance in reducing costs and risk of failure, or improving safety. Over the past years, identification of repurposed drugs has often been successful in the field of rare diseases. Taking these advantages into account, we applied a strategy of drug repurposing in two rare diseases targeting the endolysosomal and autophagy pathways in the kidney.

In the first part of thesis, we characterized a new OCRL-deficient mouse model for Lowe syndrome/Dent disease 2 and the derived primary cultures of proximal tubule (PT) cells, in order to decipher the role of OCRL in the reabsorptive function of PT cells and its involvement in endocytic trafficking. Novel pathogenic cascades linking $PI(4,5)P_2$, aberrant actin polymerization, endocytic trafficking and PT cell function were identified. These findings led us to test class I PI3K inhibitors, already developed for cancer therapy, thus potentially amenable for drug repurposing. In the second part, we used cell and animal-based models to study the pathophysiology of Methylmalonic acidemia (MMA) and we described the mechanism linking methylmalonyl-coenzyme A mutase deficiency, PINK1/Parkin-mediated mitophagy, mitochondria homeostasis and the integrity of tubular cells. We integrated these findings into a drug-disease network-based computational modeling approach and identified targetable pathways to predict drug repurposing. We validated the *in silico* analysis by showing a beneficial effect of targeting mitochondria function, which reversed cellular dysfunction associated with MMA. Taken together, these studies improved our understanding of alterations of endomembrane trafficking and cellular homeostasis in a disease context, and identified promising candidates for drug repurposing in rare genetic diseases affecting the kidneys.

List of abbreviations

AMN: amnionless

AMPK: adenosine monophosphate-activated protein kinase

AKI: acute kidney disease

AP2: adaptor protein-2

ATG: autophagy related protein

ATP: adenosine triphosphate

BAR: Bin/Amphiphysin/Rvs

CKD: chronic kidney disease

CMA: chaperone-mediated autophagy

CUB: complement subcomponents C1r/C1s, EGF-related sea urchin protein and bone morphogenic protein-1

EGF: epidermal Growth Factor

GTP: guanosine-triphosphate

HSC70: heat shock cognate 70

IMM: inner mitochondrial membrane

INPP4: inositol polyphosphate-4-phosphatase

KO: knock-out

KI: knock-in

LAMP: lysosome-associated membrane proteins

LC3: microtubules-associated protein1-light chain 3

LDL: low-density lipoprotein

LCN2: lipocalin 2

LMW: low molecular weight

MMA: methylmalonic academia

MT: mito-TEMPO

mTOR: mammalian target of rapamycin

MMUT: methylmalonyl-coenzyme A mutase

MVB: multivesicular body

NHE3: sodium hydrogen antiporter 3

OCRL: oculocerebrorenal protein

ODA: Orphan Drug Act

OMM: outer mitochondrial membrane

PARL: protease presenilin-associated rhomboid-like protein

PI: phosphatidylinositols

PI(3)P: phosphatidylinositol 3-phosphate

PI(4)P: phosphatidylinositol 4-phosphate

PI(5)P: phosphatidylinositol 5-phosphates

PI(4,5)P_2: phosphatidylinositol 4, 5-biphosphate

PI(3,4,5)P_3: phosphatidylinositol 3,4,5-triphosphate

PI3K: PI3 kinase

PINK1: PTEN-induced putative kinase 1

PT: proximal tubule

PTEN: phosphatase and tensin homologue

TMEM55: transmembrane protein 55

TPTE: transmembrane phosphatase with tensin homology

TPIP: TPTE and PTEN homologs inositol lipid phosphatase

SNARE: soluble N-ethylmaleimide-sensitive factor attachment protein receptors

SNX9: sorting nexin 9

Ub: ubiquitin

ULK1: unc-51-like kinase 1

V-ATPase: vacuolar H^+-ATPase

Vps: vacuolar protein sorting

WAS: Wiskott-Aldrich syndrome

ZO-1: zonula occludens-1

ZONAB: ZO-1-associated nucleic acid-binding protein

I. Introduction

1. The proximal tubule of the kidney

The kidneys maintain the body fluid and electrolyte homeostasis through the appropriate handling of water and solutes (van der Wijst et al. 2019). The nephron, the structural and functional unit of the kidney, is composed of a filtering component named glomerulus and a long tubule formed by differentiated segments, including the proximal tubule (PT), the loop of Henle, the distal tubule, the connecting tubule and the collecting duct (Figure 1). The human kidneys filter approximatively 180 L of fluid per day, but only 1,5 L of final urine is excreted, demonstrating the major role of this organ in the control of homeostasis via the reabsorption of essential nutrients (Zhuo and Li 2013). The ultrafiltrate is modified along the tubular passage; however, it is well known that the PT is the largest contributor to these changes. In fact, the PT is able to reabsorb 65% of the filtered load, the majority of amino acids, solutes, and low molecular weight (LMW) proteins. It is also involved in the acid-base balance (via the uptake of filtered bicarbonate), glucose metabolism (by reabsorbing glucose and regulating gluconeogenesis) and in the homeostasis and metabolism of essential vitamins (by reabsorbing and processing vitamin-binding proteins) (De Matteis et al. 2017; Eckardt et al. 2013; Christensen and Gburek 2004).

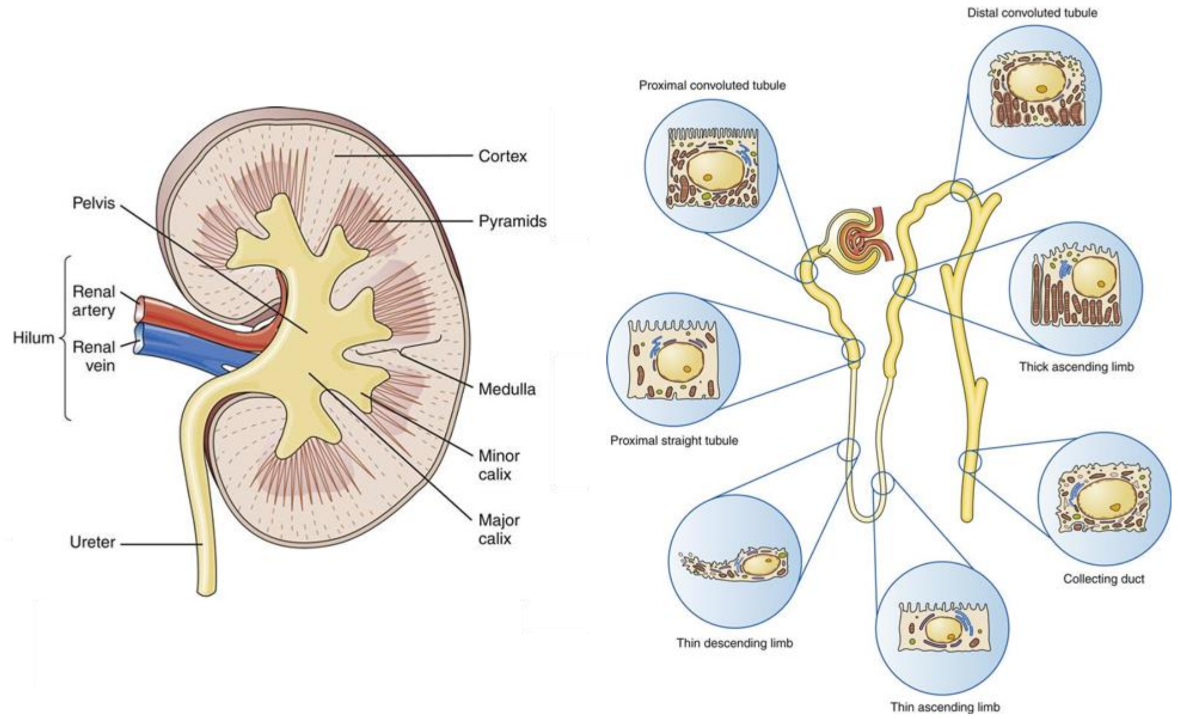

Figure 1: Structure of the nephron, functional unit of the kidney. The nephron is composed of a filtering unit named glomerulus and a long tubule formed by differentiated segments (*from Banasik, Pathology and Laboratory Medicine, 2016*).

1.1. Architecture

The PT is composed of a monolayer of polarized epithelial cells. The apical plasma membrane of the PT cells forms a brush border that consists of dense microvilli facing the lumen of the tubule. These tightly packed microvilli increase the apical surface area absorption by approximately 40 times. The basolateral membrane is also folded, increasing the surface area available for solute exchange. The PT cells are connected by tight junctions, located next to the tubule lumen, maintaining the continuity and polarity of the epithelium (Christensen, Wagner, and Kaissling 2012). The tight junctions are different along the tubular segments and are involved in several functions. In fact, these complex and dynamic structures are constituents of a barrier against paracellular movement of water and ions and are also expressed in signaling platforms regulating epithelial biogenesis and functions (Denker and Sabath 2011). The PT cells contain many elongated mitochondria that occupy a substantial part of the cell volume and are located on the basolateral side. The mitochondria provide the energy required for the high transport activity of these epithelial cells. In fact, production of ATP is necessary for the activity of the Na^+-K^+-ATPase (sodium pump) and other energy demanding transport systems associated with the apical and basolateral plasma membrane. An efficient and well developed vesicular system, consisting of endocytic invaginations (coated pits), endocytic vesicles, vacuoles (early and late endosomes) and lysosomes, characterizes the PT cells. This endolysosomal system facilitates the reabsorption and the degradation of solutes in the PT cells (Christensen, Wagner, and Kaissling 2012).

Based on electron microscopy analysis, the PT segment has been divided into three interconnecting segments: S1, S2 and S3 (Figure 3). The structural difference between S1 and S2 are subtler, while S2 changes suddenly in S3. Compared to the S3, the cells lining the S1 and S2 segments are characterized by a bigger brush border, a higher number of mitochondria and a more developed endolysosomal system (Christensen, Wagner, and Kaissling 2012; Polesel and Hall 2019). The morphological distinction between each segment suggests different reabsorptive capacity among the three segments, with higher capacity in S1 and S2 compared to S3 (Schuh *et al*. 2018).

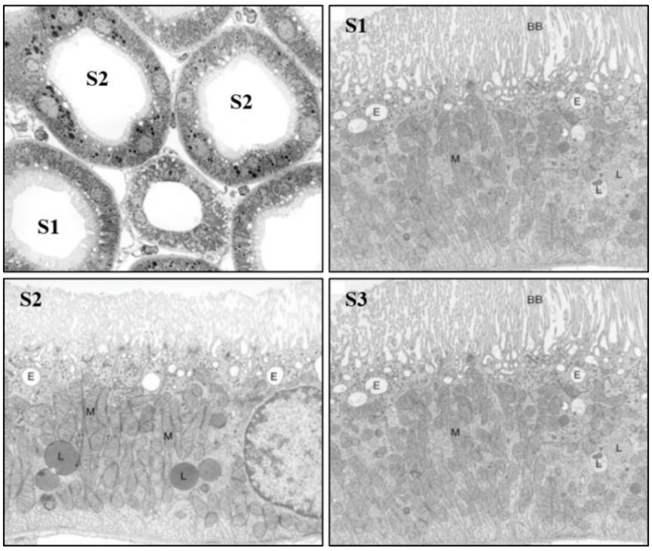

<u>Figure 2</u>: Ultrastructure of the three segments of the proximal tubule. In the first segment (S1), the brush border (BB) is taller than in the second segment (S2). The mitochondria (M) and endocytic vacuoles (E) are numerous in S1 and S2. The lysosomes appear smaller in the third segment (S3) compared to S1 and S2 *(modified from Christensen et al, Comprehensive Physiology, 2012*).

1.2. Reabsorptive function

The reabsorptive capacity of PT cells depend on the expression, trafficking and interaction of specific transport systems that are expressed on the apical and basolateral membranes. The Na^+-K^+-ATPase is expressed at the basolateral side and drives the reabsorption of solutes via specific sodium-dependent cotransporters located in the apical membrane (<u>Figure 3</u>). The sodium pump creates a low cellular Na^+ concentration and a negative membrane potential, which provides the energy required to transport a multitude of solutes (including glucose, amino acids and ions) across the plasma membrane of the PT cells. The mitochondria provide the energy necessary for Na^+-K^+-ATPase activity (Curthoys and Moe 2014).

PT cells reabsorb a significant amount of albumin (66,5 kDa) and are responsible for the massive uptake of LMW proteins (molecular weight below that of albumin) that are filtered by the glomerulus. These LMW proteins include hormones, vitamin carrier proteins, enzymes, lipoproteins, cell surface antigen components, immunoglobulin light chains, drugs and toxins (van der Wijst et al. 2019). After internalisation of the proteins via receptor-mediated and clathrin-mediated endocytosis (and potentially fluid phase), the substances are processed, metabolized in the lysosomes and released into the blood circulation. This process represents 80% of the clearance of small proteins, therefore, the human urine is virtually devoid of plasma proteins (Nielsen, Christensen, and Birn 2016). This massive uptake is essential for hormonal homeostasis, the maintenance of essential vitamins such as vitamins D, A and B12, and to conserve a protein-free environment for the cells lining the distal nephron (Christensen and Birn 2002; Dusso 2011).

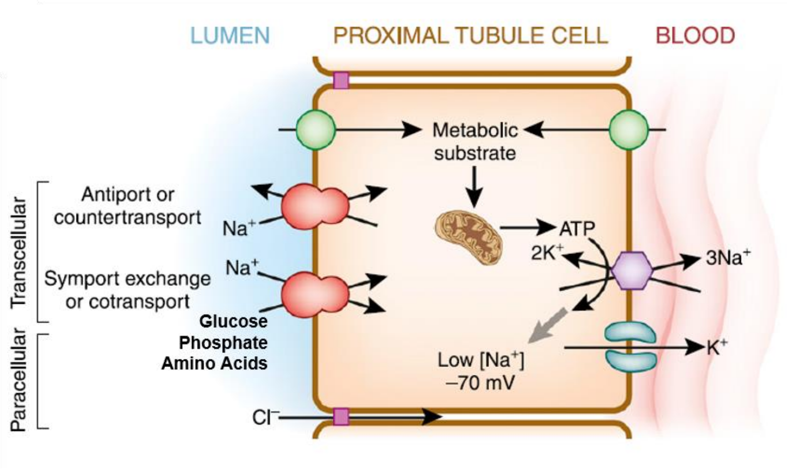

__Figure 3__**: Proximal tubule transport.** The transport systems in PT cells is driven by the electrochemical gradient generated by the basolateral Na$^+$-K$^+$-ATPase. These transport processes, that require a high energy level, are sustained by the numerous mitochondria **present in tubular cells** *(modified from Curthoys et al, CJASN, 2014*).

1.3. Renal Fanconi syndrome: global dysfunction of proximal tubule

The proximal tubule is essential for the reabsorption of water and electrolytes and processing of filtered plasma proteins. Therefore, the PT cells are very sensitive to any defect regarding differentiation, membrane trafficking and the endolysosomal system. The loss of apical transport function in these cells leads to the urinary loss of LMW proteins and solutes, including glucose, phosphate and amino acids, which is referred as renal Fanconi syndrome (Klootwijk et al. 2015; van der Wijst et al. 2019). This clinical entity was described in the 1930's by De Toni, Debré and Fanconi, who reported independently several paediatric cases presenting renal rickets, glycosuria and albuminuria. Renal Fanconi syndrome (also called De Toni – Debré – Fanconi syndrome to acknowledge their pioneering work) is characterised by a generalized PT dysfunction, leading to massive loss of amino acids, glucose, phosphate, bicarbonate, uric acid and other solutes in the urine (Klootwijk et al. 2015). This defect induces acidosis, dehydration, electrolyte imbalances, rickets and osteomalacia and osteoporosis, culminating in the onset and progression of chronic kidney disease (CKD) (Devuyst and Igarashi 2018).

The renal Fanconi syndrome can be a congenital or acquired disorder, and can be either transient or permanent (Table 1).

Table 1: Causes of proximal tubule dysfunction and renal Fanconi syndrome

Congenital

- Arthrogryposis, renal dysfunction and cholestasis 1; ARCS1 (*VPS33B*; MIM #208085)
- Arthrogryposis, renal dysfunction and cholestasis 2; ARCS2 (*VIPAS39*; MIM #613404)
- Cystinosis (*CTNS*; MIM #219800)
- Cystinuria (*SLC3A1*, *SLC7A9*; MIM #220100)
- Dent disease 1 (*CLCN5*; MIM #300009)
- Dent disease 2 (*OCRL*; MIM #300555)
- Donnai–Barrow syndrome (*LRP2*; MIM #222448)
- Fanconi renotubular syndrome 1; FRTS1 (*GATM*, MIM #134600)
- Fanconi renotubular syndrome 2; FRTS2 (*SLC34A1*; MIM #613388)
- Fanconi renotubular syndrome 3; FRTS3 (*EHHADH*; MIM #615605)
- Fanconi renotubular syndrome 4; FRTS4 (*HNF4A*; MIM #616026)
- Fanconi–Bickel syndrome (*SLC2A2*; MIM #227810)
- Galactosemia (*GALT*; MIM #230400)
- Glycogen storage disease Ia (*G6PC*; MIM #232200)
- Hereditary fructose intolerance (*ALDOB*; MIM #229600)
- Imerslund–Grasbeck syndrome 1 (*CUBN*; MIM #261100)
- Imerslund–Grasbeck syndrome 2 (*AMN*; MIM #618882)
- Iminoglycinuria (*SLC6A20*, *SLC6A19*, *SLC36A2*; MIM #242600)
- Lowe oculocerebrorenal syndrome (*OCRL*; MIM #309000)
- Maturity-onset diabetes of the young type 3 (*HNF1A*; MIM #600496)
- Renal tubular acidosis proximal, autosomal recessive (*SLC4A4*; MIM #604278)
- Tyrosinaemia type I (*FAH*; MIM #276700)
- Wilson disease (*ATP7B*; MIM #277900)
- Mitochondriopathies

Acquired

- Myeloma
- Sjögren syndrome
- Renal transplantation
- Acute tubulointerstitial nephritis with uveitis (TINU) syndrome
- Autoimmune interstitial nephritis and membranous nephropathy
- Primary biliary cirrhosis
- Renal haemosiderosis

Exogenous substances

- Drugs: aminoglycosides, salicylate, valproic acid, Chinese herbal medicine, ifosfamide, cisplatin, imatinib, mesylate, adefovir, cidofovir, tenofovir, zoledronic acid, deferasirox, dinanosine, gentamicin, azathioprine, streptozocin, ranitidine
- Chemical compounds: paraquat, bismus, methyl-3-chromone, 6-mercaptopurine, toluene
- Heavy metals: lead, cadmium, mercury, chromium, platinum
- Honeybee stings: melittin

(modified from De Matteis et al. Nature Reviews Nephrology, 2017)

Inherited disorders can be caused by mutations in genes encoding endocytic receptors (e.g. Donnai–Barrow MIM #222448 and Imerslund–Grasbeck diseases MIM #261100) (Nielsen, Christensen, and Birn 2016), components of the endolysosomal system (e.g. Lowe syndrome MIM #309000, Dent diseases (De Matteis et al. 2017) and cystinosis MIM #219800) (Cherqui and Courtoy 2017), and components of the mitochondrial network (e.g. mitochondrial cytopathies) (Emma et al. 2016). The renal Fanconi syndrome can also be induced either by exogenous substances (e.g. toxins, drugs) or is associated with autoimmune disorders (e.g. light chain monoclonal gammopathy) (Luciani et al. 2015).

The primary therapy for this syndrome is to treat the cause and replace the substances lost in the urine. For instance, the dehydration resulting from polyuria is prevented by administration of fluids and electrolytes. Rickets and ostemalacia can be improved by supplementation with phosphate, in combination with vitamin D_3 (Foreman 2019). The prognosis of the patient depends on the cause and the severity of the manifestation. The genetic disorders remain a challenge to manage because of the involvement of organs other than the kidney and growth impairment, therefore further research regarding etiology and therapy are necessary (Karatzas et al. 2017).

2. Role of endomembrane trafficking in proximal tubule

The main function of PT cells is to reabsorb water/electrolytes and to process proteins, sustained by a well-developed endolysosomal system. Proteins reabsorption occurs predominantly by receptor-mediated endocytosis, and potentially by fluid-phase (Eshbach and Weisz 2017). For both processes, the cargoes are internalized into clathrin-coated structures and degraded inside lysosomes (Dickson et al. 2014). The incapacity to internalize or process cargoes is a feature of Renal Fanconi syndrome, demonstrating the crucial role of the endolysosomal compartment to maintain kidney function (Devuyst and Luciani 2015).

2.1. Endolysosomal system

2.1.1. Receptor mediated endocytosis

The LMW proteins filtered by glomerulus are reabsorbed and metabolized by PT cells, such that the urine is almost devoid of plasma proteins in physiological conditions (Figure 4a). The endocytic receptors megalin and cubilin, which are located at the apical membrane of PT cells, coordinate the uptake of most urinary proteins (De Matteis et al. 2017).

Megalin (also known as gp330 or LRP2) is a 600 kDa protein encoded by the *LRP2* gene gene and a member of low-density lipoprotein (LDL) receptor family (Nielsen, Christensen, and Birn 2016). It is expressed at the apical surface of the PT cells, with a higher expression in S1 segment, and it is present in the apical endocytic compartments (Schuh et al. 2018). This transmembrane glycoprotein possesses a large amino-terminal extracellular domain, a single transmembrane domain, and a short carboxyl terminal cytoplasmic tail (Figure 4b). The extracellular domain of megalin mediates the interaction with ligands in the brush border. It is composed of four clusters of cysteine-rich complement-type repeats, which constitute the ligand-binding region. These motifs are separated by 17 epidermal growth factor (EGF)-type repeats and eight spacer regions, which contain YWTD motifs, implicated in the dissociation of the ligand in acidic environment and recycling of the receptor. The cytoplasmic tail contains two NPXY sequences that mediate endocytosis, and one additional 'NPXY-like' motif (VENQNY) that directs the expression of megalin at the apical membrane (Figure 4b). Megalin binds and mediates the internalization of many ligands, including plasma protein peptides, enzymes, vitamin-binding proteins, hormones, and hormone-binding proteins, drugs and toxins (Christensen and Birn 2002). For some ligands, megalin requires the interaction with another receptor, cubilin. Cubilin is a 460-kDa peripheral membrane glycoprotein, also identified as an intestinal intrinsic factor receptor with no transmembrane segments. Cubilin is composed of 27 C-terminal CUB domains which are ligand binding. The N-terminal part is composed by a stretch of 110 amino acids and by eight Epidermal Growth Factor (EGF)-type repeats (Figure 4b) (Christensen et al. 2012). The interaction between both receptors forms a multireceptor complex and increases their binding capacity. In addition, cubilin can bind exclusively other proteins that do not bind megalin such as transferrin, intrinsic-factor vitamin B12 complex and apolipoprotein A1. The membrane localization of cubilin depends on the interaction between its EGF domains and the single transmembrane protein amnionless (AMN) (Fyfe et al. 2004). Amnionless is responsible for the transport of cubilin to the apical surface; the lack of AMN in a mouse model or the mutation of the protein in a dog model causes the retention of cubilin in intracellular structures (Christensen et al. 2012).

The involvement of these apical receptors in the reabsorption of LMW proteins is supported by rare diseases associated with genetic defects of megalin (Donnai–Barrow facio-oculo-acousticorenal syndrome, MIM #222448), cubilin (Imerslund–Gräsbeck syndrome 1 or megaloblastic anemia 1, MIM #261100) or amnionless (Imerslund–Grasbeck syndrome 2, MIM #618882) and animal models deficient for megalin or cubilin (Nielsen, Christensen, and Birn 2016). The loss of megalin expression in mice is associated with emphysematous lung phenotype and forebrain defects. A typical PT dysfunction was observed in this mouse model, associated with LMW proteinuria and defective bone formation due to the impaired endocytosis of vitamin D-binding proteins (Leheste et al. 1999). These data suggest the key role of the endocytic receptors in lung and brain development, as well as for kidney function. In humans, LMW proteinuria has been described in all patients who showed loss of megalin, due to inherited or acquired conditions (Bedin et al. 2020). Albuminuria has been also observed in patients presenting variants in the *CUBN* gene. The majority of the variants were observed after the vitamin B12-binding domains, suggesting the crucial role of the C-terminal domain of cubilin in albumin reabsorption (Bedin et al. 2020). Conversely, the excessive uptake of proteins due to glomerular leakage has been involved in the progression of chronic kidney diseases by activation of several pathways, including apoptosis, endoplasmic reticulum stress, interstitial inflammation and fibrosis (Zoja, Abbate, and Remuzzi 2014; Karoui et al. 2016). However, the role of the endocytic receptors in protein overload condition is not yet deciphered. Megalin has been also described to be involved in the uptake of nephrotoxic agents leading to acute kidney injury such as gentamicin, aprotinin and aristolochic acid (Mahadevappa et al. 2013).

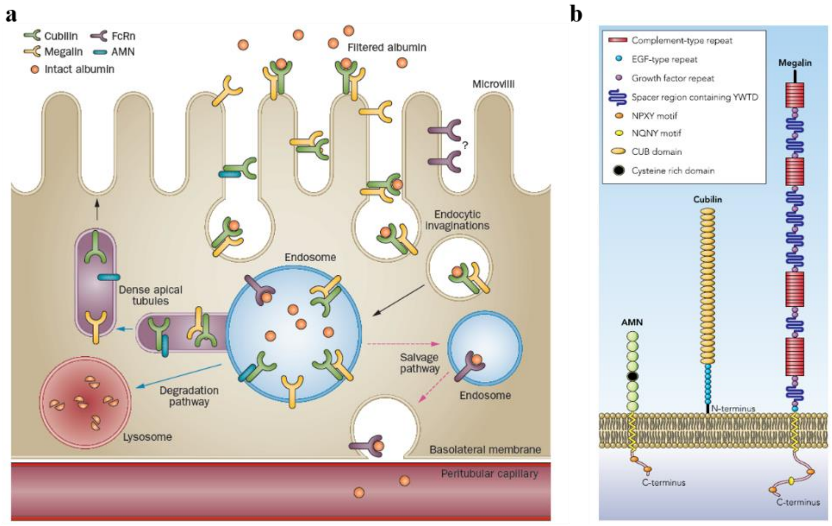

Figure 4: Receptor-mediated endocytosis. (**a**) Filtered proteins, including albumin, bind to receptors, which mediate the internalization of the complex ligand-receptor via clathrin-coated pits and their transport to the endosomes and lysosomes for degradation. (**b**) Structure of megalin, cubilin and amnionless *(from (**a**) Christensen and Birn, Nature Review Nephology, 2013 (**b**) Christensen et al, Physiology, 2012).*

2.1.2. *Endocytic transport and processing of filtered ligands*

The binding of a ligand with the endocytic receptors induces the uptake of the complex ligand-receptor into clathrin-coated vesicles (CCV) and their transport toward the endocytic compartment for the final degradation into the lysosome (Welling and Weisz 2010).

The formation of clathrin-coated vesicles is composed of five steps: initiation, cargo selection, coat assembly, scission and uncoating (Figure 5). The first event is the interaction between the ligand and the receptor, which induces the recruitment of the adaptor protein-2 (AP2) to the plasma membrane. AP2 is a highly conserved protein that binds the endocytic motifs present in the cytosolic tail of receptors (e.g. NXPY motifs for both megalin and cubilin/amnionless complex) or interacts with phosphatidylinositol 4,5-bisphosphate ($PI(4,5)P_2$), a plasma membrane-specific lipid (McMahon and Boucrot 2011). This initiation stage involves accessory proteins that define the site of the plasma membrane where it will be internalized (Kaksonen and Roux 2018). This nucleation module mediates cargo selection and the recruitment of clathrin to the plasma membrane. The polymerization of clathrin stabilizes the curvature of the membrane and helps for the formation of the invagination neck. After the assembly of the clathrin-coat, actin filaments polymerize and form the actin module, composed by actin filament network and regulatory components including Wiskott-Aldrich syndrome (WAS) proteins, myosin motor proteins and dynamin (Kaksonen and Roux 2018). This actin cytoskeleton contributes to the membrane bending. The GTPase dynamin is recruited by BAR domain-containing proteins such as sorting nexin 9 (SNX9), amphiphysin and endophilin which have an affinity for the curvature of the neck. This mechanochemical enzyme mediates the constriction and the scission of the vesicles neck (Doherty and McMahon 2009).The polymerisation of dynamin creates a helical polymer around the constricted neck, induces GTP hydrolysis and therefore the fission of the vesicle from the plasma membrane. Once the vesicle is released into the interior of the cell, the endocytic machinery proteins and the clathrin coat are disassembled and can be used for another endocytic event. The breakage of clathrin-clathrin interaction is mediated the ATPase heat shock cognate 70 (HSC70) and its co-factor auxilin. Changes in the phosphoinositide composition of CCV are necessary for the uncoating step and are mediated by the phosphatases synaptojanin or inositol polyphosphate 5-phosphatase OCRL (Oculocerebrorenal protein) (McMahon and Boucrot 2011; De Matteis et al. 2017).

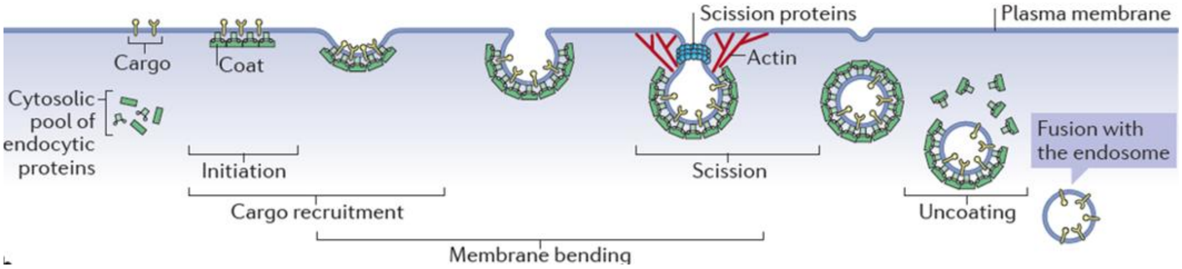

Figure 5: The clathrin-dependent endocytosis mechanism. The clathrin coat is the first module assembled. The cargo is recruited to this site and the membrane is shaped into invagination. Then, different enzymes mediate the constriction and the scission of the vesicles neck. Once the vesicle is released, it loses the clathrin coat that can be used for a new cycle (*from Kaksonen and Roux, Molecular Cell biology, 2018).*

Once the vesicles are internalized and uncoated, they converge to the endolysosomal pathway (Figure 6a). The small Rab guanosine-triphosphate (GTP)-ases control the intracellular trafficking by recruiting specific effector proteins, coordinate proteins sorting, motility and tethering of the endocytic vesicles. In the apical endosomal compartment, the ligand dissociates from the receptor by the acidification of the vesicle (Zhen and Stenmark 2015). To sustain a new cycle of ligand binding, the endocytic receptors are recycled to the apical membrane by slow or fast retrieval pathway. "Fast" recycling is regulated by Rab4 or Rab8 and occurs from early sorting endosomes, while "slow" recycling is mediated from the endocytic recycling compartment and involves Rab11 (van der Sluijs et al. 1992; Cullen and Steinberg 2018). The dissociated cargoes are transported from the early endosome to the late endosome or multivesicular body (MVB) and finally to the lysosome for degradation. This traffic depends on the progressive acidification of the vesicles, driven by the vacuolar H^+-ATPase (V-ATPase or proton pump), the $2Cl^-/H^+$ antiport ClC-5 and the sodium hydrogen antiporter 3 (NHE3) (Eshbach and Weisz 2017). The MVB is characterised by intraluminal vesicles and fuses with the lysosome to form a hybrid organelle where the degradation of endocytic proteins occurs via the action of acid hydrolases, active upon acidic lysosomal lumen. The lysosome are reformed from the hybrid organelle by membrane retrieval (Luzio et al. 2009). The resulting breakdown products generated by the endolysosomal degradation are eventually exported to the cytoplasm for further use to support energy production and metabolism (Verdon et al. 2017).

The lysosome, an ubiquitous and highly dynamic organelle, is responsible for the final degradation of the endocytosed proteins, lipids and nucleic acids (Schröder et al. 2010). This function of lysosomes is supported by the very acidic pH, the expression of soluble lysosomal hydrolases, also called acid hydrolysis, and by the lysosome-associated membrane proteins (LAMPs). About fifty lysosomal hydrolases implicated in the catabolic capacity of the lysosome have been described. In addition to the substrate degradation capacity, these enzymes are involved in antigen processing, degradation of extracellular matrix and initiation of apoptosis. The lysosomal lumen contains enzyme activators and protective effectors that sustain the degradation capacity. The intraluminal pH of the lysosome is maintained acid (pH 4.5-5.0) by the action of the V-ATPase (Saftig and Klumperman 2009). This acidic lumen is necessary for the activation of the hydrolases. The lysosomal limiting membrane expresses highly glycosylated proteins named LAMPs to protect the lysosome from degradation. These membrane proteins are also involved in diverse functions including protein import from the cytosol and transport of products derived from the lysosomal degradation. Other lysosomal membrane proteins mediate crucial functions, such as ion channels and transporters, solute carriers that mediate sugar export, cholesterol transporters and soluble *N*-ethylmaleimide-sensitive factor attachment protein receptors (SNAREs), involved in fusion events (Figure 6b). The efficacy and specificity of the lysosome fusion with organelles, including late endosomes, autophagosomes and the plasma membrane, is dependent on the expression of SNARE-complexes, the presence of additional factors including small GTPases, tethering factors and regulators, and the release of Ca^{2+} (Ballabio and Bonifacino 2020; Saftig and Klumperman 2009). Beside their degradative function, lysosomes participate to other cellular processes including metabolic signaling, gene regulation, immunity, plasma membrane repair and cell adhesion/migration.

The tight regulation of the various stages of the endolysosomal pathway, including the internalization of receptors and ligands, sorting/recycling of the receptors and lysosomal degradation is essential in PT cells to sustain the high absorptive activity. Indeed, impaired apical endocytosis in PT cells, observed in several acute, chronic and genetic diseases, causes epithelial dysfunction, loss of LMW proteins, ions and solutes in the urine, and eventually leads to kidney failure.

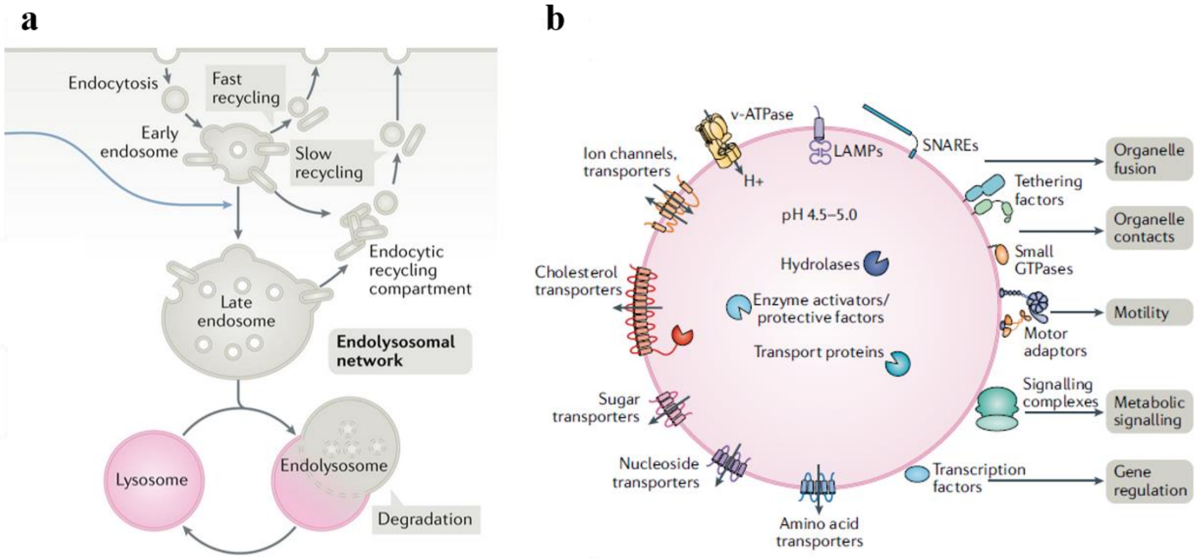

Figure 6: The endolysosomal network. (**a**) Following their endocytosis, internalized proteins enter the early endosomes, where most sorting is initiated. Selected cargo can be recycled back to the cell surface by "fast recycling", or by "slow recycling". Other cargoes can be degraded into lysosomes. (**b**) The lysosome expresses specific proteins and associated proteins essential for its different functions. Hydrolases are involved in the degradation of substrates and express in the lumen. The lysosomal membrane contains several proteins such as LAMPs involved in the membrane protection from degradation, V-ATPase essential for the lumen acidification and several transporters. The cytosolic face of lysosome expresses protein complexes involved in different signalling pathways (*modified from (**a**) Cullen and Steinberg, Molecular Cell Biology, 2018 (**b**) Ballabio and Bonifacino, Molecular Cell biology, 2020).*

2.2. Autophagy and mitophagy

Autophagy, literally meaning “self-eating”, is a lysosomal degradation pathway highly conserved in all eukaryotes. This cellular mechanism plays a crucial role in the maintenance of cellular homeostasis and other processes including development and differentiation. Autophagy is a quality control machinery that eliminates long-lived cytosolic proteins and organelles. The degradation products are recycled to the cytoplasm to sustain cell homeostasis (Chen and Klionsky 2011).

Depending on the type of pathway by which cargoes are delivered to the lysosome, autophagy can be divided into three main types: macroautophagy, microautophagy and chaperone-mediated autophagy (CMA). CMA involves the binding of chaperone proteins with unfolded substrate proteins containing a specific sequence signal, which are then transported into the lysosome for their degradation. Microautophagy refers to the translocation of cytoplasmic materials directly into the lysosomes by invagination or protusion. In the case of macroautophagy, the large cytoplasmic material is sequestered within a double-membrane organelle called autophagosome, which then fuses with the lysosome for degradation. The latter will be detailed in the next section and be referred as autophagy (Mizushima and Levine 2020).

Basal autophagy is crucial for kidney integrity, homeostasis and function. Dysregulation of autophagy is involved in the pathogenesis of acute kidney injury (AKI), CKD and kidney aging (Tang et al. 2020). Mouse models lacking autophagy related protein 7 (ATG7), essential for autophagosome formation, show autophagy defects leading to tubular dysfunction (Kawakami et al. 2015; Suzuki et al. 2019). On the contrary, persistent activation of autophagy leads to physiological changes in the PT, promoting the transition from AKI to CKD (Tang et al. 2020). This dysregulation of autophagy highlights the importance of this pathway in kidney physiology.

2.2.1. Transport of cellular components to the lysosome

The process of autophagy involves different steps: initiation, nucleation, expansion, fusion and degradation (Levine and Kroemer 2019).

Autophagy pathway is induced in response to a change in the extracellular environment of a cell, for example nutrient/energy deprivation. In this case, a non-selective cytosolic bulk degradation occurs to supply cells with energy until nutrients can be obtained (Menzies et al. 2017). The induction step is under the control of the mammalian target of rapamycin (mTOR) and adenosine monophosphate-activated protein kinase (AMPK), which exert an opposite role. mTOR, the master regulator of autophagy, inhibits autophagy by phosphorylating unc-51-like kinase 1 (ULK1) and ATG13, while AMPK activates the ATG13/ULK1 complex that triggers the formation of the phosphatidylinositol 3 kinase (PI3K) complex (Boya, Codogno, and Rodriguez-Muela 2018). This complex is composed of five different proteins (vacuolar protein sorting (Vps) 34, Vps15, Vps30/ATG6, ATG14 and ATG38) and regulates the production of phosphatidylinositol 3-phosphate (PI3P) into the phagophore membrane. The presence of PI3P at the membrane induces the recruitment of PI3P-binding proteins necessary for the phagophore expansion. Two ubiquitin-like systems are involved in this step: the formation of the multi-protein complexes containing ATG12-ATG5-ATG16L and the conversion of cytosolic microtubules-associated protein 1 light chain 3 (LC3-I) into membrane bound-LC3-II. The continuously assembly of these complexes allows the autophagosomes membrane elongation and hence autophagosomes formation (Boya, Codogno, and Rodriguez-Muela 2018; Tang et al. 2020; Levine and Kroemer 2019). The fusion of the completed autophagosomes with lysosomes, involving several lysosomal proteins such as LAMPs, SNAREs and RAb7, results in the formation of an autolysosome (Luzio, Pryor, and Bright 2007). The cargoes are degraded by lysosomal acidic hydrolases and the final products, including amino acids, lipids and nucleotides, translocate to the cytoplasm in order to be recycled and used for new anabolic reactions to sustain cell homeostasis (Yin, Pascual, and Klionsky 2016).

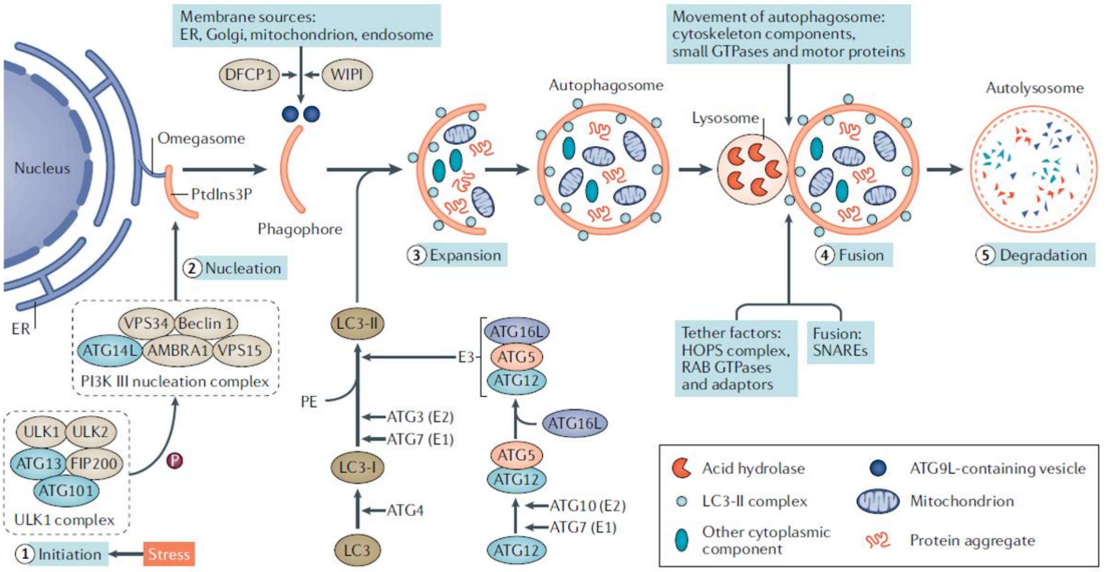

Figure 7: Autophagy dynamics and core machinery. Autophagy is a multistep pathway including initiation, nucleation, expansion, fusion and degradation *(from Tang et al, Nephrology, 2020).*

2.2.2. Mitochondrial homeostasis and quality control systems

In addition to non-selective cytosolic bulk degradation, autophagy can also selectively remove specific cargoes such as mitochondria (mitophagy), lysosomes (lysophagy), protein aggregates (aggrephagy) and lipid droplets (lipophagy). Mitophagy is the best-described form of selective autophagy and is essential for cellular homeostasis and energy metabolism (Menzies et al. 2017). Knowing the major role of mitochondria in PT cells to support energy production and transport function, mitophagy is an essential pathway maintaining the integrity of epithelial cells and therefore kidney function (Emma et al. 2016a; Luciani et al. 2020; Palikaras, Lionaki, and Tavernarakis 2018).

Autophagy is induced when cells are under stress conditions, such as nutrient deprivation, and acts as survival mechanism to maintain cell integrity by regenerating metabolic precursors and removing subcellular debris. While autophagy is a non-selective pathway, mitophagy occurs to eliminate selectively mitochondria, either to regulate their numbers, or to remove the ones that are damaged. Two pathways degrading specifically the mitochondria have been described, and are classified as ubiquitin-dependent or independent (Palikaras, Lionaki, and Tavernarakis 2018). The PINK1/Parkin pathway is an ubiquitin-dependent mitophagy that ensures the elimination of defective organelles. PINK1, a serine/threonine kinase, acts as a molecular sensor for the mitochondrial polarization state. In functional mitochondria, PINK1 is imported into the inner mitochondrial membrane (IMM), rapidly processed and cleaved by the protease presenilin-associated rhomboid-like protein (PARL). The truncated form of PINK1 is then degraded by the ubiquitin-proteasome system (Figure 8a). During mitochondrial membrane depolarization following stress, PINK1 is stabilized on the outer mitochondrial membrane (OMM) and activated by auto-phosphorylation. In this stage, PINK1 phosphorylates basal OMM ubiquitin (Ub) at serine 65 (S65), which induces the recruitment of Parkin from the cytosol to the OMM, due to its high affinity with S65-phosphorylated ubiquitin. The binding between Parkin and the phosphorylated OMM protein alters Parkin conformation triggering its E3 ligase activity. Once fully activated, Parkin conjugates additional ubiquitin onto OMM proteins, forming ubiquitin chains. Autophagy adaptor proteins recognise phosphorylated poly-Ub chains and initiates autophagosomes formation through the binding with LC3. In addition to Parkin, several other ubiquitin E3 ligases generate ubiquitin chains triggering the recruitment of autophagy adaptors (Figure 8b) (Nguyen, Padman, and Lazarou 2016; Palikaras, Lionaki, and Tavernarakis 2018; Hamacher-Brady and Brady 2016). In contrast to PINK1/Parkin system, which is ubiquitin-dependent mitophagy, some mitochondrial proteins expressed at the OMM serve as mitophagy receptors and target dysfunctional mitochondrial to autophagosomes for degradation (Figure 8c). These mitophagy receptors are transcriptionally regulated, express LC3-interacting region motifs which mediate their direct interaction with autophagosomal membrane proteins, such as LC3 and GABARAP, and therefore mitochondria removal (Hamacher-Brady and Brady 2016; Palikaras, Lionaki, and Tavernarakis 2018).

The elimination of damaged mitochondria is necessary to maintain the required number of functional mitochondria in the cell, a crucial process in several organs with high aerobic metabolism, such as kidneys, muscles and brain. (Emma et al. 2016). In fact, mitophagy impairment is associated with several disorders, including neurodegenerative, cardiovascular and kidney diseases, myopathies, metabolic disorders, inflammation and cancer. In a mouse model depleted for PINK1 in cardiomyocytes, impaired mitophagy is associated with an increase in the content of mitochondria, which are morphologically altered, leading to cardiomyopathies and ventricular dysfunction. Mutation in the genes encoding PINK1 and Parkin have been associated with familial forms of Parkinson’s disease (Palikaras, Lionaki, and Tavernarakis 2018). The identification of compounds targeting mitophagy may be a promising therapeutic strategy for mitochondrial diseases.

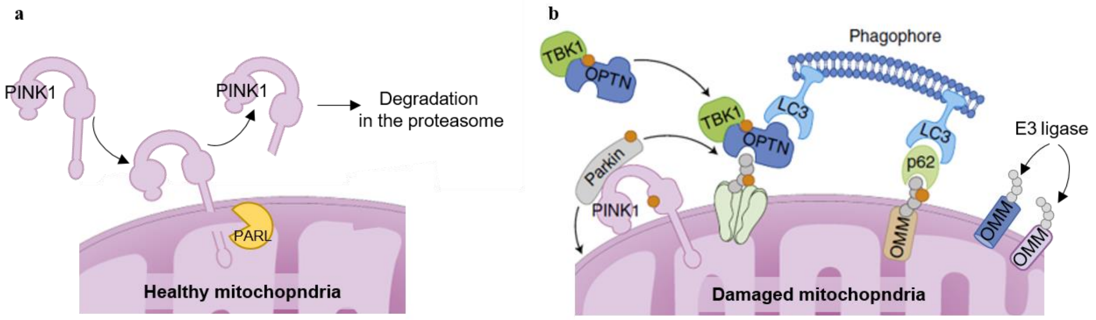

PINK1–Parkin pathway of mitophagy

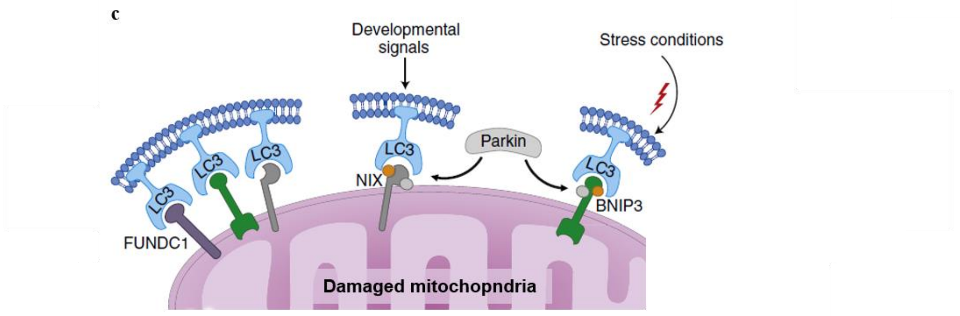

Receptor-mediated mitophagy

Figure 8: Mechanism of mitophagy, the mitochondrial selective autophagy. (**a**) In healthy mitochondria, PINK1 is imported into IMM and subsequently cleaved by PARL. (**b**) During mitochondrial membrane depolarization following stress, PINK1 is stabilized into IMM and phosphorylates Parkin, which initiates the selective targeting of damaged mitochondria. Activated Parkin conjugates ubiquitin into OMM proteins, forming ubiquitin chains that are recognised by autophagy adaptor proteins and brings the autophagy machinery towards the damaged mitochondria. (**c**) Mitophagy receptors (e.g. BNIP3, NIX and FUNDC1) are localized to the OMM and interact directly with LC3 to mediate mitochondrial elimination *(modified from (**a**) (Nguyen et al, Trend in Cell Biology, 2016, (**b-c**) Palikaras et al, Nature cell biology).*

3. Phosphoinositide: regulator of endomembrane dynamics

Endocytosis, one of the major function of PT cells, internalizes segments of plasma membrane, endocytic receptors and various soluble molecules and allows the intracellular transport of components trough vesicles (Kaksonen and Roux 2018). This process relies on dynamic changes in membrane identities, especially in the composition of lipids. Specific combinations of Rab GTPases and phosphatidylinositols (PIs) are responsible for maintaining and coordinating the identity of the different vesicle membranes, creating an identity code for each organelle (Jean and Kiger 2012). Despite their low abundance in the cell, less than 10% of all phospholipids, it is now clear that PIs are key regulator components of cell membrane for the cellular traffic via the recruitment of several PI-binding proteins that triggers signalling events (Di Paolo and De Camilli 2006).

3.1. Phosphoinositide metabolism and spatial distribution

Phosphorylated phosphatidylinositol also called phosphoinositides are a minor class of short-lived membrane phospholipids involved in crucial cellular mechanisms including signalling, motility, development and membrane dynamic. There are seven species of PIs in mammalian organisms, generated by the reversible phosphorylation at position 3, 4 and 5 of the inositol ring (Figure 9) (Phan et al. 2019). Each of species has a distinct and unique distribution, with an affinity for the cytoplasmic side of the plasma and subcellular organelle membranes (Figure 9). The precursor PI is synthesized in the ER and delivered to other membranes by vesicular transport via cytosolic PI transfer protein. The PI 4-phosphates, such as phosphatidylinositol 4-phosphate (PI(4)P) and phosphatidylinositol 4, 5-biphosphate (PI(4,5)P_2), are expressed along the exocytic pathway and the plasma membrane, while phosphatidylinositol 3,4,5-triphosphate (PI(3,4,5)P_3) is enriched at the basolateral side. PI 3-phosphates are prominent components and hallmarks of the endosomal pathways: phosphatidylinositol 3-phosphate (PI(3)P) is present on the membrane of early endosome and autophagosome, phosphatidylinositol 3,4-biphosphate (PI(3,4)P_2) is enriched in non-clathrin endocytic vesicles, and phosphatidylinositol 3,5-biphosphate (PI(3,5)P_2) is expressed on late endosome and lysosome. The phosphatidylinositol 5-phosphates (PI(5)P) has different subcellular localizations, including nucleus, plasma membrane, Golgi complex and ER, however, its precise localization has not been completely defined (Wallroth and Haucke 2018).

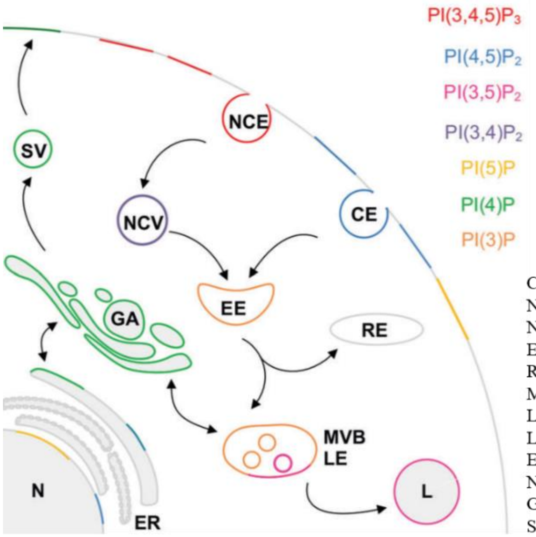

CE clathrin-dependent endocytosis
NCE clathrin independent endocytosis
NCV non-clathrin endocytic vesicles
EE early endosomes
RE recycling endosomes
MVB multivesicular bodies
LE late endosomes
L lysosome
ER endoplasmic reticulum
N nucleus
GA Golgi apparatus
SV secretory vesicles

Figure 9: The different phosphoinositide species and their subcellular distribution. The prominent localisation of PIs on plasma and organelle membranes is represented (*modified from Phan et al, Cell Death & Differentiation, 2019*).

The PIs are mediators of signalling events in the entire cellular compartment by recruiting proteins to the membrane via their phosphorylated head group or by regulating the function of membrane proteins. The interaction between PIs and cytosolic proteins is low affinity; however, it can become more stable when PIs cooperate with one or additional binding sites within the membrane. The cytosolic proteins are recruited and bind specific PIs via the expression of PI-binding domains, including FYVE, PHOX homology (PX), pleckstrin homology (PH), ENTH and ANTH domains (Matteis and Godi 2004). The conversion of these lipids and their specific interactions with adaptor proteins are essential for major cell signalling pathways, such as endocytosis and autophagy. In fact, a carrier vesicle must express the lipids necessary to promote the factors needed for its function (Di Paolo and De Camilli 2006).

The spatiotemporally control of the PIs is involved in the regulation of endocytosis (Figure 10). The conversion of PI(4,5)P_2 to PI(3,4,5)P_3 controls the maturation of endocytic coated pits. PI(4,5)P_2 is enriched in the plasma membrane and participates in nearly all events that occur or involve the cell surface (e.g. clathrin-mediated endocytosis) through its role of co-receptor for the recruitment of endocytic proteins to the plasma membrane. PI(4,5)P_2 induces the recruitment of clathrin adaptors and the AP-2 complex which activate kinases after their binding with the PI and therefore create a pool of PI(4,5)P_2 required for clathrin coated pit initiation. Following this step, the assembly of clathrin relocates the kinases and therefore reduces PI(4,5)P_2 synthesis. The maturation of the CCV is followed by the recruitment of PI(3,4,5)P_3 and several phosphatases (e.g. OCRL, synaptojanin and SHIP2) involved in the removal of PI(4,5)P_2 from the membrane. The synthesis of PI(3,4)P_2 on the CCV together with

AP-2 trigger the recruitment of SNX9. Activated SNX9 and the concomitant presence of PI(3)P and PI(4,5)P_2 promote the polymerization of actin filament at the base of the vesicle, while SNX9 and PI(3,4)P_2 mediate membrane constriction and the released of the vesicle in the cytosol. PI(3)P is the major lipid expressed on early endosome and it is mostly produced by class III PI3 kinase (PI3K) Vps34, and a small pool is derived from the action of class II PI3Ks. The conversion of PI(3)P into PI(4)P is required for endosomal exocytosis. The maturation of early endosome to late endosome is accompanied by the conversion of PI(3)P into PI(3,5)P2 (Wallroth and Haucke 2018; Wang, Lo, and Haucke 2019; Zoncu et al. 2009).

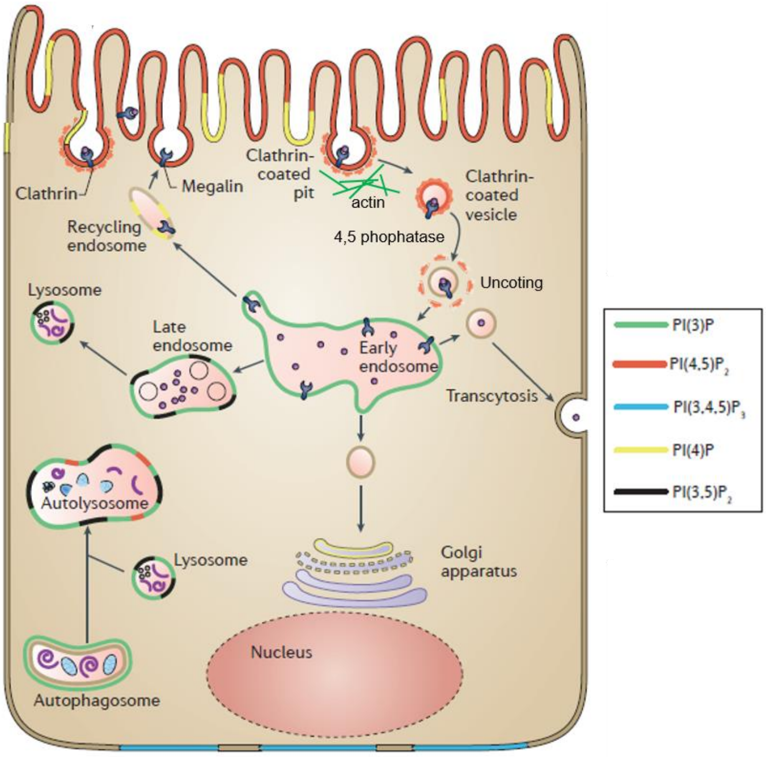

<u>Figure 10</u>: Subcellular distribution of PIs during endocytosis in healthy proximal tubule cells. The plasma membrane expresses PI(4,5)P_2 and PI(4)P at the apical surface, whereas PI(3,4,5)P_3 is enriched at the basolateral side. The early and late endosomes are enriched in PI(3)P while late endosomes and lysosomes are enriched in PI(3,5)P_2. Autophagosomes are enriched in PI(3)P and autolysosomes in PI(3)P and PI(3,5)P_2 *(from De Matteis et al. Nature Reviews Nephrology, 2017).*

The PI switch plays also a major role in the regulation of the lysosome function and autophagy initiation (<u>Figure 11</u>). The membrane of lysosome contains several pools of lipids, including PI(3)P, PI(4)P, PI(4,5)P_2, PI(3,5)P_2, PI(3,4)P_2. The regulation of these PIs is essential for lysosome function and homeostasis: PI(3)P is involved in the full activation of mTORC1 while PI(3,4)P_2 plays the opposite role (<u>Figure 11a</u>), PI(3,4)P2 regulates lysosomal sterol transport, PI(4,5)P_2 controls lysosome tabulation and proto-lysosome formation (<u>Figure 11b</u>) and PI(3)P facilitates the fusion process between the lysosome and the autophagosome (<u>Figure 11c</u>) (Ebner, Koch, and Haucke 2019). PI(3)P is also involved in the regulation of autophagy

(Figure 11d), by recruiting different proteins involved in the formation of the phagophore. The interaction between the protein WIPI and PI(3)P mediates the recruitment of ATG12-AT5-ATG16L1 E3 ligase complex to the phagophore membrane and therefore promotes autophagosome formation (Menzies et al. 2017).

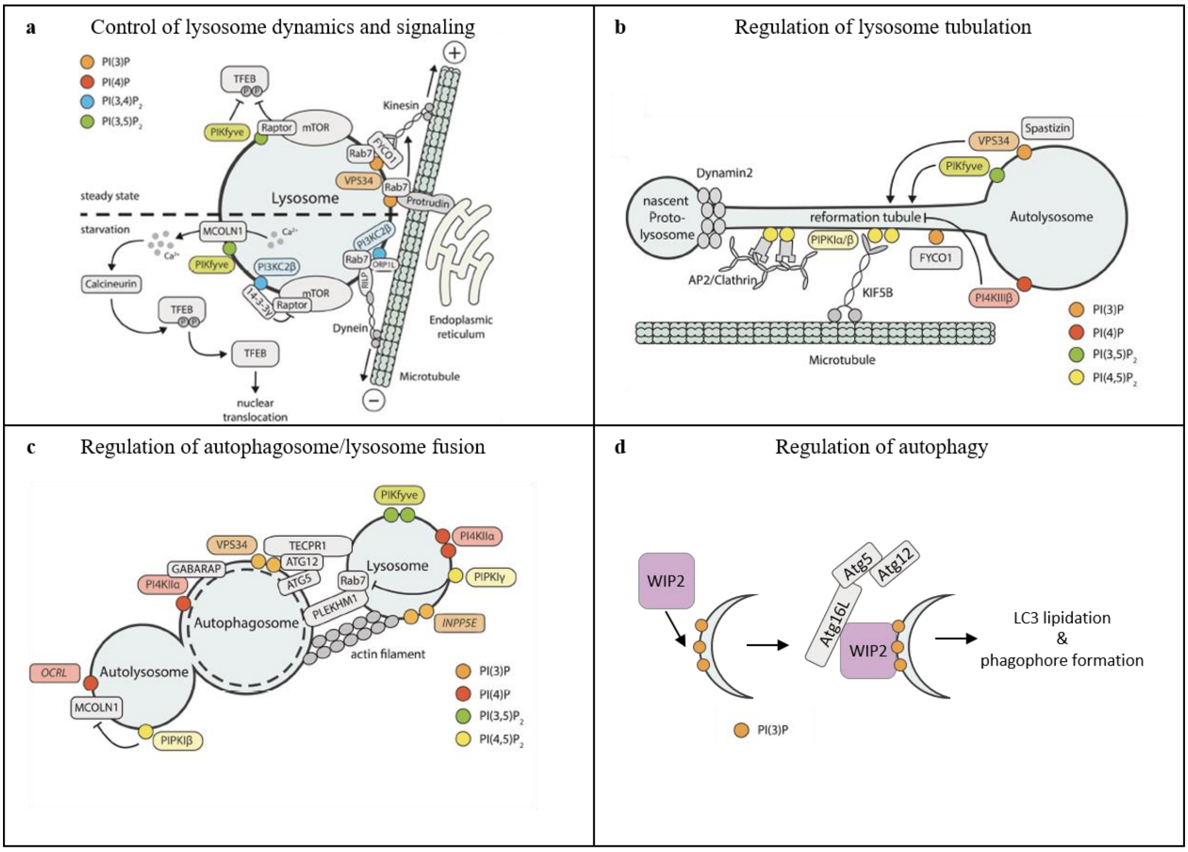

Figure 11: PIs switch in the regulation of lysosome homeostasis and autophagy initiation. PIs (**a**) regulate the lysosome positioning and dynamics, (**b**) control lysosome homeostasis and reformation, (**c**) regulate the fusion between autophagosome and lysosome, and (**d**) control the initiation of autophagy *(modified from (***a-c***) Ebner et al, Biochemical Society Transactions, 2019 and (***d***) Carlsson and Simonsen, Journal of Cell Science, 2015).*

Phosphoinositides act as second messenger and are essential in cells signalling and in the regulation of membrane traffic. However, it is still necessary to elucidate the mechanism behind the conversion of PI in the different pathways. Monogenic diseases involving PI enzymes (both phosphatase and kinases) represent a heterogeneous group of diseases, including the nervous system (Joubert syndrome, MIM #213300 caused by mutation in *INPP5E*), affecting muscles (myotubular myopathy, MIM #300219 caused by mutation in *MTM1*), eyes (fleck corneal dystrophy, MIM #121850 caused by mutation in *PIP5K1C*) and kidneys (Lowe syndrome, MIM #309000 caused by mutation in *OCRL*). These human diseases underline the importance of the enzymes involved in lipids conversion and the crucial tight regulation of PI homeostasis (Volpatti et al. 2019).

3.2. Phosphoinositide kinases and phosphatases

The spatiotemporal distribution of PIs is dynamically and tightly regulated by specific enzymes that add (kinase) or remove (phosphatase) a phosphate group from the inositol ring. Due to the fundamental role of these lipids, these enzymes are also subject to regulation through the interaction with regulatory proteins. The activity of the kinases and phosphatases are essential to coordinate the regulation of PIs. In mammals, the PIs conversion is regulated by 19 kinases and 28 phosphatases. The specific local accumulation of the PIs pools is influenced by the unique expression of PI kinases and phosphatases (Nakada-Tsukui et al. 2019).

3.2.1. Phosphoinositide kinases

Studies in PI kinases (PIKs) based on sequences conservation reveal 3 groups: the PI3Ks (class I, II and III), the PI4Ks (type II and III) and PIPKs (type I and II) (Figure12) (Burke 2018).

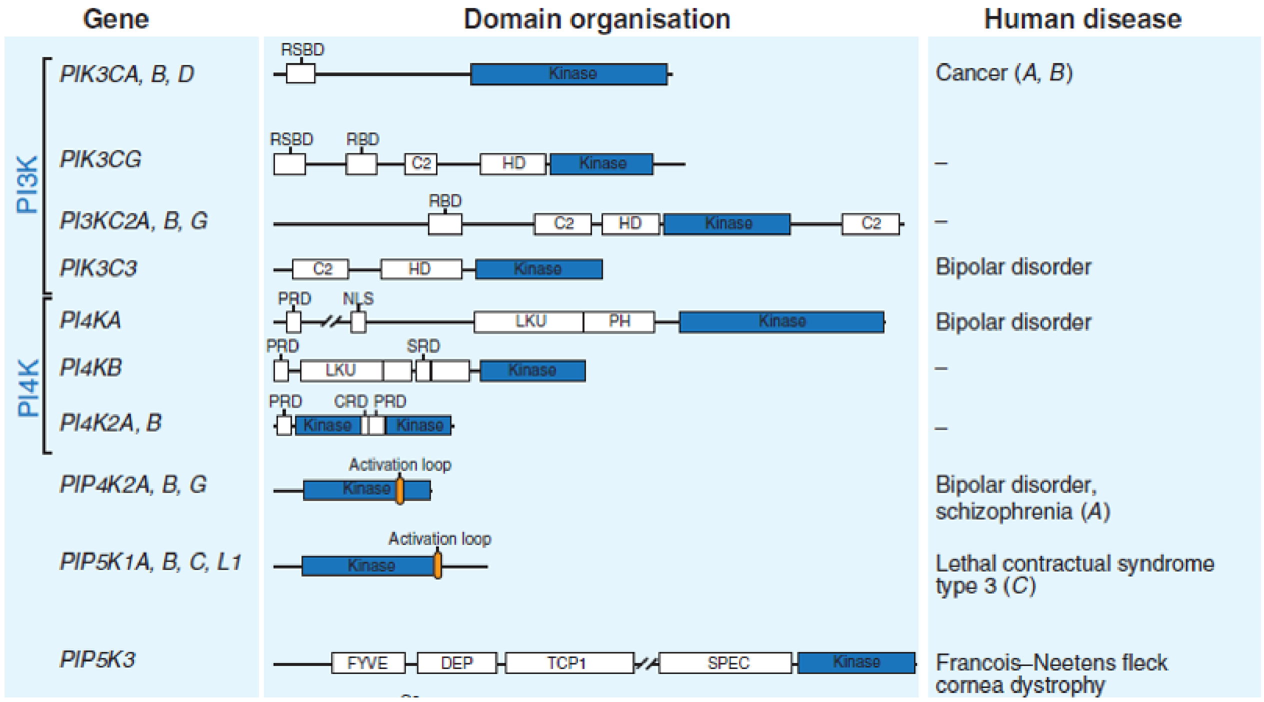

Figure 12: The PI kinases, their domain organisation and associated human diseases (*modified from Vicinanza et al, EMBO Journal, 2008).*

All PI3Ks phosphorylate in position 3 the hydroxyl group of the PI and possess a 'PI3K signature motif' composed by a C2 domain, which binds membranes, a helical domain and the catalytic kinase domain (Bilanges, Posor, and Vanhaesebroeck 2019). PI3Ks are divided into three distinct classes, based mainly on the expression of regulatory binding proteins and their specificity for lipid substrates. The class I PI3Ks, generating PIP3 from PIP2, is the most well-studied PI kinases. It is a heterodimer consisting of one of four catalytic p110 subunits (p110a, b, d or c) and a regulatory subunit (p85a, p85b, p55c, p101 or p84). The production of PIP3 at the plasma membrane triggers the recruitment of several PIP3 effectors including protein kinases (e.g. PDK1, Akt, BTK) and GTPases. These effectors play an essential role in growth, metabolism and survival. Mutations in the gene encoding PI3K class I are associated with several human diseases: an inactivating/deletion mutation is frequent in cancer, while an activating mutation is linked to congenital lipomatous overgrowth or CLOVES syndrome (Venot et al. 2018; Juric et al. 2018). The class II PI3Ks are monomeric enzymes and generate PI(3)P and PI(3,4)P_2 from PI and PI(4)P respectively. They have additional domains in both N and C-terminal extensions, such as a N-terminal clathrin-binding region, suggesting a key role in clathrin-mediated endocytosis. These kinases do not have a regulatory subunit but are regulated by interacting with proteins such as Rab5 or clathrin. No human diseases have been related to PI3K class II mutation (Bilanges, Posor, and Vanhaesebroeck 2019). The class III of PI3K, also named vacuolar protein sorting 34 (Vps34), is conserved in all eukaryotes and converts PI into PI3. Vps34 forms two different proteins complexes: the complex I (p150, Vps30, ATG14 and ATG18) is involved in autophagosome formation, while the complex II (p150, Beclin and UVRAG) is involved in the endosomal transport. No human disease has been associated with mutations in Vps34 (Burke 2018; Bilanges, Posor, and Vanhaesebroeck 2019; Fruman et al. 2017; Jean and Kiger 2012).

The PI4Ks generate PI(4)P and are subdivided in two subgroups: PI4Ks type II and type III. PI4Ks type II exist as two isoforms: PI4KIIα and PI4KIIβ and acts as monomers. They are expressed mostly at the membrane of the endosome or trans-Golgi network and are involved in endosomal exocytosis. PI4Ks type III are composed of two proteins PI4KIIIα and PI4KIIIβ. PI4KIIIα is expressed at the plasma membrane and generates PI(4)P pool which is concerted into PI(4,5)P2 and PI(3,4,5)P3, while PI4KIIIβ is expressed on the Golgi and is involved in the lipid transport, membrane trafficking and lysosome biogenesis (Burke 2018).

PIPKs generate the PI(4,5)P_2 by phosphorylating PI4P (the type I PIP4K) or by phosphorylating PI5P (PIP5K type II). These kinases are involved in several pathways including migration, adhesion, cell division and polarity (Burke 2018). Dysregulation of PIKs, due to mutations, leads to an increase or decrease of their enzymatic activity and has been observed in cancer, developmental disorders and primary immune deficiencies. In particular, PI3K has been the most studied among the kinases because of its involvement in cancer, making it a potential target for drug development. In fact, several drugs targeting PI3K signalling have been developed: PI3K/mTOR inhibitors, pan-PI3K inhibitors, and isoform-selective PI3K inhibitors. These small molecules are currently employed in several clinical trials demonstrating the effect of PI3K inhibition on tumor progression (Shah et al. 2018; J. Yang et al. 2019).

3.2.2. Phosphoinositide phosphatases

Based on catalytic mechanisms, PI phosphatases are divided into 3 major classes: PI 3-phosphatases, PI 4-phosphatases and PI 5-phosphatases (Figure 13).

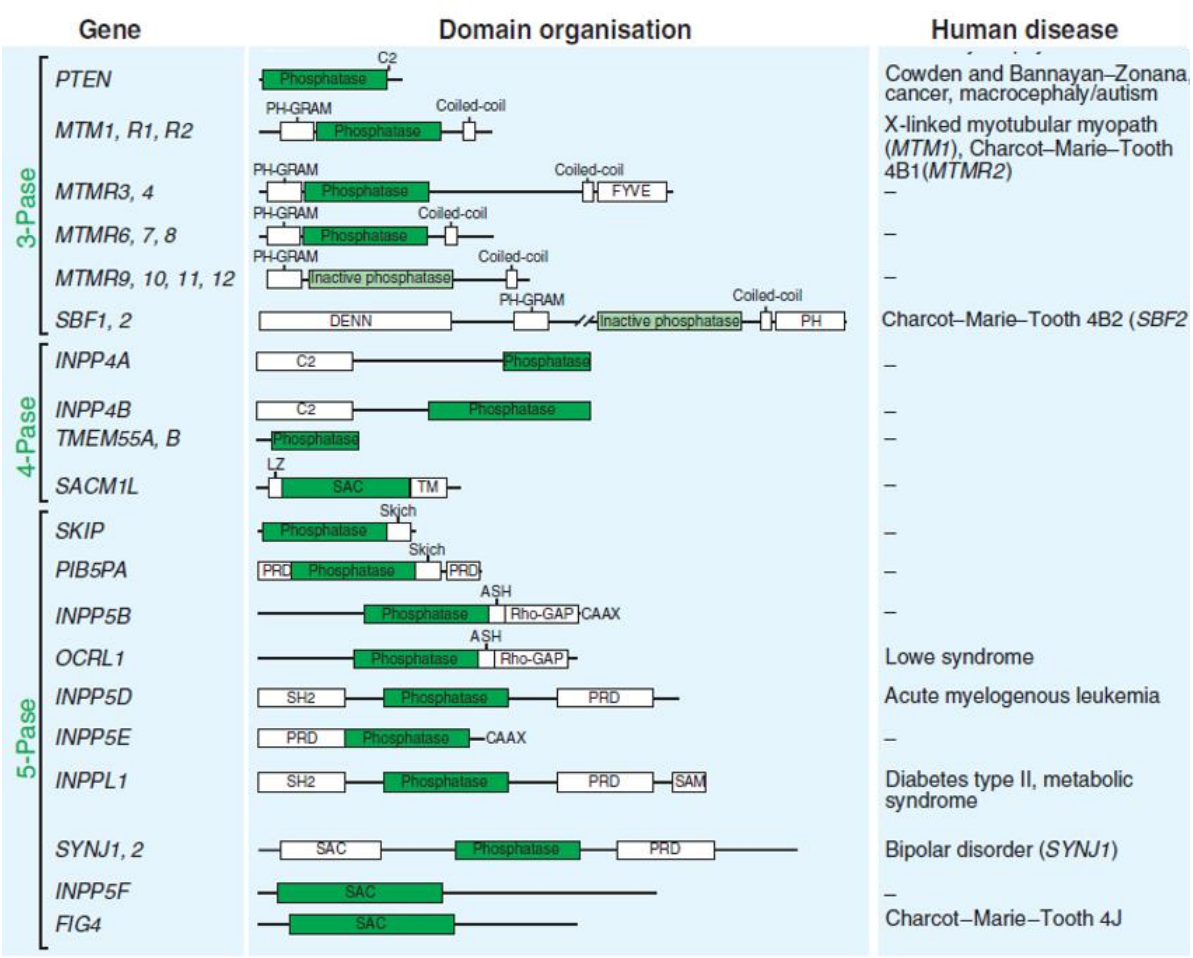

Figure 13: The PI phosphatases, their domain organisation and asscoiated human diseases (*modified from Vicinanza et al, EMBO Journal, 2008).*

PI 3-phosphatases include PTEN, TPTE and PTEN homologs inositol lipid phosphatase (TPIP) and myotubularin (MTM). PTEN is a tumor suppressor which dephosphorylates the D3 phosphate of PI(3,4,5)P_3. By its phosphatase function, it controls negatively the PI3K signalling pathway and prevents Akt activation. PTEN is therefore involved in several cellular processes such as cell polarity, adhesion, migration, metabolism and DNA repair. The function of PTEN is tightly controlled by post-transcriptional and pots-translational mechanisms. This phosphatase is found mutated in several human cancers, including breast, prostate and brain.

The TPIP, the PTEN homologue, is poorly characterized; however it does not affect the Akt pathway. MTM is only found in eukaryotes and is a highly conserved phosphatase that hydrolyses PI3P and PI(3,5)P_2. Mutated MTM leads to a congenital muscle disorder called X-linked myotubular myopathy tyrosine phosphatase (Majerus and York 2009).

PI 4-phophatases are composed of only four proteins, all expressing the CX_5R motif in the catalytic domain. They are divided in two groups: inositol polyphosphate-4-phosphatase (INPP4) and transmembrane protein 55 (TMEM55) which dephosphorylate PI(3,4)P_2 and PI(4,5)P_2 respectively. INPP4 is expressed in endosomal compartments and is involved in the recruitment of SNX9 and actin via the generation of PI3P during CCV initiation. TMEM55 is implicated in the endocytic and recycling pathway. Loss of the PI 4-phospahatse activity in a mouse model leads to neurodegeneration, suggesting its role in neuronal function (Hsu and Mao 2015).

The PI 5-phosphatases are a large family of Mg^{2+}-dependent phosphatase. They are characterized by a central catalytic domain sharing homology to the apurinic/apyrimidic family of endonucleases. This phosphatase dephosphorylate the D-5 phosphoester linkage of PI (3,5)P_2 and PI (4,5)P_2 and PI(3,4,5)P_3, generating PI(3), PI(4)P and PI(3,4)P_2 respectively. This group of phosphatases is divided in 4 classes: type I inositol polyphosphate-5-phosphatase (INPP5) A, type II includes OCRL, INPP5B, synaptojanin, INPP5J and SKIP, type III consists of 2 enzymes named SHIP1 and SHIP2s, and finally the type IV is composed of only INPP5E. OCRL and INPP5B share amino acid homology, and both are multiple-domain proteins. OCRL, which has a clathrin binding domain, regulates the vesicular traffic between endosomes and Trans-Golgi network, while INPP5B is involved in the early secretory pathway. Mutations in *OCRL*, observed in Lowe syndrome/Dent disease 2, leads to an increase of PI(4,5)P_2 levels at the early endosome with the concomitant polymerization of actin on these intracellular membranes. Therefore, the abnormal actin reorganisation impairs the vesicular trafficking involved in several pathways, such as the endo-lysosomal autophagy system (De Matteis et al. 2017). Synaptojanin is involved in endocytosis, synaptic vesicles trafficking and recycling. INPP5J and SKIP regulate Akt activation by negatively regulating PI(3,4,5)P_3. SHIP1 and 2 which converts PI(3,4,5)P_3 to PI(3,4)P_2, are involved in insulin and cytokine signalling (De Matteis et al. 2017; Majerus and York 2009).

4. Genetic disorders targeting the endo-lysosomal and autophagy pathways

4.1. Endosomal disorders: Dent disease and Lowe syndrome

Dent disease is a X-linked disorder characterized by PT dysfunction and progression to CKD and kidney failure (Blanchard et al. 2016). The clinical manifestations of the disease are LMW proteinuria associated with hypercalciuria leading to nephrocalcinosis/nephrolithiasis and progressive kidney failure. Dent disease is characterized by a genetic heterogeneity: 50-60% of the patients present a *CLCN5* mutation (Dent disease 1), ~15% with *OCRL* mutation (Lowe syndrome or Dent disease 2) and the remaining 25-35% have no identified mutations (Devuyst and Luciani 2015; De Matteis et al. 2017).

Dent disease 1 is caused by inactivating mutation in *CLCN5* (MIN #300009). This gene is located on the chromosome Xp11.22 and encodes the $2Cl^-/H^+$ exchanger ClC-5. The majority of the reported mutations (e.g. missense and nonsense) results in a truncated or absence of ClC-5 protein, which would trigger a complete loss of its antiporter function (Lloyd et al. 1996). This exchanger is expressed predominately in the early endosomes of PT cells, where it co-localizes with the V-ATPase to contribute to the endosomal acidification. The development of *Clcn*5 knock-out (KO) and knock-in (KI) animal models have provided critical insights into the mechanisms of PT dysfunction in Dent disease 1 (Gailly et al. 2008; Novarino et al. 2010). These studies have shown that the loss of ClC-5 function impairs the trafficking of endocytic receptors along the endocytic pathway, therefore decreasing their expression at the brush border of PT cells (Christensen et al. 2003) (Figure 12). *In vitro* studies have demonstrated that the lack of ClC-5 triggers a defective acidification of vesicles, which could cause the endocytic defect observed *in vivo*. However, the mechanism involved in the PT dysfunction in Dent disease 1 is more complex. Indeed, despite normal endosomal acidification, the KI mice show the same renal phenotype and similar impairment of endocytosis in PT compared to the KO mice, suggesting that defective acidification is only partially responsible for the endocytic dysfunction (Novarino et al. 2010). The endocytic defect could also be explained by the interaction of ClC-5 with megalin and cofilin, involved in LMW protein and albumin endocytosis (Hryciw et al. 2003). The loss of ClC-5 is also associated with impaired lysosomal function, and per consequence, compromises autophagy pathway (Christensen et al. 2003). The accumulation of autophagosomes containing ubiquitinated proteins and dysfunctional mitochondria leads to an increase of oxidative stress (Gailly et al. 2008). This change could explain the epithelial dysfunction observed in Dent disease 1. In fact, it has been recently shown that oxidative stress disrupts the integrity of the junctional complex proteins zonula occludens-1 (ZO-1) and promotes the release of ZO-1-associated nucleic acid-binding protein (ZONAB).

This transcription factor may promote cell proliferation and repress the transcription of megalin and cubilin in proximal tubules, leading to PT dysfunction (Devuyst and Luciani 2015; van der Wijst et al. 2019).

Mutation in *OCRL* gene, encoding the inositol polyphosphate 5-phosphatase OCRL, causes Dent disease 2 (MIM #300555). Clinically, patients harbouring Dent disease 1 and 2 present similarities: they both show PT dysfunction characterized with the loss of LMW proteins, hypercalciuria and progressive renal failure. Patients with Dent disease 2 present muscular defects, with muscle hypoplasia and increase of muscle enzymes in serum (Park et al. 2014). Some patients with OCRL mutations may present additional symptoms including cognitive disability and congenital glaucoma and therefore are refered to Lowe oculocerebrorenal syndrome (MIM #309000). It is interesting to note that *OCRL* mutations causing Dent disease 2 are different and do not overlap with those causing Lowe syndrome (Bökenkamp et al. 2009). Mutations associated with Dent disease involve the 5-phophatase domain of the proteins wherease for Lowe syndrome the mutation involves three domains of the proteins: the 5-phophatase, ASH and RhoGAP domains (De Matteis et al. 2017).

OCRL is a cytosolic ubiquitous protein, mainly expressed in the brain, liver and kidney. This enzyme is able to hydrolyze the phosphate group in position 5 of the inositol rings of $PI(4,5)P_2$ and $PI(3,4,5)P_3$ to generate PI4P and $PI(3,4)P_2$ respectively. Beside its role of phosphatase, OCRL contains other domains including the pleckstrin homology (PH) domain, the ASPM, SPD-2, Hydin (ASH) domain, and the Rho GTP activating protein (Erdmann et al. 2007). These motifs are necessary for the interaction between OCRL and several proteins and promote its targeting to the different cellular compartments (De Matteis et al. 2017). OCRL is expressed mainly in the trans-Golgi network, but it is also located on the plasma membrane, clathrin-coated vesicles, early endosomes, primary cilium and lysosomes. OCRL controls multiple pools of $PI(4,5)P_2$ at these diverse intracellular locations and the fundamental steps of clathrin-mediated endocytosis. *In vitro* studies deciphered the essential role of OCRL during endocytosis: it translocates from the plasma membrane to the early endosome via its interaction with Rab5, in order to regulate the abundance of $PI(4,5)P_{2,}$ which is essential for the correct trafficking of internalized vesicles along the endocytic pathway. The loss of function of OCRL induces accumulation of $PI(4,5)P_2$ in early endosomes. This deficient degradation of $PI(4,5)P_2$ triggers the failure to uncoat clathrin-coated vesicles and leads to a hyper-polymerization of actin impairing vesicular trafficking of receptors, including those that recycle to the apical plasma membrane, such as megalin (Vicinanza et al. 2011; Festa et al. 2018). The trapping of megalin in early endosomes might explain the link between OCRL deficiency, PT dysfunction and endocytic defect observed in Lowe syndrome/Dent disease 2 patients.

The development of mouse models has been essential to decipher the role of OCRL in kidney. The lack of OCRL in mouse models triggers PT dysfunction, characterized by LMW proteinuria, muscular defects with dysfunctional locomotricity and reduced growth, as encountered in patients with Lowe syndrome. The loss of LMW proteins in the urine can be explained by the reduced expression of the endocytic receptor megalin at the plasma membrane in PT cells (Figure 14) (Bothwell et al. 2011; Bernard and Nussbaum 2010; Festa et al. 2018). A recent study has demonstrated the role of OCRL in regulating endosomal homeostasis and function. The accumulation of PI(4,5)P$_2$ on the autolysosome membrane due to the loss of function of OCRL impairs the autophagosome-lysosome fusion and consequently leads to the accumulation of autophagosomes in OCRL-depleted cells and in kidneys of Lowe syndrome patients. Consequently, the lysosomal alteration and impaired autophagy flux could drive PT dysfunction and possibly central nervous system-related symptoms of the patients (De Leo et al. 2016). Furthermore, OCRL may regulate the primary cilium formation and composition, since it is involved in the production of the ciliary pool of PI(3,4)P$_2$ (Nachury et al. 2007). However, the exact role of OCRL in ciliogenesis is not yet clear and needs further studies.

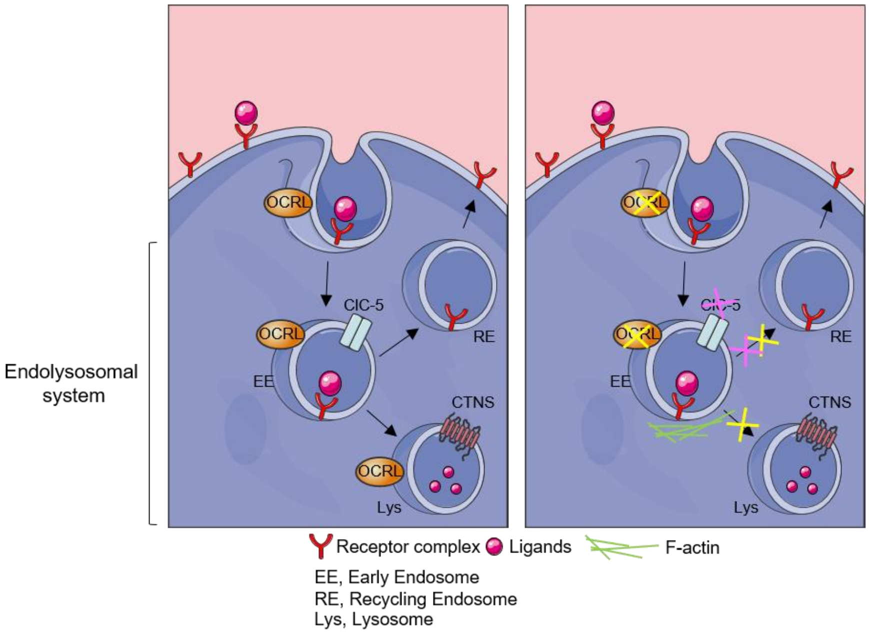

Figure 14: The role of OCRL and ClC-5 in the pathophysiology of Dent disease. ClC-5 facilitates the acidification and the trafficking of endosomes. OCRL is required for a proper vesicular trafficking between the plasma membrane and intracellular compartments *(adapted from Festa et al., Reviews of Physiology, Biochemistry and Pharmacology, 2020).*

4.2. Metabolic disorder: Methylmalonyl–CoA Mutase Deficiency

Methylmalonic academia (MMA; MIM #251000), the most common form of organic aciduria, is a rare autosomal recessive disorder caused by inactivating mutations in the *MMUT* gene encoding a mitochondrial enzyme (Oberholzer et al. 1967; Chace et al. 2001). The consequence of the mutation is the complete (*MMUT*^{0}) or partial (*MMUT*$^-$) loss of the methylmalonyl-coenzyme A mutase (MMUT) function that mediates the terminal step of branched-chain amino acid metabolism and the degradation of certain amino acids and lipids (Barness, 1996) (Figure 15). This metabolic disorder is characterized by an accumulation of toxic metabolites, including methylmalonic acid, propionic acid and 2-methylcitric acid, in plasma, urine and other body fluids, leading to abnormal mitochondria network. Therefore, the mitochondria distress triggers severe organ dysfunction, affecting primarily the brain, the liver and the kidney. Patients with a complete enzyme deficiency develop within their first day of life metabolic acidosis and hyperammonemia, progressing to coma and death if untreated (Hörster et al. 2007). There are few rational treatments for MMA, including a protein-restricted diet supplemented with vitamins and trace elements to decrease the formation of toxic metabolites. However, even with a meticulous medical management, patients can present severe, life-threatening metabolic decompensation (Baumgartner et al. 2014).

MMA patients present frequently renal tubular dysfunction and develop CKD (Haarmann et al. 2013). However, the link between MMUT deficiency and kidney dysfunction is not yet elucidated. The disruption of the tricarboxylic acid cycle (TCA) and the respiratory chain could explain the cellular damages (Morath, 2008). The mitochondrial dysfunction, increased oxidative stress and mitochondrial DNA depletion might be the cause of cellular damages observed in MMA patients (Haarmann et al. 2013).

Several studies using cells and animal models have tried to decipher the link between *MMUT* deficiency and mitochondria defect. The hepatic expression of Mmut in *Mmut*$^{-/-}$ mice, as a stable transgene under the control of the albumin promoter, rescued the neonatal lethality observed in *Mmut*$^{-/-}$ mice. This mouse model shows a kidney phenotype, including decreased glomerular filtration rate, tubulointerstitial nephritis and ultrastructural changes in PT cells. Lipocalin 2 (LCN2), a biomarker of oxidative stress and renal mitochondrial dysfunction, was decreased after treatment with the antioxidant compounds CoQ_{10} and VitE, offering a potential therapeutic approach for the disease (Manoli et al. 2013). A *Mmut*$^{KO/KI}$ mouse model carrying a mutant *Mmut* allele (p.Met698Lys, corresponding to the patient mutation p.Met700Lys) and a KO *Mmut* allele has been developed and recapitulates some biochemical and clinical hallmarks of MMA, including accumulation of MMA and aberrant mitochondria in kidney tubular cells. This mouse model allows the discovery of new biomarkers in MMA, including lipocalin 2 (Lcn2), an early marker for chronic kidney damage that could be involved in dysfunctional cells (Forny et al. 2016).

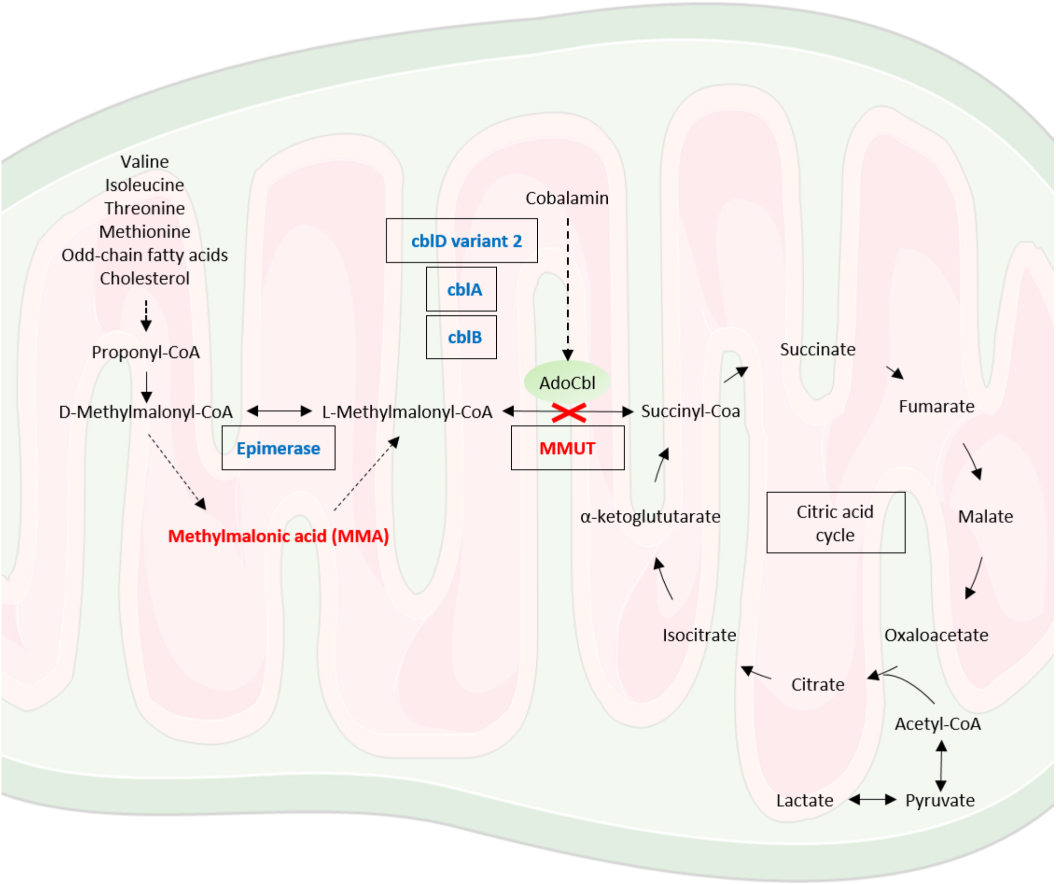

<u>Figure 15</u>: Metabolic pathways of methylmalonic acid. Mitochondrial MMUT deficiency leads to accumulation of organic acids, including methylmalonic acid and energy depletion of the citric acid cycle (AdoCbl, Adenosylcobalamin; cbl, cobalamin; MMUT, methylmalonyl-CoA mutase) (*modified from Fowler, 2008*).

5. Drug discovery and development in rare genetic diseases

A rare disease is defined when its prevalence is <1 in 2000 individuals in Europe or affecting <200,000 individuals in the USA. Approximatively 7,000 rare diseases are described, each affecting a variable number of individuals (Devuyst et al. 2014; Tambuyzer et al. 2020). Altogether, rare diseases are estimated to affect 6-7% of the population in the developed world (~350 million patients). In more than 80% of cases, these disorders have a genetic origin, caused by mutation in a single gene or due to defect in several genes. The incidence of a rare genetic disease can vary substantially between regions or ethnic groups (Tambuyzer et al. 2020). The next generation sequencing technologies have improved the diagnostic efficiency and identified novel causes of rare diseases. Yet, despite advances in our understanding of rare genetic diseases, approximately 90% of them lack an approved treatment (Kaufmann, Pariser, and Austin 2018).

Rare diseases represent an unattractive group of disorders for the drug development and biopharmaceutical industry. In fact, compared to common diseases such as diabetes, obesity or hypertension, rare diseases represent a small market opportunity and the drug development costs are as high as that of any drug development for common diseases. Consequently, the price of approved orphan drug is relatively high, thus causing accessibility issues of the compound for patients, and the pharmacological companies take economically a risk to develop the drug. (Pierzynowska, Kamińska, and Węgrzyn 2020). Therefore, to encourage pharmaceutical companies to promote the development of treatments for rare diseases, the Orphan Drug Act (ODA) was voted in 1983 in the USA. This program provide financial benefit for the development of new drugs for rare disease, such as market exclusivity, tax credit and grant for clinical trials (Sarpatwari and Kesselheim 2019). Since the act passed, the number of orphan drugs approved has risen exponentially each year, so that in 25 years, 487 orphan-designated drugs entered in the USA market, demonstrating the success of this law (Sarpatwari and Kesselheim 2019). Nerveless, even if this regulation has been essential for promoting the development of therapies for rare disease, there is still a gap between the scientific results and its translation into therapies for rare diseases (Tambuyzer et al. 2020).

The progress in molecular biology and the understanding in the pathophysiology of rare diseases have been essential for the development of new therapeutic compounds. The protein-based therapy, including proteins, peptides and antibodies, antisense oligonucleotides (ASOs), small interfering RNAs (siRNAs) and gene/cell therapies have been emerging in the last decades, offering the new therapeutic strategy for rare diseases. Small molecules, which represents the majority of the marketed therapeutics for rare diseases, have several advantages, including a well-defined structure, multiple routes of administration without an immunological profile, controlled dosing and stability. Together, all these therapeutic approaches allow to cover a broad range of targets and mechanisms, and can be expanded by combining different types of therapy, such as small-molecules conjugated to antibodies (Tambuyzer et al. 2020).

Despite the technical progress and enhanced knowledge of the diseases, the development of a new drug is relatively expensive, from \$2 to \$3 billion for a single FDA-approved drug, and it can take over a decade. The high development costs is particularly an issue for orphan diseases, as the market is small, thus limiting the potential for return-on-investment. Another issue shows that, often, a new drug performs well in the preclinical phase but fails during human tests (Tambuyzer et al. 2020). Facing such limitations, drug repurposing or repositioning is a strategy to identify new uses for already approved or investigational drugs that are outside the scope of the original medical indication (Pushpakom et al. 2019). This approach offers several advantages compared to the development of a new compound. The risk of failure is lower, the development process is shorter and cheaper, as the repurposed compounds have already showed safety in human, and some molecules have already been tested in clinical trials. In fact, the cost to bring a repurposed drug on the market have been evaluated at approximatively $300 million (Pushpakom et al. 2019). The number of patients in clinical development can be reduced as the drug has already been tested in prior clinical trials which is an important parameter to take in account for rare diseases. Finally, the last advantage of drug repurposing is the identification of new targets and pathways that can be further investigated (Fetro and Scherman 2020). However, drug repurposing presents also some risks and can fail during the clinical trial phases (e.g. Ceftriaxone, originally indicated as an antibiotic, failed to show efficacy in Amyotrophic lateral sclerosis during phase III) (Cudkowicz et al. 2014). In fact, clinical trials for new indications are still needed and may require further investments: the safety profile of one candidate may drastically change in a new context (e.g. comorbidities) or following a new indication (e.g. long-term versus short-term treatment) (Tambuyzer et al. 2020).

Drug repurposing is an attractive technology to identify new compounds for rare diseases. The identification of repurposed compounds has been successful for several rare diseases. In fact, Sildenafil, originally developed as a drug for coronary heart disease, was first repurposed in 1998 for erectile dysfunction and subsequently repurposed for a rare disease, and finally approved in 2005 for its use in pulmonary arterial hypertension (MIM #178600). Adalimumab, a monoclonal antibody targeting the cytokine tumor necrosis factor (TNF), was first approved in 2002 for rheumatoid arthritis and then gained further approval in 2008 for the rare disease polyarticular juvenile idiopathic arthritis (Tambuyzer et al. 2020). Recently, Alpelisib, an inhibitor of PI3K subunit p110α, was first approved in 2019 for breast cancer (André et al. 2019) and then has shown clinical benefits in children with PROS and CLOVES syndrome (MIM #612918) (Venot et al. 2018). These successes have encouraged the development of approaches to identify repurposed drugs. Typically, the development of drug repurposing consists in three steps: (i) identification of the compound for a given hypothesis, (ii) assessment of the compounds' effect in preclinical models, and (iii) testing the efficacy of the compounds in clinical trials. The first step is critical and can be based on experimental strategies or computational approaches (Figure 15).

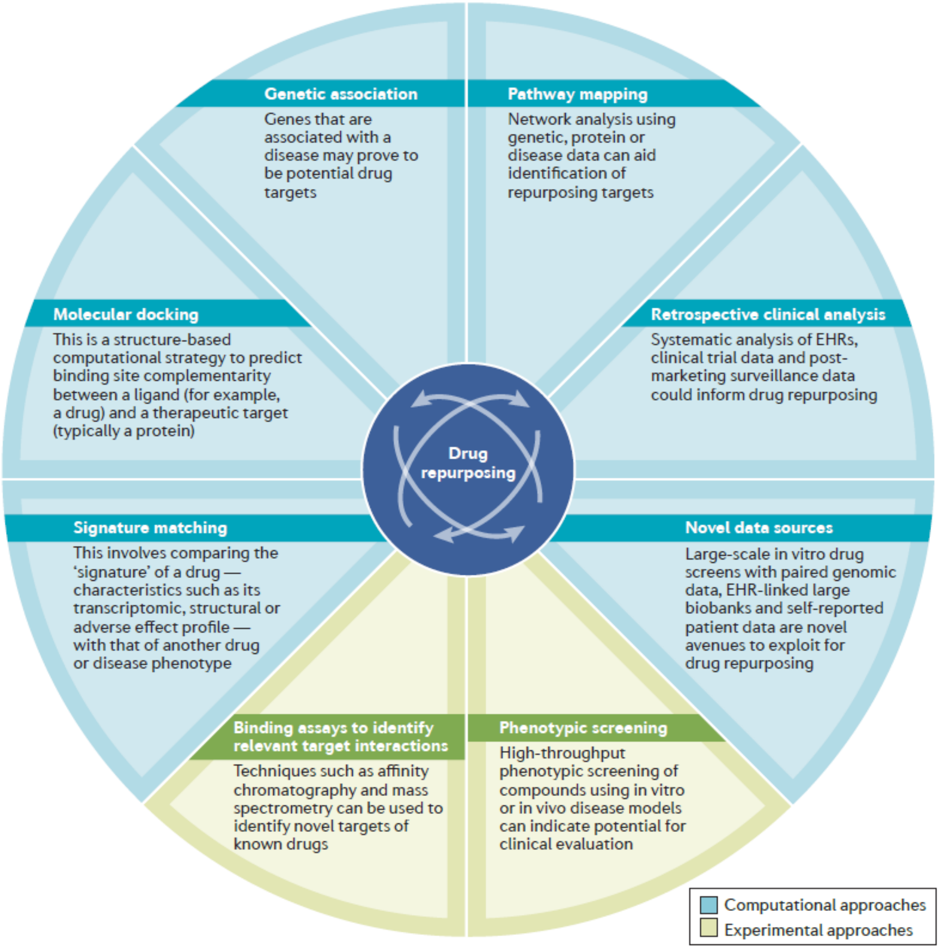

Figure 15: **The different approaches possible for drug repurposing** *(from Pushpakom et al, Nature Review Drug Discovery, 2019).*

5.1. Experimental approaches

Experimental approaches can be used to identify repurposing drug candidates. It can be based on binding assays that identify target interaction or on phenotypic screening (Pushpakom et al. 2019).

Phenotypic screening methods are used to identify compounds that have disease-relevant effects on *in vivo* or *in vitro* model systems. Advances in cellular and molecular technology allowed the screening of many compounds using cells-based assays (high throughput screening). The miniaturization of these assays (from 96-well plate to 1,536-well plates) was an essential step to reduce reagent costs and made screens more practical. Furthermore, automated robotic systems allow to screen a large collection of compounds and improve data quality by reducing human error due to repeated handling of assays (Sun, Zheng, and Simeonov 2017)

The high throughput screening assay is composed of several steps leading to the identification of one lead compound from a large library of drugs. First, it is necessary to set up an assay with a readout related to the pathophysiology of the disease and to optimize the assay in order to screen a large number of compounds. The cell-based assays generally involve the use of cell lines and include different methods such as cell viability, signalling pathways, cell apoptosis and motility. The primary screening tests compounds using a single concentration; positive hits are selected based on simple criteria such as "inhibition of proteins accumulation by 30 %". A cytotoxicity assay is performed in parallel to exclude toxic compounds. The secondary screening is based on the same assay of the first screening but is testing the selected compounds at different concentrations to generate a dose-response curve. Finally, the tertiary screening uses different formats, such as another assay (fluorescence instead of luminescence assay) or other biological models (primary cells instead of cell lines), to identify and prioritize few lead compounds (Dvela-Levitt et al. 2019; Sun, Zheng, and Simeonov 2017).

Whole-organism phenotypic assays have been also emerging in drug repurposing, such as zebrafish or *Caenorhabditis elegans* (nematode), for testing small molecules in disease models. They are good models for evaluating drugs efficiency, studying drug uptake in cells or testing the toxicity effect (Tambuyzer et al. 2020). While a full library can be tested on the worm, the assays focus more on high-quality drugs candidates for zebrafish (Volpatti et al. 2020).

The development of compound libraries has increased in the last years, offering opportunities to screen larger number of molecules and more extensive families of compounds. However, one major limitation of the high-throughput screening is to translate drug candidates from *in vitro* assay to the clinic. The development of new tools and technologies, such as inducible pluripotent stem (iPS) cells, gene editing CRISPR–Cas 9 systems, and organoids, offer the opportunity to improve the preclinical disease models and therefore the translational relevance of the screening approach (Pushpakom et al. 2019).

5.2. Computational approaches

Computational drug repurposing, also called *in silico* analysis of FDA-approved compounds, is an alternative to experimental approaches that promises to find new and effective drugs for rare diseases and to be tested faster in clinic (Paranjpe, Taubes, and Sirota 2019). It involves the analysis of big-data, including gene expression, chemical structure, genotype or proteomic data or electronic health records, the use of machine learning and leads to the elaboration of repurposing hypothesis (Hurle et al. 2013). Various computational approaches can be used individually or in combination in order to analyse large-scale data and then to elucidate the repurposing hypothesis. All these big-data need specific tools to be analysed, as they are very large and too complex to study and analyse with the traditional and classical statistical approaches (Pushpakom et al. 2019).

In the last decade, the development of transcriptome-based approaches to computational drug discovery was aiming to predict compounds that may reverse genetic signatures by comparing the gene expression signature before and after drug treatment with gene expression signatures in diseases. This approach involves matching of transcriptomic signatures and relies on the accessibility of gene expression data. The Connectivity Map (cMap) is the first large public database of gene expression profiles, generated after treatment with more than 1,300 compounds on several human cell lines (Lamb et al. 2006). The aim of this project was to generate a map used to find connections between gene expression profiles associated with disease states and following treatment. This map allows to identify drugs inducing a transcriptional response opposite to the one induced by a disease, and therefore these drugs may exert therapeutic effects (Malcomson et al. 2016). The effectiveness of this *in silico* method to predict potential compounds for a disease has been validated by using i*n vivo* models to validate the predicted drugs, such as citalopram for metastatic colon cancer (Noort et al. 2014). This technique highlights the potential of gene transcription profiling to link chemistry, biology and clinic by inferring gene profile similarities and differences.

Several resources that support the computational drug repositioning based on transcriptional data are available. For instance, the cMap has two extensions: statistically significant connections' map (sscMap) (Zhang and Gant 2009) and the mode of action by network analysis (MANTRA, https://mantra.tigem.it/) tool (Iorio et al. 2010). MANTRA has been developed to predict the drug mode of action and drug repurposing from the analysis of the cMAP. This approach, based on the network theory of gene expression data, allows us to find unexpected relationships among drugs, genes and diseases. It elucidates genome-wide targetable candidates by matching disease gene signatures against a library of 1,309 small compounds available for drug repurposing. The prediction for drug-disease pairs is based on the hypothesis that if a drug reverses the disease gene signature, it might potentially target molecular disease pathways. Moreover, this approach allows us to identify repurposed drug by searching the neighbourhood of a “seed” compound with a desired mechanism of action for compounds never linked before to that mechanism of action. Once potential compounds have been identified, *in vitro* and *in vivo* experiments are necessary to validate and to evaluate the efficiency of drug repositioning candidates (Carrella et al. 2014). Based on the MANTRA analysis, Fasudil (a Rho-kinase inhibitor) was identified as an inducer of autophagy because of its close proximity with a known autophagy inducer (2-deoxyD-glucose). Treatment on cells with Fasudil reveals the new mechanism of action of this drug as an enhancer of autophagy and may be repurposed for neurodegenerative diseases (Iorio et al. 2010). More recently, this approach has been used to identify pathways that could be targeted by chemical blockers in the context of cystic fibrosis (Hegde et al. 2015). These findings demonstrate the importance of computational approach in repurposing approved compounds for other human diseases.

II. **Aim of the thesis**

Studies of inherited kidney diseases have been key in dissecting interactions in cellular and molecular pathways that regulate the homeostasis and function of the endolysosomal system in tubular cells. The improvement of knowledge regarding cell biology-disease signatures, novel preclinical disease models and drug-based phenotypic screenings has been essential for developing targeted therapies that might deliver “first in class” drugs to the clinics. In particular, drug repurposing and the advent of compound libraries sscreenings are increasingly attractive, as they involve the use of lower risk compounds, with lower overall development costs and shorter development timelines.

The first part of the thesis is devoted to understanding the cellular and molecular mechanism of OCRL in the regulation of the endolysosomal pathways in the proximal tubule. Patients affected by Lowe syndrome or Dent disease 2, caused by mutations in the inositol polyphosphate 5-phosphatase OCRL, manifest PT dysfunction and LMW proteinuria, with only supportive care available. We characterized a mouse model lacking *Ocrl* and derived primary cultured PT cells in order to **describe the role of *OCRL* in the reabsorptive function of kidney PT cells and its involvement in endocytic trafficking.** The defect of endocytosis and PT absorption in Lowe syndrome and Dent disease 2 is due to increased levels of PI(4,5)P_2 and aberrant actin polymerization which block endosomal trafficking. Based on recent studies demonstrating that phosphatidylinositol 3-phosphates is involved in the actin pathways as co-activator with PI(4,5)P_2, **we targeted PI3 kinase (PI3K) *in vitro* and *in vivo* by using different class I PI3K inhibitors for drug repurposing in Lowe syndrome and Dent disease 2.**

In the second part of the thesis, we analyzed the mechanism linking MMUT deficiency, mitochondrial abnormalities and cell toxicity in kidney tubular cells. MMA patients, caused by the inactivating mutation of MMUT, display systemic organs dysfunction due to an accumulation of toxic organic acids, with no curative treatment. We used cell and animal-based models to **investigate the consequence of MMUT deficiency on PINK1/Parkin-mediated mitophagy and how these changes affect the mitochondria homeostasis and therefore the integrity of tubular cells**. Following these findings, we **performed a drug-disease network-based computational modeling approach to identify targetable pathways.** The *in silico* analysis indicated that targeting mitochondria function might potentially reverse cellular dysfunction associated with MMA.

The global aim of these studies is to improve our understanding of alterations of endomembrane trafficking and cellular homeostasis in a disease context, in order to find promising candidates for drug repurposing in the context of rare genetic diseases affecting the kidneys.

III. Results

1. OCRL Deficiency Impairs Endolysosomal Function in a Humanized Mouse Model for Lowe Syndrome and Dent Disease

Beatrice Paola Festa[1#], Marine Berquez[1#], Alkaly Gassama[1], Irmgard Amrein[2,3,4], Hesham M. Ismail[5], Marijana Samardzija[6], Leopoldo Staiano[7], Alessandro Luciani[1], Christian Grimm[4,6,8,], Robert L. Nussbaum[9,10], Maria Antonietta De Matteis[7], Olivier M. Dorchies[5], Leonardo Scapozza[5], David Paul Wolfer[2,3,4], Olivier Devuyst[1*]

[1]Institute of Physiology, University of Zurich, CH-8057 Zurich, Switzerland

[2]Division of Functional Neuroanatomy, Institute of Anatomy, University of Zurich, CH-8057 Zurich, Switzerland

[3]Institute of Human Movement Sciences and Sport, Department of Health Sciences and Technology, ETH Zurich, CH-8057 Zurich, Switzerland

[4]Neuroscience Center Zurich (ZNZ), University of Zurich, CH-8057 Zurich, Switzerland

[5]School of Pharmaceutical Sciences, University of Geneva, CMU 5-6, Rue Michel-Servet 1, Geneva, 1211, Switzerland

[6]Lab for Retinal Cell Biology, Department of Ophthalmology, University Hospital Zurich, University of Zurich, CH-8057 Zurich, Switzerland

[7]Telethon Institute of Genetics and Medicine (TIGEM), 80078 Pozzuoli, Naples, Italy

[8]Center for Integrative Human Physiology (ZIHP), University of Zurich, CH-8057 Zurich, Switzerland

[9]Department of Medicine and Institute of Human Genetics, University of California, CA 94143-0794 San Francisco, California; [10]Invitae Corporation, CA 94103 San Francisco

# These authors contributed equally to this work.

*Correspondence: Prof. Dr. med. Olivier Devuyst (🖂 Olivier.Devuyst@uzh.ch) University of Zurich, Institute of Physiology, Winterthurerstrasse 190, 8057 Zurich, Switzerland; Phone: +41 (0)44 635 50 82; Fax: +41 (0)44 635 68 14

Human Molecular Genetics, Volume 28, Issue 12, 15 June 2019, Pages 1931–1946

DOI.org/10.1093/hmg/ddy449

ABSTRACT

Mutations in *OCRL* encoding the inositol polyphosphate 5-phosphatase OCRL (Lowe oculocerebrorenal syndrome protein) disrupt phosphoinositide homeostasis along the endolysosomal pathway causing dysfunction of the cells lining the kidney proximal tubule. The dysfunction can be isolated (Dent disease 2) or associated with congenital cataracts, central hypotonia and intellectual disability (Lowe syndrome). The mechanistic understanding of Dent disease 2/Lowe syndrome remains scarce, due to limitations of animal models of OCRL deficiency.

Here, we investigate the role of OCRL in Dent disease 2/Lowe syndrome by using *Ocrl*$^{Y/-}$ mice, where the lethal deletion of the paralogue *Inpp5b* was rescued by human *INPP5B* insertion, and primary culture of proximal tubule cells (mPTCs) derived from *Ocrl*$^{Y/-}$ kidneys.

The *Ocrl*$^{Y/-}$ mice show muscular defects with dysfunctional locomotricity and present massive urinary losses of low-molecular-weight proteins and albumin, caused by selective impairment of receptor-mediated endocytosis in proximal tubule cells. The latter was due to accumulation of phosphatidylinositol 4,5–bisphosphate PI(4,5)P_2 in endolysosomes, driving local hyper-polymerization of F-actin and impairing trafficking of the endocytic LRP2 receptor, as evidenced in *Ocrl*$^{Y/-}$ mPTCs. The OCRL deficiency was also associated with a disruption of the lysosomal dynamic and proteolytic activity. Partial convergence of disease-mechanism and renal phenotypes observed in *Ocrl*$^{Y/-}$ and *Clcn5* $^{Y/-}$ mice suggest shared mechanisms in Dent disease 1 and 2.

These studies substantiate the first mouse model of Lowe syndrome and give insights into the role of OCRL in cellular trafficking of multiligand receptors. These insights open new avenues for therapeutic interventions in Lowe syndrome and Dent disease.

INTRODUCTION

The maintenance of body fluid and electrolyte homeostasis critically depends on the appropriate handling of solutes and water by the epithelial cells lining the proximal tubule (PT) of the kidney(1, 2). These cells are characterized by an efficient endolysosomal pathway involving the apical multiligand receptors megalin (LRP2) and cubilin (3). By processing internalized cargoes and recycling of receptors and transporters at the apical surface, the endolysosomal system of the PT cells recover essential substances that are filtered through the glomerulus, including a large variety of low-molecular-weight (LMW) proteins that would otherwise be lost in the urine (2). Congenital and acquired disorders of the endolysosomal pathway cause PT dysfunction (renal Fanconi syndrome) with massive urinary loss of solutes, dehydration, electrolyte imbalance, rickets, growth retardation, and the development of chronic kidney disease (CKD). Such PT dysfunctions are typically encountered in Dent disease, a rare, X-linked disorder characterized by LMW proteinuria, renal Fanconi syndrome, kidney stones, nephrocalcinosis and progressive renal failure (4, 5).

Dent disease is genetically heterogeneous. The majority of cases (approx. 60%) is due to mutations in the *CLCN5* gene that encodes the electrogenic Cl^-/H^+ exchanger ClC-5 (Dent disease 1, MIM # 300009) (6). In a subset of patients (~15-20%), the disease is caused by mutations in *OCRL*, the gene encoding the type II phosphatidylinositol (PI) bisphosphate 5-phosphatase OCRL (Dent disease 2, MIM #300555). Mutations in OCRL are also associated with the oculocerebrorenal syndrome of Lowe (MIM # 309000), which includes systemic manifestations such as congenital cataracts, cognitive disability and hypotonia (4, 7). OCRL is a protein of 110 kDa which, in addition to the 5-phosphatase catalytic domain, comprises: (i) a pleckstrin homology (PH) domain containing a clathrin-binding site (8); (ii) an ASPM, SPD-2, Hydin (ASH) domain, characteristic of protein that localizes to centrosome and primary cilia (9); and (iii) a RhoGAP-like domain, which mediates interactions involved in cytoskeleton dynamics and progression of cell cycle (10). Almost all the mutations associated with Lowe syndrome occur in exons 8-23 which include the 5-phosphatase catalytic domain, the ASH domain and the RhoGAP-like domain. Conversely, the majority of mutations that cause Dent disease 2 are positioned in exons 1-7 which comprise the PH domain (11). Although mutations in the catalytic domain of *OCRL* have been described in both clinical profiles, the mutations in Dent disease 2 are always missense - compatible with a residual biological activity that could explain a less severe cellular phenotype (7).

The convergence of clinical phenotypes among patients with mutations in *OCRL* and *CLCN5* raises the questions whether these genes products are part of the same pathways and how they cause dysfunction of endolysosomes in PT cells. ClC-5 is predominantly expressed in the early endosomes of PT cells of the kidney, potentially involved in their maturation towards the degradative compartments or the recycling route (6). Studies in mouse models showed that the functional loss of ClC-5 generates a trafficking defect involving megalin and cubilin, reflected by defective endocytosis and manifestations of PT dysfunction (6, 12). OCRL is located at different stations of the endo-lysosomal pathway where it maintains the cellular metabolism of phosphatidylinositol 4, 5-bisphosphate $PI(4,5)P_2$, an essential regulator of membrane trafficking. Increased $PI(4,5)P_2$ levels and marked vesicular trafficking defects affecting the endocytic network have been observed in cells lacking OCRL, resulting in defective receptor-mediated endocytosis (13).

The direct impact of OCRL on transport events leading to renal Fanconi syndrome cannot be reliably assessed on dedifferentiated cell systems including non-kidney or non-epithelial cell types, or clonal cells isolated from urine (14). Renal biopsy material, usually obtained at an advanced disease stage, is of limited value. Furthermore, limitations of animal models of OCRL deficiency impede the development of translational studies. The first *Ocrl* KO mouse showed no kidney, eye or brain defects (15), due to a compensation by INPP5B, the closest paralogue of OCRL in mice and humans (16). Accordingly, a generalized endocytic defect (affecting both receptor-mediated and fluid-phase endocytosis) was detected in a conditional tubular deletion of *Ocrl* and *Inpp5b* mouse model (17). However, studies performed in this strain do not allow to discriminate the individual role of OCRL and INPP5B in the pathophysiology of Dent disease.

Recently a mouse model expressing human INPP5B in $Ocrl^{Y/-}$; $Inpp5b^{-/-}$ background was generated (18). The replacement of mouse *Inpp5b* with human *INPP5B* in the whole body of $Ocrl^{Y/-}$ mouse provides a humanized background, which therefore allows to investigate the consequences related to the specific loss of OCRL activity. Preliminary studies revealed PT dysfunction in this line (18), with no investigation of the time-course, multi-systemic aspect, and cellular basis of this defect. Here, we analyzed in detail the multi-systemic phenotype of these $Ocrl^{Y/-}$; $Inpp5b^{-/-}$; *BAC-INPP5B* mouse model; compared the kidney dysfunction to that of *Clcn5* KO mice; and investigated the mechanisms underpinning epithelial transport defects in Lowe syndrome.

RESULTS

Ocrl$^{Y/-}$ *mice show early manifestations of proximal tubule dysfunction*

A humanized mouse model for Lowe syndrome/Dent disease 2 was generated by targeted disruption of both *Ocrl* and *Inpp5b* and oocyte injection of a bacterial artificial chromosome (BAC) containing the human gene *INPP5B* to avoid embryonic lethality (18). The mouse littermates lacking *Inpp5b* while harbouring *BAC-INPP5B* expression with *Ocrl* are referred to as *Ocrl*$^{Y/+}$ (*Ocrl*$^{Y/+}$; *Inpp5b*$^{-/-}$; *BAC-INPP5B*) whereas those lacking *Ocrl* are *Ocrl*$^{Y/\ -}$ (*Ocrl*$^{Y/-}$; *Inpp5b*$^{-/-}$; *BAC-INPP5B*) mice, respectively. All mice were born at mendelian ratio and were viable and fertile. The genotype of *Ocrl* mice was demonstrated by genomic DNA analyses of *Ocrl*, *Inpp5b* and *BAC-INPP5B* (Suppl. Fig. 1A) and immunoblotting for OCRL (Suppl. Fig. 1B) in kidney samples derived from *Ocrl*$^{Y/-}$ and *Ocrl*$^{Y/+}$ mice.

We first used the *Ocrl* mice to characterize the kidney phenotype over time. Growth retardation was observed in *Ocrl*$^{Y/-}$ mice starting from 16 weeks of age onwards (Fig. 1A), whereas manifestations of PT dysfunction appeared in *Ocrl*$^{Y/-}$ mice from 8 weeks of age, with albuminuria (Figs. 1B and 1C) and LMW proteinuria (Figs. 1D and 1E). The inappropriate loss of the LMW clara cell secretory protein 16 (CC16) in the urine of *Ocrl*$^{Y/-}$ mice was observed at all time points analyzed (Fig. 1D). Western blotting of the urine confirmed the major loss of transferrin (TFR) and vitamin D binding protein (VDBP) along CC16 in the urine of *Ocrl*$^{Y/-}$ mice (Fig. 1E). The *Ocrl*$^{Y/-}$ mice did not show manifestations of renal failure, and no polyuria, calciuria, glycosuria and phosphaturia during the timeframe of investigation, suggesting a partial renal Fanconi syndrome (Table 1). The expression levels of *BAC-INPP5B* were not associated with variable levels of PT dysfunction in *Ocrl*$^{Y/-}$ mice (Suppl. Figs. 1C-F). Since mutations in *CLCN5* and *OCRL* produce similar kidney defects in human patients, we compared the severity of PT dysfunction in the *Clcn5*$^{Y/-}$ and *Ocrl*$^{Y/-}$ mouse models. The *Ocrl*$^{Y/-}$ mice display a milder LMW proteinuria (CC16) than that observed in *Clcn5*$^{Y/-}$ mice (Fig. 1F). This difference is most likely reflecting specific roles of ClC-5 and OCRL along the endo-lysosomal pathway.

Ocrl$^{Y/-}$ *mice show a specific defect in receptor-mediated endocytosis*

To determine the mechanism of LMW proteinuria, we followed the *in vivo* uptake of the LMW protein Cy5-labelled β-lactoglobulin in the kidneys of *Ocrl*$^{Y-}$ mice compared to their control littermates. Fifteen minutes after injection, a substantial accumulation of fluorescent vesicles was observed in the brush border of PT cells of the *Ocrl*$^{Y/+}$ mice, contrasting with a considerable reduction of the signal in PT cells from *Ocrl*$^{Y/-}$ mice (Fig. 2A). A similar defective uptake in Cy5-labelled β-lactoglobulin was observed in *Clcn5*$^{Y/-}$ tubules (Fig. 2B). By contrast, the internalization of Alexa 647-dextran, a marker of fluid phase endocytosis, was unaltered in *Ocrl*$^{Y/-}$ mice (Fig. 2C), suggesting that loss of OCRL function impacts specifically on receptor-mediated endocytosis. To substantiate this observation, we investigated the LRP2 receptor and found its expression dramatically decreased in PT cells of the *Ocrl*$^{Y/-}$ kidneys whereas its mRNA level was unchanged (Figs. 2D-F). In line with absent phosphaturia and glycosuria, no modifications in the sodium-phosphate cotransporter IIa (NaPi-IIa), the sodium-glucose cotransporter 2 (SGLT2) or other PT components were observed in *Ocrl*$^{Y/-}$ kidneys (Figs. 2E and 2F).

These data reveal that a defective receptor-mediated endocytosis, caused by a decreased protein level of LRP2, characterizes *Ocrl*$^{Y/-}$ mice, similar to *Clcn5*$^{Y/-}$ mice. The renal Fanconi syndrome is restricted to LMW proteinuria in *Ocrl*$^{Y/-}$ mice, contrasting with a more severe PT dysfunction in *Clcn5*$^{Y/-}$ mice. At age 8 weeks, the latter showed a decreased expression of SGLT2 and NaPi-IIa (Suppl. Fig. 2A), explaining glycosuria and phosphaturia along polyuria and calciuria (Table 1; Suppl. Figs. 2C-D), and a defective uptake of fluid-phase endocytosis (dextran) markers (Suppl. Fig. 2B).

Loss of OCRL increases PI(4,5)P$_2$ and disrupts receptor-mediated endocytosis in vitro

In order to further analyse the endocytic defect observed *in vivo*, we developed primary cultures of PT cells (mPTC) from micro-dissected PT segments of *Ocrl*$^{Y/-}$ mice aged 8 weeks. This cell culture system preserves the differentiation and polarized transport processes and therefore represents a relevant in *vitro* model to investigate mechanisms underlying PT disorders (19). To validate the *Ocrl* cellular system, we evaluated whether the loss of OCRL in mPTC reproduced the typical endosomal accumulation of PI(4,5)P$_2$ observed in Lowe syndrome/Dent disease2 (20). Compared to control, *Ocrl*$^{Y/-}$ mPTCs exhibited a remarkable increase of PI(4,5)P$_2$ in early endosomal structures, as shown by colocalization with the early endosome marker EEA1 (Figs. 3A-B). The unchanged PI3P levels, the PI hallmark of the endosomal system, demonstrated that OCRL disruption in mPTCs exclusively targets the homeostasis of PI(4,5)P$_2$ (Suppl. Fig. 3A). These results, which are consistent with PI(4,5)P$_2$ accumulation observed in a transgenic zebrafish model of Lowe syndrome or in OCRL-depleted immortalized cells, substantiate the reliability of *Ocrl* mPTCs system (13, 21).

Given that the tight regulation of PI(4,5)P$_2$ homeostasis is fundamental for a proper endocytic trafficking, we asked whether its increase at the early endosomes might impair the endocytic function of mPTCs. Functional studies demonstrated that albumin uptake was markedly reduced in *Ocrl*$^{Y/-}$ (-84%) when compared to control mPTCs (Fig. 3C). A similar disruption of the endocytic capacity was observed in *Clc5*$^{Y/-}$ mPTCs (Fig. 3D). Confirming the observations made *in vivo,* fluid phase endocytosis was unaltered in *Ocrl*$^{Y/-}$ mPTCs (Fig. 3E), highlighting the specificity of the defect in receptor-mediated endocytosis.

OCRL deficiency perturbs expression of LRP2 through aberrant F-actin polymerization

We next examined whether the defective uptake capacity of *Ocrl*$^{Y/-}$ mPTCs was reflected by alterations of the endogenous LRP2 expression. LRP2 protein level was reduced in the total lysates of mPTCs lacking OCRL (Fig. 4A), similarly to *Clcn5*$^{Y/-}$ mPTCs (Suppl. Fig. 4A). This reduction was confirmed by the analysis of the confocal Z-stack images, evidencing a decreased LRP2 fluorescent signal in each focal plane throughout the entire volume of *Ocrl*$^{Y/-}$ mPTCs (Fig. 4B and Suppl. Fig. 4B). The latter analysis showed a shift of LRP2 signal from the apical plasma membrane towards a more intracellular compartment in *Ocrl*$^{Y/-}$ mPTCs, whose polarization is defined by the typical apical (wheat germ agglutinin, WGA) and basolateral (Na^+, K^+-ATPase) markers (Fig. 4C and Suppl. Fig. 4C). This result was corroborated by a striking decrease of LRP2 level in the plasma membrane fraction of *Ocrl*$^{Y/-}$ mPTCs (Fig. 4D). These changes were not associated with LRP2 transcriptional modifications or alterations of other PT receptors or transporters (Suppl. Fig. 3B).

The intracellular localization of LRP2 in *Ocrl*$^{Y/-}$ mPTCs prompted us to examine its organelles compartmentalization. OCRL is known to modulate the trafficking of endocytic receptors by orchestrating the recycling of endosomal vesicles to the surface (13). Thus, lack of OCRL function might disrupt the return of the endocytic receptors to the apical membrane, leading to their accumulation in endosomal structures. Imaging studies confirmed LRP2 increase within EEA1$^+$ early endosomes in *Ocrl*$^{Y/-}$ mPTCs, suggesting that loss of OCRL function impacts on both expression and distribution of this endocytic scavenger (Fig. 4E).

As PI(4,5)P_2 promote the recruitment of the actin nucleating machinery, we asked whether their endosomal accumulation, observed in *Ocrl*$^{Y/-}$ mPTCs, might locally induce an aberrant actin polymerization and, in turn, affect the trafficking of endocytic receptors (22).We observed that, in *Ocrl*$^{Y/-}$ mPTCs, the levels of actin stress fibres decreased and foci of filamentous actin (F-actin) accumulated on internal membranes ruffles (Suppl. Fig. 4D). Compared to controls, an increase of F-actin structures, colocalizing with EEA1, was observed in *Ocrl*$^{Y/-}$ mPTCs (Suppl. Fig. 4E). This uncontrolled actin dynamics might impede the entrance of the endosomes in the recycling route and coerce LRP2 to stick inside them. Supporting this hypothesis, a considerable amount of LRP2 vesicles were coalescent with F-actin membranes (Fig. 4F). Furthermore, by high magnification confocal microscopy, it was possible to visualize the formation of F-actin basket-like structure surrounding LRP2 (Suppl. Fig. 4F). These data indicate that the increased association of F-actin with early endosomes may affect the endocytic trafficking and prevent the recycling of LRP2 to the apical surface. In order to substantiate the role of OCRL in maintaining the recycling activity, we investigated the localization of the canonical recycling marker transferrin receptor (TfR), which crosses the same endocytic stations traveled by LRP2 (plasma membrane - early endosomes/recycling endosomes) (23). Our data showing the redistribution of TfR from the plasma membrane to enlarged cytoplasmic structures, which also trap LRP2, provide another evidence of defective endocytic recycling in *Ocrl*$^{Y/-}$ mPTCs (Suppl. Fig. 5A and Fig. 4G).

We also tested whether the lack of OCRL might affect the trafficking of the cation-independent mannose 6-phosphate receptor (CI-MPR), which is required for the transport of lysosomal enzymes and travels through intracellular itineraries diverging from those exploited by LRP2 (trans golgi network-late endosomes- plasma membrane) (24). An increase in the CI-MPR associated with peripheral structures and a decrease in the perinuclear pool was observed in the kidneys and mPTCs from *Ocrl*$^{Y/-}$ mice compared to controls (Suppl. Figs. 5B-C), indicating a defective retrograde transport of CI-MPR from the endosomes to the Golgi. All together, these data suggest that the actin-trapping mechanism impairing the recycling of LRP2 extends to other receptors traveling through the endosomal structures of *Ocrl*$^{Y/-}$ mice, highly relevant for the molecular basis of Lowe syndrome.

OCRL depletion alters lysosomal dynamics and function

It has been recently shown that, under lysosomal overload conditions, OCRL translocates on the lysosomal membrane, where it ensures adequate levels of PI(4,5)P_2 necessary for fusion and subsequent degradation of cargo vesicles (25). We thus explored whether loss of OCRL function might generate a rearrangement of PI(4,5)P_2 at the lysosomal membrane and, consequently, affect lysosomal morphology. Confocal microscopy analysis showed that *Ocrl* deletion increased the number of PI(4,5)P_2 positive structures colocalized with LAMP1-labeled lysosomes (Fig. 5A). These changes were associated with dramatic modifications in the dynamics of lysosomes as evidenced by their abnormal increase in number and size (Fig. 5B). As changes in lysosomal dynamics could affect their proteolytic activity, we examined whether OCRL disruption impairs the lysosomal cargo degradation in *Ocrl*$^{Y/-}$ mPTCs. To this end we used dequenched BSA (BSA-DQ) reagent, which is readily incorporated by cells via fluid-phase endocytosis. Upon fusion with endo-lysosomes, BSA-DQ is digested into smaller fragments, thereby relieving its self-quenching properties and causing a fluorescent signal that reflects lysosomal degradative capacity (26). *Ocrl*$^{Y/-}$ mPTCs showed a remarkable decrease in BSA-DQ fluorescent puncta colocalized with LAMP1 (Fig. 5C), indicating a specific impairment of lysosomal proteolysis as fluid phase endocytosis was not affected by the loss of OCRL. To substantiate the defective lysosomal activity, we tested the processing of the epidermal growth factor receptor (EGFR), an endogenous protein which, upon EGF induced internalisation, is normally sorted to endo-lysosomal proteolytic pathway for degradation (27). Control mPTCs, 90 min after EGF stimulation, showed an efficient degradation of EGFR. On the contrary, at the same time frame, the levels of EGFR remained high in *Ocrl*$^{Y/-}$ mPTCs, suggesting a delayed lysosomal processing of the receptor (Fig. 5D). One mechanism by which cargo clearance might be impeded is a defective maturation of lysosomal cathepsins. Western blot analyses of Cathepsin D (Cts-D) showed a decreased generation of the 32kDa mature Cts-D in *Ocrl*$^{Y/-}$ mPTCs compared to control (Fig. 5E). We next tested the lysosomal Cts-D activity by incubating the cell with Bodipy-FL-PepstatinA (PepA), a fluorescence-tagged PepA that binds to the active site of Cts-D in acidic lysosomes. Although the majority of lysosomes were co-stained with PepA in control mPTCs, the number of PepA-labeled vesicles colocalizing with LAMP1 were substantially lower in *Ocrl*$^{Y/-}$ mPTCs (Fig. 5F). Similarly, the lysosome-based processing of the LMW β-lactoglobulin, which is normally internalized and degraded by endolysosomes, was dramatically reduced in *Ocrl*$^{Y/-}$ proximal tubules compared to wild-type (Fig. 5G).

To investigate whether mis-sorting of lysosomal hydrolases in the extracellular space might contribute to the aberrant lysosomal proteolysis observed in *Ocrl*$^{Y/-}$ mice, we tested for and detected significantly increased levels of the lysosomal protease Cts-D (immature form) in the plasma of these mice (Suppl. Fig. 6A). This result was in line with the mis-trafficking of CI-MPR at the cell periphery and with previous studies performed in patients with Lowe syndrome (13). Collectively these data indicate that OCRL is important to maintain lysosome homeostasis, itself crucial for PT function. Of note, impaired lysosomal proteolysis and insufficient degradation of β-lactoglobulin was also observed in *Clcn5*$^{Y/-}$ proximal tubules (Suppl. Figs. 6B-D) indicating that OCRL and ClC-5 are part of the same cellular pathways.

The Ocrl$^{Y/-}$ *mice show dysfunctional locomotricity associated with muscular defects*

In order to test whether the deletion of OCRL in this model was reflected by extra-renal manifestations, we performed comprehensive behavioral tests of *Ocrl* mice to examine basic motor activity, learning and memory skills, social behaviour and vision. To identify disturbances in locomotor activity, we evaluated the general mobility of the mice by challenging them with the open field large arena test, which has been extensively used for analyzing the locomotor defects exhibited by Parkinson and Huntington mouse models (28, 29). While velocity was comparable between genotypes (data not shown), *Ocrl*$^{Y/-}$ mice exhibited an overall decreased locomotor activity, as scored by the measurement of their trajectories (Figs. 6A and 6B). The *Ocrl*$^{Y/-}$ mice presented more resting episodes than controls, as well as fewer lingering and walking events during the test (Fig. 6C). Of note, center-field avoidance was robust and equal in both genotypes (data not shown), suggesting that the impaired motor activity in *Ocrl*$^{Y/-}$ mice was more likely driven by a muscular defect rather than an abnormal anxiety-related response.

To test the latter hypothesis, we pursued mice analyses in IntelliCage, an automated system, which allowed the evaluation of the spontaneous behaviour of the animals (30). During free adaptation phase, *Ocrl*$^{Y/-}$ mice made fewer corner visits compared to controls, confirming the reduced locomotor and exploratory activity shown in the test above (data not shown). However, *Ocrl*$^{Y/-}$ mice showed an incompetent licking pattern, which became more evident during the drinking restriction protocol and was associated with slower progress of water intake during drinking sessions (Fig. 6D).We excluded an influence of the kidney defect on the licking pattern as similar water intake was detected between genotypes (Suppl. Fig. 7A). Thus, the impaired licking of *Ocrl*$^{Y/-}$ mice was most likely caused by a global muscular dysfunction, which affected also the oro-lingual motor apparatus.

To explore whether the defective locomotricity evidenced in *Ocrl*$^{Y/-}$ mice was driven by muscular defects, we performed whole body composition analysis (EchoMRI), which evidenced a striking decrease in lean mass/body weight ratio in *Ocrl*$^{Y/-}$ mice compared to controls (Fig. 6E), with a global reduction of the mass of several hind limb (gastrocnemius, triceps surae, plantaris, tibialis posterior/anterior and quadriceps) muscles relative to body weight (Fig. 6F) demonstrating skeletal muscle atrophy. These changes were paralleled by a strong increase in plasma creatine kinase (CK) activity, suggesting membrane fragility of striated muscles. (Fig. 6G). These events, which are in line with the muscle hypotonia observed in Lowe Syndrome patients (7), support the motor defect detected in *Ocrl*$^{Y/-}$ mice.

To assess the cognitive function of *Ocrl* mice we applied IntelliCage standard protocol which investigated the hippocampus-dependent spatial learning ability of the animals. No sign of dysfunctional learning was observed in OCRL deficient mice, even during the most challenging chaining task (data not shown). Aggressive behavior reported in patients with Lowe syndrome was also not reflected in *Ocrl*$^{Y/-}$ mice, which showed intact sociability (Suppl. Fig. 7B). Given that congenital cataract and glaucoma are hallmarks of Lowe syndrome, we also examined the visuospatial and visuoperceptual ability of *Ocrl* mice. During water maze cue navigation, *Ocrl*$^{Y/-}$ mice exhibited a robust learning without evidences for an inadequate vision (Suppl. Fig. 7C). In addition no noticeable differences were observed in lens epithelium and in retinal morphology between control and *Ocrl*$^{Y/-}$ mice. Irrespective of the *Ocrl* genotype, an impairment of retinal photoreceptor layer was observed in mice harboring *rd8* (retinal degeneration 8) mutation in *Crb1* gene, a spontaneous mutation associated with C57BL/6N genetic background, leading to photoreceptor rosette-like structures when expressed homozygously (*rd8/rd8*). (Suppl. Figs.7D and 7E)(31).

DISCUSSION

In these studies, we present the first OCRL-deficient mouse model that associates renal and extra-renal manifestations encountered in patients with Lowe syndrome. The absence of OCRL in kidney proximal tubule triggers endolysosomal defects and epithelial dysfunction, with a consistent LMW proteinuria reflecting defective receptor-mediated endocytosis due to decreased expression of LRP2 endocytic receptor, in absence of renal failure. We also evidence a partial convergence of disease-mechanism and kidney tubular phenotype between mouse models deficient in ClC-5 (Dent disease 1) and OCRL (Lowe syndrome/Dent disease 2). These results provide insights into the mechanisms of endocytosis and the pathophysiology of Dent disease/Lowe syndrome.

In contrast with a previous kidney tubular conditional *Ocrl* and *Inpp5b* KO mouse model, where the phenotype reflects the combined loss of OCRL and INPP5B (17), the genetic architecture of the mouse line investigated here allows to directly address dysfunctions related to the single loss of OCRL activity (18). The reinsertion of human INPP5B in the *Ocrl*$^{-/-}$; *Inpp5b*$^{-/-}$ background, irrespective of its level of expression, was fundamental for survival but it was not compensating for the renal defect. This observation is in line with studies on cells derived from patients with Lowe syndrome, which exhibit INPP5B-independent phenotypic variability (32). Although the renal defect was observed in all the *Ocrl*$^{Y/-}$ mice analysed, a noticeable spread was observed comparing individual animals. This individual variability was not due to different levels of INPP5B expression. The possibility that compensatory changes in kinases or phosphatases crossing the same metabolic pathway than OCRL may contribute to such variability should be further investigated.

The differences between the conditional double *Ocrl* and *Inpp5b* KO and the humanized transgenic *Ocrl*$^{Y/-}$ mice studied here are evident when comparing the defective tubular endocytic phenotypes. The conditional deletion of OCRL and INPP5B resulted in an unspecific impairment of the clathrin-dependent and clathrin-independent endocytosis. By contrast, the single lack of OCRL in *Ocrl*$^{Y/-}$ transgenic mice resulted in a selective dysfunction of the clathrin receptor-mediated endocytosis, as evidenced by the defective uptake of β-lactoglobulin and the unaffected internalization of the fluid-phase marker dextran. These differences are in line with the function of OCRL in regulating the membrane trafficking of clathrin-coated vesicles (33).

Defective receptor-mediated endocytosis was reflected in *Ocrl*$^{Y/-}$ mice by a consistent LMW proteinuria, occurring early, in absence of renal failure. In contrast, the *Ocrl*$^{Y/-}$ mice did not show glycosuria, phosphaturia and calciuria, even at old age, mimicking the partial renal Fanconi syndrome typically present in the majority of patients carrying mutations in OCRL (7, 34) . The *Clcn5*$^{Y/-}$ mice showed a similar defect in receptor-mediated endocytosis, causing a severe LMW proteinuria. The *Clcn5*$^{Y/-}$ mice also showed a defective uptake of fluid phase endocytosis markers, in line with previous data from mouse models and patient-derived cells (35-37) but not with others (12). The presence of a more complete form of renal Fanconi syndrome in the *Clcn5*$^{Y/-}$ mouse model was evidenced by the hypercalciuria, phosphaturia and glucosuria detected at 8 weeks, paralleled by a decreased expression of SGLT2 and NaPi-IIa in addition to LRP2.

Filtered LMW proteins are reabsorbed through megalin /LRP2 and cubilin endocytic receptors expressed at the apical membrane of PT cells. This reabsorptive function is maintained by the degradative and recycling activity of the endolysosomal system, as evidenced by severe defects in tubular homeostasis associated with endolysosomal disorders (1, 2). Our investigations characterize the involvement of LRP2 in the pathogenesis of Lowe syndrome, and demonstrate analogies with the endocytic defect associated with the loss of ClC-5 in Dent disease1/*Clcn5*$^{Y/-}$ mouse model (12). Previous studies, relying on OCRL-deficient immortalized cells expressing LRP2 mini-receptor, showed a redistribution of LRP2 from the apical membrane to the intracellular compartments rather than a defective expression (13). Here, analyses on kidney tissues reveal a remarkable decrease of LRP2 protein in the proximal tubule from *Ocrl*$^{Y/-}$ mice, similar to that observed in *Clcn5*$^{Y/-}$ mice. These findings are in line with observations made in zebrafish pronephros, demonstrating the evolutionary conservation of the role of OCRL in endocytosis (21). The identification of converging kidney phenotypes in mouse models for Lowe syndrome and Dent disease supports the view that the endosomal exchanger ClC-5 and the 5-phosphatase OCRL impact on common pathways operating in kidney tubular cells. In absence of transcriptional changes, the mechanism by which the loss of ClC-5 or OCRL might affect LRP2 protein levels remains to be clarified. First, the decrease of apical LRP2 may reflect an increased shedding of the receptor in the urine in response to the endolysosomal engorgement observed in *Ocrl*$^{Y/-}$ mice. Previous studies showed that LRP2 is a substrate for metalloproteases and is constitutively subjected to ectodomain shedding (38). This event produces LRP2 membrane-associated fragments, which in turn form the substrate for γ- secretase, the main player of regulated intramembrane proteolysis. Preliminary data showing a higher abundance of LRP2 fragments in *Ocrl*$^{Y/-}$ urine, together with a transcriptional increase of all subunits composing the γ-secretase (39) are in line with this hypothesis (data not shown). Alternatively, the loss of LRP2 could be explained by an increased urinary excretion of (full length) LRP2-containing exosomes. A third mechanism might be an aberrant degradation of LRP2, mediated by the proteasome in response to altered lysosomal proteolysis (see below). Further studies of post-translational modifications potentially triggering LRP2 to the proteasome are necessary to test this hypothesis (40).

By establishing differentiated and polarized proximal tubular cell cultures (mPTCs) directly derived from *Ocrl*$^{Y/-}$ mouse kidneys (19), we were able to reconstitute critical aspects of the disease *in vitro*. The *Ocrl*$^{Y/-}$ mPTCs recapitulate the selective impairment of receptor-mediated endocytosis and the ectopic accumulation of $PI(4,5)P_2$ in early endosomes (20). The latter is due to the loss of 5-phospatase activity of OCRL that regulates the transition from high (plasma membrane) to low (early endosomes) levels of PI(4,5)P_2 in clathrin coated vesicles, enabling progression of the cargo/receptor along the endocytic pathway (33, 41). The PI(4,5)P_2 dynamic is critical for actin assembly at the plasma membrane ruffles and early endosomes, hence, for the regulation of membrane trafficking (42, 43). Accordingly, the endosomal accumulation of PI(4,5)P_2 in *Ocrl*$^{Y/-}$ mPTCs triggers an aberrant F-actin polymerization, which impairs the recycling of residual LRP2, thus impeding the endocytic uptake. The actin-trapping mechanism impairing LRP2 recycling might be extended to other receptors, as evidenced by the redistribution of the canonical recycling marker TfR in *Ocrl*$^{Y/-}$ mPTCs. These defects in receptor recycling represent an appealing druggable target for rescuing the epithelial dysfunction associated with the disease.

It has been shown recently that OCRL can translocate to the lysosome under cargo overload conditions, where its fine regulation of PI(4,5)P_2 balance is instrumental for maintaining lysosomal function (25). Here, we demonstrate that lack of OCRL induces an abnormal lysosomal accumulation of PI(4,5)P_2 leading to altered lysosomal dynamics and defective lysosomal function, as scored by decreased expression and activity of lysosomal cathepsin D and impaired processing of lysosomal substrates in *Ocrl*$^{Y/-}$ kidney and mPTCs. These results, which are consistent with previous observations on biopsies derived from Lowe patients (25), raise the issue of the mechanisms responsible for lysosomal dysfunction associated with loss of OCRL. The peripheral mislocalization of the CI-MPR, a protein regulating the transport of lysosomal hydrolases from the Golgi to lysosomes, along with increased levels of lysosomal protease Cathepsin D (immature form) in the plasma, indicates that misrouting of lysosomal enzymes could be involved. This finding is in line with previous studies performed in Lowe syndrome patients (13). Alternatively, the lysosomal engulfment of PI(4,5)P_2 driven by the loss of OCRL may somehow alter the vacuolar-type H+-ATPase (V-ATPase) complex, thereby impairing lysosome acidification and activation of cathepsins. It should be noted that similar defects in receptor-mediated endocytosis and lysosomal dynamic and activity are observed in mouse and cellular models deficient for the endosomal ClC-5 or lysosomal cystinosin (CTNS) transporters, highlighting the role of the endolysosome network as crucial signaling hub to ensure epithelial homeostasis (44).

Studies on the locomotor, neurological and vision abnormalities detected in patients with Lowe syndrome have been hindered by the limitations of available mouse models. Deep phenotyping analyses unveiled a defective locomotricity in *Ocrl*$^{Y/-}$mice, which reflects a global impairment of the muscular apparatus, as indicated by the increased plasma activity of protein creatine kinase and atrophy of several hind limb muscles. This phenotype was reminiscent of the muscle hypotonia associated with Lowe syndrome and therefore highly relevant (45). Whether this defective muscular/motor pattern originates from a primary myopathy or is rather a consequence of neurological alterations and how OCRL contributes in maintaining muscular tone remains to be further investigated. Behavior, learning-memory function and vision were not altered in *Ocrl*$^{Y/-}$mice. The discrepant clinical manifestations in mice and humans could be partly explained by differences in tissue-specific expression of enzymes with overlapping functions or by specific roles of OCRL in the tissues affected by the disease (46, 47).

Collectively, these studies validate the first mouse model of Lowe syndrome and give insights into the role of OCRL in cellular trafficking of multiligand receptors. Partial convergence of disease-mechanism and renal phenotypes observed in *Ocrl*$^{Y/-}$ and *Clcn5* $^{Y/-}$ mice suggest shared mechanisms in Dent disease 1 and 2. These insights open new avenues for therapeutic interventions in Lowe syndrome and Dent disease.

MATERIALS AND METHODS

Antibodies and reagents. The following antibodies were used: rabbit anti-human transferrin (A0061, Dako); rabbit anti-human Gc-globulin (also known as VDBP, A0021, Dako); rabbit anti-uteroglobin (also known as CC16, ab40873, Abcam); rabbit anti-SLC1A5 (also known as SGLT2, ab84903, Abcam); rabbit NaPi-IIa (gift from C.A.Wagner, University of Zurich, Zurich, Switzerland); rabbit anti-human AQP1 (ab2219, Millipore); mouse anti-β-actin (A2228, Sigma-Aldrich); mouse conjugated to Fluorescein (FITC) anti-PI(4,5)P_2 (Z-G045, Echelon Biosciences Inc.); mouse anti-EEA1 (610456, BD Bioscience); rabbit anti-RFP (600-401-379, ROCKLAND); sheep anti-LRP2 (gift from P. Verroust and R. Kozyraki, INSERM, Paris, France); mouse anti Flotillin-1(610821, BD Bioscience); mouse anti-α-tubulin (T5168, Sigma-Aldrich); rabbit anti-GAPDH (2118, Cell Signaling Technology); rat anti-LAMP1 (sc-19992, Santa Cruz Biotechnology); goat anti-Cathepsin-D (Cts-D; sc-6486, Santa Cruz Biotechnology); rabbit anti-EGFR (1005 sc-03, Santa Cruz Biotechnology); Alexa-488 Phalloidin (F-actin , A12379, Thermofisher Scientific); mouse anti-Transferrin Receptor Antibody (H68,4, ThermoFisher Scientific), wheat germ agglutinin (WGA) FITC Conjugate (L 4895, Sigma-Aldrich), mouse anti-Na^+/K^+-ATPase subunit α1 (C464.6 EMD Millipore), rabbit anti-MPR and rabbit anti-OCRL (gift from A. De Matteis, Telethon Institute of Genetics and Medicine (TIGEM), Pozzuoli, Italy).

Mouse models. Experiments were conducted on age- and gender-matched *Ocrl*$^{Y/+}$; *Inpp5b*$^{-/-}$; and *Ocrl*$^{Y/-}$; *Inpp5b*$^{-/-}$ mouse littermates harboring BAC-*INPP5B* expression in equal copies (BAC1) (129S/SvEv * 129S6/SvEvTac * FVB/N* C57BL/6 background), (18) and *Clcn5*$^{Y/+}$and *Clcn5*$^{Y/-}$ mice littermates (C57BL/6 background) (48). All the mice used in this study were expressing similar levels of *INPP5B* as analyzed by RT-qPCR (see below). Mice were maintained under temperature-and humidity-controlled conditions with 12 h light/12 h dark cycles with free access to appropriate standard diet in accordance with the institutional guidelines of National Institutes of Health Guide for the Care and Use of Laboratory Animals.

Renal function parameters. Mice were placed overnight in metabolic cages with ad libitum access to food and drinking water. Urines were collected over ice and body weight, water intake and diuresis were measured at the indicated time point (49). Blood (from sublingual vein) was obtained after anesthesia with ketamine/xylazine or isoflurane. Urine and blood parameters were measured using a UniCel DxC 800 pro Synchron (Beckman Coulter, Fullerton, CA, USA), whereas urinary Clara cell protein (CC16) concentration was measured in duplicate by enzyme-linked immunosorbent assay (ELISA; BIOMATIK EKU03200) (44). Albuminuria was measured by Coomassie Blue staining by using ProtoBlue Safe (EC-722, national diagnostics) according to manufacturer instructions.

Kidney isolation and primary cultures of proximal tubule cells. The kidneys were harvested from *Ocrl*$^{Y/+}$ and *Ocrl*$^{Y/-}$ mice and *Clcn5*$^{Y/+}$and *Clcn5*$^{Y/-}$ mice as previously described (44). Briefly, one half of the kidney was fixed in 4% PFA and processed for immunostaining while the other half was used for protein isolation or RT-qPCR analysis. The contralateral kidney was taken to generate primary cultures of mouse proximal tubule cells (mPTCs) according to a previously established protocol (14). Confluent monolayers of mPTCs, characterized by a high endocytic uptake capacity, were expanded from tubular segments after 6–7 days.

Genotyping. Genomic DNA was isolated from ear biopsies from *Ocrl*$^{Y/+}$*; Inpp5b* $^{-/-}$*; BAC-INPP5B* and *Ocrl*$^{Y/-}$*; Inpp5b* $^{-/-}$ *; BAC-INPP5B* mice by using E.Z.N.A Forensic DNA Kit (OMEGA bio-tek) according to the manufacturer instruction. PCR was performed by using the following primers: *Ocrl wild-type:* the forward primer 5'-CCC TTT TCATCTGTTAGGAGAAATC-3'is located at the junction of intron 18 and the 5'end of exon 19. The reverse primer 5'-GCATGG TTAAACGCACTATGTGG-3' is located in intron 19, which is deleted in the *Ocrl*$^{Y/-}$ line. *Ocrl knock-out*: the forward primer 5'GCCCTTTGATTCTAATCCCTTTTC ATC-3' is located in the intron positioned just before the exon 19. The reverse primer 5'-TCT GAGCCCAGAAAGCGAAG-3' is located in the PGK promoter, which is part of the *neo*-cassette gene targeting vector. *Inpp5b knock-out*: the forward primer 5'-TAAAGTCTGAAA ATCCAAGGC-3' is located in exon 25. The reverse primer 5'-CTCATTTCTCCTTGATTC CAAT-3' is located in exon 34. *BAC-INPP5B*: the forward primer 5'-CCACCCCACGATTGACTC-3' is localized in exon 1. The reverse primer 5'-GGTGTCCCAGCCCTCAG-3' is localized also in exon 1. PCR conditions were: 32 cycles of 94°C for 30 sec, 55°C for 30 sec and 72°C for 1min.

Quantitative real-time PCR. Total RNA was extracted from mouse kidney tissues using Aurum Total RNA Fatty and Fibrous Tissue Kit according to manufacturer's protocol (Bio-Rad, Hercules, CA). DNAse I treatment was performed to eliminate genomic DNA contamination. Total RNA was extracted from primary cell cultures with RNAqueous kit (Applied Biosystems, Life Technologies). 1 µg of RNA was used to perform the reverse transcriptase reaction with iScript™ cDNA Synthesis Kit (Bio-Rad). Changes in target gene mRNA levels were determined by relative RT-qPCR with a CFX96™ Real-Time PCR Detection System (BioRad) by using iQ™ SYBR Green Supermix (Bio-Rad). RT-qPCR analyses were performed in duplicate. Specific primers were designed by using Primer3 (Supplementary Table 1). PCR conditions were 95°C for 3 min followed by 40 cycles of 15 sec at 95°C, 30 sec at 60°C. The PCR products were sequenced with the BigDye terminator kit (Perkin Elmer Applied Biosystems, Thermo Fischer Scientific). The efficiency of each set of primers was determined by dilution curves (Supplementary Table 1). The relative changes in targeted genes over *Gapdh, Actb, Hprt1, Ppiase, 18S, 36B4* mRNAs were calculated using the $2^{-\Delta\Delta}$Ct formula (50).

Immunofluorescence and confocal microscopy. Mouse kidneys were fixed by perfusion with 50–60 ml of 4% PFA in PBS before being snap-frozen in cryogenic Tissue-Tek OCT compound (Electron Microscopy Sciences, Hatfield, USA). The embedded tissues were sectioned at 5 µm and processed for immunofluorescent staining as previously described (44). The slides were acquired on Leica SP5 confocal laser scanning microscope (Center for Microscopy and Image Analysis, University of Zurich) equipped with a Leica APO 63x NA 1.4 oil immersion objective at a definition of 1024 x 1024 pixels, adjusting the pinhole diameter to 1 Airy unit for each emission channel. Quantitative image analysis was performed by selecting random visual fields containing at least 3-5 proximal tubules (LTL-positive) each one and acquired with the same setting parameters. For quantification of β-lactoglobulin and dextran internalization, the integrated density signal detected within each LTL-positive tubule was calculated. Internalization was then expressed as a ratio between the internal fluorescence and tubule area. Tubules at the border of the picture were excluded. ImageJ software was used for the analysis (17).

The mPTCs were fixed in 4% PFA and processed for immunofluorescent staining as previously described (44). Briefly, after incubation with blocking/permeabilization solution (0.1% Saponin ,0.5% BSA and 50mM NH_4Cl in PBS), mPTCs were stained overnight with the appropriate primary antibodies and 45 minutes with the suitable fluorophore-conjugated Alexa secondary antibodies (Invitrogen) or with Alexa-488 Phalloidin (F-actin) or 10 minutes with wheat germ agglutinin (WGA) FITC Conjugate. Immunostained mPTCs were analyzed by a Leica SP5 confocal laser scanning microscope using the settings described above. The quantitative cell image analyses were performed by using ImageJ software and the open-source cell image analysis software CellProfiler™ (51). More details regarding the quantifications are described in Supplementary Materials.

Endocytosis assays. Proximal tubules endocytic capacity of *Ocrl* and *Clcn5* mice was examined by measuring β-lactoglobulin and dextran uptake. β-lactoglobulin was tagged with Cy5 using TM2 Ab labeling kit (Amersham) in accordance with the manufacturer's instructions. 15 minutes after tail-vein injection of Cy5 β-lactoglobulin (1mg/kg B.W., L3908, Sigma) or 30 minutes after injection of 10 kDa Alexa 647-dextran (6 mg/kg B.W.; D22914, Thermo Fisher Scientific), mice were anesthetized and their kidneys were harvested and processed for confocal microscopy. The endocytic capacity of *Ocrl* and *Clcn5* mPTCs was examined by measuring albumin and dextran uptake as described previously (44). Briefly mPTCs were incubated at 37°C with 100µg/mL Alexa488-BSA (A13100, Thermo Fisher Scientific) or 250µg/mL Alexa 647-dextran diluted in medium without FBS supplementation, for 15 and 30 min respectively. After washing, the cells were fixed in 4% PFA and processed for confocal microscopy

PI(4,5)P_2 and PI3P staining. mPTCs were grown on 35mm dishes and PI(4,5)P_2 or PI3P staining were performed according to previously established protocols (25). Briefly, mPTCs were fixed for 15 min in 2% PFA and permeabilized for 5 min with 20µM digitonin in buffer A (20mM PIPES pH 6.8, 137mM NaCl, 2.7mM KCl) for PI(4,5)P_2 or buffer A^1 (150 mM NaCl, 20 mM Hepes, pH 7.4, and 2 mM EDTA) for PI3P. Next, mPTCs were incubated for 45 minutes with buffer A containing 10% fetal bovine serum and anti-PI(4,5)P2 antibody or in buffer A^1 supplemented with 5% goat serum and mCherry-2×FYVE PI3P-binding domain (gift from J.Gallop, Gurdon Institute, University of Cambridge). Anti –RFP was used for amplifying m-cherry staining. Studies of colocalization with early endosomes or lysosomes were performed by 1h incubation at room temperature with anti-EEA1 or anti-LAMP1 antibodies respectively. After washing and subsequent incubation with appropriate secondary antibodies, mPTCs were post-fixed for 5 min in 2% PFA and analyzed by confocal microscopy.

Lysosomal activity and degradation assays. The detection of lysosomal activity and degradative capacity in mPTCs was performed by using Bodipy-FL-PepstatinA (P12271, Thermo Fischer Scientific) and DQ-RED BSA (D12051, Thermo Fischer Scientific), respectively. Briefly, mPTCs were pulsed with 1µM Bodipy-FL-Pepstatin A or with 10µg/mL DQ-

RED BSA in pre-warmed media at 37°C for 1h. After washing, cells were fixed, immunostained with anti-LAMP1 and suitable secondary antibody and subsequently analyzed by confocal microscopy (14, 26). Lysosomal processing in *Ocrl* and *Clcn5* mice was measured by confocal analysis of kidney proximal tubules after 120 minutes from tail-vein injection of Cy5 β-lactoglobulin.

Western blotting. Proteins were extracted from mouse kidney tissues or primary cultured cells and lysed as previously described (44). Samples were normalized for protein or urinary creatinine levels before loading (20 µg/lane or 4µg/lane, respectively), diluted in Laemmli buffer and separated by SDS–PAGE in reducing conditions. Briefly, gels were blotted onto PVDF membranes, blocked in 5% non-fat milk and probed with appropriate primary and peroxidase-labeled secondary antibody. Protein bands were visualized by chemiluminescence (WBKLS0050, Millipore, Life technologies). Image intensity was measured by ImageJ.

Plasma membrane isolation. mPTCs were lysed in a fractionation buffer (250mM sucrose, 20mM HEPES, 10mM KCL, 1.5mM MgCl$_2$, 1mM EDTA, 1mM EGTA) containing protease and phosphatase inhibitors and passed through a 25G needle. Cell lysates were kept on ice for 20 minutes and centrifuged at 720 g (5 minutes at 4°C). The resultant postnuclear supernatants were centrifuged at 10,000 g (5 minutes at 4°C) to eliminate mitochondria. The postmitochondria supernatant were centrifuged at 100,000 g (1h at 4°C) to separate cytosolic (supernatant) and membrane fractions (pellet). The membrane pellets were washed in fractionation buffer by centrifugation (100,000 g for 45min at 4°C) and suspended in lysis buffer (10% glycerol and 0.1% SDS supplemented with protease and phosphatase inhibitors). The cytosolic and membrane fractions were analyzed by SDS-PAGE and western blotting.

Behavioral tests. Open field large arena test, water maze cue navigation and three chambers sociability test were performed on a cohort of 32 male mice aged 32 weeks (16 *Ocrl*$^{Y/+}$;*Inpp5b*$^{-/-}$;*BAC-INPP5B* and 16 *Ocrl*$^{Y/-}$; *Inpp5b*$^{-/-}$;*BAC-INPP5B*) in order to investigate motor coordination, vision and spatial learning and the social attitude of the mice respectively. Behavior testing procedures will be described briefly here and in more detail in the Supplementary Materials**.** ***Open field large arena test.*** Each subject was released near the wall of the arena and observed for 10 min on two subsequent days. Movements were tracked using Noldus EthoVision. ***Water-maze cue navigation.*** Animals were trained for 2 days to reach the goal platform hidden under milky-water and marked by a salient cue. The localization of the platform in the pool changed for every trial. All subjects were trained on the same sequence of goal positions and released from the same start points (52). ***Three-chambers sociability test.*** The test consisted of a 10-minutes trial where a test mouse was given the choice to spend time in the chamber with the novel object (the cylinder) plus the unfamiliar mouse (social stimulus) and the chamber containing only the empty cylinder. The time spent by the test mouse in the lateral chambers was noted (53).

IntelliCages experiments. Intellicages experiments were performed on a cohort of 28 male mice aged 24 weeks (13 *Ocrl*$^{Y/+}$; *Inpp5b*$^{-/-}$, *BAC-INPP5B* and 15 *Ocrl*$^{Y/-}$; *Inpp5b*$^{-/-}$; *BAC-INPP5B*). More details regarding the description of IntelliCage apparatus and mice preparation for IntelliCage experiments are provided in the Supplementary Materials. **Exploration and free adaptation**. During the first 4-7 days in IntelliCage all doors were open providing free access to all 8 drinking bottles (free adaptation). Data of the first 24h of free adaptation were analyzed separately to monitor exploration and habituation of the mice in the new environment (IntelliCage exploration). **Nosepoke adaptation**. During 3-7 days, all doors were closed but can be opened at any time with a nosepoke for 5s once per visit. **Drinking session adaptation**. During 3-7 days the mice were adapted to a fixed drinking schedule with doors opening in response to nose pokes only in the following time spots: 04:00-05:00, 11:00-12:00, 16:00-17:00 and 23:00-00:00. (30).

Epon embedding and retinal morphology. 36 weeks old mice were euthanized and perfused with PFA 4%. Eyes were enucleated and post-fixed in 4% PFA or 2.5% glutaraldehyde before being embedded in paraffin or epon plastic, respectively. For light microscopy, paraffin sections (including the lens, 5 µm) were stained with hematoxylin-eosin (HE), while plastic-embedded semi-thin cross-sections (0.5 µm) were counterstained with toluidine blue as described previously (54, 55) . Retinal morphology was analyzed by light microscopy (Zeiss, Axioplan, Jena, Germany).

Muscle analyses. Muscles analyses were performed on *Ocrl*$^{Y/+}$*vs. Ocrl*$^{Y/-}$ male mice aged 24 weeks. Lean mass/body weight ratio was determined in 6 pairs of live mice by using the whole body composition analyzer EchoMRI™ (Zinsser Analytic, Frankfurt, Germany) (56) . Five pairs of mice were used for muscle and blood sampling. The mice were slightly sedated using isoflurane before being anesthetized with an i.p. injection of a mixture containing urethane (1.5 g/kg) and diazepam (5 mg/kg) and killed by exsanguination. Blood and muscle tissues were collected as previously described (57). Selected leg muscles (triceps surae, soleus, plantaris, gastrocnemius, tibialis anterior, tibialis posterior, quadriceps) were carefully dissected bilaterally and weighed. Muscle mass was expressed relative to body weight. Creatine kinase (CK) activity in plasma was determined by spectrophotometry using a kit (C184-0B ; Catachem, Nuuchem, Oxford, CT, USA) according to the manufacturer's instructions (57).

Data analysis and Statistics. The quantitative data were expressed as means ± standard error of the mean (s.e.m.). Differences between experimental groups were evaluated using analysis of variance followed by post hoc test, when appropriate. When only two groups were compared, unpaired or paired two tailed Student's *t*-tests were used as appropriate. No statistical methods were used to predetermine the sample size. The sample size (n of biological replicates derived from distinct mice) of each experimental group is described in figure legends. GraphPad Prism software was used for all statistical analyses. Statistical significance was set at a $P<0.05$.

ACKNOWLEDGEMENTS & FUNDING

We are grateful to the Cystinosis Research Foundation (Irvine, CA, USA), the Swiss National Science Foundation (project grant 31003A-169850), the clinical research priority program (KFSP) RADIZ (Rare Disease Initiative Zurich) of the UZH, the Swiss National Centre of Competence in Research (*NCCR) Kidney* Control of Homeostasis (*Kidney.CH) for support and* Junior Grant (to A.L.), and the Fondation Suisse de Recherche sur les Maladies Musculaires (FSRMM).

We acknowledge Jennifer Gallop, Jonathan Gadsby, Andre Hall and Eric Olinger for fruitful discussions, Marcello Polesel, Claus-Dieter Schuh, Huguette Debaix and Nadine Nagele for providing technical assistance, Jonathan R. Gadsby, Renata Kozyraki, Pierre Verroust and Carsten A. Wagner for providing reagents. We thank the Center for Microscopy and Image Analysis of the University of Zurich (Zurich, Switzerland) for providing the equipment for imaging acquisition and the support for imaging analysis.

Competing financial interests: The authors declare no competing financial interests

AUTHOR CONTRIBUTIONS

O.D. conceptualize and supervised the study. B.P.F., M.B. and O.D. designed the experiments. B.P.F., M.B., A.G. and A.L. performed experiments and analyzed the data. I.A. and D.P.W. performed and analyzed the behavioral test on the *Ocrl* mice. H.M.I., O.M.D. and L.S. performed the muscles study and analysed the results. M.S. and C.G. performed and analysed the eyes phenotype of the *Ocrl* mice. R.L.N. provided the Ocrl mice. B.P.F., L.S. and M.A.D.M. designed, performed and analysed the eGFR experiment. B.P.F. and O.D. wrote the paper with inputs and comments from all of authors.

REFERENCES

1. Eckardt, K.U., Coresh, J., Devuyst, O., Johnson, R.J., Kottgen, A., Levey, A.S. and Levin, A. (2013) Evolving importance of kidney disease: from subspecialty to global health burden. Lancet, 382, 158-169.

2. Devuyst, O. and Luciani, A. (2015) Chloride transporters and receptor-mediated endocytosis in the renal proximal tubule. J. Physiol., 593, 4151-4164.

3. Christensen, E.I., Verroust, P.J. and Nielsen, R. (2009) Receptor-mediated endocytosis in renal proximal tubule. Pflugers. Arch., 458, 1039-1048.

4. Devuyst, O. and Thakker, R.V. (2010) Dent's disease. Orphanet J. Rare Dis., 5, 28.

5. Devuyst, O., Knoers, N.V., Remuzzi, G. and Schaefer, F. (2014) Rare inherited kidney diseases: challenges, opportunities, and perspectives. Lancet, 383, 1844-1859.

6. Devuyst, O., Christie, P.T., Courtoy, P.J., Beauwens, R. and Thakker, R.V. (1999) Intra-renal and subcellular distribution of the human chloride channel, CLC-5, reveals a pathophysiological basis for Dent's disease. Hum. Mol. Genet., 8, 247-257.

7. De Matteis, M.A., Staiano, L., Emma, F. and Devuyst, O. (2017) The 5-phosphatase OCRL in Lowe syndrome and Dent disease 2. Nat. Rev. Nephrol., 13, 455-470.

8. Mao, Y., Balkin, D.M., Zoncu, R., Erdmann, K.S., Tomasini, L., Hu, F., Jin, M.M., Hodsdon, M.E. and De Camilli, P. (2009) A PH domain within OCRL bridges clathrin-mediated membrane trafficking to phosphoinositide metabolism. Embo j., 28, 1831-1842.

9. Ponting, C.P. (2006) A novel domain suggests a ciliary function for ASPM, a brain size determining gene. Bioinformatics, 22, 1031-1035.

10. Faucherre, A., Desbois, P., Satre, V., Lunardi, J., Dorseuil, O. and Gacon, G. (2003) Lowe syndrome protein OCRL1 interacts with Rac GTPase in the trans-Golgi network. Hum. Mol. Genet., 12, 2449-2456.

11. Hichri, H., Rendu, J., Monnier, N., Coutton, C., Dorseuil, O., Poussou, R.V., Baujat, G., Blanchard, A., Nobili, F., Ranchin, B. et al. (2011) From Lowe syndrome to Dent disease: correlations between mutations of the OCRL1 gene and clinical and biochemical phenotypes. Hum. mutat., 32, 379-388.

12. Christensen, E.I., Devuyst, O., Dom, G., Nielsen, R., Van der Smissen, P., Verroust, P., Leruth, M., Guggino, W.B. and Courtoy, P.J. (2003) Loss of chloride channel ClC-5 impairs endocytosis by defective trafficking of megalin and cubilin in kidney proximal tubules. Proc. Natl. Acad. Sci. U. S. A., 100, 8472-8477.

13. Vicinanza, M., Di Campli, A., Polishchuk, E., Santoro, M., Di Tullio, G., Godi, A., Levtchenko, E., De Leo, M.G., Polishchuk, R., Sandoval, L. et al. (2011) OCRL controls trafficking through early endosomes via PtdIns4,5P(2)-dependent regulation of endosomal actin. Embo j., 30, 4970-4985.

14. Luciani, A., Sirac, C., Terryn, S., Javaugue, V., Prange, J.A., Bender, S., Bonaud, A., Cogne, M., Aucouturier, P., Ronco, P. et al. (2016) Impaired Lysosomal Function Underlies Monoclonal Light Chain-Associated Renal Fanconi Syndrome. J. Am. Soc. Nephrol., 27, 2049-2061.

15. Janne, P.A., Suchy, S.F., Bernard, D., MacDonald, M., Crawley, J., Grinberg, A., Wynshaw-Boris, A., Westphal, H. and Nussbaum, R.L. (1998) Functional overlap between murine Inpp5b and Ocrl1 may explain why deficiency of the murine ortholog for OCRL1 does not cause Lowe syndrome in mice. J. Clin. Invest., 101, 2042-2053.

16. Norris, F.A., Atkins, R.C. and Majerus, P.W. (1997) The cDNA cloning and characterization of inositol polyphosphate 4-phosphatase type II. Evidence for conserved alternative splicing in the 4-phosphatase family. J. Biol. Chem., 272, 23859-23864.

17. Inoue, K., Balkin, D.M., Liu, L., Nandez, R., Wu, Y., Tian, X., Wang, T., Nussbaum, R., De Camilli, P. and Ishibe, S. (2017) Kidney Tubular Ablation of Ocrl/Inpp5b Phenocopies Lowe Syndrome Tubulopathy. J. Am. Soc. Nephrol., 28, 1399-1407.

18. Bothwell, S.P., Chan, E., Bernardini, I.M., Kuo, Y.M., Gahl, W.A. and Nussbaum, R.L. (2011) Mouse model for Lowe syndrome/Dent Disease 2 renal tubulopathy. J. Am. Soc. Nephrol., 22, 443-448.

19. Terryn, S., Jouret, F., Vandenabeele, F., Smolders, I., Moreels, M., Devuyst, O., Steels, P. and Van Kerkhove, E. (2007) A primary culture of mouse proximal tubular cells, established on collagen-coated membranes. Am. J. Physiol. Renal. Physiol., 293, F476-485.

20. Zhang, X., Hartz, P.A., Philip, E., Racusen, L.C. and Majerus, P.W. (1998) Cell lines from kidney proximal tubules of a patient with Lowe syndrome lack OCRL inositol polyphosphate 5-phosphatase and accumulate phosphatidylinositol 4,5-bisphosphate. J. Biol. Chem., 273, 1574-1582.

21. Oltrabella, F., Pietka, G., Ramirez, I.B., Mironov, A., Starborg, T., Drummond, I.A., Hinchliffe, K.A. and Lowe, M. (2015) The Lowe syndrome protein OCRL1 is required for endocytosis in the zebrafish pronephric tubule. PLoS. Genet., 11, e1005058.

22. Senju, Y., Kalimeri, M., Koskela, E.V., Somerharju, P., Zhao, H., Vattulainen, I. and Lappalainen, P. (2017) Mechanistic principles underlying regulation of the actin cytoskeleton by phosphoinositides. Proc. Natl. Acad. Sci. U. S. A., 114, E8977-e8986.

23. Perez Bay, A.E., Schreiner, R., Benedicto, I., Paz Marzolo, M., Banfelder, J., Weinstein, A.M. and Rodriguez-Boulan, E.J. (2016) The fast-recycling receptor Megalin defines the apical recycling pathway of epithelial cells. Nat. Commun., 7, 11550.

24. Pfeffer, S.R. (2009) Multiple routes of protein transport from endosomes to the trans Golgi network. FEBS Lett., 583, 3811-3816.

25. De Leo, M.G., Staiano, L., Vicinanza, M., Luciani, A., Carissimo, A., Mutarelli, M., Di Campli, A., Polishchuk, E., Di Tullio, G., Morra, V. et al. (2016) Autophagosome-lysosome fusion triggers a lysosomal response mediated by TLR9 and controlled by OCRL. Nat. Cell. Biol., 18, 839-850.

26. Perera, R.M., Stoykova, S., Nicolay, B.N., Ross, K.N., Fitamant, J., Boukhali, M., Lengrand, J., Deshpande, V., Selig, M.K., Ferrone, C.R. et al. (2015) Transcriptional control of autophagy-lysosome function drives pancreatic cancer metabolism. Nature, 524, 361-365.

27. Miaczynska, M. (2013) Effects of membrane trafficking on signaling by receptor tyrosine kinases. Cold Spring Harb. Perspect. Biol., 5, a009035.

28. Taylor, T.N., Greene, J.G. and Miller, G.W. (2010) Behavioral phenotyping of mouse models of Parkinson's disease. Behav. Brain. Res., 211, 1-10.

29. Fowler, S.C. and Muma, N.A. (2015) Use of a force-sensing automated open field apparatus in a longitudinal study of multiple behavioral deficits in CAG140 Huntington's disease model mice. Behav. Brain. Res., 294, 7-16.

30. Vannoni, E., Voikar, V., Colacicco, G., Sanchez, M.A., Lipp, H.P. and Wolfer, D.P. (2014) Spontaneous behavior in the social homecage discriminates strains, lesions and mutations in mice. J. Neurosci. Methods., 234, 26-37.

31. Luhmann, U.F., Carvalho, L.S., Holthaus, S.M., Cowing, J.A., Greenaway, S., Chu, C.J., Herrmann, P., Smith, A.J., Munro, P.M., Potter, P. et al. (2015) The severity of retinal pathology in homozygous Crb1rd8/rd8 mice is dependent on additional genetic factors. Hum. Mol. Genet., 24, 128-141.

32. Montjean, R., Aoidi, R., Desbois, P., Rucci, J., Trichet, M., Salomon, R., Rendu, J., Faure, J., Lunardi, J., Gacon, G. et al. (2015) OCRL-mutated fibroblasts from patients with Dent-2 disease exhibit INPP5B-independent phenotypic variability relatively to Lowe syndrome cells. Hum. Mol. Genet., 24, 994-1006.

33. Nandez, R., Balkin, D.M., Messa, M., Liang, L., Paradise, S., Czapla, H., Hein, M.Y., Duncan, J.S., Mann, M. and De Camilli, P. (2014) A role of OCRL in clathrin-coated pit dynamics and uncoating revealed by studies of Lowe syndrome cells. eLife, 3, e02975.

34. Bockenhauer, D., Bokenkamp, A., van't Hoff, W., Levtchenko, E., Kist-van Holthe, J.E., Tasic, V. and Ludwig, M. (2008) Renal phenotype in Lowe Syndrome: a selective proximal tubular dysfunction. Clin. J. Am. Soc. Nephrol., 3, 1430-1436.

35. Piwon, N., Gunther, W., Schwake, M., Bosl, M.R. and Jentsch, T.J. (2000) ClC-5 Cl- -channel disruption impairs endocytosis in a mouse model for Dent's disease. Nature, 408, 369-373.

36. Gorvin, C.M., Wilmer, M.J., Piret, S.E., Harding, B., van den Heuvel, L.P., Wrong, O., Jat, P.S., Lippiat, J.D., Levtchenko, E.N. and Thakker, R.V. (2013) Receptor-mediated endocytosis and endosomal acidification is impaired in proximal tubule epithelial cells of Dent disease patients. Proc. Natl. Acad. Sci. U. S. A., 110, 7014-7019.

37. Novarino, G., Weinert, S., Rickheit, G. and Jentsch, T.J. (2010) Endosomal chloride-proton exchange rather than chloride conductance is crucial for renal endocytosis. Science (New York, N.Y.), 328, 1398-1401.

38. Biemesderfer, D. (2006) Regulated intramembrane proteolysis of megalin: linking urinary protein and gene regulation in proximal tubule? Kidney. Int., 69, 1717-1721.

39. Zou, Z., Chung, B., Nguyen, T., Mentone, S., Thomson, B. and Biemesderfer, D. (2004) Linking receptor-mediated endocytosis and cell signaling: evidence for regulated intramembrane proteolysis of megalin in proximal tubule. J. Biol. Chem., 279, 34302-34310.

40. Norden, A.G., Lapsley, M., Igarashi, T., Kelleher, C.L., Lee, P.J., Matsuyama, T., Scheinman, S.J., Shiraga, H., Sundin, D.P., Thakker, R.V. et al. (2002) Urinary megalin deficiency implicates abnormal tubular endocytic function in Fanconi syndrome. J. Am. Soc. Nephrol., 13, 125-133.

41. Zoncu, R., Perera, R.M., Balkin, D.M., Pirruccello, M., Toomre, D. and De Camilli, P. (2009) A phosphoinositide switch controls the maturation and signaling properties of APPL endosomes. Cell, 136, 1110-1121.

42. Di Paolo, G. and De Camilli, P. (2006) Phosphoinositides in cell regulation and membrane dynamics. Nature, 443, 651-657.

43. Symons, M.H. and Mitchison, T.J. (1991) Control of actin polymerization in live and permeabilized fibroblasts. J. Cell. Biol., 114, 503-513.

44. Festa, B.P., Chen, Z., Berquez, M., Debaix, H., Tokonami, N., Prange, J.A., Hoek, G.V., Alessio, C., Raimondi, A., Nevo, N. et al. (2018) Impaired autophagy bridges lysosomal storage disease and epithelial dysfunction in the kidney. Nat. Commun., 9, 161.

45. Park, E., Choi, H.J., Lee, J.M., Ahn, Y.H., Kang, H.G., Choi, Y.M., Park, S.J., Cho, H.Y., Park, Y.H., Lee, S.J. et al. (2014) Muscle involvement in Dent disease 2. Pediatr. Nephrol., 29, 2127-2132.

46. Erdmann, K.S., Mao, Y., McCrea, H.J., Zoncu, R., Lee, S., Paradise, S., Modregger, J., Biemesderfer, D., Toomre, D. and De Camilli, P. (2007) A role of the Lowe syndrome protein OCRL in early steps of the endocytic pathway. Dev. Cell., 13, 377-390.

47. Bothwell, S.P., Farber, L.W., Hoagland, A. and Nussbaum, R.L. (2010) Species-specific difference in expression and splice-site choice in Inpp5b, an inositol polyphosphate 5-phosphatase paralogous to the enzyme deficient in Lowe Syndrome. Mamm. Genome., 21, 458-466.

48. Wang, S.S., Devuyst, O., Courtoy, P.J., Wang, X.T., Wang, H., Wang, Y., Thakker, R.V., Guggino, S. and Guggino, W.B. (2000) Mice lacking renal chloride channel, CLC-5, are a model for Dent's disease, a nephrolithiasis disorder associated with defective receptor-mediated endocytosis. Hum. Mol. Genet., 9, 2937-2945.

49. Raggi, C., Luciani, A., Nevo, N., Antignac, C., Terryn, S. and Devuyst, O. (2014) Dedifferentiation and aberrations of the endolysosomal compartment characterize the early stage of nephropathic cystinosis. Hum. Mol. Genet., 23, 2266-2278.

50. Vandesompele, J., De Preter, K., Pattyn, F., Poppe, B., Van Roy, N., De Paepe, A. and Speleman, F. (2002) Accurate normalization of real-time quantitative RT-PCR data by geometric averaging of multiple internal control genes. Genome Biol., 3, Research0034.

51. Carpenter, A.E., Jones, T.R., Lamprecht, M.R., Clarke, C., Kang, I.H., Friman, O., Guertin, D.A., Chang, J.H., Lindquist, R.A., Moffat, J. et al. (2006) CellProfiler: image analysis software for identifying and quantifying cell phenotypes. Genome Biol., 7, R100.

52. Mohajeri, M.H., Madani, R., Saini, K., Lipp, H.P., Nitsch, R.M. and Wolfer, D.P. (2004) The impact of genetic background on neurodegeneration and behavior in seizured mice. Genes Brain Behav., 3, 228-239.

53. Nadler, J.J., Moy, S.S., Dold, G., Trang, D., Simmons, N., Perez, A., Young, N.B., Barbaro, R.P., Piven, J., Magnuson, T.R. et al. (2004) Automated apparatus for quantitation of social approach behaviors in mice. Genes Brain Behav., 3, 303-314.

54. Grimm, C., Wenzel, A., Williams, T., Rol, P., Hafezi, F. and Reme, C. (2001) Rhodopsin-mediated blue-light damage to the rat retina: effect of photoreversal of bleaching. Invest. Ophthalmol. Vis. Sci., 42, 497-505.

55. Heynen, S.R., Tanimoto, N., Joly, S., Seeliger, M.W., Samardzija, M. and Grimm, C. (2011) Retinal degeneration modulates intracellular localization of CDC42 in photoreceptors. Mol. Vis., 17, 2934-2946.

56. Krizo, J.A., Moreland, L.E., Rastogi, A., Mou, X., Prosser, R.A. and Mintz, E.M. (2018) Regulation of Locomotor activity in fed, fasted, and food-restricted mice lacking tissue-type plasminogen activator. BMC Physiol., 18, 2.

57. Dorchies, O.M., Reutenauer-Patte, J., Dahmane, E., Ismail, H.M., Petermann, O., Patthey- Vuadens, O., Comyn, S.A., Gayi, E., Piacenza, T., Handa, R.J. et al. (2013) The anticancer drug tamoxifen counteracts the pathology in a mouse model of duchenne muscular dystrophy. Am. J. Pathol., 182, 485-504.

Figure 1

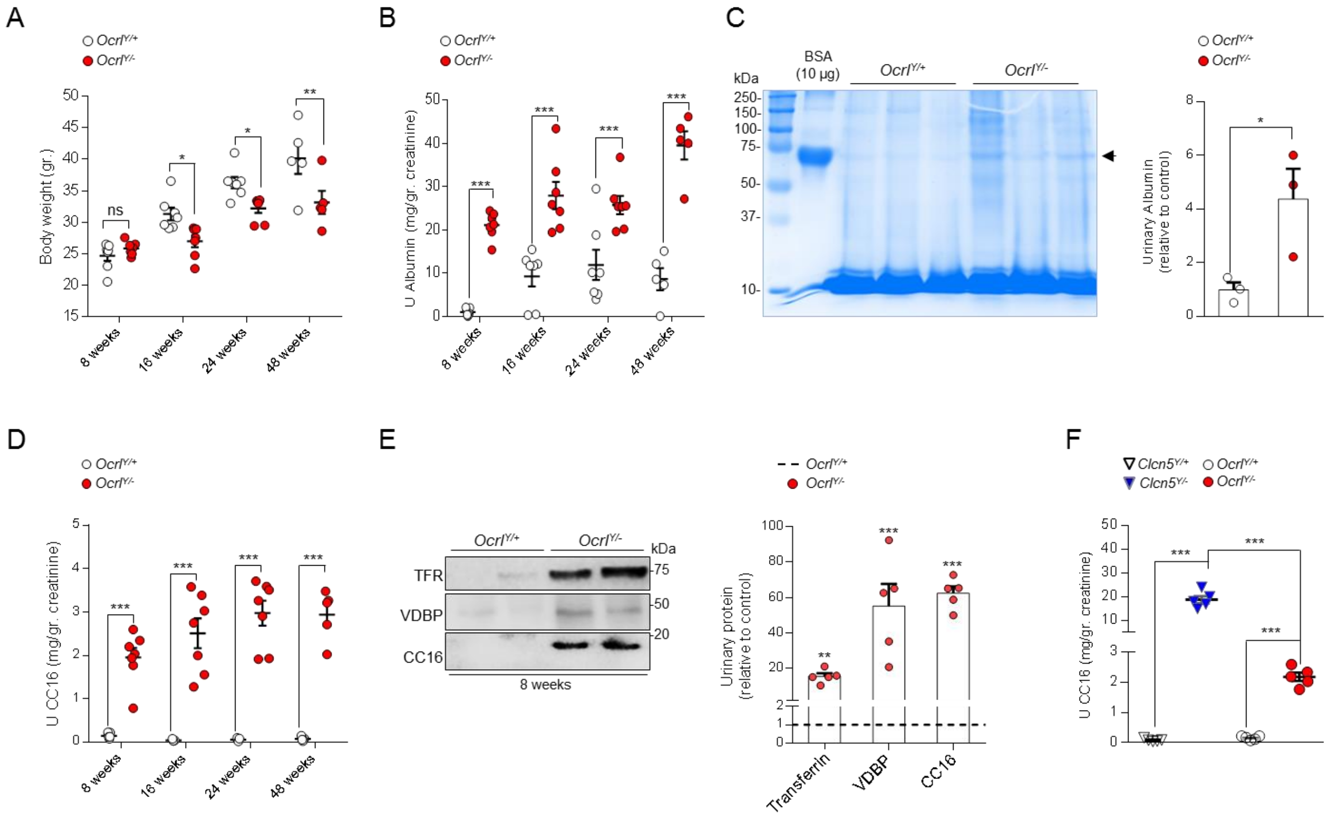

Figure 1. **Growth retardation and renal phenotype in a whole body *Ocrl*$^{Y/-}$ mouse model.** (**A**) Dot plot representing the measurement of body weight, (**B**) albumin and (**D**) clara cell protein 16 (CC16) urinary excretion in *Ocrl* male mice at 8, 16, 24 and 48 weeks after birth (8 weeks n= 7 mice per group, 16 weeks n= 7 mice per group, 24 weeks n=7 mice per group, 48 weeks n=5 mice per group). (**C**) Coomassie blue-stained SDS-PAGE analysis of urine derived from 8 weeks old *Ocrl* mice and densitometry quantification of Albumin (n=3 mice per group).10 µg of bovine serum albumin (BSA) were loaded as positive control (first lane; molecular weight (MW) ≈66.5 kDa). (**E**) Representative western blotting and densitometry quantification of transferrin (TFR), vitamin D binding protein (VDBP) and CC16 in urine derived from 8 weeks old *Ocrl* mice. (TFR, VDBP and CC16 n= 5 mice per group). (**F**) Quantification of CC16 urinary excretion in 8 weeks old *Clcn5* and *Ocrl* mice (n=5 mice per group). All the urine parameters were normalized to urinary creatinine concentration. Plotted data represent mean ± SEM. Each dot of the graphs represents one mouse. Two-tailed unpaired Student's t-test, *P < 0.05, **P < 0.01 and ***P < 0.001 relative to *Ocrl*$^{Y/+}$ or *Clcn5*$^{Y/+}$ mice. ns: not significant.

Figure 2

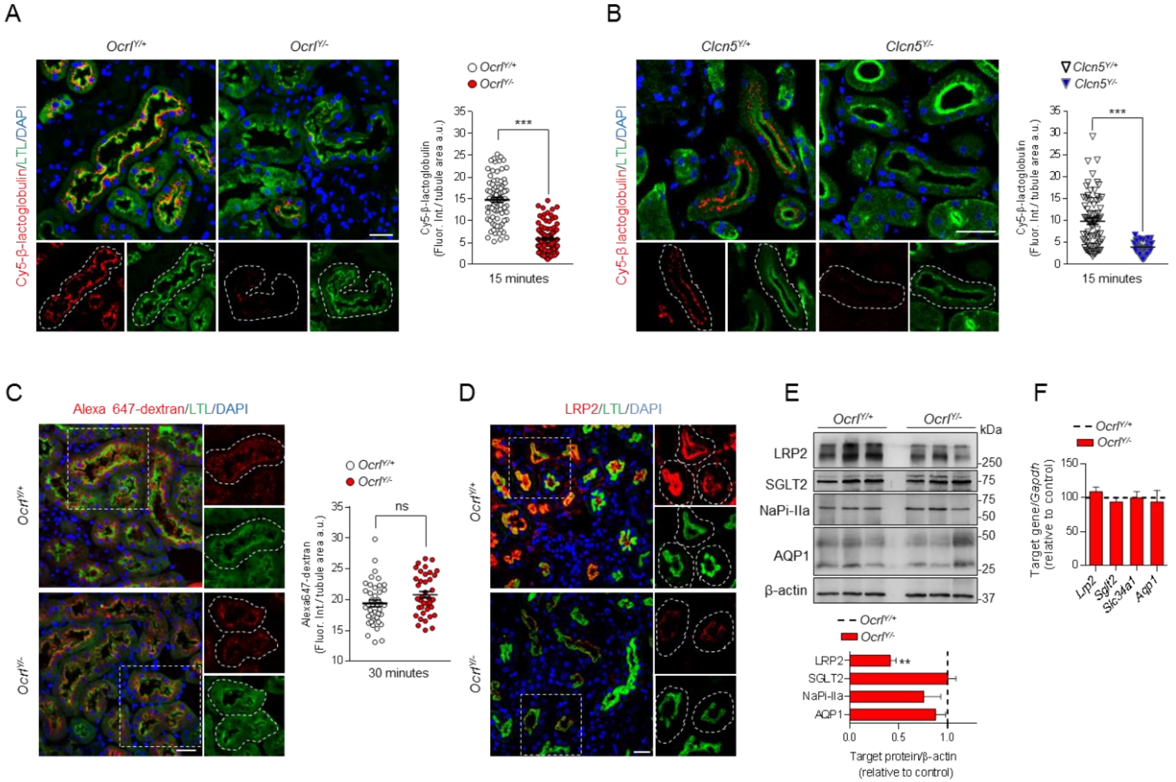

Figure 2. **Defective receptor-mediated endocytosis in *Ocrl*$^{Y/-}$ mice.** (**A-B**) Representative confocal micrographs showing Cy5 labeled β-lactoglobulin (red, 1mg/kg B.W.) or (**C**) Alexa 647–labeled dextran uptake (red, 6 mg/kg B.W.) after 15 and 30 minutes from tail vein injections respectively and quantifications of the corresponding fluorescent signal in LTL^{+} (*Lotus Tetragonolobus Lectin*, green) proximal tubules from *Ocrl* and *Clcn5* mouse kidneys (n=90 *Ocrl* and n=70 *Clcn5* proximal tubules for Cy5 labeled β-lactoglobulin uptake; n = 40 *Ocrl* proximal tubules for Alexa 647 dextran uptake); n=2 per group, each dot representing fluorescence intensity in one proximal tubule; fluorescence intensity was normalized on tubule area; two-tailed unpaired Student's t-test, ***P < 0.001 relative to *Ocrl*$^{Y/+}$*or Clcn5*$^{Y/+}$ kidneys. ns: not significant). Insets: high magnification of Cy5 labeled β-lactoglobulin^{+} or Alexa 647 dextran^{+} structures in LTL^{+} proximal tubules. (**D**) Representative confocal micrographs showing LRP2 (red) expression in LTL^{+} (green) proximal tubules of *Ocrl* mouse kidneys. Insets: high magnification of LRP2^{+} structures in LTL^{+} proximal tubules. (**E**) Western blotting and densitometry analyses of LRP2, SGLT2, NaPi-IIa and AQP1 protein levels in whole kidney lysates from *Ocrl* mice. β-actin was used as loading control. Protein levels normalized on β-actin and relative to *Ocrl*$^{Y/+}$ mice (black dotted line), (LRP2 n = 6 mice per group; SGLT2, NaPiIIa and AQP1 n=3 mice per group. Mann-Whitney U test, **P < 0.01 relative to *Ocrl*$^{Y/+}$ kidneys). (**F**) The mRNA kidney levels of *Lrp2*, *Sglt2*, *Slc34a1* and *Aqp1* were analyzed by real-time qPCR. Gene target expression normalized to *Gapdh* and relative to *Ocrl*$^{Y/+}$ mice (black dotted line), (n = 3 mice per group). Nuclei counterstained with DAPI (blue) in **A**, **B**, **C** and **D**. Scale bars 25μm. Plotted data represent mean ± SEM.

Figure 3

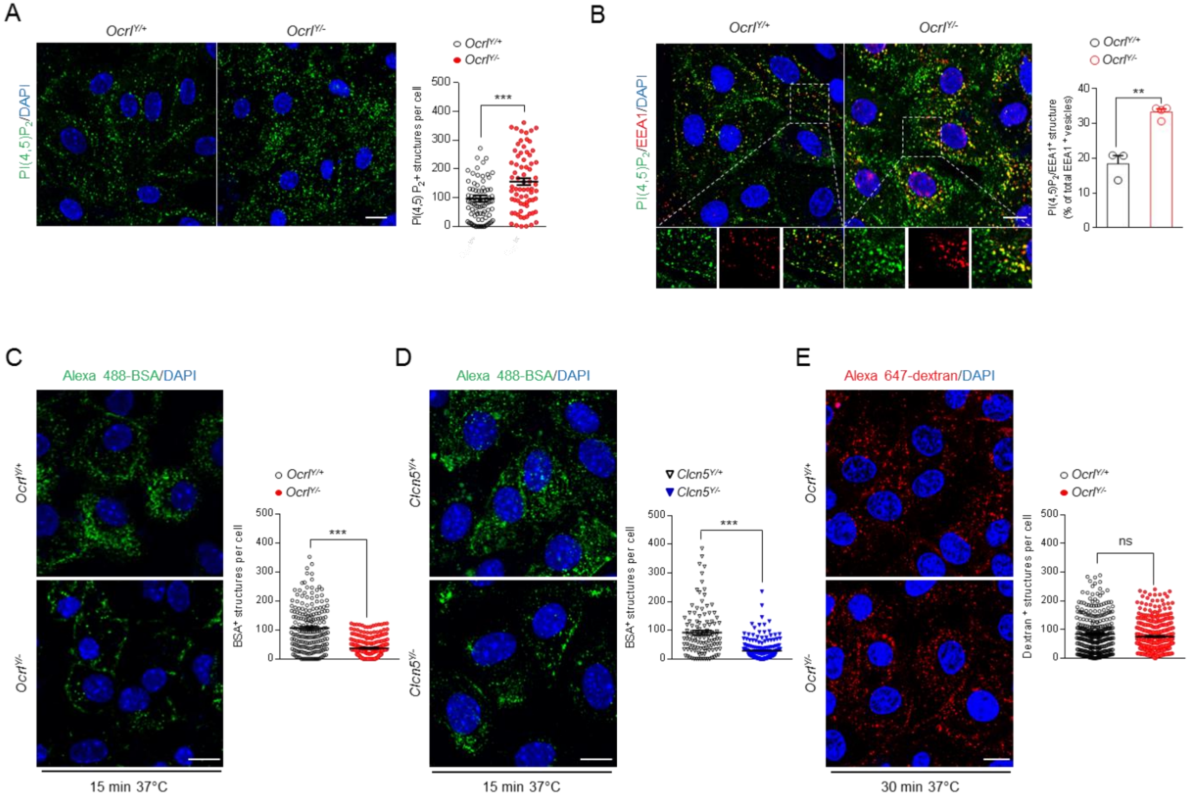

Figure 3. Altered PI(4, 5) P$_2$ subcellular distribution and receptor-mediated endocytosis in *Ocrl*$^{Y/-}$ mPTCs. (**A**) Representative confocal micrographs and quantification of PI(4,5)P$_2^+$ structures (green) in *Ocrl* mPTCs (n ≈ 80 cells pooled from three mouse kidneys per condition; each dot representing the number of PI(4,5) P$_2^+$ structures in a cell). (**B**) Representative confocal micrographs of *Ocrl* mPTCs immunostained with anti- PI(4,5)P$_2$ (green) and anti-EEA1 (red, early endosomes) and quantification (adjacent panel) of the number of PI(4,5)P$_2$/EEA1$^+$ structures by confocal microscopy (percentage of total EEA1$^+$ vesicles; n= 3 *Ocrl*$^{Y/+}$; n=4 *Ocrl*$^{Y/-}$ randomly selected fields per condition, each containing ≈ 15-20 cells). Insets: high magnification of PI(4,5)P$_2$/EEA1$^+$ structures. (**C-D**) *Ocrl* and *Clcn5* mPTCs were loaded with Alexa 488-BSA (green, 100 µg ml^{-1} for 15 min at 37 °C), fixed, and analyzed by confocal microscopy. Quantification of the number of Alexa 488-BSA$^+$ structures (n ≈150-250 cells pooled from three mouse kidneys per condition; each point representing the number of BSA$^+$ structures in a cell). (**E**) *Ocrl* mPTCs were loaded with Alexa 647-dextran 10kDa (red, 250 µg ml^{-1} for 30 min at 37 °C), fixed, and analyzed by confocal microscopy. Quantification of the number of Al647-dextran$^+$ structures (n≈ 200-250 cells pooled from three mouse kidneys per condition; each dot representing the number of dextran$^+$ structures in a cell). Nuclei counterstained with DAPI (blue). Scale bars in **A** and **B** 15µm, in **C**, **D** and **E** 10 µm. Plotted data represent mean ± SEM. Two-tailed unpaired Student's t-test, **P < 0.01, ***P < 0.001 relative to *Ocrl*$^{Y/+}$ *or Clcn5*$^{Y/+}$ mPTCs. ns: not significant.

Figure 4

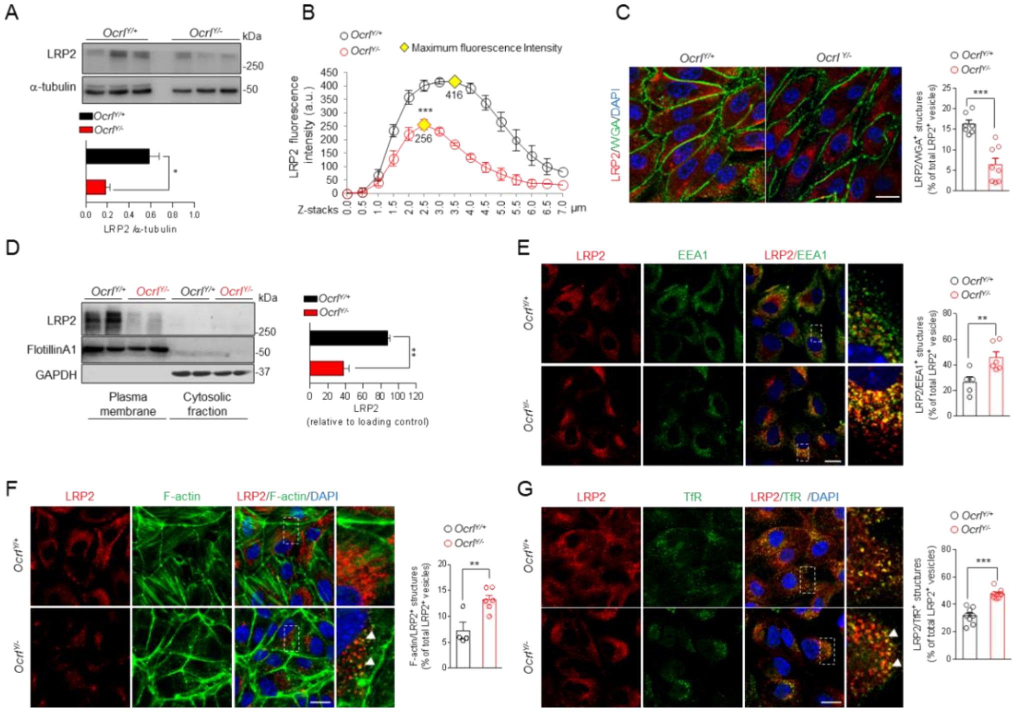

Figure 4. *Ocrl*$^{Y/-}$ mPTCs exhibit decreased expression of LRP2 and defective endocytic recycling. (**A**) Representative western blotting and quantification of LRP2 in whole *Ocrl* mPTCs lysates. α- tubulin was used as loading control (n=4 mice per group). (**B**) Dot plot representing distribution and average fluorescence intensity of LRP2 along Z-stacks projections in *Ocrl* mPTCs. Yellow rhombus represents the maximum peak of fluorescence intensity. Quantifications of Z-stacks were obtained from 3 randomly selected fields per condition, with each containing ≈ 15-20 cells. **(C)** Representative confocal micrographs and quantification of LRP2/WGA^{+} structures by confocal microscopy (in percentage of total LRP2^{+} vesicles, n=7 *Ocrl*$^{Y/+}$; n=8 *Ocrl*$^{Y/-}$ randomly selected fields per condition, each containing ≈10-15 cells). (**D**) Representative western blotting and quantification of LRP2 protein levels in plasma membrane fraction derived from *Ocrl* mPTCs. Flotillin A1 and GAPDH were used as purity marker and loading control of the plasma membrane and cytosolic fractions respectively (n=3 independent experiment). (**E**) Representative confocal micrographs of *Ocrl* mPTCs immunostained with anti-LRP2 (red) and anti-EEA1 (green, early endosomes) and quantification (adjacent panel) of the number of LRP2/EEA1^{+} structures by confocal microscopy (percentage of total LRP2^{+} vesicles; n=5 *Ocrl*$^{Y/+}$; n=6 *Ocrl*$^{Y/-}$ randomly selected fields per condition, each containing ≈ 15-20 cells). Insets: high magnification of LRP2/EEA1^{+} structures. (**F**) Representative confocal micrographs of *Ocrl* mPTCs immunostained with anti-LRP2 (red) and Alexa-Fluor-488-phalloidin (green, F-actin). Quantification (adjacent panel) of the number of F-Actin/LRP2^{+} structures (in percentage of total LRP2^{+} vesicles, n= 4 *Ocrl*$^{Y/+}$; n=6 *Ocrl*$^{Y/-}$ randomly selected fields per condition, each containing ≈10-15 cells). Insets: high magnification of F-actin/LRP2^{+} structures. (**G**) Representative confocal micrographs of *Ocrl* mPTCs stained with anti-TfR (green) and anti-LRP2 (red) and quantification of the number of TfR/LRP2^{+} structures by confocal microscopy (in percentage of total LRP2^{+} vesicles, n=8 randomly selected fields per condition, each containing ≈20-25 cells). Insets: high magnification of TfR/LRP2^{+} structures. Nuclei counterstained with DAPI (blue) in **C**, **E, F** and **G.** Scale bars in **E**, **F** and **G** 15µm and in **C** 20µm. Plotted data represent mean ± SEM. Two-tailed unpaired Student's t-test, *P < 0.05, **P < 0.01 and ***P < 0.001 relative to *Ocrl*$^{Y/+}$ mPTCs.

Figure 5

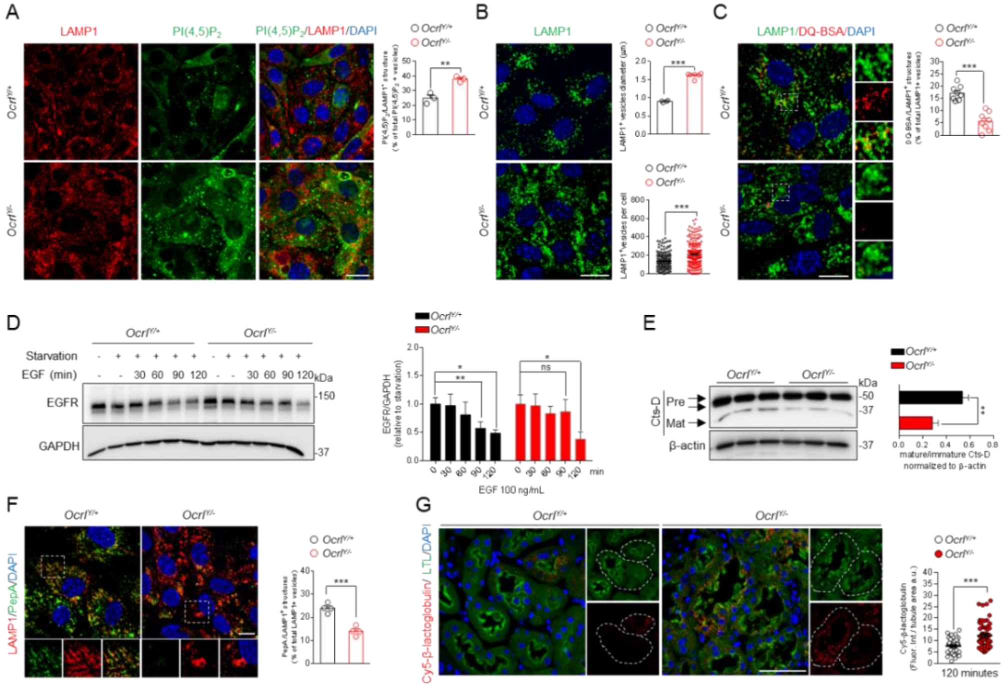

Figure 5. Altered lysosomal dynamics and degradative capacity in *Ocrl*$^{Y/-}$ mPTCs. (**A**) *Ocrl* mPTCs were immunostained with anti-PI(4,5)P$_2$ (green) and anti-LAMP1 (red, lysosomes) and the number of PI(4,5)P$_2$ /LAMP1$^+$ structures were quantified by confocal microscopy (in percentage of total PI(4,5)P$_2$$^+$ vesicles; n=3 randomly selected fields per condition, each containing ≈ 40-50 cells). (**B**) Representative confocal micrographs of *Ocrl* mPTCs immunostained with anti-LAMP1 (green). Quantification of the average LAMP1$^+$ vesicles diameter (top, n= 4 *Ocrl*$^{Y/+}$; and n=6 *Ocrl*$^{Y/-}$ randomly selected fields per condition, each containing ≈ 50-60 cells) and number of structures (bottom, n ≈ 200-220 cells pooled from 3 *Ocrl* kidneys per group, each point representing the number of LAMP1$^+$ structure in a cell). (**C**) *Ocrl* mPTCs were loaded with DQ (dequenched) Red BSA (red, 10 µg ml^{-1} for 1h at 37 °C), immunostained with anti- LAMP1 (green, lysosomes) fixed and analyzed by confocal microscopy. Quantification of number of DQ Red BSA /LAMP1+ structures (in percentage of total LAMP1$^+$ structures, n = 8 randomly selected fields per condition, with each containing ≈ 10–15 cells). Insets: high magnification of DQ Red BSA / LAMP1$^+$ vesicles. (**D**) *Ocrl* mPTCs were serum starved for 24 h and then stimulated with EGF (100 ng/ml) for the indicated times. EGFR protein levels were evaluated by western blotting and quantified relative to time 0 (starved cells). (n=3mice per group; two-tailed unpaired Student's t-test, $*P < 0.05$, $**P < 0.01$ relative to *Ocrl*$^{Y/+}$ or *Ocrl*$^{Y/-}$ starved mPTCs. ns: not significant). (**E**) Western blotting and densitometry analyses of Cathepsin D (Cts-D) protein levels in *Ocrl* mPTCs (n= 4mice per group). (**F**) *Ocrl* mPTCs were loaded with Bodipy-FL-PepA (1 µM, for 1 h at 37 °C, green), immunostained with anti- LAMP1 antibody (red) and analysed by confocal microscopy. Quantification of numbers of PepA/LAMP1$^+$ structures (in percentage of total LAMP1$^+$ structures; n = 4 randomly selected fields per condition, with each containing ~ 20–25 cells). (**G**) Representative confocal micrographs showing Cy5 labeled β-lactoglobulin (red) after 120 minutes from tail vein injections and quantifications of the corresponding fluorescent signal in LTL$^+$ proximal tubules from *Ocrl* mouse kidneys (n=50 *Ocrl* proximal tubules; each dot representing fluorescence intensity in one proximal tubule*;* fluorescence intensity was normalized on tubule area). Nuclei counterstained with DAPI (blue) in **A, B, C, F** and **G**. Scale bars in **A**, **B** and **C** 15 µm; in **F** 10 µm and in **G** 50 µm. Plotted data represent mean ± SEM. Two-tailed unpaired Student's t-test. $**P < 0.01$, $***P < 0.001$ relative to *Ocrl*$^{Y/+}$ mPTCs or kidneys.

Figure 6

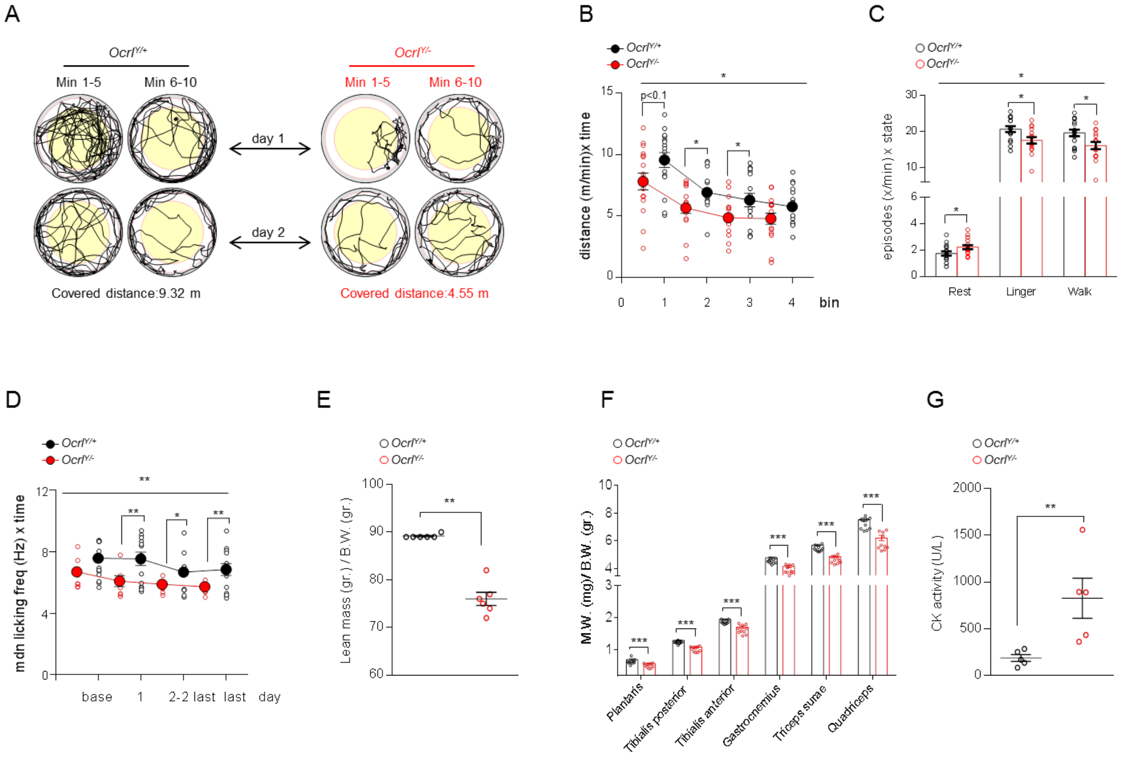

Figure 6. Impaired locomotor activity and muscular defects in *Ocrl*$^{Y/-}$ mice. (**A-C**) Open field large arena test was performed during 10 minutes of two subsequent days in a circular arena with a diameter of 150 cm on a cohort of 16 *Ocrl*$^{Y/+}$and 16 *Ocrl*$^{Y/-}$ age matched male mice. (**A**) Illustrative pictures representing the trajectories traveled by *Ocrl* mice during the open field large arena test. (**B**) Dot plot representing the distance covered by *Ocrl* mice during the large open field arena test. The distance traveled by each mouse is normalized to 1 minute observation time and plotted as function of time for each bin (bin=5 minutes) (split ANOVA effects followed by post-hoc tests between genotype for each bin: Bin1 ’P < 0.1, Bin2 *P < 0.05, Bin3 *P < 0.05). (**C**) Dotted bar graph representing the frequency of resting, lingering and walking episodes exhibited by *Ocrl* mice during the open field large arena test (split ANOVA effects followed by post-hoc tests between genotype for each state: rest *P < 0.05, linger, *P < 0.05, walk *P < 0.05). (**D**) IntelliCage experiments were performed on a cohort of age matched male *Ocrl* mice (13 *Ocrl*$^{Y/+}$and 13 *Ocrl*$^{Y/-}$). Dot plot representing the median licking frequency during drinking restriction protocol. Base indicates the licking frequency during the last 24h of nose poke adaptation phase (split ANOVA effects followed by post-hoc tests between genotype for each time point: Day1 **P < 0.01, Day 2-2last *P < 0.05, Last day **P < 0.001). (**E**) Lean mass/body weight ratio determined by whole body composition analysis in *Ocrl* mice (n=6 mice per group). (**F**) Muscle mass, relative to body weight, of selected hind limb muscles obtained by bilateral dissection of 5 pairs of *Ocrl* mice (n=10 values for symmetrical leg muscles). (**G**) Plasma creatine kinase activity (CK) in the corresponding 5 pairs of *Ocrl* mice (as in B). Plotted data represent mean ± SEM. In **B**, **C** and **D** One-way ANOVA between subject factor genotype: *P < 0.05; **P < 0.01 (on the top of each graph); in **E**, **F** and **G** Mann Withney test, **P < 0.01; ***P < 0.001 relative to *Ocrl*$^{Y/+}$ mice.

Table 1. Body weight, urine and blood parameters in *Ocrl* and *Clcn5* mice.

	8 weeks		8 weeks		16 weeks		24 weeks		48 weeks	
	***Ocrl*$^{Y/+}$ (n= 7)**	***Ocrl*$^{Y/-}$ (n= 7)**	***Clcn5*$^{Y/+}$ (n=4)**	***Clcn5*$^{Y/-}$ (n=4)**	***Ocrl*$^{Y/+}$ (n= 7)**	***Ocrl*$^{Y/-}$ (n= 7)**	***Ocrl*$^{Y/+}$ (n= 7)**	***Ocrl*$^{Y/-}$ (n= 7)**	***Ocrl*$^{Y/+}$ (n= 5)**	***Ocrl*$^{Y/-}$ (n= 5)**
Body weight (gr.)	24.6 ± 0.8	25.8 ± 0.4	31.03 ± 1.3	27.2 ± 1.2	31.3 ± 0.9	26.6 ± 0.9[a]	36.3 ± 0.9	32.2 ± 0.7[a]	40.1 ± 2.5	33.1 ± 1.8[b]
U volume (µL/12h)	2267 ± 337	3122 ± 328	1400 ± 82	3025 ± 111[c]	2414 ± 298	3571 ± 561	2388 ± 650	2462 ± 544	1655 ± 315	2138 ± 555
Diuresis (µL/gr. B.W./min)	0.12 ± 0.02	0.16 ± 0.01	0.06 ± 0.004	0.15 ± 0.004[b]	0.1 ± 0.01	0.18 ± 0.03	0.09 ± 0.02	0.11 ± 0.02	0.06 ±0.01	0.091 ± 0.02
U Albumin (mg/gr creatinine)	0.97 ± 0.3	21 ± 1.1[c]	3.3 ± 0.2	69 ± 13[b]	9.2 ± 2.3	27.9 ± 3.1[c]	11.8 ± 3.4	25.7 ± 2.1[c]	8.6 ± 2.5	39.5 ± 3.2[c]
U CC16 (mg/gr creatinine)	0.14 ± 0.02	1.9 ± 0.2[c]	0.09 ± 0.02	19.2 ± 1.9[c]	0.03 ± 0.00	2.5 ± 0.3[c]	0.05 ± 0.01	2.9 ± 0.3[c]	0.06 ± 0.02	2.9 ± 0.2[c]
U Calcium (mg/gr.creatinine)	94.9 ± 6.4	73.9 ± 14.5	58.2 ± 16.4	144 ± 11.6[b]	135 ± 11.2	148 ± 14.3	70.4 ± 20.3	93.8 ± 8	148 ± 23	109 ± 11.5
U Glucose (mg/gr. creatinine)	1561 ± 136	1451 ± 95	1122 ± 76	1982 ± 341[a]	1440 ± 171	1418 ± 163	1081 ± 179	1672.7 ± 493	3040 ± 993	1534 ± 93
U Phosphate (mg./gr. creatinine)	4051 ± 419	4316 ± 160	2684 ± 314	4294 ± 448[a]	4436 ± 403	4017 ± 372	2584 ± 422	2761 ± 423	3072. ± 434	3101 ± 106
U Creatinine (mg/dL)	26 ± 1.8	24 ± 1.5	31 ± 1.9	30 ± 2.5	23.4 ± 2.8	19.5 ± 1.9	35.5 ± 6.4	29.9 ± 3.8	25.4± 5	27.5 ± 1.9
BUN (mg/dL)	–	–	–	–	22 ± 1.5	22 ± 1.3	–	–	23.8 ± 2.7	22.3 ± 1.2
Plasma Creatinine (mg/dL)	–	–	–	–	0.09 ± 0.02	0.08 ± 0.006	–	–	0.05 ± 0.007	0.06 ± 0.01

U, Urine; CC16, Clara cell protein 16; BUN, Blood urea nitrogen. All the measurements were performed on *Ocrl*$^{Y/+}$ and *Ocrl*$^{Y/-}$ male mice matched per age. Plotted data represent mean ± SEM. Two-tailed unpaired Student’s t-test was applied between genotypes for the indicated time point.

[a] $p < 0.05$ versus *Ocrl* $^{Y/+}$ or *Clcn5*$^{Y/+}$; [b] $p < 0.01$ versus *Ocrl* $^{Y/+}$ *or Clcn5*$^{Y/+}$; [c] $p < 0.001$ versus *Ocrl* $^{Y/+}$ *or Clcn5*$^{Y/+}$.

Supplementary Material

OCRL Deficiency Impairs Endolysosomal Function in a Humanized Mouse Model for Lowe Syndrome and Dent Disease

Beatrice Paola Festa[1#], Marine Berquez[1#], Alkaly Gassama[1], Irmgard Amrein[2,3,4], Hesham M. Ismail[5], Marijana Samardzija[6], Leopoldo Staiano[7], Alessandro Luciani[1], Christian Grimm[4,6,8,], Robert L. Nussbaum[9,10], Maria Antonietta De Matteis[7], Olivier M. Dorchies[5], Leonardo Scapozza[5], David Paul Wolfer[2,3,4], Olivier Devuyst[1*]

[1]Institute of Physiology, University of Zurich, CH-8057 Zurich, Switzerland

[2]Division of Functional Neuroanatomy, Institute of Anatomy, University of Zurich, CH-8057 Zurich, Switzerland

[3]Institute of Human Movement Sciences and Sport, Department of Health Sciences and Technology, ETH Zurich, CH-8057 Zurich, Switzerland

[4]Neuroscience Center Zurich (ZNZ), University of Zurich, CH-8057 Zurich, Switzerland

[5]School of Pharmaceutical Sciences, University of Geneva, CMU 5-6, Rue Michel-Servet 1, Geneva, 1211, Switzerland

[6]Lab for Retinal Cell Biology, Department of Ophthalmology, University Hospital Zurich, University of Zurich, CH-8057 Zurich, Switzerland

[7]Telethon Institute of Genetics and Medicine (TIGEM), 80078 Pozzuoli, Naples, Italy

[8]Center for Integrative Human Physiology (ZIHP), University of Zurich, CH-8057 Zurich, Switzerland

[9]Department of Medicine and Institute of Human Genetics, University of California, CA 94143-0794 San Francisco, California; [10]Invitae Corporation, CA 94103 San Francisco

# These authors contributed equally to this work.

*Correspondence: Prof. Dr. med. Olivier Devuyst (✉ Olivier.Devuyst@uzh.ch) University of Zurich, Institute of Physiology, Winterthurerstrasse 190, 8057 Zurich, Switzerland; Phone: +41 (0)44 635 50 82; Fax: +41 (0)44 635 68 14

Supplementary Materials and Methods

Cell profiler quantifications

Behavioral tests

IntelliCages apparatus and mice preparation

Additional references

Supplementary Information

Suppl. Figures 1-7

Suppl. Table 1

Additional References

MATERIALS AND METHODS

Cell profiler quantifications. The pipeline "Speckle counting" derived from the open source Cell Profiler image analysis software was used to identify dots ($PI(4,5)P_2$ or PI3P or BSA or Dextran or LAMP1 or MPR-positive structures) surrounding nuclei and to perform per-nuclei aggregate measurements (eg. the number of dots/nucleus), as described by Carpenter et al. (2006) and De Leo et al. (2016). Briefly, the images were converted to greyscale using the module "ColorToGray". The "IdentifyPrimaryObjects" module was used to identify nuclei and dots while cells were identified by using the module "IdentifySecondaryObjects". "MaskObject" and "RelateObject" modules were used to establish a parent-child relationship between the cells and the dots, identified as masked objects, and to calculate the average of dots per cell. The module "MeasureObjectIntensityDistribution" was used to score the fluorescence intensity of MPR and TfR positive structures contained into perinuclear region (area defined by the first 10 bin) and peripheral region (area defined by the last 10 bin) of the cells. Briefly, the software generates 20 concentrically bin around the nucleus of each cell and calculates the intensity distribution for each bin. The module "MeasureObjectSizeShape" was used to score the vesicle size of LAMP1. The pipeline "Cell/particle counting, and scoring the percentage of stained objects" was used to score the percentage of $EEA1^+$ structures colocalizing with $PI(4,5)P_2$ or F-actin, the percentage of $LRP2^+$ structures colocalizing with F-actin, EEA1 or TfR and the percentage of $LAMP1^+$ structures colocalizing with $PI(4,5)P_2$, DQ-BSA or PepA. Briefly, the images were converted to greyscale using the module "ColorToGray". Then the "ObjectIdentification" module was used to identify the nuclei and the aforementioned stained structures/vesicles. The "RelateObject" module was used to establish a parent-child relationship between the stained objects. In this case, a "parent" object is one that touches, overlaps or encloses a "child" object. Objects1 that touch or overlap with an Object2 are considered to be colocalized and will be assigned as a parent to a corresponding child. The "ClassifyObjects" and "FilterObjects" modules were used to categorize structures that were either colocalizing or not-colocalizing, and to calculate the percentage of colocalizing structures on the total amount per image. Fluorescence intensity of LRP2 was measured from a Z stack of 55 serial images acquired, according to Nyquist theorem, every 0.13 µm to maximize the spatial information. The average fluorescence intensity of LRP2 was calculated every 0.5 µm of the Z-stacks projection by using ImageJ software. Qualitative analysis of F-actin dynamics was performed by maximal projection of Z-stack images acquired throughout the entire volume of the cells.

Behavioral tests. ***Open field large arena test.*** The large open-field arena is circular with a diameter of 150 cm, a slightly roughened white plastic floor, and 35cm high smooth sidewalls made of white polypropylene. Illumination is performed by indirect diffuse room light (4 40W bulbs, 12 lux). Each subject is released near the wall and observed for 10 min on two subsequent days. Movements are tracked using Noldus EthoVision. Between subjects, the arena is thoroughly cleaned with water and dried. ***Water-maze cue navigation.*** The water maze is constituted by a round white poly-propylene pool with a diameter of 150 cm with 68 cm high walls. It is filled with water (24-26° C, depth 15 cm) which is rendered opaque by addition of 1l of milk (UHT whole milk 3.5% fat, Coop, Switzerland). The white quadratic goal platform (14x14 cm) is made of metallic wire mesh and painted white. It is hidden 0.5 cm below the water surface in the center of one of the 4 quadrants, approximately 30 cm from the side wall. Salient extra-maze cues made of black cardboard are placed on the walls of the testing room. Computer and experimenter are hidden behind a curtain. Illumination is performed by indirect diffuse room light (4 40W bulbs, 12 lux at the center of the pool). During the test animals are trained for 2 days with the goal platform marked by a salient cue and placed in a different quadrant for every trial. All subjects are trained on the same sequence of goal positions and released from the same start points. ***Three-chambers sociability test.*** The 3-chamber cage is a polycarbonate type III cage (20.5 cm high, 58 × 40 cm top, 55 × 37.5 cm bottom, Techniplast, 2000P, Buguggiate, Italy). Two dividers provided with gates regulate the access of the test mouse from the middle to the lateral chambers. One unfamiliar stimulus mouse is placed inside a metallic cylinder in one of the two lateral chambers. The cylinder allows visual and olfactory contact between the test mouse and the stimulus mouse, reducing the possibility of physical contact. In the other lateral empty chamber, an empty cylinder is placed giving then the test mouse the choice to spend time in the chamber with the novel object (the cylinder) plus the unfamiliar mouse (social stimulus) and the chamber containing only the empty cylinder. This test runs for 10 minutes after which the stimulus mouse is considered to be familiar to the test mouse. The time spent by the test mouse in the lateral chambers is noted.

IntelliCage apparatus and mice preparation. The IntelliCage apparatus (TSE Systems, Bad Homburg, Germany) is placed in a polycarbonate cage (20.5 cm high, 58 × 40 cm top, 55 × 37.5 cm bottom, Techniplast, 2000P, Buguggiate, Italy) and accommodates up to 16 mice. Its aluminum top contains a freely accessible food rack filled with standard mouse chow (Standard 3430, Kliba Nafag, Kaiseraugst, Switzerland). The floor is covered with woodchip bedding and provides 4 central red shelters (Techniplast, Buguggiate, Italy). Four triangular conditioning chambers (15×15×21 cm) are fitted in the cage corners and provide room for one mouse at a time. Each chamber contains two drinking bottles, accessible via two round openings that can be opened and closed with motorized doors. Mice were tagged with RFID-transponders, subcutaneously implanted under isoflurane anesthesia, which can be read by a circular RIFD antenna located at the entrance of each chamber. The duration of their visit is determined by both the antenna reading and a temperature sensor that detects the presence of the animal inside the corner. During a visit, number and duration of individual nosepokes at each door are recorded using IR-beam sensors. Licking episodes at each bottle are monitored using lickometers (duration of the episode, number of licks, total contact time). IntelliCages have individual controllers and are connected to a central PC running the software that permits to design and control experiments remotely, as well as to analyze the recorded data (IntelliCage Plus, TSE Systems, Bad Homburg, Germany). After RIFD implantation, mice are allowed to recover for one week in groups of 8-16 mice in standard Type III cages with water and food ad libitum. The same grouping is maintained when the mice are later transferred to IntelliCages. During all adaptation phases and tasks in IntelliCage, mice are fed ad libitum. Ambient lights are on 20:00-08:00. Room temperature is kept constant at 23°C.

Additional References:

Carpenter, A.E., Jones, T.R., Lamprecht, M.R., Clarke, C., Kang, I.H., Friman, O., Guertin, D.A., Chang, J.H., Lindquist, R.A., Moffat, J. et al. (2006) CellProfiler: image analysis software for identifying and quantifying cell phenotypes. *Genome Biol.*, **7**, R100.

De Leo, M.G., Staiano, L., Vicinanza, M., Luciani, A., Carissimo, A., Mutarelli, M., Di Campli, A., Polishchuk, E., Di Tullio, G., Morra, V. et al. (2016) Autophagosome-lysosome fusion triggers a lysosomal response mediated by TLR9 and controlled by OCRL. *Nat. Cell. Biol.*, **18**, 839-850

Supplementary Figure 1

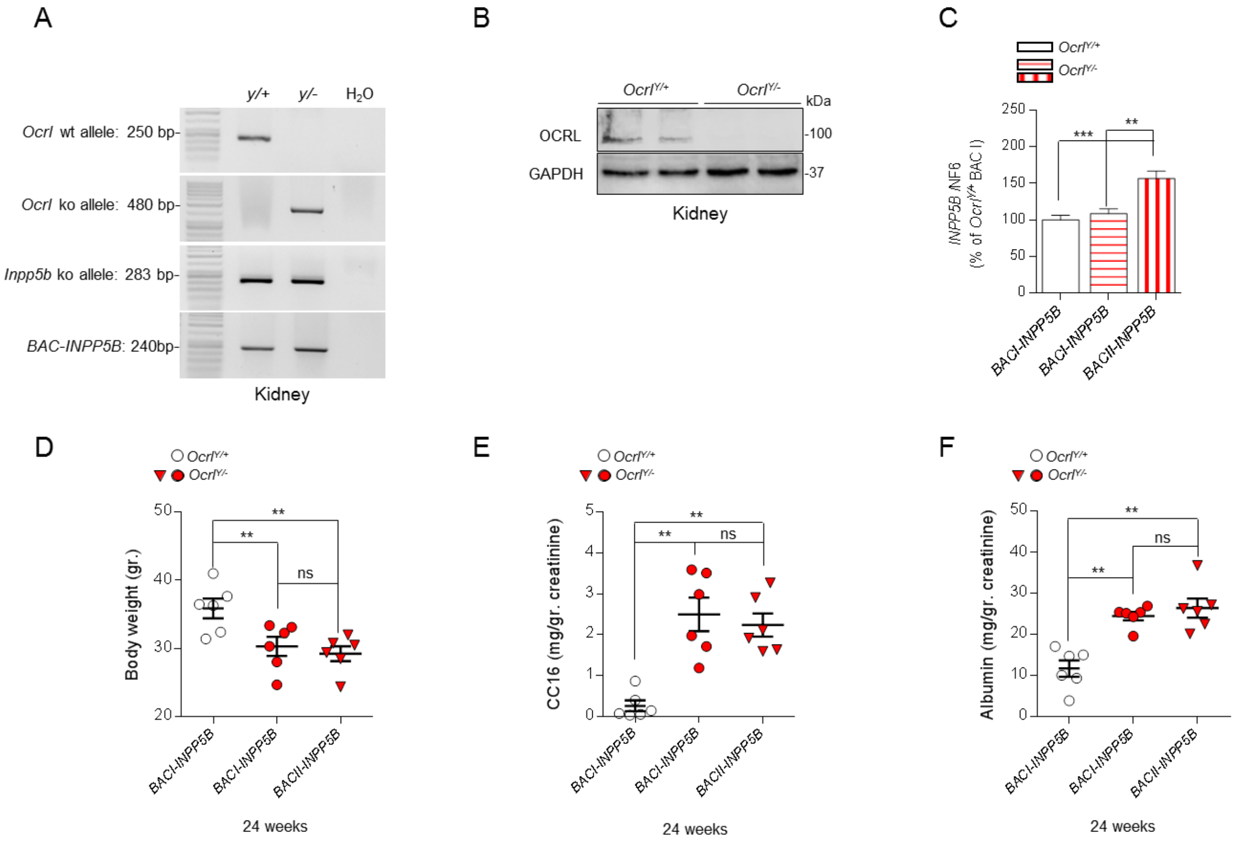

Supplementary Figure 1. **Genotype confirmation and analyses of the kidney phenotype in *Ocrl*$^{Y/-}$ mice harboring different levels of human *BAC-INPP5B* expression**. (**A**) *Ocrl*, *Inpp5b* and *BAC-INPP5B* genomic DNA analyses by PCR and agarose gel electrophoresis isolated from kidney biopsies derived from *Ocrl* mice. (**B**) Western blotting of OCRL protein level in whole kidney lysates from *Ocrl* mice. GAPDH was blotted as loading control. (**C**) *BAC-INPP5B* mRNA expression in kidneys derived from *Ocrl* mice was analyzed by quantitative RT-PCR. Gene target expression was normalized on 6 housekeeping genes and expressed as relative to *Ocrl*$^{Y/+}$ *BACI-INPP5B* (n=5 mice per condition). (**D**) Dot plot representing the measurement of the body weight, (**E**) Clara cell secretory protein (CC16) and (**F**) albumin urinary excretion in *Ocrl* mice harboring different level of *BAC-INPP5B* expression as shown in **C**. Each dot represents one mouse (n=6 mice per group). All the analyses in **D**, **E** and **F** were performed on mice matched for age (24 weeks) and gender (male). All the urine parameters were normalized to urinary creatinine concentration. Plotted data represent mean ± SEM. Two-tailed unpaired Student's t-test, **P < 0.01 relative to *Ocrl*$^{Y/+}$ or *Ocrl*$^{Y/-}$ *BACI-INPP5B* mice. ns: not significant.

Supplementary Figure 2

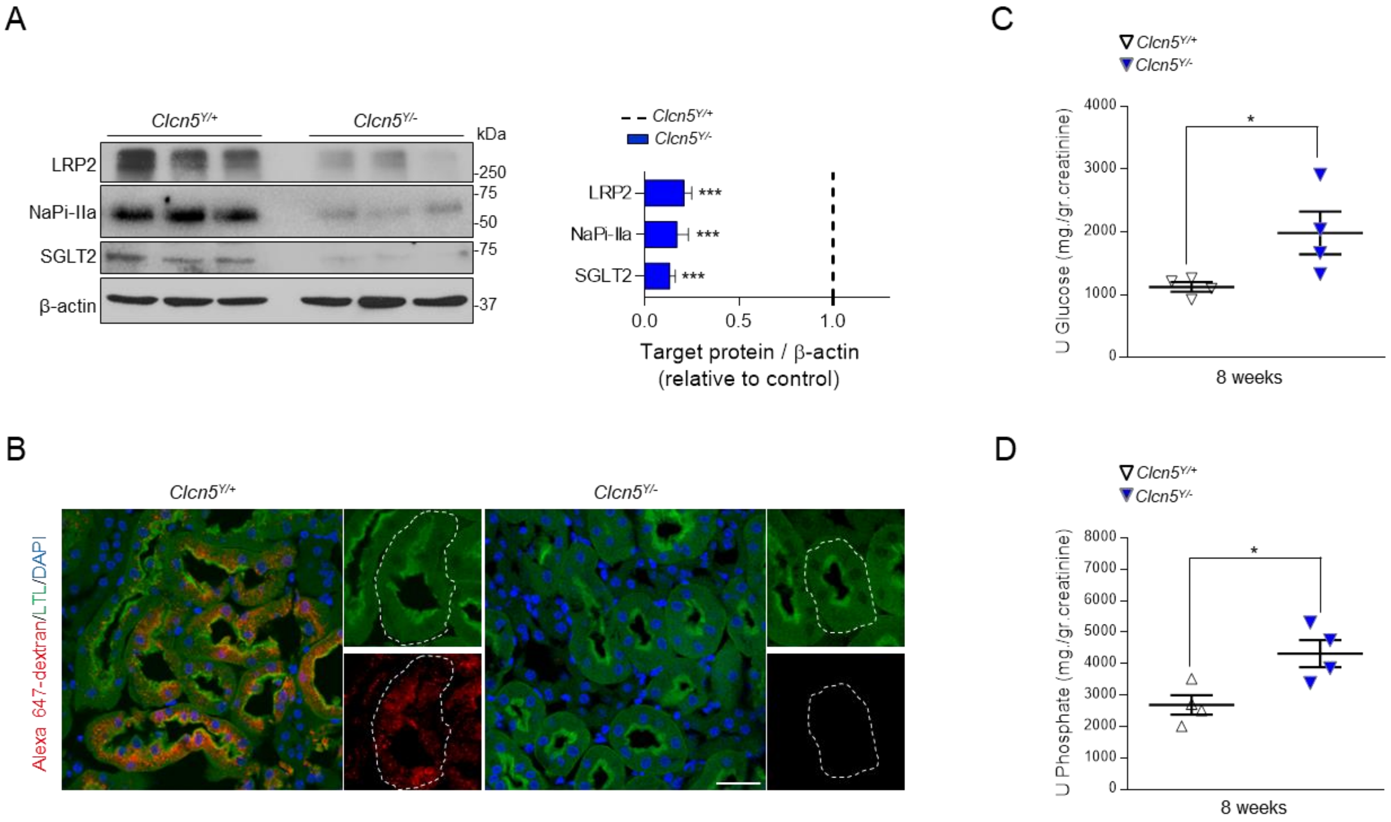

Supplementary Figure 2. **Proximal tubule dysfunction in *Clcn5*$^{Y/-}$ mice**. (**A**) Western blotting and densitometry analysis of LRP2, NaPi-IIa and SGLT2 protein levels in whole kidney lysates from *Clcn5* mice. β-actin was used as loading control. (n= 3 mice per group). (**B**) Representative confocal micrographs showing Alexa 647–labeled dextran uptake (red, 6 mg/kg B.W.) in LTL^{+} (*Lotus Tetragonolobus Lectin*, green) proximal tubules of *Clcn5* mouse model after 30 minutes from tail vein injections. Nuclei counterstained with DAPI (blue). Scale bar 25μm. (**C**) Dot plot representing the measurement of glucose and (**D**) phosphate urinary excretion in 8 weeks old *Clcn5* mice. Each dot represents one mouse (n=4 mice per group). All the urine parameters were normalized to urinary creatinine concentration. Plotted data represent mean ± SEM. Two-tailed unpaired Student's t-test, $^{*}P < 0.05$, $^{***}P < 0.001$ relative to *Clcn5*$^{Y/+}$ mice.

Supplementary Figure 3

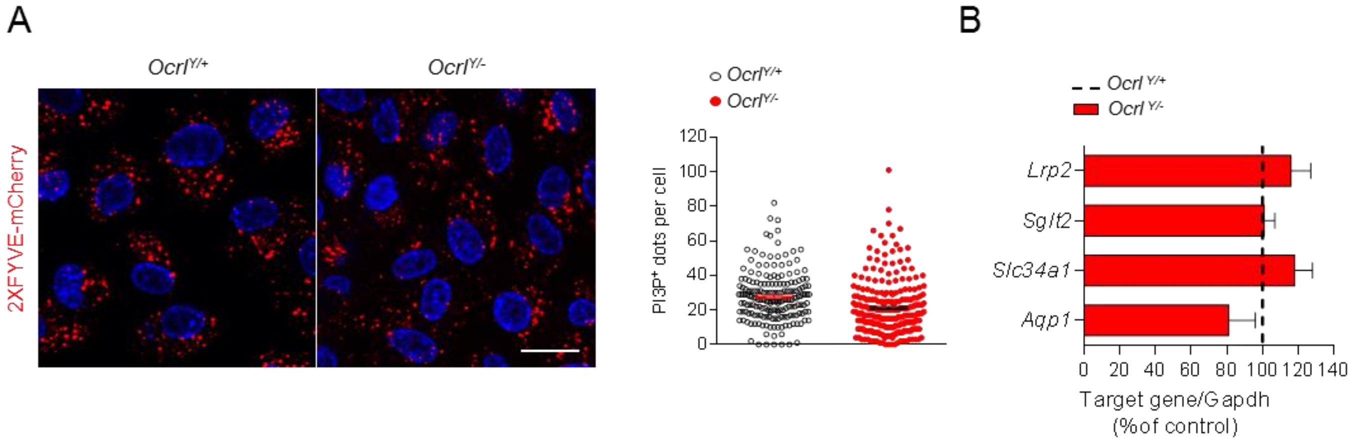

Supplementary Figure 3. *Ocrl*$^{Y/-}$ mPTCs exhibit no changes in PI3P (Phosphatidylinositol 3 phosphate) levels and no transcriptional alterations of proximal tubule receptors and channels. (**A**) Representative confocal micrographs and quantification of the number of PI3P^{+} structures stained by 2XFYVE-mcherry domain (red) in *Ocrl* mPTCs (n≈ 200-250 cells pooled from three *Ocrl* kidneys per group; each point representing the number of PI3P^{+} vesicles in a cell). Nuclei counterstained with DAPI (blue). Scale bar 15μm. **(B)** The mRNA mPTCs levels of *Lrp2*, *Sglt2*, *Slc34a1* and *Aqp1* were analyzed by real-time qPCR. Genes target expression normalized to *Gapdh* and relative to *Ocrl*$^{Y/+}$ (n = 3 mice per group). Plotted data represent mean ± SEM.

Supplementary Figure 4

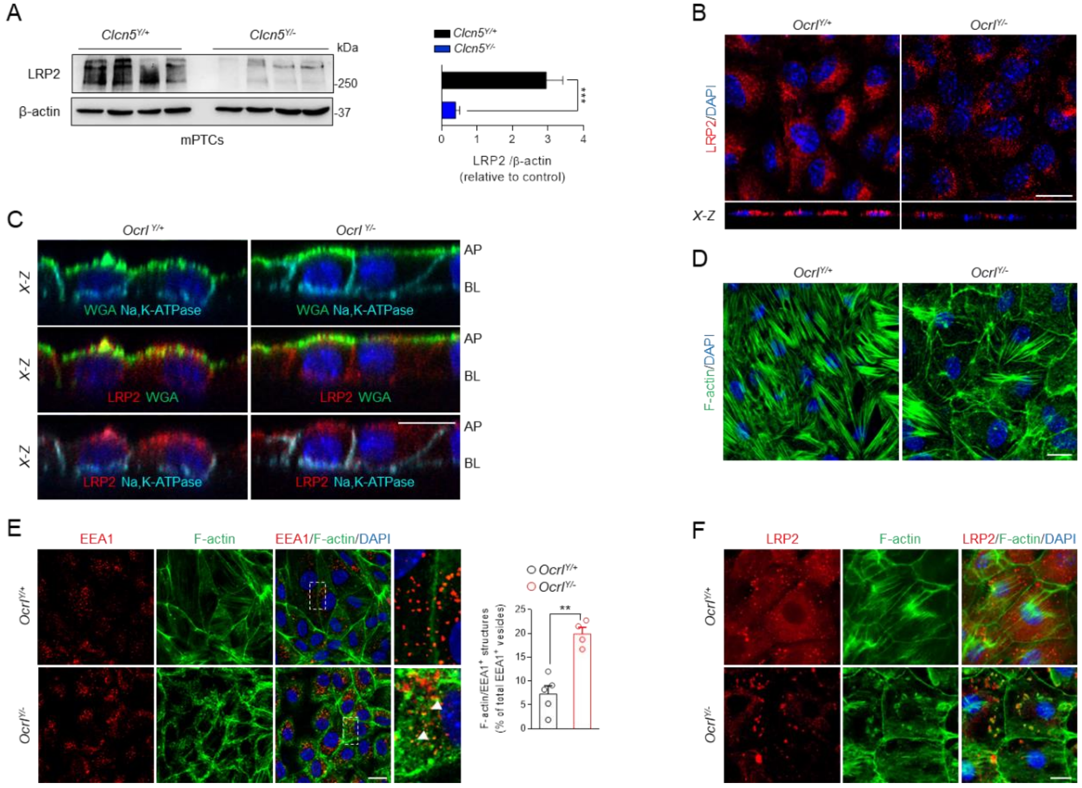

Supplementary Figure 4. LRP2 dynamics in Dent disease. ***(*A**)* Western blot and densitometry analysis of LRP2 in whole *Clcn5* mPTCs lysates. β-actin was used as loading control (n= 4 mice per group). (**B**) Representative confocal micrographs and X–Z side view of *Ocrl* mPTCs immunostained with anti-LRP2 (red). (**C**) Representative confocal micrographs of X–Z side view of a z-stack performed on *Ocrl* mPTCs immunostained with WGA (green) and Na,K-ATPase (cyan) in the upper panels, WGA (green) and LRP2 (red) in the middle panels and Na,K-ATPase (cyan) and LRP2 (red) in the lower panels. (**D**) Maximum intensity projection of a confocal Z-stacks series representing *Ocrl* mPTCs immunostained with Alexa-Fluor-488-phalloidin (green, F-actin). (**E**) Representative confocal micrographs of *Ocrl* mPTCs immunostained with anti-EEA1 (red, early endosomes) and Alexa-Fluor-488-phalloidin (green, F-actin). Quantification of F-actin/EEA1$^+$ structures (in percentage of total EEA1$^+$ vesicles, n=5 *Ocrl*$^{Y/+}$; n=4 *Ocrl*$^{Y/-}$ randomly selected fields per condition, each containing ≈ 10-15 cells). Insets: high magnification of F-actin/EEA1$^+$ structures. (**F**) High magnification confocal micrographs of *Ocrl* mPTCs immunostained with anti-LRP2 (red) and Alexa-Fluor-488-phalloidin (green, F-actin). Nuclei counterstained with DAPI (blue) in **B**-**F**. Scale bars in **C** 10μm**,** in **B**, **D**, **E** and **F** 15μm. Plotted data represent mean ± SEM. Two-tailed unpaired Student's t-test, $**P < 0.01$, $***P < 0.001$ relative to *Clcn5* $^{Y/+}$ or *Ocrl* $^{Y/+}$ mPTCs.

Supplementary Figure 5

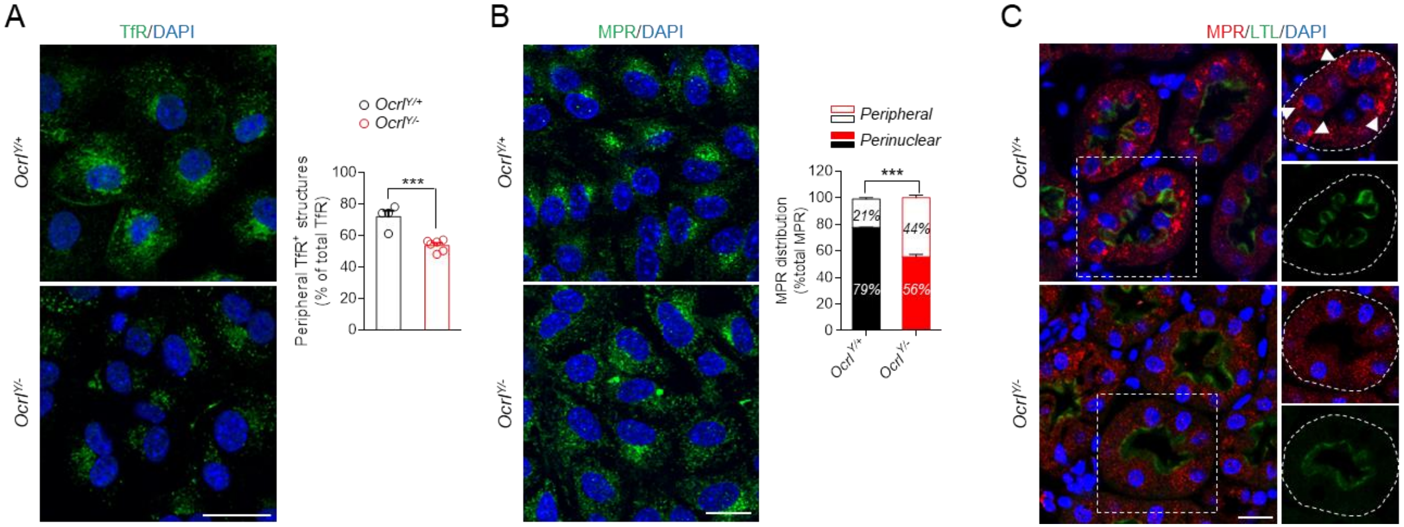

Supplementary Figure 5. Impaired trafficking of MPR and TfR cellular receptors in *Ocrl*$^{Y/-}$ mPTCs. (**A**) Representative confocal micrographs and quantification of TfR$^+$ structures distribution (green) in *Ocrl* mPTCs (in percentage of the total TfR$^+$ vesicles, n=4 *Ocrl*$^{Y/+}$; n=6 *Ocrl*$^{Y/-}$ randomly selected fields per condition, each containing ≈ 20 cells). Two-tailed unpaired Student's t-test, ***P < 0.001 relative to *Ocrl*$^{Y/+}$ mPTCs. (**B**) Representative confocal micrographs and quantification of distribution of MPR$^+$ structures (green) in *Ocrl* mPTCs (perinuclear vs peripheral in percentage of the total MPR$^+$ vesicles, n=3 randomly selected fields per condition, each containing ≈ 40-50 cells). Two-tailed unpaired Student's t-test, Peripheral/perinuclear MPR$^+$ vesicles ***P < 0.001 relative to *Ocrl*$^{Y/+}$ mPTCs. (**C**) Representative confocal micrographs showing MPR$^+$ structures (red) in LTL$^+$ (*Lotus Tetragonolobus Lectin*, green) proximal tubules of *Ocrl* mouse kidneys. Plotted data represent mean ± SEM. Nuclei counterstained with DAPI (blue). Scales bars in **A** 20µm **B** and **C** 15µm.

Supplementary Figure 6

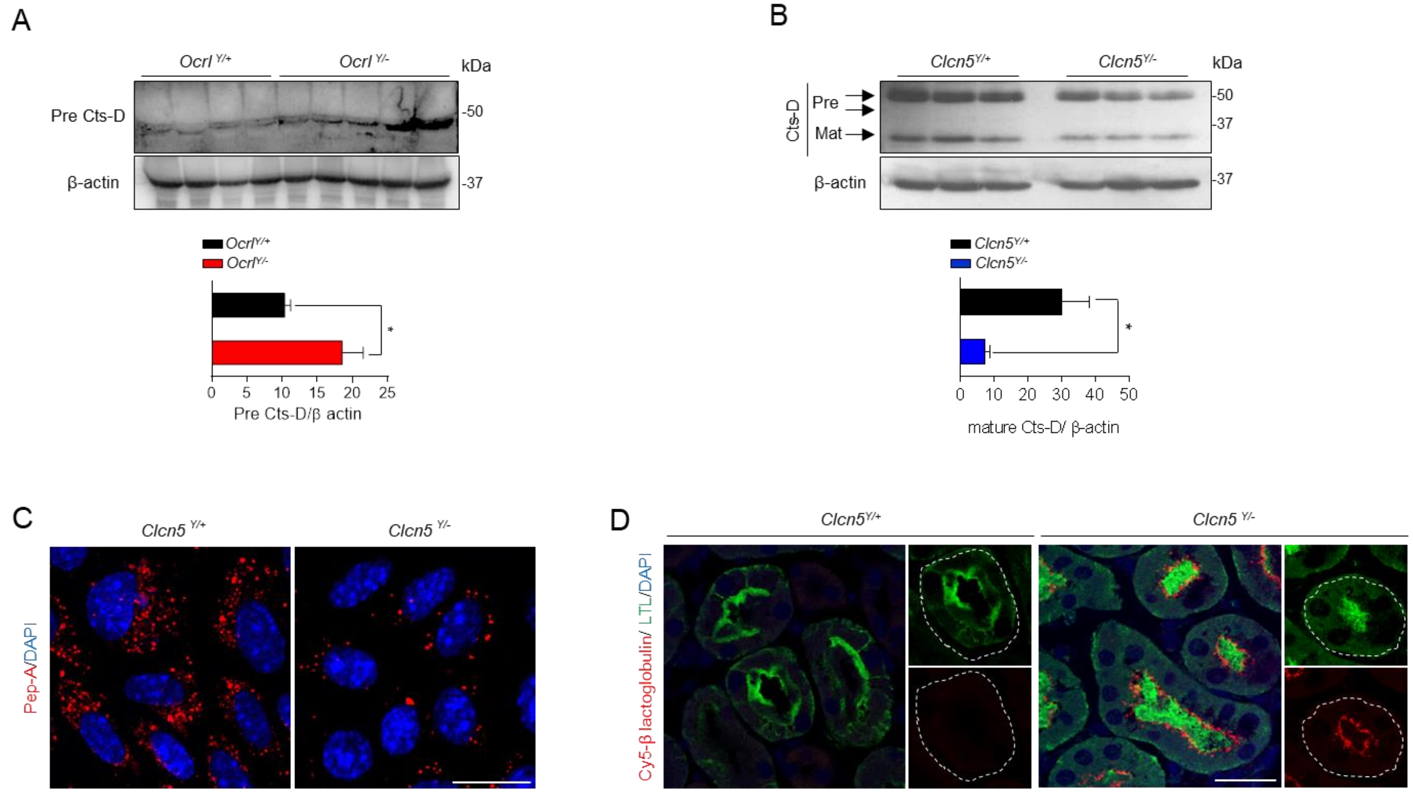

Supplementary Figure 6. Altered lysosomal activity in Dent disease. (**A-B**)Western blotting and densitometry analysis of Cathepsin D (Cts-D) protein levels in (**A**) plasma samples from *Ocrl* mice (n= 4 *Ocrl*$^{Y/+}$ and n= 5 *Ocrl*$^{Y/-}$ mice) and in (**B**) *Clcn5* mPTCs (n= 3 mice per group). β-actin was used as loading control. Plotted data represent mean ± SEM. Two-tailed unpaired Student's t-test, $^{*}P < 0.05$ relative to *Ocrl*$^{Y/+}$ plasma or *Clcn5*$^{Y/+}$ mPTCs. (**C**) Confocal micrographs showing *Clcn5* mPTCs immunostained with Bodipy-FL-PepA (1 μM, for 1 h at 37 °C, green). (**D**) Representative confocal micrographs showing Cy5 labeled β-lactoglobulin (red, 1mg/kg B.W.) after 120 minutes from tail vein injections in LTL^{+} proximal tubules from *Clcn5* mouse kidneys. Nuclei counterstained with DAPI (blue) in **C** and **D**. Scale bars 15μm in **C** and 25μm in **D.**

Supplementary Figure 7

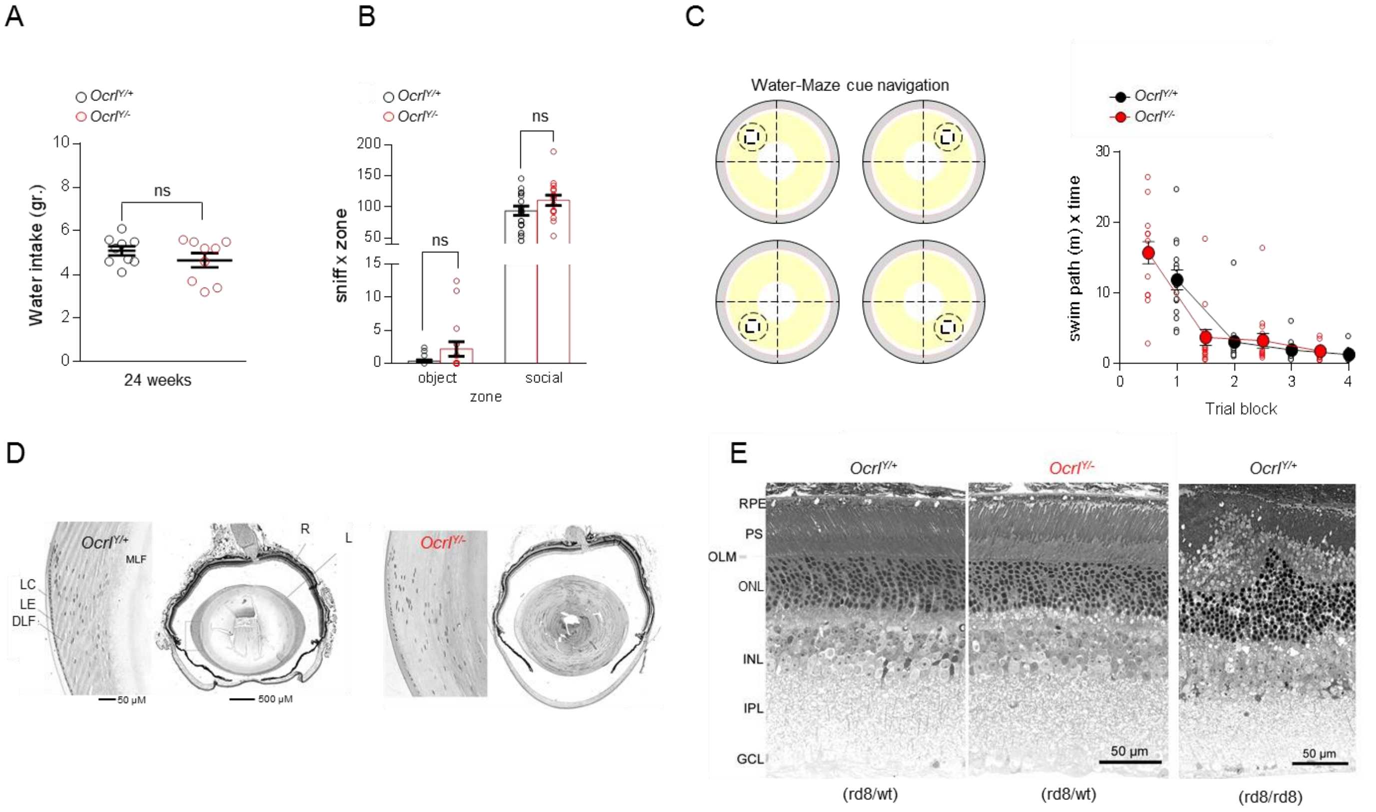

Supplementary Figure 7. **No impairment of social behavior neither defective ocular morphology is observed in *Ocrl*$^{Y/-}$ mice.** (**A**) Dot plot representing the measurement of water intake, over 12 hours, in 24 weeks old *Ocrl* male mice. Each dot represents one mouse. (**B**) Dotted bar graph representing the number of nose contact time with the social (cage with mouse) and object (empty cage) stimulus during the 3 chambers sociability test. Plotted data represent mean ± SEM. Each dot of the graphs represents one mouse. (**C**) Schematic representation of the water maze cue navigation test (left panel): animals are trained in the water maze to reach a platform marked by a salient cue and placed in a different quadrant for every trial. Dot plot (right panel) representing the swim path as function of 3 trial blocks. Each dot of the graphs represents one mouse. (**D**) Light microscopy representative pictures of high magnification hematoxylin-eosin stained lens (left panels, scale bars 50μm) and midsagittal sections of whole eyes (right panels, scale bars 500μm) derived from *Ocrl* mice. LC (lens capsule), LE (lens epithelium), DFL (differentiating lens fiber), MFL (mature lens fiber), L (lens) and R (retina). (**E**) Toluidine blue stained retina derived from *Ocrl* mice in presence or absence of the spontaneous rd8 (retinal degeneration 8) mutation in *Crb1* gene (right panel, rd8/rd8). RPE (retinal pigment epithelium), PS (photoreceptor segments), OLM (outer limiting membrane), ONL (outer nuclear layer), INL (inner nuclear layer), IPL (inner plexiform layer), GCL (ganglion cell layer); Scale bars 50μm. ns: not significant.

Table S1: Primer pairs for gene expression analysis.

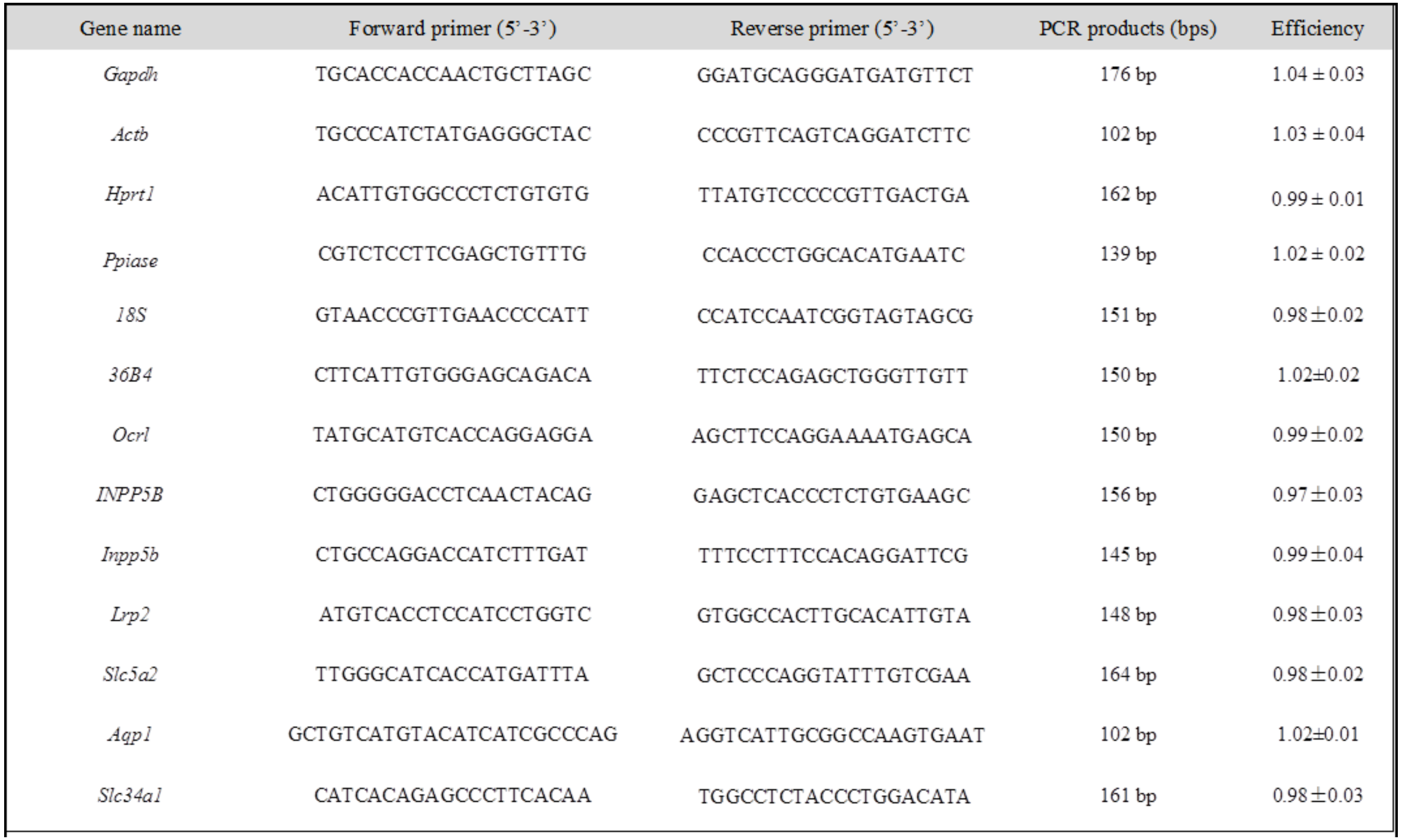

Gene name	Forward primer (5’-3’)	Reverse primer (5’-3’)	PCR products (bps)	Efficiency
Gapdh	TGCACCACCAACTGCTTAGC	GGATGCAGGGATGATGTTCT	176 bp	1.04 ± 0.03
Actb	TGCCCATCTATGAGGGCTAC	CCCGTTCAGTCAGGATCTTC	102 bp	1.03 ± 0.04
Hprt1	ACATTGTGGCCCTCTGTGTG	TTATGTCCCCCGTTGACTGA	162 bp	0.99 ± 0.01
Ppiase	CGTCTCCTTCGAGCTGTTTG	CCACCCTGGCACATGAATC	139 bp	1.02 ± 0.02
18S	GTAACCCGTTGAACCCCATT	CCATCCAATCGGTAGTAGCG	151 bp	0.98 ±0.02
36B4	CTTCATTGTGGGAGCAGACA	TTCTCCAGAGCTGGGTTGTT	150 bp	1.02±0.02
Ocrl	TATGCATGTCACCAGGAGGA	AGCTTCCAGGAAAATGAGCA	150 bp	0.99 ±0.02
INPP5B	CTGGGGGACCTCAACTACAG	GAGCTCACCCTCTGTGAAGC	156 bp	0.97 ±0.03
Inpp5b	CTGCCAGGACCATCTTTGAT	TTTCCTTTCCACAGGATTCG	145 bp	0.99 ±0.04
Lrp2	ATGTCACCTCCATCCTGGTC	GTGGCCACTTGCACATTGTA	148 bp	0.98 ±0.03
Slc5a2	TTGGGCATCACCATGATTTA	GCTCCCAGGTATTTGTCGAA	164 bp	0.98 ±0.02
Aqp1	GCTGTCATGTACATCATCGCCCAG	AGGTCATTGCGGCCAAGTGAAT	102 bp	1.02±0.01
Slc34a1	CATCACAGAGCCCTTCACAA	TGGCCTCTACCCTGGACATA	161 bp	0.98 ±0.03

2. Phosphoinositide 3-kinase inhibitor alpelisib restores actin organization and improves proximal tubule dysfunction in Lowe syndrome and Dent disease

Marine Berquez*, Jonathan R. Gadsby*, Beatrice Paola Festa*, Richard Butler, Stephen P. Jackson, Valeria Berno, Alessandro Luciani, Olivier Devuys†, and Jennifer L. Gallop†.

1 Institute of Physiology, University of Zurich, Zurich, Switzerland.
2 Gurdon Institute and Department of Biochemistry, Tennis Court Road, University of Cambridge, Cambridge, CB2 1QN, UK
3 Gurdon Institute, Tennis Court Road, University of Cambridge, Cambridge, CB2 1QN, UK
4 Experimental Imaging Center, ALEMBIC, IRCCS San Raffaele Scientific Institute, 20132, Milan, Italy

* Equal contribution; † Co-directed the study, correspondence to OD or JLG.

Kidney International, Volume 98, Issue 4, 01 October 2020, Pages 883-896
DOI: https://doi.org/10.1016/j.kint.2020.05.040

ABSTRACT

Loss-of-function mutations in the *OCRL* gene, which encodes the phosphatidylinositol [PI] 4,5-bisphosphate [PI(4,5)P_2] 5-phosphatase OCRL, cause defective endocytosis and proximal tubule dysfunction in Lowe syndrome and Dent disease 2. The defect is due to increased levels of PI(4,5)P_2 and aberrant actin polymerization, blocking endosomal trafficking. PI 3-phosphate [PI(3)P] has been recently identified as a coactivator with PI(4,5)P_2 in the actin pathway. Here, we tested the hypothesis that phosphoinositide 3-kinase (PI3K) inhibitors may rescue the endocytic defect imparted by OCRL loss, by rebalancing phosphoinositide signals to the actin machinery. The broad-range PI3K inhibitor copanlisib and class IA p110α PI3K inhibitor alpelisib reduced aberrant actin polymerization in OCRL-deficient human kidney cells *in vitro*. Levels of PI 3,4,5-trisphosphate, PI(4,5)P_2 and PI(3)P were all reduced with alpelisib treatment, and siRNA knockdown of the PI3K catalytic subunit p110α phenocopied the actin phenotype. In a humanized *Ocrl*$^{Y/-}$ mouse model, alpelisib reduced endosomal actin staining while restoring stress fiber architecture and levels of megalin at the plasma membrane of proximal tubule cells, reflected by improved endocytic uptake of low molecular weight proteins *in vivo*. Thus, our findings support the link between phosphoinositide lipids, actin polymerization and endocytic trafficking in the proximal tubule and represent a proof-of-concept for repurposing alpelisib in Lowe syndrome/Dent disease 2.

INTRODUCTION

Epithelial cells lining the proximal tubules (PTs) of the kidney possess an efficient receptor-mediated endolysosomal pathway that recovers and processes essential substances that are filtered through the glomerulus. Congenital disorders affecting endolysosomes cause PT dysfunction (renal Fanconi syndrome) with urinary loss of solutes and low-molecular-weight (LMW) proteins, often complicated by metabolic and growth complications and development of chronic kidney disease (1). Inactivating mutations in *OCRL* have been associated with Dent disease 2 (MIM #300555), a disorder characterized by PT dysfunction, kidney stones, and progressive kidney failure, and with the oculocerebrorenal syndrome of Lowe (MIM #309000), which displays, in addition to the PT dysfunction and kidney failure, systemic manifestations such as congenital cataracts, cognitive disability, and hypotonia (2-4).Current treatments for Dent disease 2 and Lowe syndrome are only supportive.

LMW proteinuria is a consistent feature observed in Lowe syndrome/Dent disease 2, revealing that *OCRL* affects receptor-mediated endocytosis (5). *OCRL* encodes the phosphatidylinositol (PI) 4,5-bisphosphate [PI(4,5)P_2] 5-phosphatase OCRL (6), which controls lipid identity in the endolysosomal pathway by degrading PI(4,5)P2 (Figure 1a). Deficient degradation of PI(4,5)P_2 through OCRL is implicated in the failure to uncoat clathrin-coated vesicles in fibroblasts, accompanied by the formation of “comet” structures of polymerized, filamentous actin from the resulting aberrant early endosome-like organelles (7-9). In other cell types, most notably the PT cells of the kidney, OCRL deficiency results in F-actin “basket” structures surrounding aberrant endolysosomal organelles (10). The excess F-actin blocks membrane trafficking through the endocytic and endolysosomal pathway, and is suggested to decrease recycling of the multiligand receptor megalin to the apical membrane, aggravating the defect within the endolysosomal pathway (11). In agreement with a prime role of aberrant F-actin, defective endocytic uptake caused by *OCRL* mutations is alleviated by targeting the actin machinery with latrunculin B, or by depleting actin regulatory proteins as well as by small, interfering RNA (siRNA)-mediated depletion of PI(4)P 5-kinase to adjust the synthesis of PI(4,5)P_2 (7,10) (Figure 1a).

Actin polymerization is increasingly understood as arising not only from PI(4,5)P_2 but also from other phosphoinositide lipids. For example, PI(3,4,5)P_3 activates Rho-type GTPase Rac and PI(3)P acts in conjunction with PI(4,5)P_2 to stimulate actin polymerization downstream of another Rho-type GTPase, Cdc42 (12-14). The interconversion of these phosphoinositides is coupled to the movement of lipids through the endocytic and endosomal pathway. PI(4,5)P_2 is phosphorylated by class I phosphatidylinositol-3′-kinase (PI3K) to PI(3,4,5)P_3 at the plasma membrane and becomes progressively dephosphorylated to PI(3,4)P_2 and PI(3)P or PI(4,5)P_2 (14,15). PI(3)P is enriched at endosomes, where it is essential for their function and predominantly made by direct by phosphorylation of PI by class III PI3K, Vps34 (16) (Figure 1a). In an OCRL-deficient retinal pigmented epithelial (RPE) cell line, actin comets generated are reduced by treatment with PI3K inhibitors wortmannin and Vps34-IN1, in agreement with biochemical studies showing a coregulation of actin via the coincidence of both PI(3)P and PI(4,5)P_2 (14).

The rescue of endocytosis observed when targeting the actin machinery in OCRL patient and knockout (KO) cells (7,10),together with upstream regulation of actin by PI3K activity (14) and the highly interconnected nature of PI conversion, provides an intriguing possibility that class I PI3K inhibitors may be of utility in Lowe syndrome. Such inhibitors, developed for cancer therapy, are approved for clinical use (17) and are thus potentially amenable for drug repurposing. Although compounds such as copanlisib (18) have a broad specificity and side effects, recent success has been demonstrated for more specific inhibitors. Idelalisib (19), which targets PI3K subunit p110δ, is approved for chronic lymphocytic lymphoma, and alpelisib, which targets p110α, is approved for use in breast cancer (20,21). Moreover, alpelisib has shown clinical benefit in children with PROS/CLOVES syndrome (22), a rare overgrowth syndrome resulting from activation of PIK3A.

Here, we tested the hypothesis that class I PI3K inhibitors may rescue the endocytic defect due to the loss of OCRL, using established cellular and mouse models (10,11,23).
We show that the inhibition of PI3K activity via copanlisib or alpelisib, or siRNA-mediated depletion of the alpelisib-target catalytic subunit p110α reduces the excess actin polymerization in human kidney (HK2) cells deficient in OCRL. Focusing on alpelisib as the most specific compound for clinical use, we show that it reduces actin polymerization and improves uptake through the endolysosomal pathway in PT cells from humanized *Ocrl*$^{Y/-}$ mice *in vitro*. Furthermore, alpelisib treatment *in vivo* alleviates proteinuria, reduces PT dysfunction, and rescues the cellular levels of megalin in humanized *Ocrl*$^{Y/-}$ mice. These results support alpelisib as a candidate for drug repurposing in Lowe syndrome and Dent disease 2.

RESULTS

Class I PI3K inhibitors reduce actin aggregation in OCRL-KO HK2 cells

We used CRISPR-Cas9 gene editing to knockout (KO) *OCRL* in the HK2 cell line to allow testing of class I PI3K inhibitors on the characteristic actin aggregation at endolysosomal compartments (7,810,14). Western blotting verified a 98.0 ± 0.7% reduction in OCRL expression in lysates from the KO HK2 cells (Figure 1b). The *OCRL* KO recapitulated the actin basket phenotype in the HK2 cells, as indicated by an increased overlap between F-actin and early endosome antigen 1 (EEA1), quantified on Airyscan confocal microscopy z-stacks (Figure 1c–e). This increased overlap observed in *OCRL* KO cells was reversed by treatment with copanlisib (C), a broad-range PI3K inhibitor that targets p110α and δ and to a lesser extent the p110β and γ isoforms (Figure 1c). By western blotting of HK2 whole cell extracts, we found that the PI3K p110 regulatory subunits α, β, and δ were all well expressed in both wild-type (WT) and KO cells, with only trace levels of the p110γ isoform present (Supplementary Figure S1A).

We distinguished the PI3K specificity of the inhibition of F-actin using alpelisib (A), a selective inhibitor of p110α, and GSK2636771 (G) and idelalisib (I), selective inhibitors of p110β and p110δ, respectively (Supplementary Figure S1A). Although alpelisib treatment gave a similar reduction in endosomal actin polymerization compared with copanlisib (Figure 1d), GSK2636771 and idelalisib had a little effect on actin accumulation (Figure 1e). The class I PI3K inhibitors had no increased toxicity on *OCRL* KO relative to unmodified cells, based on the MTT assay (Supplementary Figure S1B).

Alpelisib and p110α knockdown rescue the actin phenotype in HK2 cells

For our ensuing studies, we focused on alpelisib as it is the most selective and least toxic PI3K inhibitor developed so far, and is currently used to treat a mosaic overactivation of PI3K class Iα in children with PROS/CLOVES syndrome (22). Alpelisib reduced the actin baskets in *OCRL* KO HK2 cells in a dose-responsive fashion (Figure 2a). The effects were observed at 10 µM dosage as soon as 4 hours after treatment, without apparent toxicity (Supplementary Figure S2). To test whether PI3K inhibition by alpelisib was the source of the decreased actin staining, we specifically reduced its target, the p110α subunit, using siRNA (Figure 2b). Compared with treatment with a control (sequence-scrambled) siRNA, siRNA against p110α yielded a 78.3 ± 4.8% and 68.9 ± 7.7% depletion of p110α protein in WT and *OCRL* KO HK2 cells, respectively, reflected by a significant reduction in actin baskets (Figure 2c).

Reduced levels of PI(3,4,5)P3, PI(4,5)P2, and PI(3)P in alpelisib-treated HK2 cells

To examine how phosphoinositide lipids are affected by *OCRL* KO and alpelisib treatment, we stained HK2 cells with antibodies or protein domains against PI(3,4,5)P_3, PI(3)P, and PI(4,5)P_2, using optimized fixation conditions for the plasma membrane or intracellular staining (24,25). PI(3,4,5)P_3 has a diffuse localization to the plasma membrane, and alpelisib treatment (10 μM) induced a robust decrease in staining for PI(3,4,5)P_3 in both WT and *OCRL* KO cells, as expected from its mechanism of action and specificity for class IA PI3K p110α (Figure 3a). PI(3,4,5)P_3 is expected to be dephosphorylated progressively as membranes are endocytosed and trafficked into endosomes (14,26,27). By fixing cells such that intracellular PI(3)P is preserved (25), we found that PI(3)P punctae were also reduced by alpelisib treatment (in a dose-responsive fashion apparent from concentrations as low as 10 μM for the 16-hour treatment) in both WT and *OCRL* KO cells (Figure 3b and Supplementary Figure S2C). As expected, the KO of *OCRL* in HK2 cells induced a marked increase in the levels of PI(4,5)P_2 both at the plasma membrane (Figure 3c) and intracellularly (Figure 3d), compared with WT cells (10,28). Treatment with alpelisib markedly reduced the elevation of PI(4,5)P_2 generated by *OCRL* KO in both compartments, whereas it had no effect in WT cells (Figure 3c and d). Alpelisib is reported to inhibit PI 4-kinase β with a 50% inhibitory concentration of 0.5 μM (19), which is a possible source of the reduction in PI(4,5)P_2. Collectively, our data suggested that alpelisib inhibits actin assembly on *OCRL* KO endosomes via a bispecific effect on the PI(4,5)P_2 and PI(3)P levels.

Alpelisib reduces intracellular phosphoinositides and alleviates cytoskeletal defects in Ocrl$^{Y/–}$ mPTCs

We next tested whether alpelisib had the same effects in primary cells of PT cells derived from the humanized *Ocrl*-deficient mouse model (*Ocrl*$^{Y/–}$), which recapitulates the abnormal actin polymerization and endocytic defect observed in patient-derived cells (10,11). The mouse PTCs (mPTCs) expressed similar class I PI3K regulatory subunits to HK2 cells in both WT and *Ocrl*$^{Y/–}$ mice, and displayed a similar toxicity profile toward alpelisib when assessed by MTT assays (Supplementary Figure S3). Imaging by confocal microscopy revealed a striking disruption of the normal F-actin stress fiber architecture in mPTCs from *Ocrl*$^{Y/–}$ compared with *Ocrl*$^{Y/+}$ mice, likely due to the relocation of actin regulatory proteins from their normal cellular locations to endosomes, as large assemblies of actin surround these organelles and are thought to be the origin of the trafficking defect (10,29). Treatment of *Ocrl*$^{Y/–}$ mPTCs with alpelisib (10 μM) restored the stress fiber architecture (Figure 4a).

As the main problem in Lowe syndrome and Dent disease 2 is reduced endosomal trafficking and consequent megalin degradation, we sought to distinguish endosomal actin from the stress fibers. We collected laser-scanning confocal z-stacks throughout the cells, reconstructed the staining pattern in 3D surface renderings, and used size shape/parameters to identify punctate actin structures and the degree to which they overlapped with endosomal structures (Supplementary Figure S4 and Movies S1–S3). This analysis revealed that treatment with alpelisib decreased aberrant polymerization of F-actin at endosomes stained with EEA1, distinct from the stress fiber architecture (Figure 4b). The mPTCs derived from *Ocrl*$^{Y/-}$ mice showed significant changes in intracellular staining for PI(3)P (decreased) and PI(4,5)P_2 (increased), compared with mPTCs from WT *Ocrl*$^{Y/+}$ mice (Figure 4c and d). Treatment of mPTCs from *Ocrl*$^{Y/-}$ mice with alpelisib resulted in a significant reduction in intracellular PI(3)P and PI(4,5)P_2 staining (Figure 4c and d).

Alpelisib improves endocytic uptake in Ocrl$^{Y/-}$ mPTCs

We next assessed whether the effect of alpelisib on the cytoskeletal and vesicular defects observed in mPTCs resulted in changes in the endocytic uptake capacity. To differentiate the effect of alpelisib on binding and/or internalization of the ligand, mPTCs were first incubated with labeled bovine serum albumin (BSA), to induce binding of the probe with the endocytic receptors, and then incubated with growth medium, to follow the internalization of albumin (Figure 5a). The *Ocrl*$^{Y/-}$ cells showed a lower plasma membrane binding of Alexa 488-bovine serum albumin along with impaired internalization of albumin compared with *Ocrl*$^{Y/+}$ cells. Treatment with alpelisib rescued both the binding and the uptake of albumin in the *Ocrl*$^{Y/-}$ cells, with a 50% overall rescue of endocytic uptake (Figure 5b and c). These data were supported by the measurement of total albumin uptake (Supplementary Figure S5a and b). We noted that the internalized/bound Alexa 488-bovine serum albumin ratio remained similar between the different conditions (Figure 5d), implying that the reduced uptake of albumin is mainly due to impaired binding rather than a defective internalization process *per se.*

Alpelisib improves PT dysfunction and receptor-mediated endocytosis in Ocrl$^{Y/-}$ mice

We tested the potential therapeutic effect of alpelisib on PT dysfunction *in vivo*. *Ocrl* mice were administered with either vehicle or alpelisib (50 mg/kg body weight per day) by oral gavage for 6 weeks (Figure 6a). This regimen was chosen according to previous *in vivo* studies demonstrating efficacy and safety (22,30). In line with alpelisib administration being known to cause insulin resistance and hyperglycemia (22), alpelisib treatment led to a significant increase in glycosuria in both *Ocrl*$^{Y/+}$ and *Ocrl*$^{Y/-}$ mice, which could be considered as a biomarker for drug dosing (Supplementary Table S1). After 6 weeks of alpelisib treatment, the *Ocrl*$^{Y/-}$ mice displayed a significant reduction in the urinary excretion of the LMW proteins CC16 (−34%) and albumin (−38%), compared with vehicle-treated controls (Figure 6b and c), whereas volume of urine and other parameters were unaffected (Supplementary Table S1). Alpelisib-treated mice of both genotypes showed a similar reduction in growth rate relative to control mice, as previously described (22). Nevertheless, both vehicle and treated mice gained body weight, indicating that the drug does not severely affect postnatal development (Figure 6d and Supplementary Table S1).

To test whether the effect of alpelisib on LMW proteinuria reflected recovery of receptor-mediated endocytosis in PT cells, we followed the *in vivo* uptake of Cy5-labeled β-lactoglobulin in a mouse kidney. Alpelisib-treated *Ocrl*$^{Y/-}$ mice displayed a significant rescue of Cy5-labeled β-lactoglobulin uptake, close to the extent of internalization observed in vehicle-treated *Ocrl*$^{Y/+}$ mice (Figure 6e). This was mirrored by a significant rescue in expression of the endocytic receptor megalin in PT cells, as observed by immunolabeling and western blotting of the kidney lysates of alpelisib-treated *Ocrl*$^{Y/-}$ mice; note that there was no change in expression of the PT marker AQP1 (Figure 6f and g and Supplementary Figure S5C and D). These data show that the PI3K inhibitor alpelisib induces a substantial improvement of the PT endocytic machinery and reduces LMW proteinuria in a humanized mouse model for Lowe syndrome.

DISCUSSION

There is currently no treatment to alleviate the defective endocytosis causing PT dysfunction in Lowe syndrome and Dent disease 2. Our findings reveal that alpelisib alleviates the aberrant actin phenotype by reducing levels of PI(4,5)P_2 and PI(3)P, causing a substantial improvement of the endocytic machinery and absorptive capacity in cellular systems and a humanized mouse model for Lowe syndrome/Dent disease 2. These results support the link between phosphoinositide lipids, actin polymerization, and endocytic trafficking, with immediate relevance for highly active epithelial cells involved in crucial homeostatic processes (Figure 7). Given the lack of effective therapies and the apparent safety of this class of PI3K inhibitors, alpelisib is a promising candidate for drug repurposing in Lowe syndrome and Dent disease.

LMW proteinuria is the most consistent feature encountered in patients with Lowe syndrome and Dent disease 2 due to inactivating mutations in *OCRL* (4). These LMW proteins can readily be detected and quantified, offering a faithful biomarker of defective receptor-mediated endocytosis in PT cells (1). LMW proteinuria is particularly relevant, as it is detected more consistently and often earlier than other solutes (e.g., glucose, phosphate, amino acids) being part of the classical “renal Fanconi syndrome”—at least in congenital disorders of the endolysosomal pathway (1).

Here, we show that alpelisib rescues the apical endocytic uptake capacity of PT cells *in vitro* and *in vivo*, due to restored levels of megalin receptor at the plasma membrane. This effect is reflected by significant reductions in the urinary loss of LMW proteins (CC16 and albumin) in *Ocrl*$^{Y/-}$ mice treated with alpelisib for 6 weeks. These effects of alpelisib have been observed in mPTCs, which keep their apical differentiation and are particularly well suited to investigate receptor-mediated endocytosis in physiology and disease (9). In particular, we obtained mPTCs from a humanized mouse model expressing human INPP5B in *Ocrl*$^{Y/-}$;*Inpp5b*$^{-/-}$ background, which allows us to investigate the specific consequences of the loss of OCRL activity (11,23).

The rescue of endocytosis by alpelisib is explained by its effect on actin machinery, clearly evidenced in *OCRL* KO HK2 cells and mPTCs. Our observations thus confirm and extend previous studies showing the link between control of the phosphoinositide balance and F-actin in the early endosomal pathway in OCRL patient and KO cells (7,10). The functional loss of OCRL activity impairs the degradation of PI(4,5)P_2, which, in turn, leads to a failure to uncoat clathrin-coated vesicles resulting in aberrant endosomal organelles in various cell types including the PT cells (7-10).

We recently showed that the excess F-actin decreases the recycling of the multiligand receptor megalin to the apical membrane of PT cells, causing defective endocytosis and LMW proteinuria (11).

Our data indicate that the mechanism of action of alpelisib on endosomal actin arises from a bispecific effect of alpelisib inhibition: first on production of $PI(3,4,5)P_3$ and its conversion to PI(3)P, and second on production of $PI(4,5)P_2$. The decrease in $PI(4,5)P_2$ levels directly counteracts the OCRL deficiency and is in agreement with previous work alleviating excess actin and increasing endocytic flux by reduction in the levels of phosphatidylinositol 4-phosphate 5-kinase, an enzyme that generates $PI(4,5)P_2$ (10).

Alpelisib has a 0.5 μM 50% inhibitory concentration on the $PI(4,5)P_2$ generating kinase PI4Kβ, which may be responsible, or it could result from more general effects on phosphoinositide balance resulting from the combination of *OCRL* KO and alpelisib treatment. We have identified that class IA PI3K inhibition by alpelisib is relevant to actin inhibition as siRNA-mediated depletion of p110α inhibits actin accumulation similarly to alpelisib treatment and copanlisib (which is not reported to inhibit PI4Ks). In RPE cells we have previously observed that siRNA of INPP4A, which converts $PI(3,4)P_2$ to PI(3)P, inhibits actin assembly in *OCRL* KO cells, providing a pathway from inhibition of $PI(3,4,5)P_3$ production to a decrease in endosomal PI(3)P. We showed that some PI(3)P remains, presumably the pool produced at the early endosome by class III PI3K, Vps34, because we found that endosomal trafficking is enhanced rather than suppressed by alpelisib treatment. The complex coregulation of PI metabolism and its relevance for OCRL inactivation has also been highlighted in a recent study where noncatalytic functions of phosphoinositide 3-phosphatase PTEN activates $PI(4,5)P_2$ degradation via PLCXD, alleviating cellular phenotypes and absorption of ligands in a zebrafish model (31).

The alleviation of the actin phenotype by reduced levels of $PI(4,5)P_2$ and PI(3)P by alpelisib treatment agrees with the synergistic action of $PI(4,5)P_2$ and PI(3)P in recruiting SNX9 to activate the actin machinery at *Ocrl* endosomes (14), suggesting a very effective match of alpelisib specificity to manipulate the molecular regulation of actin activation at endosomes. In turn, as previously demonstrated, reduced endosomal actin assembly in turn leads to an improvement in PT endocytosis in OCRL-deficient cells (10). Further characterization will be needed to better understand whether regulation of actin through phosphoinositide metabolism is the true source of the therapeutic effect that we observe with alpelisib in the *Ocrl*$^{Y/-}$ mouse model. Because class I PI3K regulate pathways control cell growth, proliferation, survival, metabolism, and autophagy (32), we cannot exclude that the endocytic rescue is due to effects on PI(3,4,5)P_3 directly and the combined effect on other pathways modulated by class I PI3K. More work is also needed to test whether PI3K inhibitors might also alleviate the neurologic and other clinical manifestations of patients harboring *OCRL* mutations (4).

The recent experience of alpelisib in pediatric patients with PROS/CLOVES syndrome suggests that the drug has the potential to be well tolerated. Alpelisib is taken orally, selectively targets the α isoform of PI3K class I, and shows a minor toxicity profile compared with pan-PI3K inhibitors. As alpelisib does not completely block PI3K activity, thus maintaining functions of the signaling pathway, it may be particularly suitable for long-term use. Of interest, the hyperglycemia arising from alpelisib use may be manageable by dietary changes (22). Because PT dysfunction is the first manifestation of kidney disease observed in young infants with Dent disease 2 and Lowe syndrome, an early treatment of such PT dysfunction, leading to improvements in the metabolic profile and growth, might therefore slow progression to chronic kidney disease and therefore have a significant impact on lifespan and quality of life (33). Although the disease manifestations of *OCRL* mutation are particularly wide, recent studies based on large cohorts of genotyped patients with Lowe syndrome of Dent disease 2 did not evidence significant effects of the type of mutation or the location of the mutation on renal survival (34). Collectively, our data highlight the potential for repurposing alpelisib for treating PT dysfunction in Lowe syndrome/Dent disease 2, thus providing a basis for rapid and cost-effective deployment in human clinical trials.

METHODS

Full details can be found in the Supplementary Methods.

HK2 cells were treated with copanlisib, alpelisib, GSK2636771, or idelalisib at indicated concentrations for 16 hours unless otherwise stated. Proteins were extracted using standard methods from cells or kidney tissues and western blotting performed using published or commercially available antibodies. siRNA knockdown was performed using 2 transfections 72 and 24 hours before analysis. We used age- and gender-matched *Ocrl*$^{Y/+}$;*Inpp5b*$^{-/-}$; and *Ocrl*$^{Y/-}$;*Inpp5b*$^{-/-}$ mouse littermates harboring BAC-INPP5B expression. Primary cultures of mPTCs were generated from the kidneys harvested from 8 week-old *Ocrl* mice and the endocytic capacity of *Ocrl* mPTCs assessed by measuring albumin uptake. Alpelisib treatments were 10 µM for 16 hours, unless otherwise stated. Albumin uptake in mPTCs was assessed using a "pulse-chase" protocol to assess apical binding and resultant uptake. mPTCs were stained overnight with the appropriate primary antibody and for 45 minutes with suitable fluorophore-conjugated secondary antibodies and/or Alexa-488 Phalloidin. PI(3)P staining on mPTCs was performed using the FYVE domain probe. Image analysis was performed with CellProfiler, using custom pipelines to measure actin/EEA1 overlap and number of puncta, and with ImageJ to measure immunofluorescence intensity and detected edges to calculate stress fiber score. Quantitative data were expressed as means ± standard error of the mean. For the *in vivo* experiments, mice aged 6 weeks were treated with vehicle or alpelisib 50 mg/kg body weight. Urine was collected every 14 days and animals were sacrificed after 42 days of treatment, with blood and kidneys harvested. The PT endocytic capacity of *Ocrl* mice was examined by measuring β-lactoglobulin uptake.

DISCLOSURE

JLG has funding from AstraZeneca for a studentship in her lab. SPJ is on the advisory boards and has equity ownership of Mission Therapeutics, Carrick Therapeutics, and Adrestia Therapeutics, and is a Science Partner for Ahren Innovation Capital. All the other authors declared no competing interests.

ACKNOWLEDGEMENT

This work was supported by European Research Council Grant 281971, Wellcome Trust Research Career Development Fellowship WT095829AIA, Wellcome Senior Research Fellowship 219482/Z/19/Z, Wellcome Trust Developing Concept Fund 209749/Z/17/Z, Isaac Newton Trust Research Grant 18.23(j) to JLG, and Wellcome Investigator Award 206388/Z/17/Z to SPJ, and we acknowledge the Gurdon Institute funding from the Wellcome Trust (092096) and CRUK (C6946/A14492). We are grateful to the Cystinosis Research Foundation (Irvine, CA), the Swiss National Science Foundation (project grant 310030_189044), the clinical research priority program (KFSP) RADIZ (Rare Disease Initiative Zurich) of the UZH, the Swiss National Centre of Competence in Research (NCCR) Kidney Control of Homeostasis (Kidney.CH) for support, and the NIDDK/NIH and the Lowe Syndrome Trust/UK for supporting development of the *Ocrl* mice. We acknowledge Robert L. Nussbaum (Invitae Corporation and UCSF, San Francisco, CA) and Maria Antonietta De Matteis (Telethon Institute of Genetics and Medicine, University Federico II Naples, Naples, Italy) for providing the founders for the *Ocrl* mouse colony; and Eric Olinger (UZH, Zurich) for fruitful discussions. We thank Nadine Näegele and Daniela Nieri for providing technical assistance during the urine collection and analysis; Guillaume Canaud (Hôpital Necker-Enfants Malades, Paris) for sharing with us the detailed protocol for the preparation of Alpelisib for the *in vivo* treatment; and Renata Kozyraki and Pierre Verroust for providing reagents. We also thank the Center for Microscopy and Image Analysis of the University of Zurich (Zurich, Switzerland) and Zurich integrative rodent physiology (ZIRP) facility for providing the equipment for imaging acquisition and technical support during the *in vivo* experiments.

AUTHOR CONTRIBUTIONS

O.D. and J.L.G. conceptualized and supervised the study. B.P.F., M.B. and O.D. designed the experiments and performed the mouse and mPTCs study. J.L.G and J.G. designed the experiments and performed the HK2 study. A.L. and V.B. helped for the confocal microscopy experiments and the quantification of the pictures. R.B. and S.P.J. helped for the phospholipids study. M.B., B.P.F., J.G., J.L.G. and O.D. wrote the paper with inputs and comments from all of authors.

REFERENCES

1. van der Wijst J, Belge H, Bindels RJM, Devuyst O. Learning physiology from inherited kidney disorders. Physiol Rev. 2019;99:1575–1653.

2. Loi M. Lowe syndrome. Orphanet J Rare Dis. 2006;1:16.3. Lewis RA, Nussbaum RL, Brewer ED. Lowe syndrome. In: Adam MP, Ardinger HH, Pagon RA, et al., eds. GeneReviews_ [internet]. Seattle (WA): University of Washington, Seattle; 1993-2020. Available at: https:// www.ncbi.nlm.nih.gov/books/NBK1480/. Published July 24, 2001; Updated April 18, 2019. Accessed August 8, 2019.

4. De Matteis MA, Staiano L, Emma F, Devuyst O. The 5-phosphatase OCRL in Lowe syndrome and Dent disease 2. Nat Rev Nephrol. 2017;13: 455–470.

5. Devuyst O, Luciani A. Chloride transporters and receptor-mediated endocytosis in the renal proximal tubule. J Physiol. 2015;593:4151–4164.

6. Zhang X, Jefferson AB, Auethavekiat V, Majerus PW. The protein deficient in Lowe syndrome is a phosphatidylinositol-4,5-bisphosphate 5- phosphatase. Proc Natl Acad Sci U S A. 1995;92:4853–4856.

7. Nández R, Balkin DM, Messa M, et al. A role of OCRL in clathrin-coated pit dynamics and uncoating revealed by studies of Lowe syndrome cells. eLife. 2014;3:e02975.

8. Mehta ZB, Pietka G, Lowe M. The cellular and physiological functions of the Lowe syndrome protein OCRL1. Traffic. 2014;15:471–487.

9. De Leo MG, Staiano L, Vicinanza M, et al. Autophagosome-lysosome fusion triggers a lysosomal response mediated by TLR9 and controlled by OCRL. Nat Cell Biol. 2016;18:839–850.

10. Vicinanza M, Di Campli A, Polishchuk E, et al. OCRL controls trafficking through early endosomes via PtdIns4,5P(2)-dependent regulation of endosomal actin. EMBO J. 2011;30:4970–4985.

11. Festa BP, Berquez M, Gassama A, et al. OCRL deficiency impairs endolysosomal function in a humanized mouse model for Lowe syndrome and Dent disease. Hum Mol Genet. 2019;28:1931–1946.

12. Welch HC, Coadwell WJ, Ellson CD, et al. P-Rex1, a PtdIns(3,4,5)P3- and Gbetagamma-regulated guanine-nucleotide exchange factor for Rac. Cell. 2002;108:809–821.

13. Gallop JL, Walrant A, Cantley LC, Kirschner MW. Phosphoinositides and membrane curvature switch the mode of actin polymerization via selective recruitment of toca-1 and Snx9. Proc Natl Acad Sci U S A. 2013;110:7193–7198.

14. Daste F, Walrant A, Holst MR, et al. Control of actin polymerization via the coincidence of phosphoinositides and high membrane curvature. J Cell Biol. 2017;216:3745–3765.

15. Malek M, Kielkowska A, Chessa T, et al. PTEN regulates PI(3,4)P2 signaling downstream of class I PI3K. Mol Cell. 2017;68:566–580.e510.

16. Gillooly DJ, Morrow IC, Lindsay M, et al. Localization of phosphatidylinositol 3-phosphate in yeast and mammalian cells. EMBO J. 2000;19:4577–4588.

17. Fruman DA, Chiu H, Hopkins BD, et al. The PI3K pathway in human disease. Cell. 2017;170:605–635.

18. Liu N, Rowley BR, Bull CO, et al. BAY 80-6946 is a highly selective intravenous PI3K inhibitor with potent p110alpha and p110delta activities in tumor cell lines and xenograft models. Mol Cancer Ther. 2013;12:2319–2330.

19. Fritsch C, Huang A, Chatenay-Rivauday C, et al. Characterization of the novel and specific PI3Kalpha inhibitor NVP-BYL719 and development of the patient stratification strategy for clinical trials. Mol Cancer Ther. 2014;13:1117–1129.

20. Furet P, Guagnano V, Fairhurst RA, et al. Discovery of NVP-BYL719 a potent and selective phosphatidylinositol-3 kinase alpha inhibitor selected for clinical evaluation. Bioorg Med Chem Lett. 2013;23:3741–3748.

21. Andre F, Ciruelos E, Rubovszky G, et al. Alpelisib for PIK3CA-mutated, hormone receptor-positive advanced breast cancer. N Engl J Med. 2019;380:1929–1940.

22. Venot Q, Blanc T, Rabia SH, et al. Targeted therapy in patients with PIK3CA-related overgrowth syndrome. Nature. 2018;558:540–546.

23. Bothwell SP, Chan E, Bernardini IM, et al. Mouse model for Lowe syndrome/Dent Disease 2 renal tubulopathy. J Am Soc Nephrol. 2011;22: 443–448.

24. Chen R, Kang VH, Chen J, et al. A monoclonal antibody to visualize PtdIns(3,4,5)P(3) in cells. J Histochem Cytochem. 2002;50:697–708.

25. Hammond GR, Schiavo G, Irvine RF. Immunocytochemical techniques reveal multiple, distinct cellular pools of PtdIns4P and PtdIns(4,5)P(2). Biochem J. 2009;422:23–35.

26. He K, Marsland R III, Upadhyayula S, et al. Dynamics of phosphoinositide conversion in clathrin-mediated endocytic traffic. Nature. 2017;552:410–414.

27. Bilanges B, Posor Y, Vanhaesebroeck B. PI3K isoforms in cell signalling and vesicle trafficking. Nat Rev Mol Cell Biol. 2019;20:515–534.

28. Montjean R, Aoidi R, Desbois P, et al. OCRL-mutated fibroblasts from patients with Dent-2 disease exhibit INPP5B-independent phenotypic variability relatively to Lowe syndrome cells. Hum Mol Genet. 2015;24: 994–1006.

29. Suchy SF, Nussbaum RL. The deficiency of PIP2 5-phosphatase in Lowe syndrome affects actin polymerization. Am J Hum Genet. 2002;71:1420–1427.

30. Mizrachi A, Shamay Y, Shah J, et al. Tumour-specific PI3K inhibition via nanoparticle-targeted delivery in head and neck squamous cell carcinoma. Nat Commun. 2017;8:14292.

31. Mondin VE, Ben El Kadhi K, Cauvin C, et al. PTEN reduces endosomal PtdIns(4,5)P2 in a phosphatase-independent manner via a PLC pathway. J Cell Biol. 2019;218:2198–2214.

32. Jean S, Kiger AA. Coordination between RAB GTPase and phosphoinositide regulation and functions. Nat Rev Mol Cell Biol. 2012;13:463–470.

33. Devuyst O, Knoers NV, Remuzzi G, et al. Rare inherited kidney diseases: challenges, opportunities, and perspectives. Lancet. 2014;383:1844–1859.

34. Zaniew M, Bokenkamp A, Kolbuc M, et al. Long-term renal outcome in children with OCRL mutations: retrospective analysis of a large international cohort. Nephrol Dial Transplant. 2018;33:85–94.

Figure 1

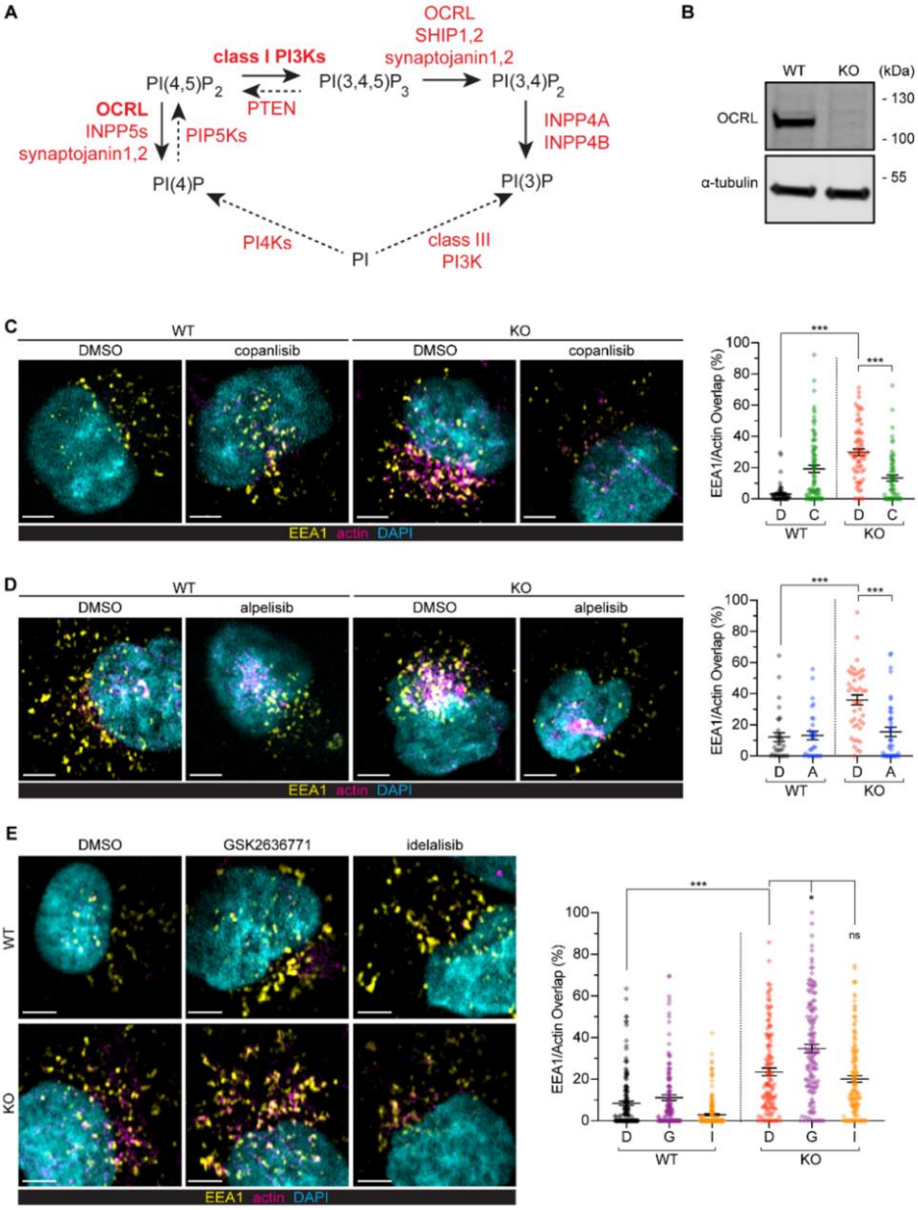

Figure 1. PI3K inhibitors relieve aberrant actin assembly at endosomes in an OCRL-deficient human kidney (HK2) cell model. (**a**) Steps of phosphoinositide lipid conversion relevant for this study indicating the conversions between $PI(4,5)P_2$, $PI(3,4,5)P_2$, and $PI(3)P$ with the most relevant enzymes in bold, most relevant conversions in solid lines, and others in dashed lines. $PI(4,5)P_2$ is elevated in Lowe syndrome due to the lack of 5-phosphatase activity from OCRL and is made from the phosphorylation of PI by phosphatidylinositol 4-kinases (PI4Ks) and PI(4)P 5-kinase (PIP5K). $PI(4,5)P_2$ is phosphorylated by class I PI3Ks to produce $PI(3,4,5)P_3$. $PI(3,4,5)P_3$ can be dephosphorylated to $PI(4,5)P_2$ by PTEN or to $PI(3,4)P_2$ by SH-2–containing inositol 50 polyphosphatase (SHIP) 1 and 2, synaptojanin 1 and 2, and also OCRL, although this is thought to be minor. $PI(3,4)P_2$ is dephosphorylated to PI(3)P by inositol polyphosphate-4-phosphatase type I A (INPP4A) and B. PI(3)P is also made at endosomes via the phosphorylation of PI by class III PI3K, vacuolar sorting protein Vps34. (**b**) Western blots illustrating OCRL expression loss in the HK2 OCRL CRISPR knockout (KO) cell line compared with wild-type (WT) HK2 control cells with atubulin as loading control. (**c**–**e**) Representative Airyscan confocal micrographs and quantification of early endosome antigen 1 (EEA1)/actin overlap (expressed as a percentage of total detected EEA1þ vesicles) for HK2 WT or OCRL KO cells treated with either dimethylsulfoxide (DMSO) (**d**) or the indicated inhibitor and fixed using the 4% formaldehyde fix. In all cases, the images illustrate a single z-slice from an Airyscan-processed confocal stack of cells immunolabeled for EEA1 (yellow), phalloidin (actin, magenta), and 40,6-diamidino-2-phenylindole (DAPI) (cyan). Bars=5 mm. In the quantifications, the lines indicate the mean ± SEM and each data point is an individual cell. In all experiments, treatments were applied 16 hours before fixation. In all quantifications, statistical significance was assessed by a Kruskal-Wallis (KW) analysis of variance with Dunn's multiple comparisons test. (**c**) WT or KO cells treated with either DMSO or 100 nM of copanlisib, demonstrating rescue of the actin-endosomal overlap. K-W test: ***P < 0.001, multiple comparisons; WT DMSO versus KO DMSO, KO DMSO versus KO copanlisib both ***P < 0.001, WT copanlisib versus KO copanlisib P=0.44 (not significant [ns]). N=52, 85, 67, and 63 cells for WT DMSO, WT copanlisib, KO DMSO, and KO copanlisib, respectively. (d) WT or KO cells treated with either DMSO or 10 mM of alpelisib, demonstrating rescue of the actin-endosomal overlap. K-W test: ***P < 0.001, multiple comparisons; WT DMSO versus KO DMSO, KO DMSO versus KO alpelisib both ***P < 0.001, WT alpelisib versus KO alpelisib. P > 0.99 (ns). N=31, 30, 43, and 41 cells for WT DMSO, WT alpelisib, KO DMSO, and KO alpelisib, respectively. (**e**) WT or KO cells treated with either DMSO, 10 mM of GSK2636771, or 10 mM of idelalisib, demonstrating that neither compound is able to significantly reduce the actin-endosomal overlap. K-W test: ***P < 0.001, multiple comparisons; WT DMSO versus KO DMSO, ***P < 0.001, KO DMSO versus KO GSK, *P=0.04, KO DMSO versus KO idelalisib, P > 0.99 (ns). N=159, 130, 203, 122, 131, and 145 cells for WT DMSO, WT GSK2636771, WT idelalisib, KO DMSO, KO GSK2636771, and KO idelalisib, respectively.

Figure 2

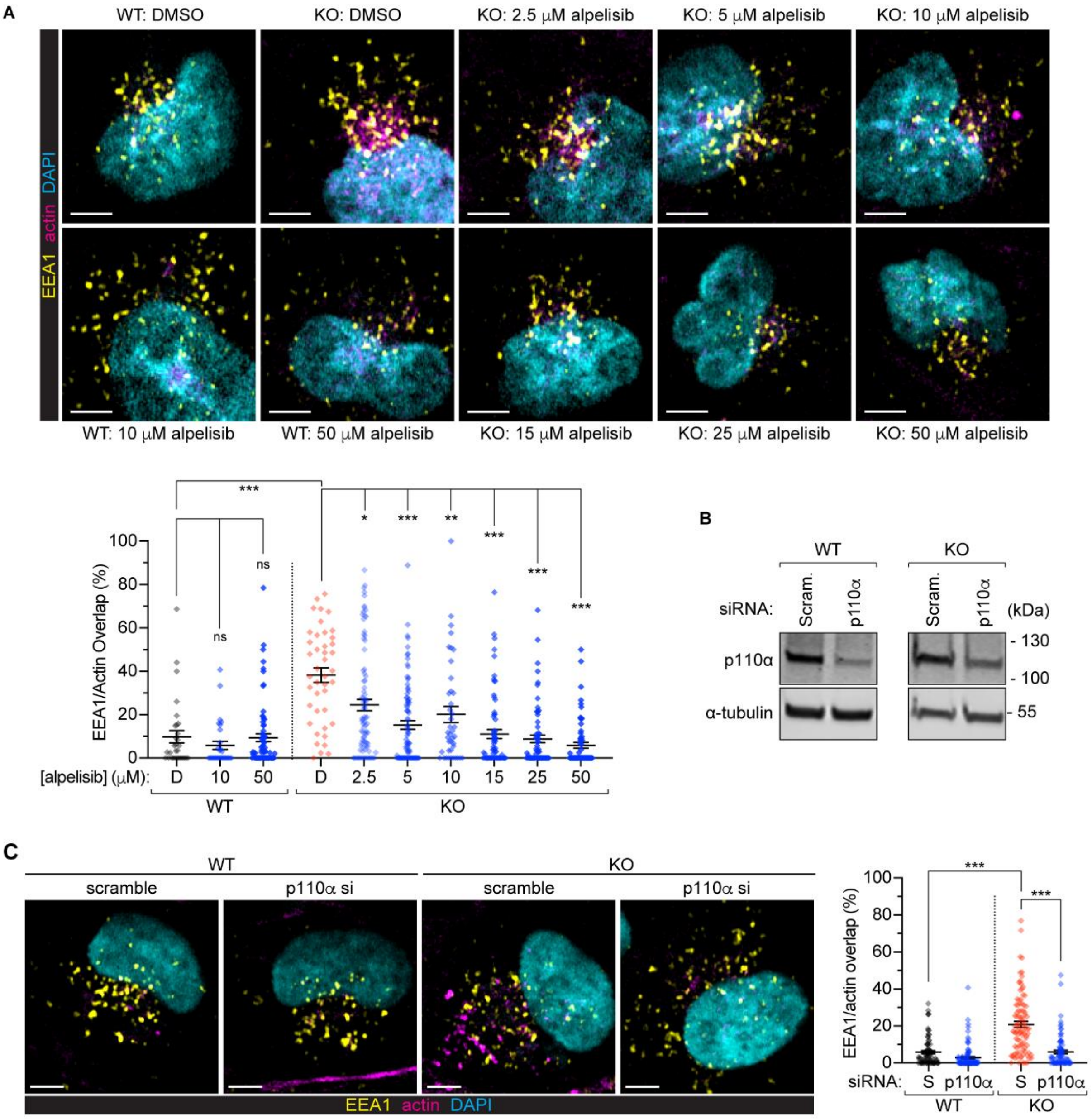

Figure 2. Alpelisib effects on actin are dose-responsive and recapitulated by siRNA of PI3K p110a. (**a**) Representative Airyscan confocal micrographs (fixed using the 4% formaldehyde fix and immunolabeled for early endosome antigen 1 [EEA1], yellow; actin [phalloidin], magenta; and 40,6-diamidino-2-phenylindole [DAPI], cyan; bars=5 mm) and quantification of wild-type (WT) or knockout (KO) human kidney (HK2) cells treated with dimethylsulfoxide (DMSO) or the indicated doses of alpelisib for 16 hours, demonstrating dose-responsive rescue of the actin-endosomal overlap. In all cases, the lines indicate mean ± SEM and the points indicate individual cells. N=31, 30, 71, 42, 90, 89, 41, 69, 66, and 67 cells for WT control, WT 10 mM, WT 50 mM, KO DMSO, and KO 2.5, 5, 10, 15, 25, and 50 mM alpelisib, respectively. Statistical significance assessed by the Kruskal-Wallis (K-W) test with Dunn's multiple comparisons test: overall ***P < 0.001, multiple comparisons; WT DMSO versus KO DMSO, KO DMSO versus KO 5, 15, 25, and 50 mM alpelisib all ***P < 0.001, KO DMSO versus KO 2.5 mM alpelisib *P ¼ 0.0131, KO DMSO versus KO 10 mM alpelisib **P=0.0043, WT DMSO versus both WT 10 and 50 mM alpelisib P > 0.9999 (not significant [ns]). (**b**) Western blot for p110a and the loading control a-tubulin of WT or KO cells treated with either scramble (Scram.) or p110a siRNA. (**c**) Representative Airyscan confocal micrographs (fixed using the 4% formaldehyde fix and immunolabeled for EEA1, yellow; actin [phalloidin], magenta; and DAPI, cyan; bars=5 mm) and quantification of WT or KO cells treated with either scramble (S) or p110a siRNA, demonstrating reduction of EEA1-actin overlap on p110a depletion. K-W test with Dunn's multiple comparisons test: ***P < 0.001, multiple comparisons; WT scramble versus KO scramble, KO scramble versus KO p110a siRNA both ***P < 0.001. N=79, 108, 93, and 131 cells, respectively. HK2, human kidney; PI3K, phosphatidylinositol-30-kinase; siRNA, small, interfering RNA.

Figure 3

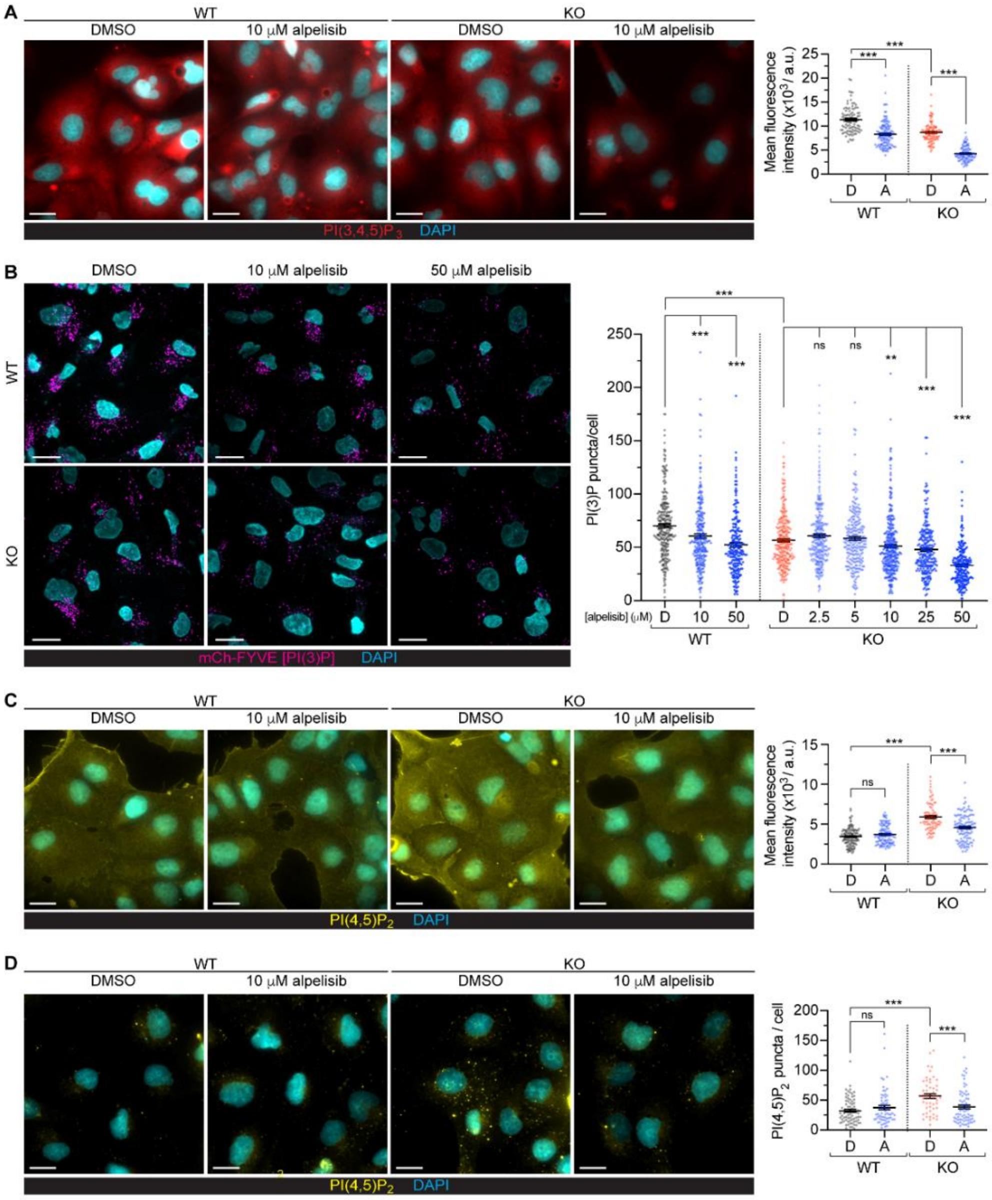

Figure 3. Levels of phosphatidylinositol (PI) 4,5-bisphosphate [PI(4,5)P2] are elevated with OCRL knockout (KO), and PI(3,4,5)P3, PI(4,5)P2, and PI(3)P are suppressed by alpelisib treatment. In all experiments, the indicated treatments were applied 16 hours before fixation. In the quantifications, the lines indicate the mean ± SEM and each data point results from an individual cell. In all quantifications, statistical significance was assessed by a Kruskal-Wallis (K-W) analysis of variance with Dunn's multiple comparisons test. Bars=20 mm in all images. (**a**) Representative widefield micrographs of wild-type (WT) or KO human kidney (HK2) cells treated with dimethylsulfoxide (DMSO) or 10 mM of alpelisib and then fixed with the plasma membrane fix and immunolabeled for PI(3,4,5)P3 (red) and 40,6-diamidino-2-phenylindole (DAPI) (cyan), with quantification of the mean cellular PI(3,4,5)P3 labeling intensity, showing the effectiveness of alpelisib treatment on PI(3,4,5)P3 synthesis. N=96, 128, and 109 cells for WT DMSO, WT alpelisib, KO DMSO, and KO alpelisib, respectively. K-W (test: overall ***P < 0.001, multiple comparisons; WT DMSO versus KO DMSO, WT DMSO versus WT alpelisib, and KO DMSO versus KO alpelisib all ***P < 0.001. (**b**) Representative confocal micrographs of WT or KO HK2 cells treated with either DMSO, 10 mM-,or 50-mM alpelisib for 16 hours and then fixed with the Golgi fix and labeled using the mCh-2xFYVE PI(3)P probe (magenta) and DAPI (cyan), with quantification of the number of PI(3)P-positive puncta detected in cells treated with a range of alpelisib concentrations, as indicated, showing PI(3)P-positive punctae are reduced in a dose-responsive fashion. N=280, 254, 210, 287, 324, 239, 340, 250, 240, and 215 cells for WT control, WT 10 mM, WT 50 mM, KO DMSO, and KO 2.5, 5, 10, 25, and 50 mM alpelisib, respectively. K-W test: overall ***P < 0.001, multiplecomparisons; WT DMSO versus KO DMSO, WT DMSO versus WT 10 and 50 mM alpelisib, KO DMSO versus KO 50 mM alpelisib all ***P < 0.001; KO DMSO versus KO 2.5 and 5 mM alpelisib both P > 0.9999 (not significant [ns]); KO DMSO versus KO 10 mM alpelisib **P=0.0049; KO DMSO versus KO 25 mM alpelisib ***P=0.0002. (**c**) Representative widefield micrographs of WT or KO HK2 cells treated with DMSO or 10 mM of alpelisib and then fixed with the plasma membrane fix and immunolabeled for PI(4,5)P2 (yellow) and DAPI (cyan), with quantification of the mean cellular PI(4,5)P2 labeling intensity, showing increased plasma membrane PI(4,5)P2 in KO cells, which is reduced by alpelisib treatment, specifically in KO cells. N=126, 112, 85, and 116 cells for WT DMSO, WT alpelisib, KO DMSO, and KO alpelisib, respectively. K-W test: overall ***P < 0.001, multiple comparisons; WT DMSO versus KO DMSO and KO DMSO versus KO alpelisib both ***P < 0.001; WT DMSO versus WT alpelisib P=0.4752 (ns). (d) Representative widefield micrographs of WT or KO HK2 cells treated with DMSO or 10 mM of alpelisib and then fixed with the 4% formaldehyde fix and immunolabeled for PI(4,5)P2 (yellow) and DAPI (cyan), with quantification of the number of PI(4,5)P2-positive puncta, showing increased PI(4,5)P2 puncta in KO cells, which is reduced by alpelisib treatment, specifically in KO cells. N=75, 65, 52, and 69 cells for WT DMSO, WT alpelisib, KO DMSO, and KO alpelisib, respectively. K-W test: overall ***P < 0.001, multiple comparisons; WT DMSO versus KO DMSO and KO DMSO versus KO alpelisib both ***P < 0.001; WT DMSO versus WT alpelisib P > 0.99 (ns). a.u., arbitrary units.

Figure 4

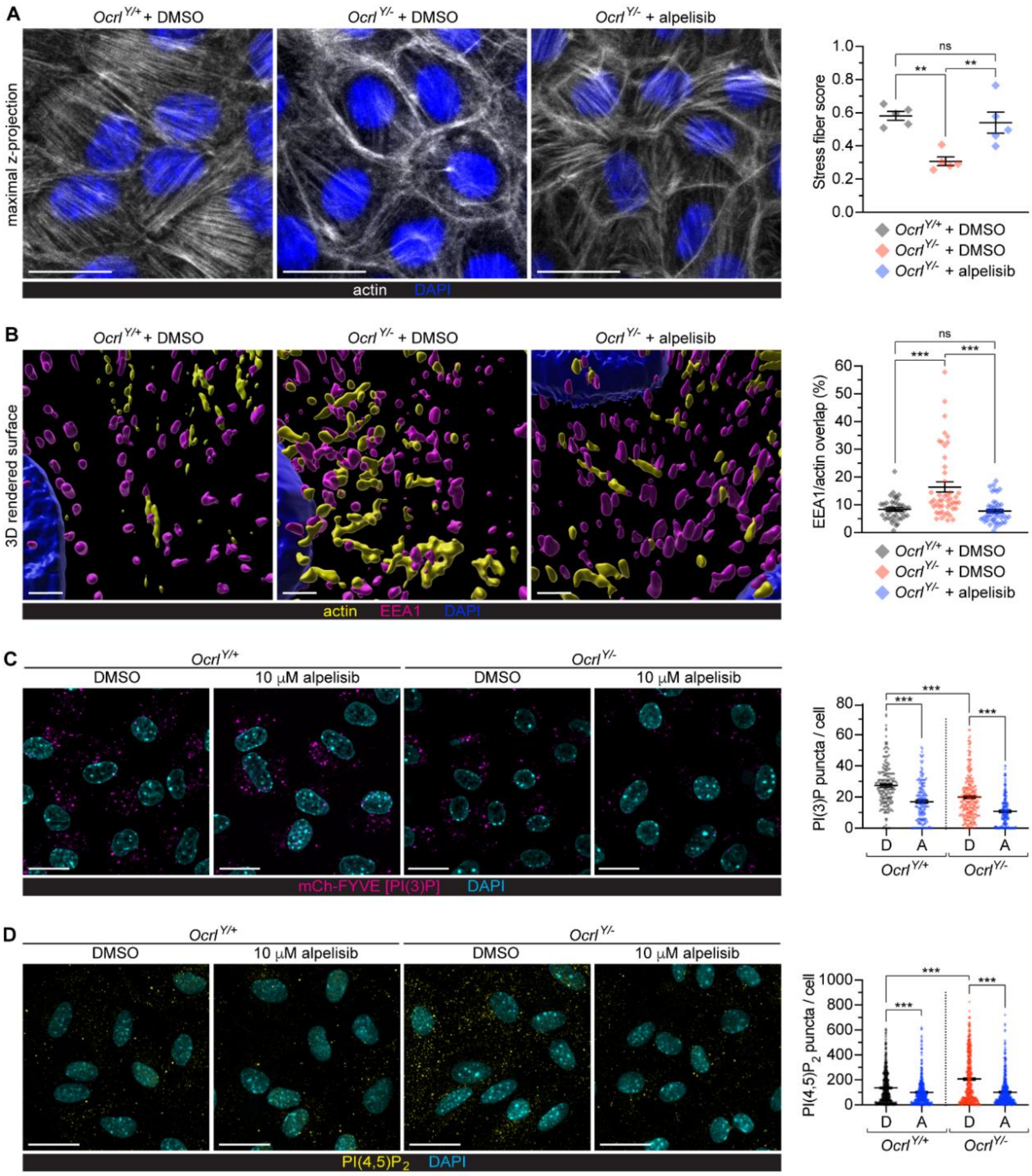

Figure 4. Alpelisib alleviates actin defects of Ocrl in cultured humanized OcrlY/_ mouse PTCs (mPTCs). (**a**) Representative maximum intensity Z-projection confocal micrographs of *Ocrl*$^{Y/+}$ or *Ocrl*$^{Y/-}$ mPTCs treated with DMSO or 10 µM of alpelisib for 16 hours then fixed with the 4% formaldehyde fix and immunolabelled for actin [phallodin] (white) and DAPI (blue), with quantification of the degree to which stress fibres are present in each condition, showing that stress fibres lost in *Ocrl*$^{Y/-}$ mPTCs are rescued by alpelisib treatment. Lines indicate means ± SEM, data points indicate each imaging region: N=5 imaging regions per condition (each containing ≈15-20 cells). Significance was assessed by ordinary one-way ANOVA with Holm-Sidak's multiple comparison test, **P=0.001, multiple comparisons; *Ocrl*$^{Y/+}$ DMSO vs *Ocrl*$^{Y/-}$ DMSO **P=0.002, *Ocrl*$^{Y/-}$ DMSO vs *Ocrl*$^{Y/-}$ alpelisib **P=0.004, *Ocrl*$^{Y/+}$ DMSO vs *Ocrl*$^{Y/-}$ alpelisib P=0.50 (ns). Scale bars=20µm. (**b**) Representative 3D surface rendering of *Ocrl* mPTCs treated with DMSO or 10 µM of alpelisib for 16 hours then fixed with the 4% formaldehyde fix and immunolabelled for EEA1(purple), actin [phalloidin] (yellow) and DAPI (blue) and quantification illustrating rescue of the rescue of the actin-endosomal overlap by alpelisib. Lines indicate mean ± SEM. N=42, 47 and 45 randomly selected fields for *Ocrl*$^{Y/+}$ + DMSO, *Ocrl*$^{Y/-}$ + DMSO and *Ocrl*$^{Y/-}$ + alpelisib conditions respectively, in each case pooled from four mouse kidneys per condition. Significance was tested by Kruskal Wallis ANOVA with Dunn's multiple comparisons test: overall ***P < 0.001; multiple comparisons; *Ocrl*$^{Y/+}$ DMSO vs *Ocrl*$^{Y/-}$ DMSO and *Ocrl*$^{Y/-}$ DMSO vs *Ocrl*$^{Y/-}$ alpelisib ***P < 0.001, *Ocrl*$^{Y/+}$ DMSO vs *Ocrl*$^{Y/-}$ alpelisib P > 0.99 (ns). Scale bars = 5µm in the upper panels and 1µm in the lower panels. (**c**) Representative confocal micrographs of *Ocrl*$^{Y/+}$ or *Ocrl*$^{Y/-}$ mPTCs treated with DMSO or 10 µM of alpelisib then fixed with the golgi fix and labelled using the mCh-2xFYVE PI(3)P probe (magenta) and DAPI (cyan), with quantification of the number of PI(3)P positive puncta detected in cells. N = 188, 177, 246, 206 cells from *Ocrl*$^{Y/+}$ + DMSO, *Ocrl*$^{Y/+}$ + alpelisib, *Ocrl*$^{Y-}$ + DMSO, and *Ocrl*$^{Y/-}$ + alpelisib respectively; cells were pooled from three *Ocrl* kidneys per group. K-W test: overall ***P < 0.001; multiple comparisons; *Ocrl*$^{Y/+}$ DMSO vs *Ocrl*$^{Y/-}$ DMSO, *Ocrl*$^{Y/+}$ DMSO vs *Ocrl*$^{Y/+}$ alpelisib and *Ocrl*$^{Y/-}$ DMSO vs *Ocrl*$^{Y/-}$ alpelisib, all ***P < 0.001. (**d**) Representative confocal micrographs of *Ocrl*$^{Y/+}$ or *Ocrl*$^{Y/-}$ mPTCs treated with DMSO or 10 µM of alpelisib then fixed with the 4% formaldehyde fix and immunolabelled for PI(4,5)P$_2$ (yellow) and DAPI (cyan), with quantification of the number of PI(4,5)P$_2$ positive puncta, showing increased plasma membrane PI(4,5)P$_2$ cells in *Ocrl*$^{Y/-}$ cells, and reduction of PI(4,5)P$_2$ by alpelisib treatment. N=477, 444, 423 and 494 from *Ocrl*$^{Y/+}$ + DMSO, *Ocrl*$^{Y/+}$ + alpelisib, *Ocrl*$^{Y/-}$ + DMSO, and *Ocrl*$^{Y/-}$ + alpelisib respectively; cells were pooled from three *Ocrl* kidneys per group. K-W test: overall ***P < 0.001; multiple comparisons; *Ocrl*$^{Y/+}$ DMSO vs *Ocrl*$^{Y/-}$ DMSO, *Ocrl*$^{Y/+}$ DMSO vs *Ocrl*$^{Y/+}$ alpelisib and *Ocrl*$^{Y/-}$ DMSO vs *Ocrl*$^{Y/-}$ alpelisib, all ***P < 0.001.

Figure 5

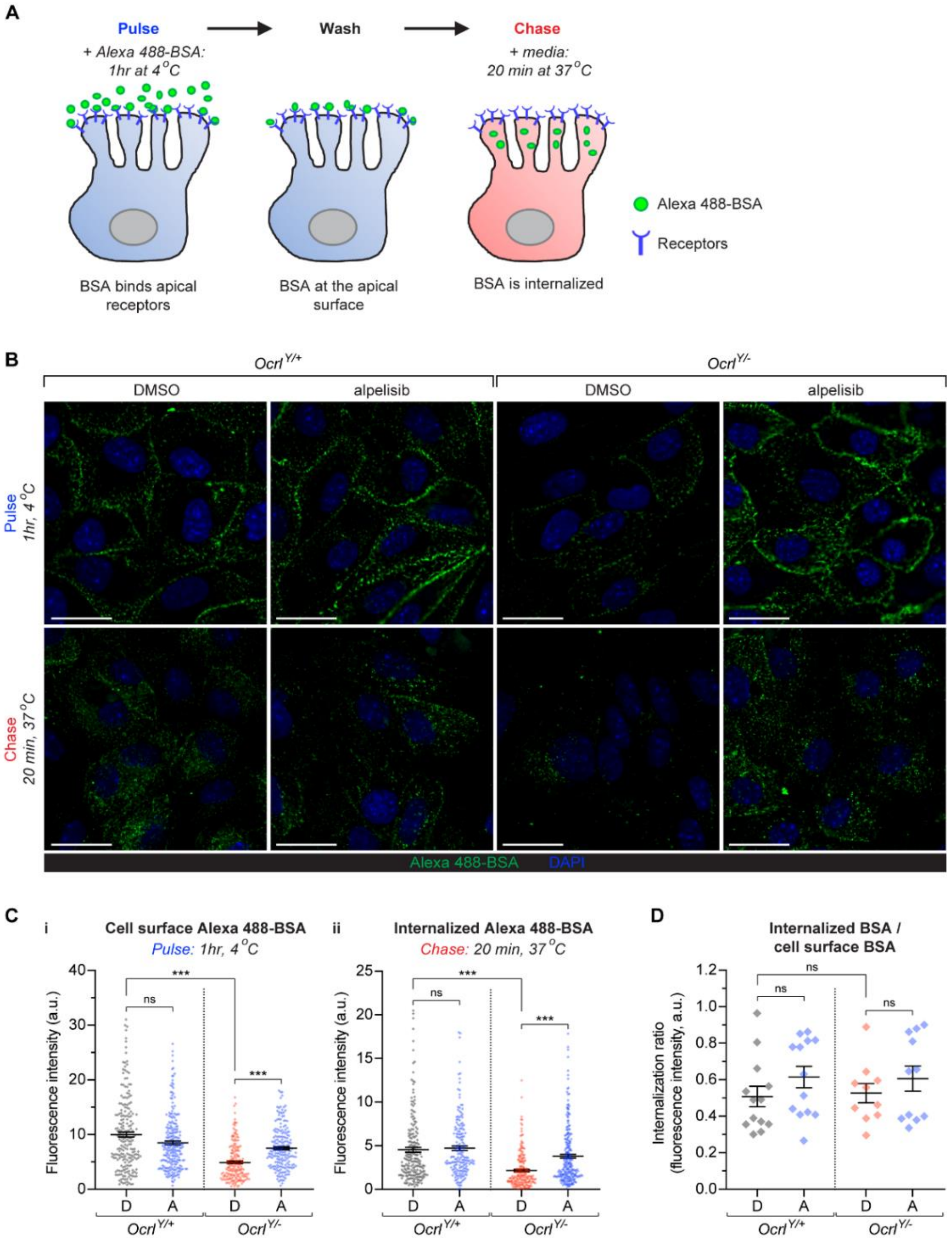

Figure 5. **Alpelisib improves endocytic uptake of humanized *Ocrl*$^{Y/-}$ mPTCs. (a)** Schematic illustrating the pulse-chase experiment used to examine the binding and internalization of Alexa 488-BSA into mPTCs. Cells were exposed to Alexa 488-BSA (0.2 mg ml^{-1}) for 1h at 4°C to allow BSA to bind to cell surface receptors (pulse) and then warmed to 37°C in cell medium for 20min before fixation to allow ligand internalization (chase). **(b)** Representative confocal micrographs of *Ocrl*$^{Y/+}$ or *Ocrl*$^{Y/-}$ mPTCs treated with DMSO or 10 µM of alpelisib and subjected to the Alexa 488-BSA (green) pulse-chase experiment, before being fixed and labelled for DAPI (blue). The pulse phase of the experiment is shown in the top panel for each condition, with the chase below. Scale bars = 20µm. **(c)** Quantification of cell surface Alexa 488-BSA **(i)** and internalized Alexa 488-BSA **(ii)**, evaluated as mean fluorescence intensities per cell. Alpelisib rescues the rescued BSA binding and internalization observed in *Ocrl*$^{Y/-}$ *cells.* N=209, 228, 186 , 196 cells for *Ocrl*$^{Y/+}$ DMSO, *Ocrl*$^{Y/+}$ alpelisib, *Ocrl*$^{Y/-}$ DMSO and *Ocrl*$^{Y/-}$ alpelisib conditions respectively in **(i)** and n=203, 183, 199, 233 cells for *Ocrl*$^{Y/+}$ DMSO, *Ocrl*$^{Y/+}$ alpelisib, *Ocrl*$^{Y/-}$ DMSO and *Ocrl*$^{Y/-}$ alpelisib conditions respectively in **(ii)**, in each case pooled from two mouse kidneys per condition; each data point represents the mean fluorescence intensity in an individual cell. Significance was tested by Kruskal Wallis ANOVA with Dunn's multiple comparisons test: for **(i)** cell surface BSA, overall ***P < 0.001, multiple comparisons: *Ocrl*$^{Y/+}$ DMSO vs *Ocrl*$^{Y/-}$ DMSO and *Ocrl*$^{Y/-}$ DMSO vs *Ocrl*$^{Y/-}$ alpelisib ***P < 0.001, *Ocrl*$^{Y/+}$ DMSO vs *Ocrl*$^{Y/+}$ alpelisib P=0.60 (ns), for **(ii)** internalized BSA, overall ***P < 0.001, multiple comparisons: *Ocrl*$^{Y/+}$ DMSO vs *Ocrl*$^{Y/-}$ DMSO and *Ocrl*$^{Y/-}$ DMSO vs *Ocrl*$^{Y/-}$ alpelisib ***P < 0.001, *Ocrl*$^{Y/+}$ DMSO vs *Ocrl*$^{Y/+}$ alpelisib P=0.66 (ns). **(d)** Quantification of the ratio between the cell surface Alexa 488-BSA and the internalized Alexa 488-BSA fluorescence intensities, showing no significant differences in ratios between each condition. Each point representing the average of the ratio in a field containing ≈15-20 cells, (n=13, 13, 10 and 11 randomly selected fields for *Ocrl*$^{Y/+}$ DMSO, *Ocrl*$^{Y/+}$ alpelisib, *Ocrl*$^{Y/-}$ DMSO and *Ocrl*$^{Y/-}$ alpelisib conditions respectively, in each case pooled from two mouse kidneys per condition). Significance was tested by Kruskal Wallis ANOVA with Dunn's multiple comparisons test: overall P=0.46 (ns), multiple comparisons: *Ocrl*$^{Y/+}$ DMSO vs *Ocrl*$^{Y/-}$ DMSO and *Ocrl*$^{Y/-}$ DMSO vs *Ocrl*$^{Y/-}$ alpelisib P > 0.99 (ns), *Ocrl*$^{Y/+}$ DMSO vs *Ocrl*$^{Y/+}$ alpelisib P=0.84 (ns).

Figure 6

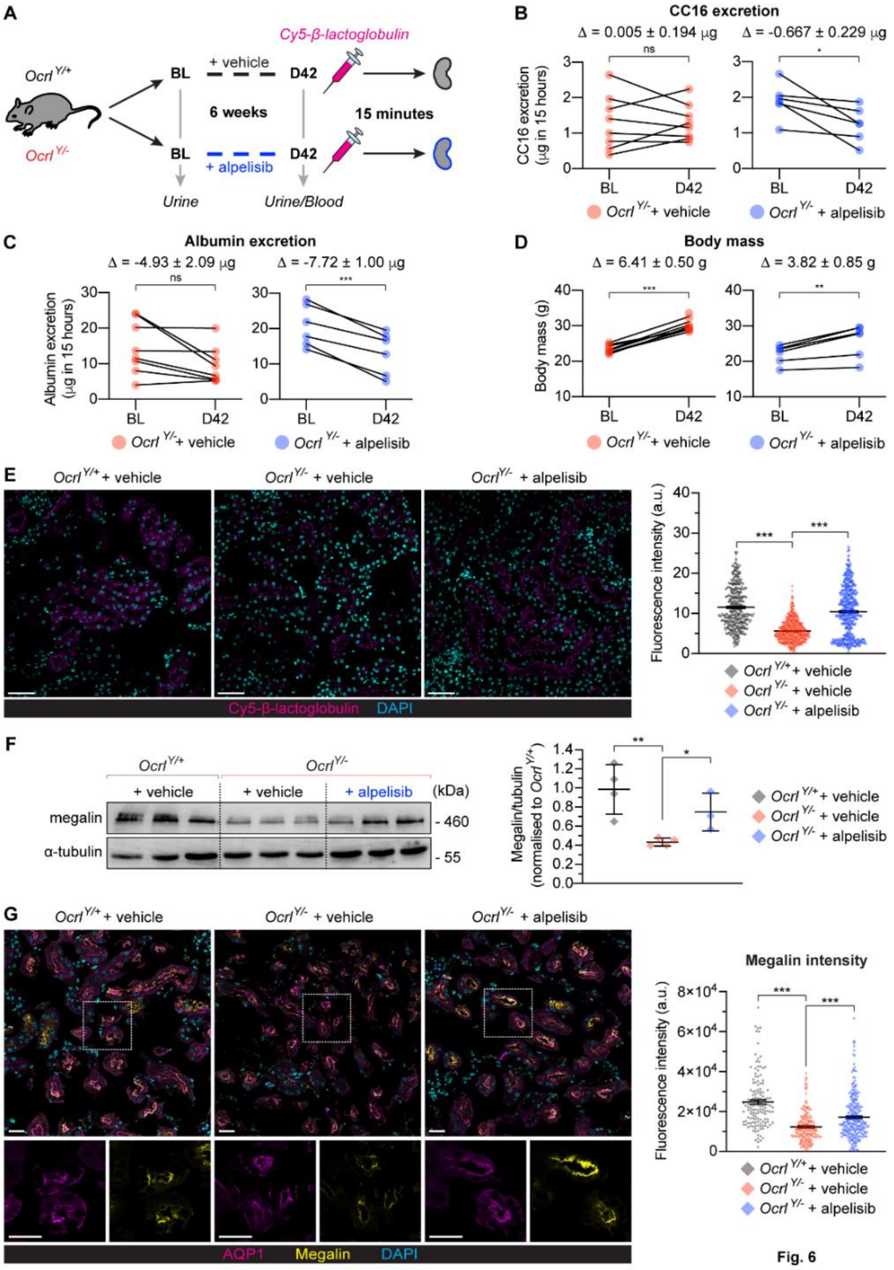

Fig. 6

Figure 6. **Alpelisib improves the PT function of *Ocrl*$^{Y/-}$ mice.** (**a**) Experimental setup of the study. *Ocrl* mice were treated for 6 weeks with a daily oral dose of either carboxymethylcellulose 1% (vehicle) or alpelisib (50 mg kg^{-1} body weight). On the last day of the treatment, mice were injected with Cy5-labelled β-lactoglobulin (N=6 *Ocrl*$^{Y/-}$, or 8 *Ocrl*$^{Y/-}$ mice per group). **(b-d)** the Δ values shown indicate the mean change from BL to D42 for the condition ± SEM. (b) Clara Cell protein 16 (CC16), (**c**) albumin urinary output (both within 15 hours), and (**d**) Body mass was measured in *Ocrl*$^{Y/-}$ mice treated with either vehicle or alpelisib at the indicated time point. Each dot represents one mouse. Significance was assessed by two-tailed paired Student's t-test; in **(b)** CC16 output change relative to baseline; + vehicle, P=0.9802 (ns), + alpelisib, *P=0.0334, in **(c)** albumin output change relative to baseline; + vehicle, P=0.0502 (ns), + alpelisib, P=0.0006 (***), in (**d**) Body mass change relative to baseline; + vehicle, ***P < 0.0001, + alpelisib, **P=0.0083. (**e**) Representative confocal micrographs showing Cy5-labeled β-lactoglobulin (magenta) 15 min after tail vein injection and labelled for DAPI (cyan), plus quantification of the corresponding fluorescent signals from *Ocrl* mouse kidneys (n= 412, 500 and 588 tubules respectively for *Ocrl*$^{Y/+}$+ vehicle, *Ocrl*$^{Y/-}$ + vehicle and *Ocrl*$^{Y/-}$ + alpelisib) for 3 mice per treatment group. β-lactoglobulin uptake is recued by alpelisib treatment. Scale bars = 20 μm. In the quantifications, each dot represents fluorescence intensity normalized by tubule area; plotted data indicates the mean ± SEM. Significance was assessed by Kruskal-Wallis followed by Dunn's multiple comparison test; ***P < 0.001, multiple comparisons, *Ocrl*$^{Y/+}$+ vehicle vs *Ocrl*$^{Y/-}$ + vehicle and *Ocrl*$^{Y/-}$ + vehicle vs *Ocrl*$^{Y/-}$ + alpelisib, both ***P < 0.001. **(f)** Western blotting and densitometry analysis of megalin levels in whole kidney lysates from Ocrl mice. α-tubulin was used as a loading control. The reduced megalin expression in *Ocrl*$^{Y/-}$ is rescued by alpelisib. In the quantification of the densitometry analysis, each dot represents 1 mouse (N=4 *Ocrl*$^{Y/+}$+ vehicle and *Ocrl*$^{Y/-}$ + vehicle and N=3 *Ocrl*$^{Y/-}$ + alpelisib mice) lines indicate mean ± SEM. Significance was assessed by 2-tailed unpaired Student's test: *Ocrl*$^{Y/+}$+ vehicle vs *Ocrl*$^{Y/-}$ + vehicle, **P=0.0057, *Ocrl*$^{Y/-}$ + vehicle vs *Ocrl*$^{Y/-}$ + alpelisib, *P=0.0246. (**g**) Representative confocal micrographs with high-magnification insets and quantification of megalin (yellow) intensity in Aqp1^{+} PTs (magenta) from Ocrl kidneys also labeled for DAPI (cyan) illustrating rescue of megalin levels after alpelisib treatment. Bars= 20 mm. In the quantifications, each dot represents fluorescence intensity normalized by tubule area; plotted data indicate the mean ± SEM; N=142, 191, and 266 tubules, respectively, for *Ocrl*$^{Y/+}$+ vehicle, *Ocrl*$^{Y/-}$ + vehicle, and *Ocrl*$^{Y/-}$ + alpelisib for 3 mice per treatment group. Significance was assessed by K-W analysis of variance followed by Dunn's multiple comparison test; overall ***P < 0.001, multiple comparisons; *Ocrl*$^{Y/+}$+ vehicle versus *Ocrl*$^{Y/-}$ + vehicle and *Ocrl*$^{Y/-}$ + vehicle versus *Ocrl*$^{Y/-}$ alpelisib, both ***P < 0.001.

Figure 7

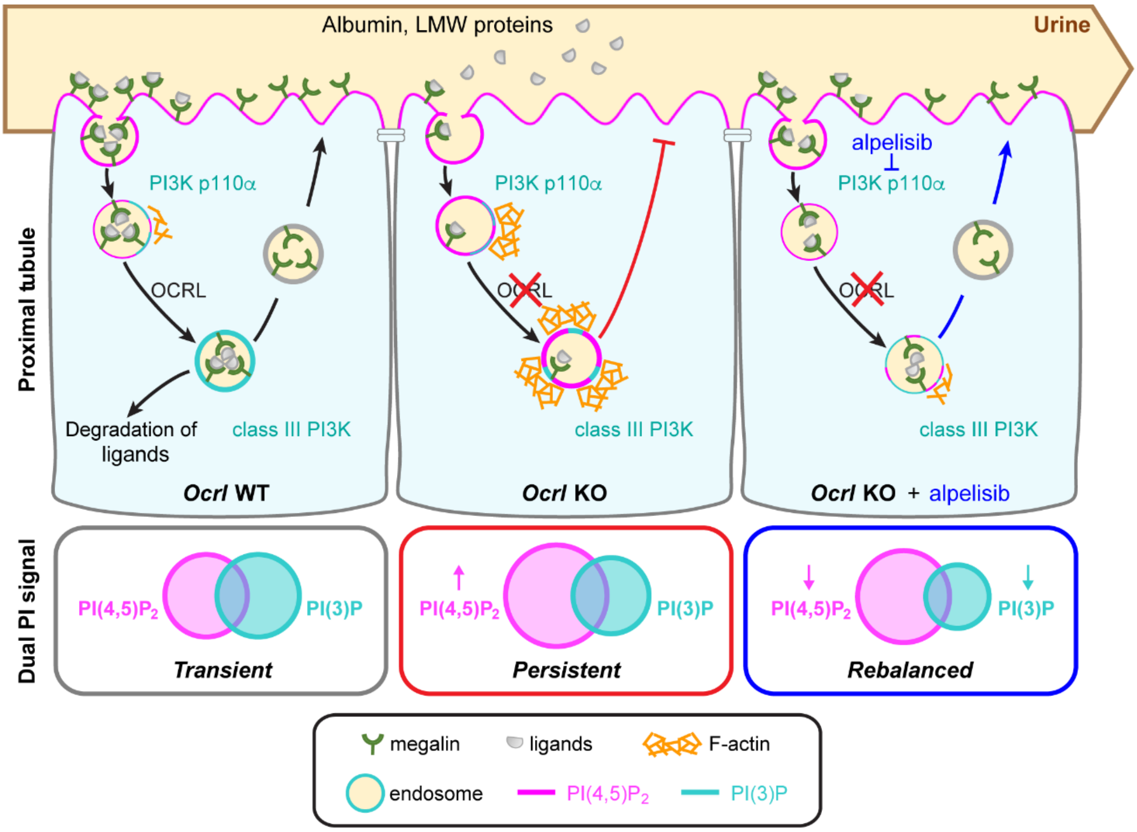

Figure 7. Proposed model depicting the therapeutic effect of alpelisib on proximal tubule cells in Lowe syndrome. Proximal tubule cells reabsorb urinary ligands (e.g., albumin and low-molecular-weight proteins) through megalin-mediated endocytosis. The 5-phosphatase activity of OCRL regulates the transition from high phosphatidylinositol (PI) 4,5-bisphosphate [PI(4,5)P_2] at the plasma membrane to low levels at the early endosome with a transient coincidence of PI(4,5)P_2 and PI(3)P in the vesicles. Once in the early endocytic compartment, the ligands dissociate from the receptors and are delivered to the lysosome for degradation, whereas the receptors recycle back to the plasma membrane for a new cycle of cargo binding. The loss of OCRL leads to an ectopic accumulation of PI(4,5)P_2 at the endosomal compartment, which results in a persistent coincidence with PI(3)P. We suggest that this event is responsible for aberrant F-actin polymerization blocking endocytic recycling and preventing ligand reabsorption (middle panel). Alpelisib rebalances the levels of PI(4,5)P_2 and PI(3)P, which results in decreased actin polymerization and improvement of the endocytic machinery and absorptive capacity of proximal tubule cells (right panel).

Supplementary Material

Phosphoinositide 3-kinase inhibitor alpelisib restores actin organization and improves proximal tubule dysfunction in Lowe syndrome and Dent disease

Marine Berquez*, Jonathan R. Gadsby*, Beatrice Paola Festa*, Richard Butler, Stephen P. Jackson, Valeria Berno, Alessandro Luciani, Olivier Devuys†, and Jennifer L. Gallop†.

1 Institute of Physiology, University of Zurich, Zurich, Switzerland.
2 Gurdon Institute and Department of Biochemistry, Tennis Court Road, University of Cambridge, Cambridge, CB2 1QN, UK
3 Gurdon Institute, Tennis Court Road, University of Cambridge, Cambridge, CB2 1QN, UK
4 Experimental Imaging Center, ALEMBIC, IRCCS San Raffaele Scientific Institute, 20132, Milan, Italy

* Equal contribution; † Co-directed the study, correspondence to OD or JLG.

SUPPLEMENTARY METHODS

Cell culture and CRISPR KO cell line generation. Human Kidney 2 (HK2) cells (ATCC, CRL-2190) were maintained in a 37 oC, 5% CO2 humidified incubator in DMEM/F12 media (containing GlutaMAX; Gibco, 31331) supplemented with 10% fetal bovine serum (Sigma-Aldrich) and 100 µg/ml penicillin/100 U/ml streptomycin (Gibco), and were sub-cultured twice weekly. HK2 OCRL KO cell lines were generated exactly as previously described to generate RPE-1 OCRL KO lines1. Briefly, the all-in-one Cas9D10A vector was used alongside the following single-guide RNA (sgRNA) pairs: sense sgRNA; forward (5'-3')-ACCGCCTCCTGATATCTACTGCAT, reverse (5'-3')-AAACATGCAGTAGATATCAGGAGG, antisense sgRNA; forward (5'-3')-ACCGCAAGGTTCTAACCCGCTATC, reverse (5'-3')-AAACGATAGCGGGTTAGAACCTTG, and following transfection into HK2 cells were sorted by FACS to generate monoclonal cultures, then screened by western blot to confirm *OCRL* KO.

Drug treatments in HK2 cells. Drugs were dissolved in DMSO at appropriate dilutions such that the maximum dosage added to cells was no more concentrated than a final dilution of 1:1000. Drugs were added to cells at the indicated concentrations and time points (16 hours prior to analysis, unless otherwise stated). Alpelisib and copanlisib were from Selleck chemicals (alpelisib: S2814, copanlisib: S2802). GSK2636771 and idelalisib were from Apexbio (supplied via Stratech Scientific; GSK2636771 B2186, idelalisib A3005).

siRNA treatments. Cells were grown in antibiotic free medium. siRNA was transfected into cells using Lipofectamine RNAiMAX (Thermo-Fisher) according to manufacturer's instructions. Briefly, cells were subjected to a two-shot protocol, with transfections at 72 and 24 hours prior to analysis. siRNA was added at a final concentration of 25 nM. Sequences were from Dharmacon; p110a: ON-TARGETplus Human PIK3CA (J-003018-15), scramble: siGENOME Non-Targeting siRNA #2 (D-001210-02).

Mouse models. Experiments were conducted on age- and gender-matched *OcrlY/+;Inpp5b-/-*; and *OcrlY/-;Inpp5b-/-* mouse littermates harbouring BAC-INPP5B expression (129S/SvEv * 129S6/SvEvTac * FVB/N* C57BL/6 background)2. Mice aged 6 weeks were treated with vehicle (1% carboxymethylcellulose, n=8 mice per genotype) or with alpelisib (MedChem Express; 50 mg/kg body weight in 1% carboxymethylcellulose, n=8 mice per genotype) daily by oral gavage and sacrificed after 42 days of treatment. Urine samples were collected every 14 days. Blood and kidneys were harvested at the time of sacrifice. During the treatment, two *OcrlY/-* mice treated with alpelisib were injured by the oral gavage, euthanized and excluded from the analysis. All of the experiments were performed in accordance with the ethical guidelines at University of Zurich and the legislation of animal care and experimentation of Canton Zurich, Switzerland (ZH039/19).

Renal function parameters and glycaemia. Urine and blood parameters were measured as described2, 3. The urinary excretion values were obtained from overnight (15 hours) urine collection. Plasma glucose was analysed using GLU-TEST STRIPS (Nova Biomedical, 42214) according to manufacturer's instructions.

Primary cultures of mouse proximal tubule cells. The kidneys were harvested from *Ocrl* mice (8 weeks) and used to generate primary cultures of mPTCs as previously described (3). Where indicated, the cells were treated with alpelisib (10 µM for 16 h, unless otherwise stated). The cells were processed and analysed as described below.

Cell viability assay. The viability of HK2 cells and mPTCs after drug treatments were assessed via MTT assay (ab211091, Abcam) in accordance with the manufacturer'sinstructions. Briefly, the cells were washed three times with PBS and then incubated with 0.5 mg/ml of MTT diluted in medium. After 4 hours of incubation at 37 °C and until appearance of intracellular purple formazan crystals, the remaining crystals were dissolved with dimethyl sulfoxide (276855, Sigma-Aldrich) or SDS, and the absorbance measured at 570 nm.

Immunofluorescence. HK2 cells were grown on glass coverslips. The kidneys and mPTCs were harvested and processed as previously described2, 3. Samples were fixed using one of the following fixation methods (typically the 4% formaldehyde fix, unless otherwise stated). Washes were performed between each step in all of the protocols.

1. <u>4% formaldehyde fix</u>

Samples were fixed in 4% formaldehyde and permeabilised in permeabilization/blocking buffer for 20 minutes (0.1% saponin, 50 mM NH4Cl, 10% goat serum (HK2 cells) or 0.5% BSA (mouse samples) in PBS). Samples were stained for either 1 hour (HK2 cells) or overnight (kidneys and mPTCs) with primary antibodies, and for 45 minutes with secondary antibodies, then with DAPI for 5 minutes prior to mounting.

2. <u>Plasma membrane fix</u>

This was specifically used to preserve and examine plasma membrane labelling of PI(4,5)P_2 and PI(3,4,5)P_3 in HK2 cells, based on methods of Hammond et al4. Samples were fixed in 4% formaldehyde + 0.2% glutaldehyde for 15 minutes. After fixation, samples were transferred to 4 oC (and were kept at this temperature until the post fixation step). They were blocked and permeabilized using a buffer containing 10% goat serum and 0.5% saponin in buffer A (150 mM NaCl, 20 mM Na-HEPES, pH 7.4, 2 mM EDTA) for 45 minutes. Primary antibodies were made up in antibody incubation solution (1% goat serum and 0.1% saponin in buffer A), and incubated with the samples for 1 hour. Secondary antibodies were incubated with the sample for 45 minutes, followed by DAPI for 5 minutes prior to mounting. Cells were then subjected to a post-fixation step in 2% formaldehyde, which was added at 4^{o}C for 5 minutes, followed by 10 minutes warming to room temperature before mounting.

3. <u>Golgi fix</u>

This was specifically used to preserve PI(3)P staining on endosomes, and was modified from previously established protocols1, 5 . Solutions were made up in buffer A. Briefly, cells were fixed in 2% formaldehyde for 15 mins, after which they were permeabilized using 20μM digitonin. Cells were blocked in 10% goat serum containing 1 μg/ml purified mCh-2xFYVE, then immunolabelled using an anti-RFP primary antibody and DAPI. Cells were post-fixed in 2% formaldehyde for five minutes prior to mounting. The following antibodies and other fluorescent reagents were used; mCherry-2xFYVE1, mouse anti-PI(4,5)P2 (abcam ab11039; used in HK2 cells), mouse anti-PI(4,5)P2 (Echelon ZA045; used in mPTCs), mouse anti-PI(3,4,5)P3 (Echelon, Z-A345), mouse anti-EEA1 (BD Bioscience, 610456), sheep anti-megalin (gift from P. Verroust and R. Kozyraki, INSERM, Paris, France), rabbit anti-AQP1 (ab2219, Millipore), rabbit anti-RFP (Rockland, 600-401-379), Alexa-Fluor conjugated secondary antibodies (Goat anti rabbit AF 568, A11011, Goat anti mouse 647 A21235, Thermo-Fisher), Alexa-488 Phalloidin (A12379, Thermo-Fisher), and DAPI (62247, Thermo-Fisher). Samples were mounted with either hydromount (National Diagnostics, in HK2 cells) or Prolong Gold Anti-fade reagent (mouse samples).

Microscopy. HK2 cell EEA1/actin colocalization images were acquired on a Zeiss LSM 880 equipped with Airyscan and Plan-Apochromat 40x NA 1.3 or Plan-Apochromat 63x NA 1.4 objectives using the Airyscan Fast imaging mode. Images were processed using Airyscan processing, strength 6. HK2 cell confocal images were taken on an inverted microscope (Ti-E; Nikon) equipped with a 250-μm piezo-driven Z stage/controller (NanoScanZ) as an 11 x 0.4 μm Zstack using a spinning disk unit (X-light Nipkow; Crest) and LED illumination (Lumencor
Spectra X) through a Plan Apo 60x 1.4 NA oil objective (Nikon). Images were captured on an EMCCD camera (Evolve Delta; Photometrics) in 16-bit depth using Metamorph (software version 7.8.2.0). HK2 cell widefield images were taken on an inverted microscope (Ti-E; Nikon) through a Plan Apo 60x 1.4 NA oil objective (Nikon). Images were captured on an EMCCD camera (iXon Ultra 897; Andor) in 16-bit depth using Nikon NIS-Elements AR (software version 4.50). All mPTCs and mouse tissue images were obtained using either a Leica SP5 confocal laser scanning microscope, or a Leica SP8 inverse FALCON microscope (Center for Microscopy and Image Analysis, University of Zurich), in both cases equipped with a Leica APO 63x NA 1.4 oil immersion objective, with images taken at a definition of 1024 x 1024 pixels, and the pinhole diameter adjusted to 1 Airy unit for each emission channel. The quantitative cell image analyses were performed by using ImageJ software and the open-source cell image analysis software CellProfilerTM 6 (Broad Institute, Cambridge, MA).

Immunofluorescent image quantifications.

<u>Quantification of "mean fluorescence intensity"</u>

For all measurement of "mean fluorescence intensity", an outline of each cell was drawn by
hand using FIJI (Image J), and the mean fluorescence intensity recorded. For measurements of PI(3,4,5)P3 and PI(4,5)P2 intensity in HK2 cells, 10 imaging regions were taken for each condition. For measurement of 488-BSA

(binding or internalized) and Cy5-β-lactoglobulin uptake in mPTCs, results were taken from 10 separate imaging regions for each mouse.

Quantification of “puncta per cell”

The pipeline “Speckle counting” in CellProfilerTM was used to the number of PI(3)P or PI(4,5)P2 puncta surrounding nuclei and to perform per-nuclei aggregate measurements (eg. the number of dots/nucleus), as previously described5, 6. Briefly, the images were converted to greyscale using the module “ColorToGray”. The “IdentifyPrimaryObjects” module was used to identify nuclei and dots while cells were identified by using the module “IdentifySecondaryObjects”. “MaskObject” and “RelateObject” modules were used to establish a parent-child relationship between the cells and the dots, identified as masked objects, and to calculate the average of dots per cell.

Quantification of “EEA1/actin overlap” in HK2 cells

The optical airyscan sections just above the section at which stress fibers could be observed were used for the quantification, with the CellProfilerTM pipeline “Cell/particle counting, and scoring the percentage of stained objects” used to score the percentage of EEA1-positive structures colocalizing with F-actin. Briefly, the images were converted to greyscale using the module “ColorToGray”. Then the “ObjectIdentification” module was used to identify the nuclei, the EEA1-positive and the F-actin stained structures/vesicles. The “RelateObject” module was used to establish a parent-child relationship between the stained objects. In this case, a “parent” object (endosomes) is one that touches, overlaps or encloses a “child” object (F-actin structures). When Object1 touches or overlasp with Object2, they are considered to be colocalized and will be assigned as a parent to the corresponding child. The “ClassifyObjects” and “FilterObjects” modules were used to categorize structures that were either colocalizing or not-colocalizing, and to calculate the percentage of colocalizing structures on the total amount of endosomes per image. Approximately 10 images from each sample were analyzed.

Quantification of “EEA1/actin overlap” in mPTCs

Z-stack images acquired by confocal microscope were first deconvolved using Huygens (SVI) software in order to increase object resolution in x, y and z, to improve the signal, and correct the noise. The final z-stack images were loaded into CellProfilerTM, followed by segmentation of images and identification of objects. The process is characterized by three main steps: segmentation of actin and endosomes, identification of overlap objects and tabulation of measurements. The “ObjectIdentification” and “Filter” modules were used to identify the EEA1+ (Endosomes) and the F-actin marked-structures/vesicles. In order to filter out actin fibers and better visualize the above subcellular EEA1/actin-positive structures, limits in shape (Eccentricity factor below 0.75) and size (Area size in pixel below 80) of the F-actin object were applied. The “RelateObject”, “ClassifyObjects” and “FilterObjects” modules were then used as described above to assign colocalization, “parent” and “child” status, and ultimately the percentage of colocalizing objects. Approximately 14 images from each sample were quantified. The 3D reconstructions of EEA1 positive vesicles and actin were generated in Imaris software (Oxford Instruments) using the full confocal z-stacks (around 45) of each imaging region.

Quantification of “stress fiber score”

The presence of actin fibers in these images was quantified using a custom script in FIJI(ImageJ). Briefly, the script measures directionality of signal without tracing fibers as required for detailed analysis of actin organisation such as that carried out by Rogge et al (7). It selects the z-slice containing the highest intensity of f-actin labelling and applies Laplacian of Gaussian processing with a sigma value of 2 pixels to suppress noise and detect fibers. It then divides the image into 576 (24x24) tiles of equal area with an overlap factor of 0.2 at each edge, and convolves the tile with each of the 8 Kirsch directional edge detection kernels. The gradient magnitude is the maximum magnitude from any of the resulting images, and its direction is determined by the kernel producing the maximum response. Since we are interested in fiber direction rather than gradient direction, $\pi/2$ is added to the kernel direction to give the principal direction of detected edges. The directionality of actin signal is measured as:

$$\text{tile score} = \frac{\max(E) - \min(E)}{Sum(E) - \min(E)} \times 8$$

where E is the set of responses in the 8 gradient directions. This scale normalisation gives a measure of relative contribution of the principal direction to the total gradient present in the tile independent of the magnitude of the gradient. The tile-based approach allows unbiased analysis of small regions of cells to give a set of local measurements representing the degree of directionality of actin signal which can be used to compare the overall level of organisation between conditions.
The script is available on github at https://github.com/gurdon-institute/Stress_Fibre_Scores.

Endocytosis uptake assays. The endocytic capacity of *Ocrl* mouse proximal tubules was examined by measuring Cy5-β-lactoglobulin (L3908, Sigma) uptake as previously described2. The endocytic capacity of *Ocrl* mPTCs was examined by measuring albumin uptake using a pulse-chase assay analysed by either immunofluorescence or intracellular fluorescence intensity using a microplate reader8, 9. mPTCs were seeded at appropriate densities on either glass coverslips for immunofluorescence experiments or in 96 well plates for plate reader experiments, then treated with 10 μM alpelisib for 16 h. For both types of experiment, cells were washed three times in PBS, then incubated with 0.2 mg/ml Alexa 488-BSA (A13100, Thermo Fisher Scientific) at 4 o C for 1 hour ("pulse"). Following this, cells were rinsed in serum free media and then incubated in standard serum containing media for 20 mins at 37 o C ("chase") to follow the internalization of albumin. For immunofluorescence experiments, cells were washed and fixed (using the 4% formaldehyde fix) at the end of the "pulse", "wash", and "chase" phases of the experiment, labelled for DAPI, and imaged on a laser scanning confocal microscope, then the fluorescence intensity of Alexa 488-BSA in individual cells measured. For measurement of internalized albumin uptake on the plate reader, cells were lysed with RIPA buffer supplemented with protease inhibitors and the fluorescence signal was measured using the microplate reader (Infinite M Plex, Tecan) at an excitation wavelength of 493nm and emission wavelength of 520nm. Protein concentration was determined by bicinchoninic acid (BCA) protein assay kit (Thermo Fischer Scientific). The albumin uptake was normalized to the protein content of the cells in each well.

Western blotting. HK2 cells were lysed in the following buffer: 50 mM Na-HEPES (pH 7.4), 50 mM NaCl, 1 mM EDTA, 10% (v/v) glycerol. 1% (v/v) Triton X-100, Halt-EDTA protease inhibitor tablets for 30 minutes and scraped from the plate. Lysate concentration was determined by BCA protein assay (Pierce) and equal samples loaded and ran on 4-20% mini-PROTEAN polyacrylamide gels (Bio-Rad). Transfer was performed using the iBlot 2 dry blotting system (Life Technologies), blocking was performed in 5% milk-TBST, antibody incubations and washes in 0.5% milk-TBST, and detection was performed using IRDye antigen detection (Goat anti-mouse (926-32210) and anti-rabbit (926-32211) IRDye 800CW) and an Odyssey Sa reader (all LI-COR Biosciences). Densitometry analysis of band intensity was performed from 3-5 biologically independent replicates in Image Studio Lite (software version 5.2.5; LI-COR Biosciences). For mouse work, proteins were extracted from mouse kidney tissues or primary culture cells and western blotting was performed as previously described3, with the signals revealed using the ChemiDocTM imaging system (Bio-Rad Laboratories) and image intensity was measured in FIJI (ImageJ). The primary antibodies used were as follows: rabbit anti-OCRL ([EP10256], abcam ab 181039) sheep anti-megalin (gift from P. Verroust and R. Kozyraki, INSERM, Paris, France), rabbit anti-Aqp1 (ab2219, Millipore), rabbit anti-PI3 Kinase p110α (4249, Cell Signaling), rabbit anti-PI3 Kinase p110β (3011, Cell Signaling), rabbit anti-PI3 Kinase p110γ (5405, Cell Signaling), rabbit anti-PI3 Kinase p110δ (Cell Signaling) and mouse anti-α-tubulin (T5168, Sigma-Aldrich - used in mouse experiments or Abcam ab7291 - used in HK2 experiments).

Data analysis and Statistics. The quantitative data were expressed as means ± standard error of the mean (SEM). Differences between experimental groups were evaluated using one-way analysis of variance (ANOVA) followed by Bonferroni test or Kruskal Wallis followed by Dunn's multiple comparison test, or unpaired or paired two tailed Student's ttest, when appropriate, and as indicated in the figure legends. The sample size of each experimental group is described in the figure legends. GraphPad Prism software was used for all statistical analyses. Statistical significance was set at a $P<0.05$.

REFERENCES

1. Daste F, Walrant A, Holst MR, *et al.* Control of actin polymerization via the coincidence of phosphoinositides and high membrane curvature. *The Journal of cell biology* 2017; **216:** 3745-3765.

2. Festa BP, Berquez M, Gassama A, *et al.* OCRL Deficiency Impairs Endolysosomal Function in a Humanized Mouse Model for Lowe Syndrome and Dent Disease. *Human molecular genetics* 2018.

3. Festa BP, Chen Z, Berquez M, *et al.* Impaired autophagy bridges lysosomal storage disease and epithelial dysfunction in the kidney. *Nature communications* 2018; **9:** 161.

4. Hammond GR, Schiavo G, Irvine RF. Immunocytochemical techniques reveal multiple, distinct cellular pools of PtdIns4P and PtdIns(4,5)P(2). *The Biochemical journal* 2009; **422:** 23-35.

5. De Leo MG, Staiano L, Vicinanza M, *et al.* Autophagosome-lysosome fusion triggers a lysosomal response mediated by TLR9 and controlled by OCRL. *Nature cell biology* 2016; **18:** 839-850.

6. Carpenter AE, Jones TR, Lamprecht MR, *et al.* CellProfiler: image analysis software for identifying and quantifying cell phenotypes. *Genome biology* 2006; **7:** R100.

7. Rogge H, Artelt N, Endlich N, *et al.* Automated segmentation and quantification of actin stress fibres undergoing experimentally induced changes. *Journal of microscopy* 2017; **268:** 129-140.

8. Terryn S, Jouret F, Vandenabeele F, *et al.* A primary culture of mouse proximal tubular cells, established on collagen-coated membranes. *American journal of physiology Renal physiology* 2007; **293:** F476-485.

9. Wong DW, Yiu WH, Wu HJ, *et al.* Downregulation of renal tubular Wnt/beta-catenin signaling by Dickkopf-3 induces tubular cell death in proteinuric nephropathy. *Cell death & disease* 2016; **7:** e2155.

3. Impaired Mitophagy Links Mitochondrial Disease to Epithelial Stress in Methylmalonyl–CoA Mutase Deficiency

Alessandro Luciani[1,*], Anke Schumann[1,2,*], Marine Berquez[1,*], Zhiyong Chen[1,11], Daniela Nieri[1], Mario Failli[3], Huguette Debaix[1], Beatrice Paola Festa[1], Natsuko Tokonami[1], Andrea Raimondi[4], Alessio Cremonesi[5], Diego Carrella[6], Patrick Forny[2], Stefan Kölker[7], Francesca Diomedi Camassei[8], Francisca Diaz[9], Carlos T. Moraes[9], Diego Di Bernardo[6], Matthias R. Baumgartner[2] and Olivier Devuyst[1,10]

[1]Institute of Physiology and NCCR Kidney.CH, University of Zurich, 8057 Zurich, Switzerland
[2]Division of Metabolism and Children's Research Center, University Children's Hospital, 8032 Zurich, Switzerland
[3]Department of Biomedicine, University of Eastern Finland, Kuopio 70211, Finland
[4] San Raffaele Scientific Institute, Experimental Imaging Center, 20132 Milan, Italy;
[5]Division of Clinical Chemistry and Biochemistry, University Children's Hospital Zurich, 8032 Zurich, Switzerland
[6]Telethon Institute of Genetics and Medicine, Pozzuoli, 80078 Naples, Italy
[7]Division of Inherited Metabolic Diseases, University Children's Hospital Heidelberg, 69120 Heidelberg, Germany
[8]Department of Laboratories–Pathology Unit, Bambino Gesù Children's Hospital, 00165 Rome, Italy
[9]Department of Neurology, University of Miami Miller School of Medicine, 33136 Miami, USA
[10]Division of Nephrology, Cliniques Universitaires Saint–Luc, 1040 Brussels, Belgium;
[*]These authors contributed equally

Correspondence: alessandro.luciani@uzh.ch (A.L.) or olivier.devuyst@uzh.ch (O.D.)

Nature Communication 11, 970 (2020)

DOI: https://doi.org/10.1038/s41467-020-14729-8

ABSTRACT

Deregulation of mitochondrial network in terminally differentiated cells contributes to a broad spectrum of disorders. Methylmalonic acidemia (MMA) is one of the most common inherited metabolic disorders, due to deficiency of the mitochondrial methylmalonyl–coenzyme A mutase (MMUT). How *MMUT* deficiency triggers cell damage remains unknown, preventing the development of disease–modifying therapies. Here we combine genetic and pharmacological approaches to demonstrate that *MMUT* deficiency induces metabolic and mitochondrial alterations that are exacerbated by anomalies in PINK1/Parkin–mediated mitophagy, causing the accumulation of dysfunctional mitochondria that trigger epithelial stress and ultimately cell damage. Using drug–disease network perturbation modeling, we predict targetable pathways, whose modulation repairs mitochondrial dysfunctions in patient–derived cells and alleviate phenotype changes in *mmut*–deficient zebrafish. These results suggest a link between primary *MMUT* deficiency, diseased mitochondria, mitophagy dysfunction and epithelial stress, and provide promising therapeutic perspectives for MMA.

INTRODUCTION

Mitochondria – the intracellular powerhouse in which energy from nutrients is converted into ATP – are highly dynamic, double–membraned organelles that sustain cellular metabolism and physiology (1,2). The maintenance of these dynamic and functionally pleiotropic organelles is particularly relevant in terminally differentiated cells that are highly dependent on aerobic metabolism (3). Genetic dysfunctions of the mitochondrial network and homeostasis might therefore confer a potentially devastating vulnerability to many different cells contributing to a broad spectrum of diseases (4).

Mitochondrial diseases are among the most common type of inherited metabolic disorders, which often manifest in early childhood and are associated with high morbidity and mortality (5,6). Methylmalonic acidemia (MMA; MIM #251000) – the most common form of organic aciduria (7,8) – is caused by recessive, inactivating mutations in the *MMUT* gene encoding the mitochondrial enzyme methylmalonyl–coenzyme A mutase (MMUT) that mediates the terminal step of branched–chain amino acid metabolism (9). Complete (*mmut* ^{0}) and/or partial (*mmut* $^{-}$) loss of MMUT function results in the accumulation of toxic metabolites (*e.g.* methylmalonic acid [MMA], propionic acid and 2–methylcitric acid) within mitochondrial matrix that trigger ultrastructural (*e.g.* presence of megamitochondria with abnormal cristae; ref.10) and/or functional (*e.g.* abnormal mitochondrial energetic and redox profiling) mitochondrial alterations (10, 11), causing severe organ dysfunctions that primarily affect brain, liver and kidney (12,13). The mechanisms linking *MMUT* deficiency to mitochondrial dysfunctions and cell toxicity remain largely unknown, restricting therapeutic avenues for this devastating disorder to supportive care (14).

The epithelial cells that line kidney tubules are enriched in mitochondria, whose energy production maintains transport functions and overall kidney integrity (15). Disruption of mitochondrial homeostasis in inherited mitochondrial cytopathies drives various degrees of epithelial (tubular) dysfunction and kidney disease (16). For instance, a systematic study of 42 patients with mitochondrial disorders showed that 21 patients had kidney tubular dysfunction and 8 had renal failure, confirming the underestimated prevalence of kidney involvement in these disorders (17). Conversely, modulating mitochondrial function might restore kidney function in mouse models of acute (18) and chronic kidney disease (19).

Cells possess quality control systems to maintain a requisite number of functional mitochondria to meet the energy demands (20). These pathways concur to eliminate damaged mitochondrial proteins or dysfunctional parts of mitochondrial network by autophagy (aptly termed mitophagy; ref. 21). Biochemical and genetic evidences reveal that the PTEN–induced putative kinase1 (PINK1) and Parkin are the key drivers of mitophagy, driven by the loss of mitochondrial membrane potential (22). This homeostatic mitochondrial process is particularly active in kidney tubular cells (23). Deletion of genes encoding mitophagy–promoting molecules damages tubular cells through defective mitochondrial clearance and increased reactive oxygen species (ROS) (24). Abnormal mitochondria with disorganized cristae have been described in kidney cells (25) and biopsies from MMA patients (10,26), suggesting an involvement of mitochondrial quality control mechanisms in the disease.

In the present study, using MMA as a paradigm of complex mitochondrial dysfunction, we decipher a pathway that links loss–of–function of a mitochondrial enzyme, mitochondrial abnormalities, defective PINK1/Parkin–mediated quality control and mitochondria–derived stress in kidney tubular cells. These insights might offer potential therapeutic avenues for modulating mitochondrial function and epithelial cell damage in MMA.

RESULTS

MMUT deficiency impairs mitochondria in kidney tubular cells

As MMUT is robustly expressed within the mitochondria of kidney tubular cells (Supplementary Fig. 1a–e), we first investigated the consequences of *MMUT* deficiency on mitochondrial function and homeostasis in these cells. To this aim, we analyzed the properties of mitochondrial network in kidney tubular cells derived from the urine of either healthy controls or *mut*^{0} MMA patients harboring inactivating mutations in *MMUT* (Supplementary Table 1; ref. 25). Compared to their control cells, the MMA patient–derived tubular cells (hereafter referred to as MMA cells) exhibited a marked decrease in MMUT protein (Fig. 1a) and in its mitochondrial enzymatic activity (Fig. 1b, c), reflected by the accumulation of methylmalonic acid (MMA; Fig. 1d). Transmission electron microscopy (TEM) analyses revealed that mitochondria, which appear as an interconnected meshwork of elongated or curvilinear organelles in control cells, were fragmented or characterized by a prominent rod–like shape with perturbed cristae organization in MMA cells (Fig. 1e) and in the kidneys of a patient with MMA (Fig. 1f), in line with recent studies showing an abnormal mitochondrial ultrastructure in both kidney and explanted livers of patients with MMA (26). Confocal microscopy of the mitochondrially–targeted green fluorescent protein (mito–GFP) and semi–automated image analyses confirmed in MMA cells the presence of mitochondria which appear circular and robustly fragmented when compared to control cells (Fig. 1g).

The morphological abnormalities prompted us to examine whether MMUT deficiency alters the homeostasis of the mitochondrial network. Using immunoblotting analyses for mitochondrial proteins that label outer (*e.g.* VDAC1) and inner membrane (*e.g.* SDH, MT–CO2 and COX IV), intermembrane space (*e.g.* Cyt C) and matrix (*e.g.* PDHA1), we noted an increased abundance of overall mitochondrial proteins in MMA compared to control cells (Fig. 2a). These changes were confirmed by measuring the ratio between mitochondrial (mt–DNA) and nuclear (n–DNA) through quantitative PCR analyses (Fig. 2b) and by quantifying the ATP5B–flagged mitochondrial structures using confocal microscopy (Fig. 2c). These mitochondrial alterations did not result from an effect of *MMUT* deficiency on cell viability (Supplementary Fig. 1f) and proliferation (Supplementary Fig. 1g), nor transcriptional changes in mitochondrial genes (*MFN1/2, DRP1, OPA1*) regulating fusion/fission process (Supplementary Fig. 1h), which were similar between MMA and control cells. Taken together, these data indicate that the deficiency of *MMUT* alters the homeostasis of the mitochondrial network, hence increasing the content of mitochondria organelles.

Mitochondrial dysfunction drives stress in MMA cells

As *MMUT* deficiency alters mitochondrial homeostasis, we next assessed potential consequences on mitochondrial function. Consistent with increased numbers of morphologically aberrant mitochondria, the mitochondrial membrane potential ($\Delta\psi_m$) was drastically reduced in MMA cells (Fig. 2d), as evidenced by live cell imaging analyses of the mitochondrial network with cell–permeant, fluorescent dye tetramethylrhodamine methyl ester (TMRM, that readily accumulates within functional mitochondria) and MitoTracker (a fluorescent probe that localizes to mitochondria). These changes were paralleled by a major mitochondrial oxidative stress (Fig. 2e), as testified by the elevated production of mitochondria (mt)–derived ROS (MitoSOX, a live–cell permeant indicator of mitochondrial ROS) and augmented antioxidant response (SOD1; Fig. 2g). Treatment with the mitochondrial complex I inhibitor Rotenone (5μM for 24h), which did not alter the cell viability, exacerbated mitochondrial alterations (*e.g.* decreased mitochondrial membrane potential and increased mt–ROS levels) to a greater extent in MMA compared to control cells (Fig. 2d, e). Seahorse metabolic flux analyses measuring oxygen consumption rate (OCR) confirmed impaired mitochondrial bioenergetics in MMUT–deficient cells, as evidenced by a significant reduction in the baseline respiration, ATP turnover, and total respiratory capacity (Fig. 2f), suggesting that *MMUT* deficiency impinges on the function and homeostasis of mitochondrial network in both normal and stress–evoked conditions.

Previous studies in transgenic *Mmut*–deficient mice and in a large cohort of patients with MMA (10, 26) showed that mitochondrial dysfunction and oxidative stress are linked to increased production of lipocalin–2 (LCN2, also known as NGAL), a small iron–transporting protein largely produced by kidney tubular cells following cellular damage (27). In line with these observations, we noticed an increase in *Lcn2* mRNA and protein expression in MMA compared to control cells (Fig. 2g; Supplementary Fig. 1i). The link between compromised mitochondria, oxidative stress and LCN2 overproduction was substantiated by loss–of–function interventions in primary proximal tubule (PT) cells derived from wild–type mouse kidneys (28). Short–hairpin (sh) RNA–induced knockdown of *Atg7* encoding an essential protein necessary for autophagy causes mitochondrial dysfunction and mitochondrial oxidative stress with increased production of LCN2 in these cells (Supplementary Fig. 2a–e). These data indicate a functional link between mitochondrial dysfunction, oxidative stress and LCN2 overproduction, hence the existence of mitochondria–derived epithelial stress in kidney tubular cells.

MMUT deficient phenotypes in model organisms

To explore the consequences of the *MMUT* deficiency *in vivo*, we investigated a *Mmut* $^{\mathrm{KO/KI}}$ mouse model carrying a mutant *Mmut* allele (p.Met698Lys, corresponding to the patient mutation p.Met700Lys) and a knock–out *Mmut* allele (29). The loss of Mmut was reflected by the accumulation of MMA (Supplementary Fig. 3a) and distorted kidney mitochondria which appear rod–like shape with impaired cristae organization (Supplementary Fig. 3b). Consistent with morphologically aberrant mitochondria, the membrane potential ($\Delta\psi_{\mathrm{m}}$) was drastically reduced in MMA accumulating kidney PT cells derived from *Mmut*$^{\mathrm{KO/KI}}$ mice (TMRM staining; Supplementary Fig. 3c). These changes were paralleled by a major mitochondrial oxidative stress, as testified by elevated mtROS levels (MitoSOX staining; Supplementary Fig. 3d). Despite the metabolic and/or mitochondrial alterations (Supplementary Fig. 3a, d), *Mmut*$^{\mathrm{KO/KI}}$ mice displayed mildly increased levels of urea (Supplementary Fig. 3e); no significant changes in kidney function (plasma levels and clearance of creatinine; Supplementary Fig. 3f, g); no changes in LCN2 levels in kidneys as well as in plasma and/or urine - even in aged mutant mice (Supplementary Fig. 3h–j); and no structural damage (Supplementary Fig. 3k) nor interstitial inflammation (Supplementary Fig. 3l, m) in the kidneys compared to control littermates.

As the *Mmut*$^{\mathrm{KO/KI}}$ mouse model does not show key features of kidney disease in MMA, we established the first *mmut*–knockout zebrafish model using CRISPR/Cas9 genome editing. We obtained a zebrafish mutant line carrying an 11–bp–CRISPR/Cas9–induced deletion (*mmut*$^{\mathrm{del11/de111}}$), generating a premature stop codon within exon 3, resulting in a truncated protein deprived of its catalytic activity (Supplementary Fig. 4a–c). Homozygous *mmut*$^{\mathrm{del11/del11}}$ zebrafish larvae, which appear morphologically normal and display no obvious development defects (Supplementary Fig. 4d), exhibit accumulation of MMA (Fig. 3a), which was abolished by re–expressing wild–type *mmut* cDNA in the liver (Supplementary Fig. 4e), validating the specificity of the deletion model. When compared to control littermates, both the kidney and the liver of *mmut*–deficient zebrafish exhibited altered mitochondrial morphology characterized by increased mitochondrial circularity (Fig. 3b, c) with perturbed cristae organization. Seahorse metabolic flux analyses revealed impaired mitochondrial bioenergetics in *mmut*–deficient zebrafish when compared to control larvae (Fig. 3d). These changes were paralleled by a major mitochondrial oxidative stress, as testified by *in vivo* imaging and ratiometric confocal microscopy–based analyses of glutathione redox fluorescent signals in liver Grx1–roGFP2–labeled mitochondria (Fig. 3e), demonstrating the evolutionary conservation of this connection. Furthermore, *mmut*–deficient zebrafish larvae markedly swim over shorter distances (Fig. 3f; Supplementary Fig. 3f) and show an excessive mortality (Fig. 3g) compared to control larvae.

Both traits were rescued by feeding *mmut*–deficient zebrafish larvae (Fig. 3f, g) with low protein diet–a strategy used in the MMA management care (12). Re–expressing wild–type *mmut* cDNA in the liver of *mmut*–deficient zebrafish larvae, which normalized the levels of MMA metabolite and blunted the excessive mortality (Fig. 3g; Supplementary Fig. 4e), did not rescue the abnormal swimming phenotype (Supplementary Fig. 4g). Collectively, these results demonstrate that *MMUT* deficiency compromises the function and the homeostasis of mitochondrial network, both *in vitro* and *in vivo*.

MMUT deficiency induces autophagy

As damaged mitochondria are normally removed by autophagy–lysosome pathways (30), we hypothesized that mitochondrial abnormalities in MMA cells might reflect changes in autophagy–lysosome degradation systems. We measured autophagy by detecting the conversion of the non–lipidated form of LC3–I to the lipidated, autophagosome–associated form LC3–II through immunoblotting and/or by quantifying the numbers of punctate $LC3^+$ vesicles through confocal microscopy and/or the abundance of electron microscopy (EM)–structures compatible with autophagic vacuoles (31). Compared to control cells, we detected in MMA cells elevated conversion of LC3–I to LC3–II (Fig. 4a) and higher numbers of punctate LC3–positive structures (Fig. 4b), and more EM structures compatible with autophagic vacuoles (AVs; Fig. 4c), whose nature was confirmed by correlated light electron microscopy (CLEM; Supplementary Fig. 5a).

An increased number of AVs might arise from the stimulation of autophagosome biogenesis or from alteration of their degradation by lysosomes. To distinguish between these two possibilities, we treated at two different time points (2h and 4h) control and MMA cells with Bafilomycin A1 (BfnA1), a lysosome–proteolysis inhibitor that blocks the cellular degradation of autophagosomes that subsequently accumulate. Treatment of MMA cells with Bfn A1 further increased the already elevated steady–levels of LC3–II and the numbers of punctate $LC3^+$ structures at two different time points where any changes would reflect altered autophagosome biogenesis (Fig. 4a, b; ref. 31). These cellular alterations were not associated with changes in autophagosome trafficking (as measured by LC3/LAMP1–positive structures in cells in response to short incubations with non–saturating concentration of BfnA1; Supplementary Fig. 5b); nor in autophagosome–lysosome fusion, as testified by augmented protein levels of Rab7–a small GTPase protein that regulates autophagosome–lysosome fusion (31) (Supplementary Fig. 5c); nor in lysosome dynamics, as scored by the abundance of lysosome–associated protein LAMP1 and cathepsin–D (Supplementary Fig. 5c); nor in lysosome–based degradative capacity, as monitored by Bodipy–FL–Pepstatin A, a fluorescence–tagged Pep A that binds to the active site of cathepsin–D in acidic lysosomes (Supplementary Fig. 5d), implying that the *MMUT* deficiency stimulates autophagosome biogenesis rather than slowing down their degradation.

The connection between *MMUT* deficiency and induction of autophagy was substantiated by the increased formation of SQSTM1/p62$^+$ aggregates containing polyubiquitinated proteins in MMA cells, despite unchanged levels of *SQSTM1* and unmodified activity of the proteasome (Supplementary Fig. 5e, f). These changes were rescued by treating the MMA cells with the mitochondrially–targeted ROS scavenger mito–TEMPO (MT; 10 μM for 24h; Supplementary Fig. 5f), in line with recent observations that increased levels of SQSTM1/p62 might enable a more efficient autophagy to maintain cellular homeostasis during oxidative stress (32,33). Similar findings were observed in human kidney: LC3–marked autophagy vesicles and SQSTM1$^+$ aggregates remarkably accumulated in kidney tubules from a patient with MMA (Supplementary Fig. 5g).

Furthermore, the upstream signalling cascade regulating autophagy, such as mTORC1 complex, was markedly reduced in MMA compared to control cells (Fig. 4d). This was paralleled by activation of the ULK1 complex–the most upstream autophagy machinery controlling autophagosome biogenesis, as indicated by increased protein levels of ULK–1 complex subunits FIP200 and Atg13 (Fig. 4e) and numbers of initiation foci containing ULK–1 complex subunit Atg13 (Fig. 4f, top panel). In turn, these changes were reflected by the heightened production of the autophagy–relevant pool of PtdIns–3P (Fig. 4f, middle panel), triggering the recruitment of downstream autophagy effector WIPI2 that stimulates the biogenesis of autophagosomes (Fig. 4f, bottom panel). Conversely, exposing MMA cells to the class III phosphoinositide 3–kinase (PI3K) vacuolar protein sorting 34 (Vps34) kinase inhibitor SAR405, which blocks the production of PtdIns–3P (34), prevented the LC3–I–to–LC3–II conversion, hence the formation of autophagosomes induced by the MUT deficiency (Supplementary Fig. 6a, b). Collectively, these data suggest that *MMUT* deficiency stimulates autophagy by regulating, at least in part, upstream signalling cascades that regulate autophagosome biogenesis.

MMUT deficiency impairs degradation of damaged mitochondria

Considering the persistence in MMA cells of dysfunctional (ROS–producing) mitochondria and high numbers of autophagic vesicles/autophagosomes, we reasoned that *MMUT* deficiency might sabotage the mitophagy–mediated demolition of MMA damaged mitochondria. To verify our hypothesis, we treated both control and MMA cells with Rotenone to damage mitochondria and selectively activate their mitophagy–mediated degradation. After 24h treatment with Rotenone, control cells showed a marked decrease in overall mitochondrial proteins (Fig. 5a) and in the ratio between mt–DNA and n–DNA (Fig. 5b), whereas both parameters were conversely retained in MMA cells. These changes were verified by measuring the overall mitochondrial proteins in cells cultured with other mitochondria–damaging compounds such as the electron transport chain inhibitors Oligomycin and Antimycin A (4 μM and 0.8 μM, respectively; Supplementary Fig. 7a). The depletion of MMUT did not alter the content of other cellular organelles producing ROS, such as peroxisomes, both under normal and autophagy/mitophagy–evoked conditions (Supplementary Fig. 7b), nor the dynamics and homeostasis of endolysosome system (Supplementary Fig. 5c, d).

As the loss of MMUT function results in a block of basal and stress–induced mitophagy, we hypothesized that *MMUT* deficiency might paralyse the delivery of MMA damaged mitochondria to autophagy–lysosome degradation systems. To tackle this hypothesis, we utilized the ratiometric pH–sensitive imaging–based method (22,35) to measure the delivery of dysfunctional mitochondria (which were labelled by the mitochondrially targeted–form of a fluorescent Keima protein, mt–Keima) to lysosomes. When damaged mitochondria are delivered and engulfed within autolysosomes (*e.g.* mito–autolysosome), a spectral shift of mt–Keima occurs owing to the low pH (Fig. 5c). We validated mt–Keima as a *bona fide* reporter of mito–autolysosome formation in autophagy–deficient PT cells derived from the kidneys of *Atg7*$^{fl/fl}$ mice (adenovirus–mediated, Cre–induced deletion of floxed *Atg7* alleles; Supplementary Fig. 7c; ref. 36) or from kidneys of *Pink1* or *Prkn2* (encoding Parkin) knockout (KO) mice (Supplementary Fig. 7e, f), and treated with Rotenone. Compared to controls cells, the deletion of *Atg7*, *Pink1* or *Prkn2* was reflected by a loss of the expected shift of mt–Keima from a green mitochondrial to a red punctate appearance (Supplementary Fig. 7d, g) induced by Rotenone. Of note, basal mitophagy was reduced in autophagy (ATG7)–deficient PT cells (Supplementary Fig. 7d) whereas it was comparable in wild–type and *Pink1* or *Prkn2* KO cells (Supplementary Fig. 7g), in line with recent reports suggesting that basal mitophagy might occur independently of PINK1 in mouse tissues of high metabolic demand including the kidneys (37).

Next, we similarly expressed mt–Keima in both control and MMA cells (Supplementary Fig. 7h) and exposed the cells to Rotenone to follow the delivery of damaged mitochondria to lysosomes. After 24h Rotenone treatment, control cells showed a substantial green–to–red fluorescent shift– indicative of delivery of damaged mitochondria to lysosomes, whereas this shift was abolished in MMA cells (Fig. 5c). Notably, under control conditions, MMA cells displayed lower steady–state mt–Keima red/ green ratio values than controls, suggesting that *MMUT* deficiency compromises the delivery of damaged mitochondria to autolysosomes in both normal and stress–induced conditions (Fig. 5c).

Mitophagy–mediated quality control in COX10 deficiency

In order to test whether the altered mitophagy associated with the functional loss of MMUT is present in other mitochondrial diseases, we investigated the contribution of mitophagy–mediated removal and quality control systems in a model of impaired cytochrome oxidase assembly (*COX10* deficiency)–taken as a paradigm of primary mitochondrial disease (38). We transduced PT cells derived from the kidneys of floxed *Cox10*$^{\mathrm{fl/fl}}$ mice with Cre–recombinase bearing adenoviral particles to conditionally inactivate the floxed *Cox10* alleles *in vitro* (Supplementary Fig. 8a, b). The deletion of *Cox10* was verified by reverse transcription–quantitative PCR (Supplementary Fig. 8c) and indirectly by immunoblotting for mitochondrial COX IV (Supplementary Fig. 8d; ref. 39). The *Cox10*–deleted cells showed significant mitochondrial alterations (*e.g.* decreased membrane mitochondrial potential and increased generation of mitochondrial ROS; Supplementary Fig. 8e–f). These alterations were not associated with major changes in mitochondrial content as indicated by comparable ratios of mt–DNA/n–DNA (Supplementary Fig. 8g) and by similar levels of mitochondrial proteins (Supplementary Fig. 8h) between control and *Cox10*–deleted PT cells. Notably, under normal conditions *Cox10*–deleted PT cells displayed higher steady–state mt–Keima red/green ratio values than control cells (Supplementary Fig. 8i), which were reflected by elevated transcript levels of mitophagy regulating gene *Pink1* (Supplementary Fig. 8j). Treatment with Rotenone induced in both control and *Cox10*–depleted PT cells the green–to–red fluorescent shift–indicative of delivery and engulfment of damaged mitochondria within autolysosomes (Supplementary Fig. 8i). Collectively, these data suggest that mitochondrial alterations encountered in *Cox10* deficient kidney cells are not linked to anomalies in mitophagy–mediated degradation, in contrast to the defective mitochondrial homeostasis and mitophagy–mediated quality control caused by *MMUT* deficiency in patient–derived kidney cells.

MMUT deficiency skews PINK1/Parkin–mediated mitophagy

The PINK1/Parkin–induced mitophagy maintains the quality of the mitochondrial network by priming dysfunctional mitochondria for autophagy–lysosome degradation pathways (40). Therefore, we hypothesized that *MMUT* deficiency might compromise the PINK1/Parkin–

mediated priming of MMA stressed mitochondria to autophagic–lysosomal degradation. Due to the lack of commercially available antibodies able to detect endogenous PINK1, we resorted to the translocation of Parkin to damaged mitochondria–a key downstream step following the activation of PINK1–as a *bona fide* reporter to assess the PINK1/Parkin–priming mechanisms (22,41,42). We labelled the mitochondrial network by transducing both control and MMA cells with an adenovirus that expresses the mitochondrially–targeted green fluorescent protein (mt–GFP). 24 hour post–transduction, we exposed the mt–GFP expressing cells to Rotenone (5 μM for 4h) and scored the translocation of Parkin to mt–GFP–flagged mitochondria by confocal microscopy (42). Using a validated α–Parkin antibody (see the below Supplementary Fig. 10e), we observed that Rotenone treatment expectedly heightened the numbers of Parkin$^+$ clusters and the translocation of Parkin to mt–GFP$^+$–damaged mitochondria in control cells (Fig. 5d–f), indicating a proper PINK1/Parkin–mediated quality control. Conversely, MMA cells displayed a decrease in numbers of Parkin$^+$ clusters and translocation of Parkin to damaged mitochondria at baseline and in Rotenone–evoked stress conditions (Fig. 5d–f). These changes were complemented by the lack of engulfment of damaged mitochondria within EM–compatible autophagy vacuoles in MMA cells (Fig. 5g), supporting the concept of defective marking of diseased mitochondria for autophagy–lysosome–based degradation.

The role of defective PINK1–mediated quality control systems was further assessed by transducing MMA cells with an adenovirus that expresses human hemagglutinin (HA)–tagged PINK1 (Ad–HA–*PINK*1).The functional re–expression of PINK1 at mt–GFP–flagged mitochondria in MMA cells markedly increased the numbers of Parkin$^+$ clusters and rescued the translocation of Parkin to MMA damaged mitochondria (Fig. 6a–c), inducing their delivery and degradation by autophagy–lysosome systems, as indicated by mt–Keima reporter (Fig. 6d; Supplementary Fig. 9a) and analyses of mitochondrial proteins (Fig. 6e). In parallel, PINK1 re–expression improved mitochondrial functions in MMA cells (Fig. 6f–h; Supplementary Fig. 9b, c), compared to cells transduced with empty vector.

Mmut deletion damages mitochondria causing stress

To causally demonstrate the link between MMUT loss, PINK1–directed mitophagy, mitochondrial dysfunctions and epithelial stress, we used gain and loss–of–function interventions in kidney cells carrying floxed *Mmut* alleles (*Mmut*$^{fl/fl}$). The *Mmut*$^{fl/fl}$ mice do not show any clinical phenotype, have normal growth and display normal metabolite levels (43). Primary PT cells derived from *Mmut*$^{fl/fl}$ mouse kidneys were transduced with adenovirus particles bearing Cre–recombinase to conditionally delete *Mmut in vitro* (Fig. 7a, b).

The deletion of *Mmut* was reflected by augmented levels of MMA (Fig. 7c), and by reduced engulfment of damaged and/or dysfunctional mitochondria (*e.g.* decreased membrane potential and altered bioenergetics profiling; Fig. 7d, e) within autolysosomes (as scored by reduced mt–Keima red/green fluorescence ratio; Fig. 7f). Under these conditions, *Mmut*–deleted cells showed no significant increase in overall mitochondrial proteins compared to control cells (Supplementary Fig. 9d). In line with defective mitochondrial disposal, *Mmut*–deleted PT cells exhibited elevated mitochondrial oxidative stress (Fig. 7g) and cell damage (LCN2 overproduction; Fig. 7h), which were abolished by restoring PINK1–directed mitophagy with an adenovirus expressing (HA)–tagged *PINK1* (Fig. 7g, h; Supplementary Fig. 9e).

Conversely, CRISPR/Cas9–mediated KO of *PINK1* or *PRKN2* (encoding Parkin) in human HAP–1 cells (Supplementary Fig. 10) led to mitochondrial alterations, *i.e.* decreased mitochondrial membrane potential (Supplementary Fig. 11a), reduced bioenergetics profiling and elevated mitochondrial ROS production (Supplementary Fig. 11b, c), that were similar to, albeit milder than, those encountered in patient–and–in *Mmut*–deleted cells. Notably, we did not detect differences in mitochondrial morphology between PINK1 and Parkin wild–type and KO cells (Supplementary Fig. 11d). Taken together, these data suggest that the deficiency of *Mmut* impedes the PINK1–induced translocation of Parkin to MMA damaged–mitochondria, halting their delivery and subsequent degradation by autophagy–lysosome systems. In turn, these cellular defects promote the accumulation of dysfunctional (ROS–producing) mitochondria that ultimately trigger epithelial stress and damage.

Drug–disease network perturbations in MMA cells

We used a drug–disease network–based computational modeling approach (Mantra 2.0; Mode of Action by Network Analysis; http://mantra.tigem.it; ref. 44) to identify potential druggable pathways to overcome cellular dysfunctions associated with MMA. MANTRA elucidates genome–wide targetable candidates by systematically matching disease gene signature (Supplementary Fig. 12a), here derived from the comparison of expression profiles between MMA and their related control cells (Supplementary Fig. 12b, c; Supplementary Table 2), against a library of 1309 small bioactive drug compounds. Predictions for drug–disease pairs were based on the hypothesis that, if a drug reverses the disease gene signature, that drug might potentially target disease–relevant biological pathways (44). Based on this assumption, the top–35 drug compounds transcriptionally closer to the inverse disease gene profile were identified. To determine the targeted–biological pathways in MMA, we transcriptionally phenotyped the top–35 drug compounds by performing Drug Set Enrichment Analysis (DSEA; ref. 45) – a tool identifying, from transcriptional responses, the molecular pathways that are significantly modulated by drug compounds in a set. We run DSEA using as pathway databases Gene Ontology terms: biological process, molecular function and cellular component. Interestingly, DSEA revealed that the top–scored drug compounds modulate redox homeostasis–related pathways (Fig. 8a), in line with the mitochondrial oxidative stress encountered in MMA cells and with recent mouse transcriptomic profiling denoting a chronic activation of stress–related pathways in a transgenic mouse model expressing *Mmut* in the muscle (26). It also yielded candidates affecting pathways that regulate mitochondrial homeostasis and functioning such as calcium import, fatty acid β–oxidation and cellular respiration; or that control mitochondrial dynamics such as fusion; or that modulate cellular responses to mitochondrial stress (Fig. 8a). These *in silico* analyses strongly support that mitochondria–targeting strategies might potentially reverse disease phenotype in MMA cells.

Mitochondrial targeting in MMA cells and animal models

Inspired by the biological evidence and the MANTRA analysis, we tested whether mitochondria–targeted interventions might correct phenotypes in MMA. Control and MMA cells were cultured in presence and in absence of a mitochondria–targeted antioxidant mito–TEMPO (MT, 10 μM for 24h), which rescues mitochondrial–based cell dysfunctions associated with the lysosome storage disease cystinosis (46). Despite unchanged levels of MMA metabolite (Fig. 8b), treatment with MT effectively recovered mitochondrial morphology (as scored by presence of curvilinear or elongated mitochondria; Fig. 8c) and partially the homeostasis of mitochondrial network (as testified by immunoblotting analyses for mitochondrial proteins; Fig. 8d), improved mitochondrial functionality and bioenergetics (Fig. 8e), lowered the formation of SQSTM1$^+$ aggregates containing polyubiquitinated proteins (Supplementary Fig. 5f), and neutralized mitochondrial oxidative stress (Fig. 8f) and LCN2 overproduction (Fig. 8g) in MMA cells.

To explore the translational potential of these findings, we treated *mmut*–deficient zebrafish larvae with low, non–toxic doses of the mitochondrially–targeted antioxidant MitoQ (200 nM for 24h). Treatment with MitoQ effectively reduced mitochondrial oxidative stress (Fig. 9a), improved the behavioural phenotype (Fig. 9b) and reduced the excessive mortality observed in *mmut*–deficient zebrafish larvae (Fig. 9c), in absence of any significant changes in the MMA levels (Fig. 9d). Taken together, these findings suggest that repairing mitochondrial function might serve as an attractive therapeutic strategy for treating MMA.

DISCUSSION

The proper functioning of mitochondria is crucial for the homeostasis of specialized cell types, for instance those requiring high ATP levels for reabsorptive/transport activities (23, 47–49). Inherited defects in mitochondrial–localized proteins and/or enzymes, as exemplified by MMA, drive the accumulation of potentially toxic metabolites within mitochondrial matrix, promoting ultrastructural and/or functional alterations that ultimately cause life–threatening metabolic complications and organ dysfunction (10–13). Here, combining gain–and–loss–of function interventions *in vitro* and *in vivo*, we decipher the link between mitochondrial abnormalities induced by *MMUT* deficiency and anomalies in PINK1/Parkin–mediated quality control and surveillance systems, triggering a level of mitochondrial dysfunction that drives epithelial stress and kidney damage in MMA.

Kidney tubular cells derived from MMA patients and zebrafish lacking MUT exhibit mitochondrial fragmentation and lower membrane potential, impaired respiration and ATP production, and heightened mitochondrial ROS, generating epithelial stress and cell damage (Fig. 10). In particular, *MMUT* deficiency disables the PINK/Parkin–mediated mitophagy, leading to the accumulation of MMA damaged and/or dysfunctional mitochondria that trigger cellular stress. Unbiased drug–disease network perturbation modeling predicted targetable biological processes including redox homeostasis whose modulation repairs mitochondria in patient–derived cells and alleviates disease–relevant phenotypes in a zebrafish model of MMA. These findings reveal the importance of mitophagy–mediated organelle quality control systems in safeguarding the functioning and homeostasis of the mitochondrial network homeostasis and offer potential therapeutic strategies for repairing mitochondrial dysfunctions in MMA and in other mitochondrial–related human diseases.

The epithelial cells that form the kidney tubules are enriched in mitochondria to sustain their specialized transport functions and integrity (23). Defects that impair mitochondrial protein homeostasis or assembly might drastically lead to kidney tubule dysfunction in various types of diseases (50). MMA patient–derived kidney cells show fragmented mitochondria and a marked increase in the abundance of mitochondrial DNA and resident mitochondrial proteins, suggesting that *MMUT* deficiency alters the homeostasis of the mitochondrial network. Furthermore, MMA cells display decreased mitochondrial membrane potential and reduced mitochondrial bioenergetics. These dysfunctions result in the generation of large amounts of oxygen radicals and cellular stress, which are observed in other mitochondrial diseases (51). A similar accumulation of morphologically aberrant and dysfunctional mitochondria is observed in the kidney tubule cells of *Mmut*$^{KO/KI}$ mice, demonstrating the key role of MMUT function for the mitochondrial network homeostasis and function. However, despite the metabolic and mitochondrial abnormalities, the *Mmut*$^{KO/KI}$ mice develop no structural changes nor significant kidney failure, thus failing to recapitulate the kidney disease associated with MMA.

To overcome this difficulty, we established the first *mmut*–knockout zebrafish model using CRISPR/Cas9 genome editing. The patterning of the kidney tubule is remarkably conserved in the zebrafish pronephros versus mammalian kidney, including junctional complexes, endolysosomal apparatus, and receptors and transporters (52). Deficiencies in genes encoding receptors, enzymes and transporter that cause tubular dysfunction in humans have been shown to trigger similar pathological changes in zebrafish (46,53–55). Further characteristics including high fecundity, unrivalled optical transparency, and the possibility of housing in multi–well plates offer unique opportunities to perform (high–throughput) phenotypic screens in an *in vivo* context (56).

Analogous to the metabolic and mitochondrial alterations encountered in the *Mmut*$^{KO/KI}$ and patient–derived kidney cells, the *mmut*–deficient zebrafish exhibit altered mitochondrial morphology and excessive mitochondrial damage, with an exaggerated mitochondrial oxidative stress and markedly decreased mitochondrial bioenergetics flux rates when compared to their control littermates. The demonstration of this conserved connection will require a more comprehensive elucidation of the similarities and differences between zebrafish and human mitochondrial biology. The *mmut*–deficient zebrafish showed an MMA disease–relevant phenotype, including liver/kidney mitochondriopathy, impairment of the behavioural phenotypes and an excess of mortality. Of note, these two features are rescued by feeding the mutant zebrafish with a low protein diet–a strategy used in MMA patients as it prevents the accumulation of methylmalonic acid (14). Intriguingly, our findings revealed that restoring *mmut* activity in the liver, which normalizes the levels of methylmalonic acid metabolite and blunts the excessive mortality, does not protect the *mmut*-deficient zebrafish from the abnormal swimming phenotype. The latter observation suggests that *mmut*–induced mitotoxicity in other cell types and organs (*e.g.* central nervous system, optic nerve and/or muscle) might govern the phenotypes encountered in *mmut*-deficient zebrafish.

The concept that mitochondrial dysfunctions and uncontrolled cellular stress might contribute to the MMA disease is in line with the observed correlation between mitochondrial dysfunction, oxidative stress and circulating LCN2 in a cohort of patients with MMA (10, 26). LCN2 is a secreted iron–transporting protein produced by kidney tubules following cellular damage; it is associated with kidney disease progression (27) and metabolic disease (57). Our studies performed on aged *Mmut*$^{KO/KI}$ mice did not show any significant increase in the levels of LCN2, in plasma, urine and kidney. The difference could reflect specific compensatory mechanisms (10, 26), or a specific time–course of induction in *Mmut*$^{\mathrm{KO/KI}}$ mice (29).

A central question is how the loss of MMUT enzyme activity disrupts mitochondrial network homeostasis and its function. The first line of defense to cope with mitochondrial damage is represented by the cellular quality control system (58). The latter involves the degradation of dysfunctional mitochondria through an evolutionary conserved, catabolic self–eating process called macroautophagy (hereafter autophagy; ref. 58) and the renewal of components through biogenesis (20). Normally, these homeostatic processes suffice to clean the cells of damaged organelles.

We first noted that *MMUT* deficiency promotes autophagy. Indeed, MMUT–deficient cells show a heightened conversion of LC3–I to LC3–II, with increased autophagosome–associated LC3^{+} puncta as well as CLEM and/or EM structures compatible with autophagic vacuoles. MMUT deficiency may affect autophagy either by stimulating autophagosome biogenesis or by inhibiting the fusion between autophagosomes and lysosomes or by controlling the degradative function of lysosomes. These last hypotheses do not sound plausible in view of the similar coalescence of LAMP–1–positive and LC3–positive vesicles and the unchanged lysosomal dynamics and lysosomal–based cellular degradation under MMUT–depleting conditions. Also, treatment with Bfn A1 further increased the already elevated steady–levels of LC3–II and the numbers of punctate LC3^{+} structures at two different time points where any changes would reflect altered autophagy biogenesis. Furthermore, downstream events regulating the degradation of autophagosomes remained unchanged. Several mechanisms may account for the stimulation of autophagy in MMUT–deficient cells: (1) reduced mTORC1 signalling, whose activity downregulates autophagy; (2) increased levels of ULK1 complex subunits FIP200 and Atg13 and numbers of initiation foci containing ULK1 complex subunit Atg13, whose activation regulates autophagy machinery involved in autophagosome formation; (3) augmented abundance of autophagy–relevant pool of PtdIns–3P, which recruits downstream autophagy effector WIPI2, hence stimulating autophagosome biogenesis; and (4) redox–dependent formation of intracellular SQSTM1/p62^{+} aggregates containing polyubiquitinated proteins, whose accumulation might activate autophagy (32). Thus, deficiency of *MMUT* may stimulates autophagy by regulating upstream signalling cascades that regulate autophagosome biogenesis, in line with recent studies stating elevated autophagy markers in mitochondria–related diseases (59) and dysregulation of autophagy–lysosome degradation pathways in tissue samples from patients with MMA (26).

A growing body of evidence suggests that exhausted mitochondria are selectively targeted for autophagy by the PINK1/Parkin–dependent pathways (22). PINK1 and Parkin also regulate mitochondrial quality control through other pathways including fusion/fission and biogenesis (60). Mitochondrial damage activates the mitochondria–associated kinase PINK1, which recruits and activates Parkin's E3 ubiquitin ligase activity, forming the basis of multiple signalling events that culminate in the engulfment of damaged mitochondria within lysosomes (40,41). Considering the accumulation of MMA damaged and dysfunctional mitochondria and the stimulation of autophagy, we hypothesized that *MMUT* deficiency might compromise the PINK1/Parkin–mediated priming of MMA stressed mitochondria to autophagy–lysosome degradation systems. Indeed, our studies show that MMA cells (1) fail to clear dysfunctional mitochondria in both normal and mitophagy (*e.g.* treatment with Rotenone)–induced conditions, as reflected by analyses of mitochondrial proteins and mitochondrial DNA; (2) fail to deliver damaged mitochondria to autophagy–lysosome degradation systems, as scored by the sensitive mt–Keima imaging–based assay; and (3) show decreased recruitment of Parkin to MMA mitochondria–a key downstream step following the activation of PINK1 (22,40,41). The dysfunction of the PINK1/Parkin–priming system impacts on the delivery and elimination of ROS–producing mitochondria through autophagy–lysosome degradation pathways, triggering epithelial stress in MMA. Accordingly, restoring mitophagy–mediated degradation through gain–of–function approaches targeting PINK1–mediated priming was sufficient to rescue the mitochondrial network, preserving homeostasis in MMA patient–derived cells. Conversely, depleting *MMUT* in PT cells reduces the PINK1–mediated delivery and engulfment of mt–Keima tagged–mitochondria within autophagy–lysosome degradation compartments, promoting mitochondrial stress and cell damage. Of note, when compared to control cells, *Mmut*–deleted PT cells showed no increase in mitochondrial proteins, contrasting with the situation observed in MMA patient–derived cells. The difference could reflect effects of chronic mitotoxicity on mitochondrial clearance and quality control systems.

The genetic deletion of *PRKN2* (encoding Parkin) or *PINK1* in HAP–1 cells leads to mitochondrial alterations similar to, albeit milder than, those encountered in MMA patient derived–and in *Mmut*–deleted kidney cells. Thus, anomalies in PINK1/Parkin–mediated quality control might intersect the mitochondrial alterations induced by *MMUT* deficiency and contribute to the pathogenesis of MMA. The latter hypothesis is substantiated by our comparative studies of *Cox10* deletion – a model that recapitulates a primary mitochondrial respiratory chain disease (38). The deletion of *Cox10* in PT cells triggered mitochondrial alterations that are not linked to anomalies in mitophagy–mediated clearance and quality control systems, in contrast with the dysregulation induced by *Mmut* deletion. The possibility of a cumulative effect of the metabolic and/or mitochondrial perturbations resulting from the *MMUT* deficiency and the loss of PINK1/Parkin–mediated quality control systems is also supported by the observation that patients harbouring loss–of–function mutations of PINK1 causing Parkinson's disease survive in the absence of functional PINK1–dependent mitophagy pathway (61). In these patients, locomotor symptoms do not usually manifest until the second and third decades of life, when a sufficient level of mitochondrial dysfunction is coupled to the loss of PINK1 to have a detrimental effect on neuron integrity (62).

The mechanisms by which *MMUT* deficiency suppresses PINK1 signalling and mitophagy remain elusive. We speculate that *MMUT* deficiency might alter the stability of PINK1 by disabling the interaction with yet–to be–defined factors that protect PINK1 from processing and degradation (63). Alternatively, *MMUT* deficiency might trigger stress–related posttranslational modification such as S–nitrosylation that inhibits PINK1 kinase activity, hence mitophagy (64). Regardless of the mechanism(s) involved, these findings support a role of MMUT–beyond its function in metabolism–in maintaining the mitochondrial quality control system, hence epithelial integrity and homeostasis.

There is an urgent need to identify targetable interventions in the early course of MMA. Previous studies showed that kidney dysfunction and levels of circulating LCN2 could be abrogated in a transgenic mouse model of MMA by administrating ubiquinone, a bioavailable form of CoQ10 that acts on mitochondria, and Vitamin E (10). Using an *in silico* approach based on matching gene expression profile from patient–derived cells against a large compendium of small bioactive drug compounds, we inferred that targeting mitochondrial oxidative stress might reverse disease phenotypes associated with *MMUT* deficiency. In particular, we explored the potential benefit of mitochondria–targeted antioxidants, which are clinically tested in a variety of diseases (65). Treatment of MMA cells with mito–TEMPO restored partially mitochondrial homeostasis, improved mitochondrial function, normalized mitochondrial ROS and autophagy markers, and prevented the overproduction of LCN2. Furthermore, treatment with low doses of MitoQ alleviated the mitochondrial oxidative stress and ameliorated behavioral phenotypes and blunted the excessive mortality in the *mmut*–deficient zebrafish model of MMA. Importantly, both pharmacological interventions did not modify the levels of MMA metabolite in either MMA cells or *mmut*–deficient zebrafish, supporting the concept that mitochondrial targeting acts independently of the elevation of toxic MMA metabolites.

In conclusion, we identify a pathway that links a genetic deficiency of a mitochondrial enzyme with mitophagy dysfunction and accumulation of damaged mitochondria that generate epithelial stress and tissue damage. These findings substantiate the role of PINK1/Parkin–directed mitophagy in safeguarding mitochondrial network homeostasis, which is crucial for the properly functioning of specialized epithelial cells. Antioxidant compounds specifically targeting mitochondria offer a promising therapeutic strategy for repairing mitochondria in MMA and other mitochondrial disorders.

Methods

Antibodies, reagents and cell lines. Anti–MMUT (Abcam, ab67869, 1:200), anti–SDH (Abcam, ab14715, 1:500), anti–PDHA1 (Abcam, ab110334, 1:500), anti–MT–CO2 (Abcam, ab110258, 1:500), anti–VDAC1 (Cell signaling technology, 4866, 1:500), anti–COX IV (Abcam, ab14744, 1:500), anti–Cytochrome C (Abcam, ab110325, 1:500), anti–SOD1 (Santa Cruz Biotechnology, SC-11407, 1:500), anti–LCN2 (Abcam, ab63929, 1:500), anti–ATP5B (Abcam, ab14730, 1:500), anti–LC3 (MBL, PM036, 1:200), anti–phospho ULK1 (Ser757; Cell signaling technology, 6888, 1:200), anti–phospho–S6 Ribosomal Protein (Ser235/236) (Cell signaling technology, 4858, 1:500), anti–S6 Ribosomal Protein (Cell signaling technology, 2217, 1:500), anti–phospho–4E–BP1 (Ser65; Cell signaling technology, 9451, 1:500), anti–4E–BP1 (Cell signaling technology, 9644, 1:500), anti–ULK1 (Cell signaling technology, 8054, 1:200), anti–FIP200 (Cell signaling technology, 12436, 1:500), anti–ATG13 (Cell signaling technology, 13468, 1:200), anti–WIPI2 (Abcam, ab105459, 1:200), mCherry–2XFYVE Ptdins–3P–binding domain (1:100) was kindly provided by Dr. J. Gallop (University of Cambridge), anti–Parkin (Abcam, ab77924, 1:500 for IF and immunoblotting analyses), anti–Parkin (Santa Cruz Biotechnology, SC-32282, 1:500; for immunoblotting analyses), anti–HA (Roche, 11867423001, 1:500), anti–α–tubulin (Sigma–Aldrich, T5168, 1:10000), anti–RFP (600–401–379, ROCKLAND), anti–UMOD (Meridian, K90071C, 1:500), anti–AQP2 (Santa Cruz Biotechnology, sc-9882, 1:500), anti–CD3 (Abcam, ab16669, 1:200), anti–Ly6G (Biosciences, 551459, 1:100), anti–LAMP1 (Santa Cruz Biotechnology, sc–19992, 1/1000), anti–PMP70 (Sigma, SAB4200181, 1:500), anti–ubiquitin (Santa Cruz Biotechnology, sc–8017, 1:1000), anti–SQSTM1/p62 (MBL, PM045, 1:200), anti–cathepsin D (Santa Cruz Biotechnology, sc–6486, 1:500), anti–Rab7 (Abcam, 126712, 1/400), anti–β–actin (Sigma, A5441, 1/10000), anti–ATG7 (Sigma, A2856,1/500), anti–GAPDH (Cell signaling technology, 2118, 1:1000), Picro Sirius Red staining kit (Abcam, ab150681) were used. Compounds included Bafilomycin A1 (Bfn A1; Enzo Life Sciences, ALX-380-030, 250 μM), Rotenone (Sigma, R8875, 5 μM), mito–TEMPO (Enzo Life Sciences, ALX–430–150–M005, 10 μM), MG132 (Abcam, ab141003. 50 μM), MitoQ (Focus Biomolecules, 10–1363, 200 nM), SAR405 (APExBIO, A8883; 5 μM), Oligomycin A (Sigma Aldrich, 495455, 4 μM) and Antimycin A (Sigma Aldrich, A8674, 0.8 μM). The HeLa cell line was kindly provided by Dr. L. Borsig (University of Zurich) and the Hap–1 cell line was purchased from Horizon Discovery (www.horizondiscovery.com). The cells lines used here do not appear in the database of commonly misidentified cell lines (International Cell Line Authentication Committee), except the HeLa cell line that was analysed for the detection of Parkin expression in Supplementary Figure 7f. All the cells used in this study were negatively tested for mycoplasma contamination using MycoAlert™ Mycoplasma Detection Kit (LT07–118, Lonza, Switzerland).

Human kidney biopsies.Human kidney biopsies were obtained from an individual patient with clinical diagnosis of MMA and from a healthy control (non–transplanted, normal human kidney). Informed consent was obtained, and the use of the human biopsy samples was in accordance with the ethical regulations at Bambino Gesù Children's Hospital and approved by the EURenOmics consortium (FP7, 2007–2013, grant agreement no. 305608) and by the institutional review board at Bambino Gesù Children's Hospital.

Immunofluorescence on human kidney samples. Paraffin blocks of human kidney samples were sectioned into consecutive slices with a thickness of 6μm using a Leica RM2255 rotary microtome (Thermo–Fisher Scientific) on Superfrost Plus glass slides (12–550–15, Thermo-Fisher Scientific). Before staining, slides were deparaffinized in changes of CitriSolv (22–143–975, Thermo–Fisher Scientific) and 70% isopropanol. Antigen retrieval was accomplished by incubating in sodium citrate buffer (1.8% 0.1 M citric acid, 8.2% 0.1 M sodium citrate, in distilled water, pH 6.0) in a rice cooker for 30 min. The slides were blocked with PBS blocking buffer (1% BSA, 0.2% non–fat dry milk in PBS) for 30 min and stained with primary antibody specific for LC3 and SQSTM1/p62 in blocking buffer overnight at 4°C. After two washes in 0.1% Tween 20 (v/v in PBS), the slides were incubated with the corresponding fluorophore–conjugated secondary antibodies (Life Technologies) diluted in blocking buffer at room temperature for 1 h and counterstained with 1μg Biotinylated Lotus Tetragonolobus Lectin (LTL; B–1325 Vector Laboratories) and 1 μM 4',6–Diamino–2–phenylindole dihydrochloride (DAPI; #D1306, Thermo Fischer Scientific). The slides were subsequently mounted in Prolong Gold Anti–fade reagent (Life Technologies) and images were acquired using the Leica SP8 confocal laser scanning microscope (Center for Microscopy and Image Analysis, University of Zurich) as described below.

Electron microscopy on human kidney samples. Biopsy specimens were immersed in ice-cold 2.5% glutaraldehyde in 0.1 M cacodylate buffer (pH 7.4) immediately after their extraction and sectioning, and fixed for 4 h at 4 °C, carefully handling samples to avoid ex vivo artefacts. After washing in cacodylate buffer, kidney fragments were then post–fixed in 1% osmium tetroxide for 1 h, dehydrated through ascending grades of alcohol, and embedded in Epon resin (Electron Microscopy Science, Hatfield, PA). Ultrathin sections (70 to 75 nm) were cut on an ultramicrotome (Leica reichert ultracut S), stained with uranyl acetate and lead citrate, and examined with TEM (Jeol 1400 PLUS).

Enzymatic activity. Crude cell homogenates were sonicated and 1 mM DL–2–[methyl-^{14}C] methylmalonyl–CoA (ARC; specific activity 7.03 MBq/mmol in assay) was added in presence (total MMUT activity) and in absence (holo–MMUT activity) of the cofactor Adenosylcobalamin (AdoCbl; 50 μM) in darkroom safelight red conditions. The reaction was terminated by the addition of 5N KOH (Merck, Darmstadt, Germany). The samples were enriched with succinic acid (Merck, Darmstadt, Germany) to visualize the succinate peak during HPLC separation. Succinate and methyl malonate peaks were detected at 210 nm by an UV detector. Quantification of the [^{14}C] succinate fraction was performed with Optiphase HiSafe2 counting cocktail (PerkinElmer) in a Tri–Carc C1 900TR scintillator spectrometer (Packard). The protein concentration of the cell lysates was determined using the Lowry method. The MCM activity is given as pmol succinate which is formed per minute per mg protein [pmol/min/mg].

Methylmalonic acid measurement. Mouse tissues or cells were sonicated and lysed in 100 µL of Acetonitrile /10 mM Ammonium formate 1:1 (v/v). The concentration of methylmalonic acid was measured in an accredited laboratory using the standard protocol from Recipe (Recipe, Munich, Germany) with some minor adaptations. Briefly, 50 µL of lysate or urine were mixed with 200 µL precipitation reagent containing the internal standard d_3-methylmalonic acid (Recipe, Munich, Germany). After vortexing the sample for 30 s, the protein precipitate was removed by centrifugation for 5 min at 16’000 g and the clean supernatant is transferred to a LC–MS vial, which is kept at 10°C in a thermostatic autosampler until LC–MS analysis. From each vial, 2 μL of sample were loaded and separated on an ClinMass column (2.1 x 100 mm, Recipe, Munich, Germany), kept at 25°C using an Ultimate 3000XRS (Thermo Scientific, Olten, Switzerland) instrument interfaced to a SCIEX TripleQuad 5500 (AB Sciex, Zug, Switzerland) mass spectrometer. The chromatography was performed at a flow rate ~700 µL/min by using mobile phase A (MPA) and B (MPB) from Recipe (Recipe, Munich, Germany). The elution was achieved using a step gradient (100% MPA for 0.3 min, 70% MPA for 0.3 min, 40% MPA for 0.7 min and 0% MPA for 0.1 min followed by 1.2 min at 100% MPA). The source parameters were the following: CAD = 7 psi, CUR = 30 psi, GS1 = 60 psi, GS2 = 70 psi, IS = 4.0 kV, TEM = 550°C. Multiple reaction monitoring (MRM) in negative ion mode is used to identify and quantify Methylmalonic acid (quan: 117/73; qual: 117/55) and d_3-Methylmalonic acid (quan: 120/76; qual: 120/58). A collision energy of -12V is used for the 117/73 and 120/76 transitions, while a collision energy of -31V is used for the 117/55 and 120/58 transitions. The declustering potential was -40V for all four transitions.

Kidney tubule cells from urines of patients with MMA. Tubular epithelial cells were derived from urines of either three healthy donors or three *mut^{o}* MMA patients (Supplementary table 1, ref. 25) and cultured in a selective medium containing Dulbecco’s Modified Eagle Medium and Ham’s F12 medium, supplemented with dialyzed fetal calf serum (FCS), insulin, hydrocortisone, selenite, transferrin, hEGF, NAD and 3,3,5 triiodo–L–thyronine. The identity of *MMUT* mutations were confirmed by Sanger sequencing. Confluent cells were sub–cultivated until 3rd passage and, subsequently, immortalized using pRSVneo vector containing SV40 DNA (pRNS1). Afterwards, immortalized kidney tubule epithelial cells were characterized for morphology and expression of kidney markers, and MMUT protein and its enzymatic activity as described previously (25). Where indicated, lysosomal proteolysis was inhibited by adding Bafilomycin A1 (250nM for 2h and 4h, unless otherwise stated). Where indicated, the mitochondrial damage and the activation of mitophagy was triggered by treating the cells with Rotenone (5 μM for 24h) or with Oligomycin A and Antimycin (O/A; 4 μM and 0.8 μM, respectively), in fresh culture medium for the indicated times. Where indicated, the cells were starved by washing them with Hank’s balanced salt solution (55021 C, Sigma–Aldrich) and placing them in nutrient–deprived medium. Where indicated, the autophagy was inhibited by culturing the cells in presence or in absence of a highly selective PIK3C3/Vps34 inhibitor SAR405 (5 μM in fresh culture medium for 4h). Where indicated, the cells were treated with the proteasome inhibitor

MG132 (5 μM in fresh culture medium). Where indicated, the cells were treated with the mitochondrially–targeted reactive oxygen species (ROS) scavenger Mito–TEMPO (MT; 10 μM in fresh culture medium for 24h, Enzo Life Sciences). The cells were processed and analyzed as described below.

Generation of PINK1 and PRKN2 knockout cell lines. *PRKN2* (HZGHC003208c002) and *PINK1* (HZGHC000798c008) KO cells were created through CRISPR–Cas9 gene editing technology and purchased from Horizon Discovery (www.horizondiscovery.com). The cells were tested negative for mycoplasma contamination and subjected to PCR analysis, followed by Sanger sequencing to identify CRISPR–Cas9 induced–deletion. The cells were maintained in Iscove's Modified Dulbecco's Medium (IMDM) supplemented with 10 % dialyzed FCS, 100 U/mL Penicillin and 100μg/mL Streptomycin. The cells were afterwards processed and analyzed as described below.

Generation and maintenance of mmut zebrafish. pT7–gRNA and pT3TS–nCas9n plasmids were obtained from Addgene (# 46759 and # 46757, respectively). CRISPR–Cas9 –targeted site (5'-GGGCCAGCAGGGTCTGTCTGTGG-3') contains a restriction site for AlwNI (CAGNNNCTG), which has been used for monitoring CRISPR–Cas9–mediated mutation and genotyping. Oligonucleotides containing sgRNA–targeting sequence were annealed and cloned into the Esp3I (BsmBI)–digested pT7–gRNA vector (pT7–gRNA–*mmut*). The sequence of oligonucleotides is CRISPR–*mmut*–S: 5'–TAGGGCCAGCAGGGTCTGTCTG–3' and CRISPR–*mmut*–AS: 5'–AAACCAG ACAGACCCTGCTGGC–3'. XbaI–linearized pT3TS–nCas9n vector was used to produce Cas9 mRNA using mMESSAGE mMACHINE T3 kit (Invitrogen). Both sgRNA–*mmut* and Cas9 messenger RNAs were co– injected into two or four–cell stage TU zebrafish (*Danio rerio*) embryos. For detection of CRISPR–Cas9–induced deletion, genomic DNA was extracted from 2dpf embryos which developed normally. The CRISPR–Cas9–injected mosaic TU embryos were raised to adulthood (F0) and outcrossed with wild–type TL zebrafish. The embryos were then raised to adulthood (F1) for screening of heterozygous carriers. We identified a heterozygous carrier harboring *mmut*$^{+/del11}$ mutation and (F1) generations were crossed again with wild–type TL zebrafish to generate (F2) heterozygous zebrafish. Homozygous zebrafish larvae carrying *mmut*$^{del11/del11}$ mutation were obtained from incross of (F2) heterozygous zebrafish. Zebrafish were kept at day/night cycle of 14/10 h at 28°C. Zebrafish larvae were anesthetized by immersion in E3 medium (for 5dpf) or system water (for 10dpf) containing 168μg mL^{-1} tricaine methane sulfonate (MS222, Sigma Aldrich) and analysed as described below. Animal care and experimental procedures were approved by the institutional animal care and use committee at Canton Zurich in accordance with the ethical guidelines at University of Zurich, Switzerland.

Rescue experiments in mmut zebrafish. A transgenic line expressing *mmut*–mCherry was generated under the control of the liver fatty acid binding protein (*lfabp or fabp10a*) promoter. Primers used to clone *lfabp* promoter are *lfabp*–Fwd: 5'–AAATGCAAATTCTGAGCAAATGAC–3'; and *lfabp*–Rev: 5'–GCTTTCTGGAGAAGCTCAACA–3'. Primers used for amplification of mut cDNA are *mut*–Fwd: 5'–CCCGATGCCTACATAACAACA–3'; and *mut*–Rev: 5'–GAACCACCTGATGGTGAGTGA–3'. Stable zebrafish line expressing *mmut*–mCherry in the liver was established and outcrossed with *mmut*$^{+/del11}$zebrafish to generate transgenic mutant line, which was crossed with *mmut*$^{+/del11}$zebrafish to produce homozygous larvae. Ten zebrafish embryos at 5–dpf or 10–dpf were pooled and homogenized by sonication in solution containing 50% acetonitrile and 10 mM ammoniaformate, and prepared for methylmalonic acid measurements. Where indicated, zebrafish larvae were treated at 9–dpf with system water containing DMSO or MitoQ (200 nM; Focus Biomolecules) for 24 hours. The fluorescence signal of reporter protein mito–Grx1–roGFP2 (as described below) and the larval swimming were analyzed at 10–dpf. For larval movement tracking, 10–dpf zebrafish larvae were kept individually in fish system water in 24–well plate. After 10 min of adaptation, the larvae swimming tracking is recorded and analyzed in live with zebra box (ViewPoint) with light stimulation during 5min. Where indicated, 5–dpf zebrafish were fed with low protein diet (kindly provided by Dr. Carvalho, University of Porto) until to the sampled day (14–dpf), and the distribution of *mmut* zebrafish larvae was assessed. A range of 100–120 embryos obtained from in–cross strategies between heterozygous zebrafish were raised to the sampled day, and the percentage of wild type, heterozygous and homozygous were determined after genotyping procedure.

Detection of mitochondrial ROS in mmut zebrafish. To measure mitochondrial ROS in zebrafish larvae, we generated a transgenic line expressing the reporter protein mito–Grx1–roGFP2 under the control of the liver fatty acid binding protein (*lfabp*) promoter. The plasmid pLPCX–mito Grx1–roGFP2 was kindly provided from Dr. Dick (Addgene plasmid # 64977). Plasmid DNA *pDestTol2CG2–lfabp::mito–Grx1–roGFP2* was co–injected with Tol2 transposase mRNA into zebrafish embryo at 1–cell stage. Mosaic larvae expressing *lfabp::mito–Grx1–roGFP2* were raised to adulthood and then outcrossed with *mmut*$^{+/\mathrm{del11}}$ zebrafish to produce *mmut*$^{+/\mathrm{del11}}$ zebrafish expressing mito–Grx1–roGFP2 in the liver. The fluorescence signal of Grx1–roGFP2is analyzed by Lightsheet microscope (Zeiss, Z.1) after excitation at 405 nm and 488 nm and detected through the same emission filter (505–545nm). Imaging settings were maintained with the same parameters for comparison between different experimental conditions. The acquired data was processed by Huygens software for deconvolution, and the mean fluorescence intensities of randomly selected ROIs were measured and expressed as blue/green fluorescence intensity ratio.

Mouse models. The mice were maintained under temperature–and humidity–controlled conditions with 12 h light/12 h dark cycles with free access to appropriate standard diet in accordance with the institutional guidelines of National Institutes of Health Guide for the Care and Use of Laboratory Animals. The mice bearing floxed *Cox10* (*Cox10* $^{\mathrm{fl/fl}}$) alleles, in which the exon 6 is flanked by two *loxP* sequences, were kindly provided by Dr. Moraes (Department of Neurology, University of Miami). The mice bearing floxed *Atg7* (*Atg7* $^{\mathrm{fl/fl}}$) alleles were kindly provided by the RIKEN BRC through the National–Bio–Resource Project of the MEXT, Japan. The mice bearing germline *Prkn2* and *Pink1* knockout were purchased from Jackson Laboratory. The mice bearing floxed *Mmut* (*Mmut* $^{\mathrm{fl/fl}}$) alleles, in which the exon 3 is flanked by two *loxP* sequences, and the mice carrying M698K point mutation in the *Mmut* gene was performed by Polygene (Rümlang, Switzerland) using the C57Bl/6–derived embryonic stem cell targeting. To obtain *Mmut* $^{\mathrm{KO/KI}}$ mice, females *Mmut* $^{\mathrm{WT/KO}}$ were crossed to *Mmut* $^{\mathrm{KI/KI}}$ males as previously described (29). Mouse genotyping was performed on genomic DNA extracted from ear punch biopsies using the primers 5′–GTGGGTGTCAGCACACTTG–3′ (forward) and 5′–CGTATGACTGGGATGCCT–3′ (reverse) for the KI allele and 5′–ACAACTCCTTGTGTAGGTC–3′ (forward) and 5′–CCTTTAGGATGTCATTCTG–3′ (reverse) for the KO allele. All the mice were maintained on a C57BL/6 background. Animal care and experimental procedures were approved by the institutional animal care and use committee at Canton Zurich in accordance with the ethical guidelines at University of Zurich, Switzerland.

Kidney function. The mice were placed overnight in metabolic cages with ad libitum access to food and drinking water; urine was collected on ice, body weight, water intake and diuresis were measured (46). Blood (from sublingual vein) was obtained after anesthesia with ketamine/xylazine or isoflurane. Urea and creatinine were measured using UniCel DxC 800 pro Synchron (Beckman Coulter, Fullerton, CA, USA). The creatinine clearance was calculated using the equation Urine $_{\text{(creatinine)}} \times$ Diuresis/Plasma $_{\text{(creatinine)}}$. Plasma and urinary levels of LCN2 were measured by using an enzyme–linked immunosorbent assay in according to the manufacturer's instructions (EMLCN2, Thermo Fischer Scientific, Waltham, MA).

Picro Sirius Red staining. Picro Sirius Red (ab150681, Abcam) staining was performed on 5 μm thick paraffin sections from kidneys of *Mmut*$^{WT/KI}$ and *Mmut*$^{KO/KI}$. Briefly, the sections were deparaffinised, rehydrated and subsequently incubated with Picro Sirius Red for 1 hour at room temperature. Sections were then washed twice in acidified water (0.05% acetic acid in distilled water), dehydrated and mounted. Images were acquired with a ZEISS AxioScan.Z1 slide scanner (ZEISS).

Primary cultures of mouse proximal tubule cells. The kidneys were harvested from *Mmut* $^{\mathrm{WT/KI}}$ and *Mmut* $^{\mathrm{KI/KO}}$ or from *Mmut* $^{\mathrm{fl/fl}}$ or *Atg7* $^{\mathrm{fl/fl}}$ or *Cox10* $^{\mathrm{fl/fl}}$, and from *Pink1* or *Prkn2* KO and from their corresponding control littermates: one kidney was split transversally, and one half was fixed and processed for immunostaining while the other half was flash-frozen, homogenized by Dounce homogenizer in 1 mL of RIPA buffer that contains protease and phosphatase inhibitors and processed for western blot analysis (46). The contralateral kidney was taken to generate primary cultures of mPTCs (46). Freshly micro–dissected PT segments were seeded onto collagen-coated chamber slides (C7182, Sigma–Aldrich) and/or collagen–coated 6– or 24–well plates (145380 or 142475, Thermo Fisher Scientific), and cultured at 37°C and 5% CO_2 in DMEM/F12 (21041–025, Thermo Fisher Scientific) with 0.5% dialyzed fetal bovine serum (FBS), 15mM HEPES (H0887, Sigma–Aldrich), 0.55mM sodium pyruvate (P2256, Sigma Aldrich), 0.1ml L^{-1} non–essential amino acids (M7145, Sigma Aldrich), hydrocortisone, human EGF, epinephrine, insulin, triiodothyronine, TF, and gentamicin/amphotericin (Single Quots® kit, CC–4127, Lonza), pH 7.40, 325mOsm kg^{-1}. The medium was replaced every 48 h. Confluent monolayers of mPTCs were expanded from the tubular fragments after 6–7 days, characterized by a high endocytic uptake capacity. These cells were negative tested for mycoplasma contamination. All experiments were performed on confluent monolayers grown on chamber slides or 24–well or 6–well tissue culture plates. Where indicated, the mitochondrial damage and mitophagy were triggered by treating primary cultures of proximal tubule cells with Rotenone (5 μM in the fresh culture medium for 24h) Oligomycin A and Antimycin (4 μM and 0.8 μM, respectively, in the fresh culture medium for the indicated times). Afterwards, the cells were processed and analyzed as described below.

Adenovirus transduction. For RNA interference studies, the adenovirus constructs include scrambled short hairpin (Scmb–shRNA) or shRNAs encoding individually mouse *Atg7*. For expression studies, adenovirus constructs used include CMV (control vector, Ad–CMV–GFP, Vector Biolabs) or an individually carrying Cre–recombinase (Ad–Cre–GFP, Vector Biolabs) or carrying human hemagglutinin (HA) tagged–*PINK1*, or carrying mouse green fluorescence protein (GFP)–tagged–*Map1lc3b* or expressing green fluorescent protein (GFP) or the coral–derived protein Keima with the mitochondrially–targeting sequence of the human cytochrome C oxidase subunit VIII (COXVIII). All adenovirus constructs were purchased from Vector Biolabs (University City Science Center, Philadelphia, USA). The cells were plated onto collagen–coated chamber slides or 24–well or 6–well tissue culture plates. Adenovirus transduction was performed 24 h after plating when the cells reached approximately 70–80% confluence. The cells were subsequently incubated for 16 h at 37°C with culture containing the virus at the concentration (0.2125×10^9 PFU mL^{-1}). The cells were afterwards challenged with fresh culture medium every 2 days, cultured for 5 days (unless otherwise specified) and collected for analyses.

Microarray profiles and drug-disease network modelling. The Affymetrix Gene–Chip (HG-U113A) hybridization experiments were performed in triplicate at the Coriell Genotyping and Microarray Center, Coriell Institute for Medical Research, Camden, New Jersey, USA, on total RNA extracted from tubular cells derived from three healthy donors and three *mut^o* MMA patients (Supplementary Table 1; ref. 25). To identify downstream transcriptional effects of loss–of–MMUT function, microarray data were pre–processed using the Bioconductor package Affy52 and normalized with the RMA method (66). Differentially expressed (DE) genes between conditions (MMA patient–derived versus their control cells) were identified using a Bayesian *t*-test (67). For each *P* value, the Benjamin–Hochberg procedure was used to calculate the false discovery rate (FDR) to avoid the problem of multiple testing. Mode of Action by Network Analysis (*MANTRA 2.0*, http://mantra.tigem.it) and Drug Set Enrichment Analysis (*DSEA*, http://dsea.tigem.it) were employed to predict either effective therapeutics or druggable biological processes in MMA patient–derived kidney cells. Taking advantage of the connectivity map data set –which includes transcriptional profiles following treatment of 1309 small molecules across five different cell lines –MANTRA aims to identify compounds transcriptionally similar or different to a disease profile just providing as input the ranked list of genes sorted according to their differential expression. This analysis enabled us to capture the top–ranked small bioactive molecules that transcriptionally reverse the MMA gene signature molecular pathways consistently up– or down–regulated by these set of drugs were then detected using DSEA.

Reverse transcription–quantitative PCR. Total RNA was extracted from mouse tissues using Aurum ™ Total RNA Fatty and Fibrous Tissue Kit (Bio-Rad, Hercules, CA). DNAse I treatment was performed to eliminate genomic DNA contamination. Total RNA was extracted from cell cultures with RNAqueous^R kit (Applied Biosystems, Life Technologies). One μg of RNA was used to perform the reverse transcriptase reaction with iScript ™ cDNA Synthesis Kit (Bio-Rad). Changes in mRNA levels of the target genes were determined by relative RT–qPCR with a CFX96^{TM} Real–Time PCR Detection System (Bio-Rad) using iQ ™ SYBR Green Supermix (Bio–Rad). The analyses were performed in duplicate with 100nM of both sense and anti-sense primers in a final volume of 20 µL using iQ^{TM} SYBR Green Supermix (Bio-Rad). Specific primers were designed using Primer3 (Supplementary Tables 3–5). PCR conditions were 95°C for 3 min followed by 40 cycles of 15 sec at 95°C, 30 sec at 60°C. The PCR products were sequenced with the BigDye terminator kit (Perkin Elmer Applied Biosystems) using ABI3100 capillary sequencer (Perkin Elmer Applied Biosystems). The efficiency of each set of primers was determined by dilution curves (Supplementary Tables 3–5). The program geNorm version 3.4 was applied to characterize the expression stability of the candidate reference genes in kidneys and six reference genes were selected to calculate the normalization factor. The relative changes in targeted genes over *Gapdh* mRNAs were calculated using the $2^{-\Delta\Delta Ct}$ formula. For the absolute quantification of mitochondrial: nuclear DNA ratio, relative values for *ND1* and *ACTB* (in human cells) or for *Nd1* and *Hbb* (in murine cells) were compared within each sample to generate a ratio representing the relative level of mitochondrial DNA per nuclear genome. Primers used for mitochondrial DNA: nuclear DNA ratio in human cells are: *ND1*–Fwd: 5'–ACACTAGCAGAGACCAACCG–3'; and *ND1*–Rev: 5'–GAAGAATAGGGCGAAGGGGC–3'; *ACTB*–Fwd: 5'– TCACCCACACTGTGCCCATCTACGA –3'; *ACTB*–Rev: 5'–CAGCGGAACCGCTCATTGCCAATGG–3'. Primers used for mitochondrial DNA: nuclear DNA ratio in murine cells are: *Nd1*–Fwd: 5'–TAGAACGCAAAATCTTAGGG –3'; and *Nd1*–Rev: 5'– TGCTAGTGTGAGTGATAGGG –3'; *Hbb*–Fwd: 5'–AGGCAGAGGCAGGCAGAT –3'; *Hbb*–Rev: 5'– GGCGGGAGGTTTGAGACA –3'.

Lysosomal–based degradation activity. The detection of lysosomal activity was performed in live in kidney cells by using Bodipy–FL–PepstatinA (P12271, Thermo Fischer Scientific) according to the manufacturer's specifications. The cells were pulsed with 1μM Bodipy–FL–Pepstatin A in Live Cell Imaging medium (A14291DJ, Thermo Fischer Scientific) for 1h at 37°C, fixed and subsequently analyzed by confocal microscopy (46). The numbers of PepA–positive structures per cell were quantified by using the open–source cell image analysis software CellProfiler^{TM} as described below.

Mitochondrial membrane potential measurement. The mitochondrial membrane potential ($\Delta\psi$) was measured in accordance with the manufacturer's specifications. The cells were pulsed with 50 nM Tetramethylrhodamine Methyl Ester Perchlorate (TMRM, T668 Thermo Fisher Scientific) and 1 μM MitoTracker Red FM (Invitrogen, M22426) for 30 min in live cell imaging at 37°C. After washing, the cells were subsequently analysed by confocal microscopy (46) in a chamber heated to 37°C at 5% CO_2. Images were acquired using Leica SP8 confocal laser scanning microscope (Center for Microscopy and Image Analysis, University of Zurich) and the fluorescence intensity was quantified by the open source image processing Fiji (which is just ImageJ, NIH) as described below.

Mitochondrial ROS detection. The cells were pulsed with 2.5 μM MitoSOX Red Mitochondrial Superoxide Indicator (M36008, Thermo Fisher Scientific) and 1 μM MitoTracker Green FM (Invitrogen, M7514) for 10 min in live cell imaging at 37°C. After washing, the cells were subsequently analysed by confocal microscopy in a chamber heated to 37°C at 5% CO_2. Images were acquired using Leica SP8 confocal laser scanning microscope (Center for Microscopy and Image Analysis, University of Zurich) and the fluorescence intensity was quantified by the open source image processing Fiji (which is just ImageJ, NIH) as described below.

mt–Keima mitophagy assay. Cells expressing mt–Keima were treated in presence and in absence of mitochondrial complex I inhibitor Rotenone or electron transport chain inhibitors Oligomycin A and Antimycin as previously described and analysed by confocal microscopy in a chamber heated to 37°C at 5% CO_2. mt–Keima protein was excited both at 458nm (neutral, pseudo–coloured in green) and 561nm (acidic, pseudo–coloured in red) and detected through the same emission filter (570–695nm). Laser power was set up at the lowest output which would enable the clear visualization of the mt–Keima signal, and were individualized for each experimental condition. Imaging settings were maintained with the same parameters for comparison between different experimental conditions. Images were acquired using Leica SP8 confocal laser scanning microscope (Center for Microscopy and Image Analysis, University of Zurich) and the fluorescence intensity was quantified by the open source image processing software Fiji (ImageJ, NIH) as described below.

Extracellular flux analysis and metabolic measurement. Oxygen consumption rate (OCR) in mouse or human kidney tubule cells and in zebrafish larvae was measured with XFp Extracellular Flux Analyzers (Agilent Seahorse Biosciences). The cells were incubated with XF-Base Medium (non-buffered RPMI 1640 containing either 2mM L-glutamine, 1mM sodium pyruvate and 10mM glucose, pH 7.4). Three measurements were assessed under basal conditions and upon addition of 2μM Oligomycin (Oligo), 0.5μM FCCP, and 1μM Rotenone (ROT)/Antimycin–A (ANT). All the reagents were provided by XFp Cell Mito Stress Test Kit (Agilent Seahorse biosciences). OCR measurements were normalized to the numbers of cells (TC10^{TM} automated cell counter, Bio-Rad). The zebrafish larvae were anesthetized with 125mg/L of MS222 and placed individually into the wells of a 24–wells microplate, filled with 500 mL of E3 media (pH 7.4) containing anesthesia solution MS222 and covered by capture screens. After incubation in a non–CO_2 incubator at 28.5°C for 20 min, the metabolic measurements were analyzed in live. One measurement cycle consisted of a brief wait period to acclimate the plate, 2 min mix, 1 min wait, and 2 min data acquisition. Eight measurement cycles were performed to establish the average value.

Detection of PtdIns–3P. PtdIns–3P staining was performed according to previously established protocols (68). Briefly, kidney cells were fixed for 15 min in 2% PFA and permeabilized for 5 min with 20 µM digitonin in buffer A (150 mM NaCl, 20 mM Hepes, pH 7.4, and 2 mM EDTA). Cells were subsequently incubated for 45 min with buffer A supplemented with 5% goat serum and mCherry–2×FYVE PtdIns–3P–binding domain and immunostained with the anti–RFP antibody to amplify the detection of mCherry probe. The cells were washed and post–fixed with 2% PFA for 5 min, and analyzed by confocal microscopy and quantified by using the open–source cell image analysis software CellProfiler^{TM} as described below.

Immunofluorescence and confocal microscopy. Fresh mouse kidneys were fixed by perfusion with 50–60 mL of 4% paraformaldehyde in PBS (158127, Sigma–Aldrich), dehydrated and embedded in paraffin at 58C. Paraffin blocks were sectioned into consecutive 5µm–thick slices with a Leica RM2255 rotary microtome (Thermo–Fisher Scientific) on Superfrost Plus glass slides (Thermo-Fisher Scientific). Before staining, slides were deparaffinized in changes of CitriSolv (22–143–975, Thermo–Fisher Scientific) and 70% isopropanol. Antigen retrieval was accomplished by heating the slides at 95°C for 10 min in 10 mM sodium citrate buffer (pH 6.0). The slides were quenched with 50 mM NH_4Cl, blocked with 3% BSA in PBS Ca/Mg (D1283, Sigma–Aldrich) for 30 min and stained with primary antibodies specific for Mutase, UMOD, AQP2, CD3, Ly6G diluted in blocking buffer overnight at 4°C. After two washes in 0.1% Tween 20 (v/v in PBS), the slides were incubated with the corresponding fluorophore–conjugated Alexa secondary antibodies (Invitrogen) diluted in blocking buffer at room temperature for 1h and counterstained with 1µg Biotinylated Lotus Tetragonolobus Lectin (LTL; B–1325 Vector Laboratories) and 1µM 4',6-Diamino-2-phenylindole dihydrochloride (DAPI; D1306, Thermo Fischer Scientific). The slides were mounted in Prolong Gold Anti–fade reagent (P36930, Thermo Fisher Scientific) and analyzed by confocal microscopy. The images were acquired using Leica SP8 confocal laser scanning microscope (Center for Microscopy and Image Analysis, University of Zurich) equipped with a Leica APO 63x NA 1.4 oil immersion objective at a definition of 1,024 x 1,024 pixels (average of eight or sixteen scans), adjusting the pinhole diameter to 1 Airy unit for each emission channel to have all of the intensity values between 1 and 254 (linear range). The micrographs were processed with Adobe Photoshop (version CS5, Adobe System Inc., San Jose, USA) software. Quantitative image analysis was performed by selecting randomly ~5–10 visual fields per each slide that included at least 3–5 PTs (LTL–positive), using the same setting parameters (*i.e.*, pinhole, laser power, and offset gain and detector amplification below pixel saturation). The numbers of CD3 or Ly6G positive structures per field were manually counted.

The cells were fixed for 10 min with 4% PFA in PBS, quenched with 50 mM NH_4Cl and permeabilized for 20 min in blocking buffer solution containing 0.1% Triton X-100 and 0.5% BSA dissolved in PBS. Subsequently, cells were incubated overnight with the appropriate primary antibodies at 4°C. After repeated washing with PBS, the slides were incubated for 45 min with the suitable fluorophore-conjugated Alexa secondary antibodies (Invitrogen), counterstained with 1µM DAPI for 5 min, mounted with the Prolong Gold Anti-fade reagent and analyzed by a Leica SP8 confocal laser scanning microscope (Center for Microscopy and Image Analysis, University of Zurich) using the settings described above. Quantitative image analysis was performed by selecting randomly 5 visual fields pooled from biological triplicates, with each field including at least 10–15 cells, using the same setting parameters (i.e. pinhole, laser power, and offset gain and detector amplification below pixel saturation). The quantitative cell image analyses of mitochondrial morphology (69) were performed using mitochondrial morphology plug in of the open–source cell image software Fiji. The quantitative cell image of mitochondrial membrane potential, production of mitochondrial ROS and mt–Keima red/green signal, the analyses of fluorescence were performed following background subtraction over cellular regions of interests (ROIs) and quantified using the multi–measure plug–in of Fiji. Mean fluorescence intensity ratios of selected ROIs matching cells were determined and expressed as TMRM/MitoTracker, MitoSOX and mt–Keima red/green ratios, respectively. The quantitative cell image analyses of subcellular structures were determined by using the open–source cell image analysis software CellProfiler^{TM} (70). In particular, the specific module "Measure–Object–Intensity–Distribution" was used to score the number of ATP5B, PtdIns–3P, ATG13, WIPI2, Parkin, LC3, and PMP70 or Pep–A^+ structures. The pipeline "Cell/particle counting and scoring the percentage of stained objects" was used to score either the fractions of Lamp1/$LC3^+$ or mito–GFP/$Parkin^+$ structures.

Electron microscopy. Animal tissue samples and cultured cells were fixed in 2.5 % glutaraldehyde in 100 mM sodium cacodylate, at pH=7.43 for 1 h at room temperature, post–fixed in 1% osmium tetroxide, 1.5% potassium ferrocyanide in 0.1 M cacodylate for 1 hour on ice. After washing in distilled water, the samples were stained with 0.5% uranyl acetate in water overnight at 4°C. The samples were finally dehydrated in a graded ethanol series, embedded in Epon 812 and finally cured at 60°C for 48 hours. Ultrathin (70–90nm) sections were cut using a Leica Ultracut UCT ultramicrotome and collected on copper grids, stained with uranyl acetate and Sato's lead citrate before been imaged with a FEI Talos 120kV transmission electron microscope (FEI Company, Netherlands) and images were acquired by a 4k×4K Ceta CMOS camera. Autophagic vacuoles (AVs) were identified and categorized as autophagosomes or autolysosomes according to conventional criteria (31). Autophagosome should have a double membrane (completely or partially visible), absence of ribosomes in the outer membrane, luminal density comparable to the surrounding cytosol and identifiable organelles or regions of organelles in their lumen; autophagolysosomes should have single membrane, luminal density lower than surrounding cytosol with luminal material partially recognizable as specific organelles or heterogeneous amorphous material. Primary and secondary lysosomes were excluded from the quantification. The term autophagic vacuole was used for identifying both autophagosomes and autophagolysosomes structures. At least 20 random selected cellular profiles were acquired and analysed using ImageJ software. For the quantification of content of AVs, the percentage of cytosolic area occupied by autophagic vacuoles was calculated. For the quantification of the morphology of mitochondrial network, the cross–section area (A) and perimeter (P) derived from each mitochondrion was measured and circularity (c) was calculated according to the formula circularity = 4π (area/perimeter^2).

Correlative light electron microscopy. The cells were grown on finder grids and prepared for confocal microscopy analyses. Z–stacks of cells of interest were taken with the PerkinElmer Ultra View ERS confocal microscope. The coordinates of the cells on the finder grid were determined by bright–field microscopy. Cells were fixed in 1% glutaraldehyde in 0.1 M cacodylate buffer (Sigma) and post–fixed with 1.5% potassium ferricyanide, 1% OsO4 in 0.1M cacodylate buffer. Cells were stained overnight with 0.5% uranyl acetate, dehydrated in ethanol, and embedded in epon. After baking for 48 h at 60 °C, the resin was released from the glass coverslip by temperature shock in liquid nitrogen. Serial sections (70–90 nm) were collected on carbon–coated formvar slot grids and imaged with a FEI Talos 120kV transmission electron microscope (FEI Company, Netherlands) and images were acquired by a 4k×4K Ceta CMOS camera. LM and EM images were aligned using Ec–CLEM Icy plugin and overlaid using Photoshop software.

Soluble and insoluble fractionation. The cells were lysed in buffer containing 50 mM Tris–HCl, pH 7.5, 150mM NaCl, 0.1% SDS, 1% Triton X–100, 1% sodium deoxycholate supplemented with protease (1836153001, Roche) and phosphatase inhibitors (04906845001, PhosSTOP Sigma), and centrifuged at 16,000 *g* at 4°C for 20 min, to collect the soluble fraction (supernatant). The pellet was suspended in a buffer containing 4% SDS and 20 mM HEPES, pH 7.5, protease and phosphatase inhibitors, and further centrifuged at 18,000 *g* at room temperature for 10 min, to collect the insoluble fraction (supernatant). The samples were boiled at 95 °C for 5 min and analyzed by western blotting.

Immunoblotting. Proteins were extracted from mouse tissues or cultured cells, lysed using a buffer which contains protease (1836153001, Roche) and phosphatase inhibitors (04906845001, PhosSTOP Sigma), followed by sonication and centrifugation at 16,000xg for 10 min at 4°C. The samples were thawed on ice, normalized for protein (20μg/lane), dissolved in Laemmli sample buffer and separated by SDS–PAGE under reducing conditions. After blotting onto PVDF and blocking with 5% non–fat milk (1706404, Bio–Rad Laboratories), the membranes were incubated overnight at 4°C with primary antibody, washed, incubated with peroxidase–labeled secondary antibody, and visualized with enhanced chemiluminescence (WBKLS0050, Millipore, Life technologies). Signal intensity was assessed by measuring the relative density of each band normalized to β-actin, GAPDH or α-tubulin with ImageJ software.

Cell viability assay. Cell viability was determined by the Cell Counting Kit–8 (CCK–8) assay (Dojindo, Rockville, USA). Cells were seeded at a density of 5000 cells/well of 96 well plates and grown until they reached 90% confluence. The cell medium was replaced by water–soluble tetrazolium salt solution and incubated for 30 min at

37°C according to the manufacturer’s protocol. The amount of formazan dye generated by dehydrogenase activity was measured at 450 nm in a TECAN infinite 200 reader (Männedorf, Switzerland) in according to the manufacturer's specifications.

Cell proliferation. To measure cell proliferation, the cells were seeded in 24–well plates at a density of 2.0 × 104 cells per well. The cells were cultured for 2 days and cell medium was renewed daily. Where indicated, the cells were treated with Rotenone (24h at the indicated concentrations), then trypsinized every 24 h and quantified using the Countess automated cell counter TC10 automated cell counter (BIO-RAD). The time–course experiments were repeated three times.

Data analysis and Statistics. The plotted data were presented as mean ± standard error of the mean (SEM). Statistical comparisons between experimental groups were determined by using one–way analysis of variance (ANOVA) followed by Bonferroni or Dunnet *post hoc* test or Kruskal Wallis followed by Dunn’s multiple comparison test, when appropriate. When only two groups were compared, two tailed Student’s *t*–tests or nonparametric Mann Whitney *t* tests were used as appropriate. Statistical comparisons between untreated and MitoQ treated–*mmut* zebrafish in Figure 9c was determined by *Chi*–square goodness of fit test. The sample size and reproducibility for each figure were denoted in figure legends. Experiments in Figure 9c were performed once. All of the other experiments reported here were independently performed two to three times or more as indicated in the legends. The investigators were not blinded to allocation during the experiments and outcome assessment. Graph Pad Prism software v. 7.0a (GraphPad software) was used for all statistical analyses and the *p* values are indicated in each figure legend along with the statistical tests.

Data Availability. The Source data underlying figs 1a–b, 1d, 1e, 1g, 2a–g, 3a–g, 4a–f, 5a–f, 6b–h, 7b–h, 8b–g, 9a–d, and Supplementary Figs 1a–c, 1f, 1i, 2a–e, 3a, 3c–j, 3l–m, 4c, 4e, 4g, 5b–f, 6a–b,7b, 7d–e, 7g–h, 8c–j, 9d–e, 10b, 11a–d are provided in the Source Data file. Microarray data that support the findings of this study are provided in the Supplementary Table 2, and the latter have been deposited in NCBI Gene Expression Omnibus (GEO) under the accession number GSE120683 [https://www.ncbi.nlm.nih.gov/geo/query/acc.cgi?acc=GSE120683]. Additional data supporting the findings of this study are available from corresponding author on reasonable request.

ACKNOWLEDGEMENTS

We thank Gery Barmettler, Nadine Naegele and Benjamin Klormann for technical assistance, and the Center for Microscopy and Image Analysis at the University of Zurich for providing equipment and confocal and electron microscopy assistance as well as the Bioinformatics core Facility of the Telethon Institute of Genetics and Medicine for help with bioinformatics analysis. We also thank Claire Boulange, Manuja Kaluarachchi, Elisabetta Biglieri and Lubor Borsig, Luca Scorrano, Elena Ziviani, Leonardo Salviati and Francesco Emma for their advice and fruitful discussions. We acknowledge Euro–BioImaging (www.eurobioimaging.eu) for providing access to imaging technologies and services via the Italian Node (ALEMBIC, Milan–Italy). We are grateful to Fonds National de la Recherche Scientifique and the Fonds de la Recherche Scientifique Médicale (Brussels, Belgium), the European Community's Seventh Framework Programme (FP7/2007-2013) under grant agreement number 305608 (EURenOmics) and under the grant agreement number 608847 (IKPP2), the Cystinosis Research Foundation (Irvine, CA, USA), the Swiss National Science Foundation (project grant 31003A–169850), the clinical research priority programs (KFSP) radiz (Rare Disease Initiative Zurich) and Molecular Imaging Network Zurich (MINZ) at the University of Zurich, the Swiss National Centre of Competence in Research (NCCR) Kidney Control of Homeostasis (Kidney.CH) for support and Junior Grant (to A.L.). A.S. was supported by grants from Swiss National Science Foundation (project grant 310030_146490) and the Wolfermann–Nägeli Shiftung.

AUTHOR CONTRIBUTIONS

A.L. and O.D. conceptualize and supervised the study. A.L., A.S., M.B. and O.D. designed the experiments. A.L., A.S., M.B. and D.N. performed experiments and analyzed the data. B.P.F. helped with primary cell cultures and confocal microscopy experiments. M.F., D.C. and D.D.B. generated the drug−disease network modeling and analyzed the data. Z.C generated the *mmut* knockout zebrafish model, performed zebrafish experiments and analyzed the data. N.T performed seahorse metabolic flux measurements and analyzed the data. H.D. performed RNA interference and gene expression experiments and molecular biology studies, and analysed the data. A.C. performed the methylmalonyl acid measurements and analyzed the data. F.D.C. provided patient sample biopsy and performed electron microscopy analysis. A.R. performed transmission electron and CLEM microscopy studies, and analyzed the data. S.K. provided the control and patient–derived kidney cells. C.T.M. and F.D. provided the floxed *Cox10* mice. P.F. and M.R.B. provided *Mmut*$^{\mathrm{KO/KI}}$ mice and contributed to the interpretation and analysis of the data. A.L. generated Figure 10 and Supplementary Figure 8b. A.L. and M.F. generated Supplementary Figure 12b. A.L. and O.D. wrote the paper with inputs and comments from all of authors.

Conflict of interest statement: The authors declare no competing financial interests

REFERENCES

1. Mc Bride, H.M., Neuspiel, M., and Wasiak, S. Mitochondria: More than just a powerhouse. *Current Biology* **16**, 1484–1498 (2006).

2. Nunnari, J., and Suomalainen, A. Mitochondria: in sickness and in health. *Cell* **148**, 1145–1149 (2012).

3. McWilliams, T.G., and Muqit, M.M.K.PINK1 and Parkin: emerging themes in mitochondrial homeostasis. *Current Opinion in Cell Biology* **45**, 83–91 (2017).

4. Johannsen, D.L., and Ravussin, E. The role of mitochondria in health and disease. *Current Opinion in Pharmacology* **9**, 780–786 (2009).

5. Gorman, G.S., et al. Mitochondrial diseases. *Nature Reviews Disease Primers* **2**, 16080 (2016).

6. Koopman, W.J.H., Willems, P.H.G.M., and Smeitink, J.A.M. Monogenic mitochondrial disorders. *New England Journal of Medicine* **366**, 1132–1141 (2012).

7. Oberholzer, V.G., Levin, B., Burgess, E.A. and Young, W.F. Methylmalonic aciduria. An inborn error of metabolism leading to chronic metabolic acidosis. *Archives of Disease in Childhood* **42**, 492-504 (1967).

8. Chace, D.H., Di Perna, J.C., Kalas, T.A., Johnson, R.W., and Naylor, E.W. Rapid diagnosis of methylmalonic and propionic acidemias: quantitative tandem mass spectrometric analysis of propionylcarnitine in filter-paper blood specimens obtained from newborns. *Clinical Chemistry* **47**, 2040–2044 (2001).

9. Fenton, W.A., Gravel, R.A., and Rosenblatt, D.S. Disorders of propionate and methylmalonate metabolism. The Metabolic and Molecular Bases of Inherited Disease, C.R. Scriver, A.L. Beaudet, W.S. Sly, and D. Valle, eds. (McGraw-Hill), pp. 2165–2193 (2001).

10. Manoli, I., et al. Targeting proximal tubule mitochondrial dysfunction attenuates the renal disease of methylmalonic acidemia. *PNAS* **110**, 13552–13557 (2013).

11. Chandler, R.J., et al. Mitochondrial dysfunction in *mut* methylmalonic acidemia. *FASEB Journal* **23**, 1252–1261 (2009).

12. Hörster, F., et al. Long–term outcome in methylmalonic acidurias is influenced by the underlying defect (mut0, mut–, cblA, cblB). *Pediatr Research* **62**, 225–23011 (2007).

13. Baumgartner, M.R., et al. Proposed guidelines for the diagnosis and management of methylmalonic and propionic acidemia. *Orphanet Journal of Rare Diseases* **9**, 130 (2014)

14. Fraser, J.L., and Venditti, C.P. Methylmalonic and propionic acidemias: clinical management update. *Current Opinion in Pediatrics **28***, 682–693 (2016).

15. Forbes, J.M. Mitochondria–power players in kidney function? *Trends in Endocrinology & Metabolism* **27**, 441–442 (2016).

16. Emma, F., Montini, G., Parikh, S. M., and Salviati, L. Mitochondrial dysfunction in inherited renal disease and acute kidney injury. *Nature Reviews Nephrology* **12**, 267–280 (2016).

17. Martín–Hernández, E., et al. Renal pathology in children with mitochondrial diseases. *Pediatric Nephrology* **20**, 1299–1305 (2005).

18. Jesinkey, S. R. et al. Formoterol restores mitochondrial and renal function after ischemia-reperfusion injury. *Journal American Society of Nephrology* **25**, 1157–1162 (2014).

19. Chacko, B. K., et al. Prevention of diabetic nephropathy in Ins2 (+/-)(AkitaJ) mice by the mitochondria-targeted therapy MitoQ. *Biochemical Journal* **432**, 9–19 (2010).

20. Pickles, S., Vigié, P., and Youle, R.J. Mitophagy and quality control mechanisms in mitochondrial maintenance. *Current Biology* **28**, R170–R185 (2018).

21. Eiyama, A., and Okamoto, K. (2015). PINK1/Parkin–mediated mitophagy in mammalian cells. *Current Opinion in Cell Biology* **33**, 95–101 (2015).

22. Lazarou, M., Sliter, D.A., Kane, L.A., Sarraf, S.A., Wang, C., Burman, J.L., Sideris, D.P, Fogel, A.I. and Youle, R.J. The ubiquitin kinase PINK1 recruits autophagy receptors to induce mitophagy. *Nature* **524**, 309–314 (2015).

23. Bhargava, P., and Schnellmann, R.G. Mitochondrial energetics in the kidney. *Nature Reviews Nephrology* **13**, 629–646 (2017).

24. Tang, C. et al. PINK1-PRKN/PARK2 pathway of mitophagy is activated to protect against renal ischemia-reperfusion injury. *Autophagy* **5**, 880–897 (2017).

25. Ruppert, T., Schumann, A., Gröne, H.J., Okun, J.G., Kölker, S., Morath, M.A., Sauer, S.W. Molecular and biochemical alterations in tubular epithelial cells of patients with isolated methylmalonic aciduria. *Human Molecular Genetics* **24**, 7049–59 (2015).

26. Manoli, I., et al. FGF21 underlies a hormetic response to metabolic stress in methylmalonic acidemia. *JCI Insight* **3**: e124351 (2018).

27. Mishra J, et al. Identification of neutrophil gelatinase-associated lipocalin as

a novel early urinary biomarker for ischemic renal injury. *Journal American Society of Nephrology* **14**, 2534–2543 (2003).

28. Luciani, A., et al. Impaired lysosomal function underlies monoclonal light chain–associated renal Fanconi syndrome. *Journal American Society of Nephrology* **27**, 2049-2061(2016)

29. Forny, P. et al. Novel mouse models of methylmalonic aciduria recapitulate phenotypic traits with a genetic dosage effect. *Journal of Biology Chemistry* **291**, 20563–20573 (2016).

30. Anding, A.L., and Baehrecke, E.H. Cleaning house: Selective autophagy of organelles. *Development Cell* **41**, 10–22 (2017).

31. Klionsky, D. J. et al. Guidelines for the use and interpretation of assays for monitoring autophagy (3rd edition). *Autophagy* **12**, 12–22 (2016).

32. Carroll, B., et al. Oxidation of SQSTM1/p62 mediates the link between redox state and protein homeostasis. *Nature Communications* **9**, 256 (2018).

33. Galluzzi, L., Yamazaki, T., and Kroemer, G. Linking cellular stress to systemic homeostasis. *Nature Reviews Molecular Cell Biology* **19**, 731–745 (2018).

34. Pasquier, B. SAR405, a PIK3C3/Vps34 inhibitor that prevents autophagy and synergizes with MTOR inhibition in tumour cells. *Autophagy* **11**, 725–726 (2015).

35. Katayama, H., Kogure, T., Mizushima, N., Yoshimori, T. and Miyawaki, A. A sensitive and quantitative technique for detecting autophagic events based on lysosomal delivery. *Chemical Biology* **18**, 1042–1052 (2011).

36. Komatsu, M. et al. Impairment of starvation–induced and constitutive autophagy in Atg7–deficient mice. *Journal of Cell Biology* **169**, 425–434 (2005).

37. McWilliams, T.G., et al. Basal mitophagy occurs independently of PINK1in mouse tissues of high metabolic demand. *Cell Metabolism* **27**, 439–449 (2018).

38. Diaz, F., Thomas, C.K., Garcia, S., Hernandez, D., Moraes, C.T. Mice lacking COX10 in skeletal muscle recapitulate the phenotype of progressive mitochondrial myopathies associated with cytochrome c oxidase deficiency. *Human Molecular Genetics* **14**, 2737–2748 (2015).

39. Diaz, F., Fukui, H., Garcia, S., Moraes, C.T. Cytochrome c oxidase is required for the assembly/stability of respiratory complex I in mouse fibroblasts. *Molecular and Cell Bioloy* **26**, 4872–4881 (2006).

40. Palikaras, K., Lionaki, E., and Tavernarakis, N. Mechanisms of mitophagy in cellular homeostasis, physiology and pathology. *Nature Cell Biology* **20**, 1013–1022 (2018).

41. Bingol, B., et al. The mitochondrial deubiquitinase USP30 opposes parkin-mediated mitophagy. *Nature* **510**, 370–375 (2014).

42. Cummins, N., Tweedie, A., Zuryn, S., Bertran–Gonzalez, J. and Götz, J. Disease–associated tau impairs mitophagy by inhibiting Parkin translocation to mitochondria. *EMBO Journal* **38**, (2019).

43. Rebacle, N., et al. New in vitro model derived from brain–specific Mut-/- mice confirms cerebral ammonium accumulation in methylmalonic aciduria. *Mol Genetics and Metabolism* **124**, 266–277 (2018).

44. Carrella, D., Napolitano, F., Rispoli, R., Miglietta, M., Carissimo, A., Cutillo, L., Sirci, F., Gregoretti, F. and di Bernardo, D. Mantra 2.0: an online collaborative resource for drug mode of action and repurposing by network analysis. *Bioinformatics* **30**, 1787–1788 (2014).

45. Napolitano, F., Sirci, F., Carrella, D. and di Bernardo, D. Drug–set enrichment analysis: a novel tool to investigate drug mode of action. *Bioinformatics* **32**, 235–241 (2016).

46. Festa, B. P., et al. Impaired autophagy bridges lysosome storage disease and epithelial dysfunction in the kidney. *Nature Communications* **9**, 161 (2018).

47. Wallace, D.C, and Fan, W. Energetics, epigenetics, mitochondrial genetics. *Mitochondrion* **10**, 12–31 (2010).

48. Chandel, N.S. Evolution of mitochondria as signaling organelles. *Cell Metabolism* **22**, 204–206 (2015).

49. Pagliarini, D. J., and Rutter, J. Hallmarks of a new era in mitochondrial biochemistry. *Genes and Development* **27**, 2615–2627 (2013).

50. Suomalainen, A., and Battersby, B. J. Mitochondrial diseases: the contribution of organelle stress response to pathology. *Nature Reviews Molecular Cell Biology* **19**, 77-92 (2018).

51. Fakruddin, M. et al. Defective mitochondrial tRNA taurine modification activates global proteostress and leads to mitochondrial disease. *Cell Reports* **22**, 482–496 (2018).

52. Anzenberger, U., et al. Elucidation of megalin/LRP2-dependent endocytic transport processes in the larval zebrafish pronephros. *Journal of Cell Science* **119**, 2127–2137 (2006).

53. Kur, E., et al. Loss of Lrp2 in zebrafish disrupts pronephric tubular clearance but not forebrain development. *Developmental Dynamics* **240**, 1567–1577 (2011).

54. Oltrabella, F., et al. The Lowe syndrome protein OCRL1 is required for endocytosis in the zebrafish pronephric tubule. *PLOS Genetics* **11**, e1005058 (2015).

55. Elmonem, M.A., et al. Cystinosis (ctns) zebrafish mutant shows pronephric glomerular and tubular dysfunction. *Scientific Reports* **7**, 42583 (2017).

56. MacRoe, C.A., and Peterson R.T. Zebrafish as tools for drug discovery. *Nature Reviews Drug Discovery* **14**, 721–730, 2015.

57. Wang, Y., et al. Lipocalin 2 is an inflammatory marker closely associated with obesity, insulin resistance, and hyperglycaemia in humans. *Clinical Chemistry* **53**, 34-41 (2017).

58. Mizushima, N., Levine, B., Cuervo, A.M., and Klionsky, D.J. Autophagy fights disease through cellular self–digestion. *Nature* **451**, 1069–1075 (2008).

59. Fang, E. F., Scheibye–Knudsen, M., Brace, L.E., Kassahun, H., SenGupta, T., Nilsen, H., Mitchell, J. R., Croteau, D.L., and Bohr, V. L. Defective mitophagy in XPA via PARP–1 hyperactivation and NAD^+/SIRT1 reduction. *Cell* **157**, 882–896 (2014).

60. Nguyen, T. N., Padman, B.S., and Lazarou, M. Deciphering the molecular signals of PINK1/Parkin mitophagy. *Trends in Cell Biology* **26**, 733–744 (2016).

61. McWilliams, T.G. and Muqit, M.M. PINK1 and Parkin: emerging themes in mitochondrial homeostasis. *Current Opinion in Cell Biology* **45**, 83–91 (2017).

62. Exner, N., Lutz, A.K., Haass, C. and Winklhofer, K.F. Mitochondrial dysfunction in Parkinson's disease: molecular mechanisms and pathophysiological consequences. *EMBO Journal* **31**:3038–3062 (2012).

63. Jian, F., et al. Sam50 regulates PINK1–Parkin mediated mitophagy by controlling PINK1 stability and mitochondrial morphology. *Cell Reports* **23**, 2989–3005 (2018).

64. Oh, C. K. et al. S–Nitrosylation of PINK1 attenuates PINK1/Parkin dependent mitophagy in hiPSC-based Parkinson's disease models. *Cell Reports* **21**, 2171–2182 (2017).

65. Wang, W., Karamanlidis, G., and Tian, R. Novel targets for mitochondrial medicine. *Science Translational Medicine* **8**, 32rv3 (2016).

66. Parrish, S.R, and Spencer III, H.J. Effect of normalization on significance testing for oligonucleotide microarrays. *Journal of Biopharmaceutical Statics* **4**, 249–264 (2004).

67. Baldi, P., and Long, A. D. A Bayesian framework for the analysis of microarray expression data: regularized t **-**test and statistical inferences of gene changes. *Bioinformatics* **171**, 509–519 (2001).

68. Festa, B.P., et al. OCRL Deficiency Impairs Endolysosomal Function in a Humanized Mouse Model for Lowe Syndrome and Dent Disease. *Human Molecular Genetics* **28**, 1931–1946 (2018).

69. Dagda, R.K., Cherra, S.J. 3rd, Kulich, S.M., Tandon, A., Park, D. and Chu, C.T. Loss of PINK1 function promotes mitophagy through effects on oxidative stress and mitochondrial fission. *Journal of Biology Chemistry* **284**, 13843–13855 (2009).

70. Carpenter, A. E. et al. Cell Profiler: image analysis software for identifying and quantifying cell phenotypes. *Genome Biology* **7**, R100 (2006).

Figure 1

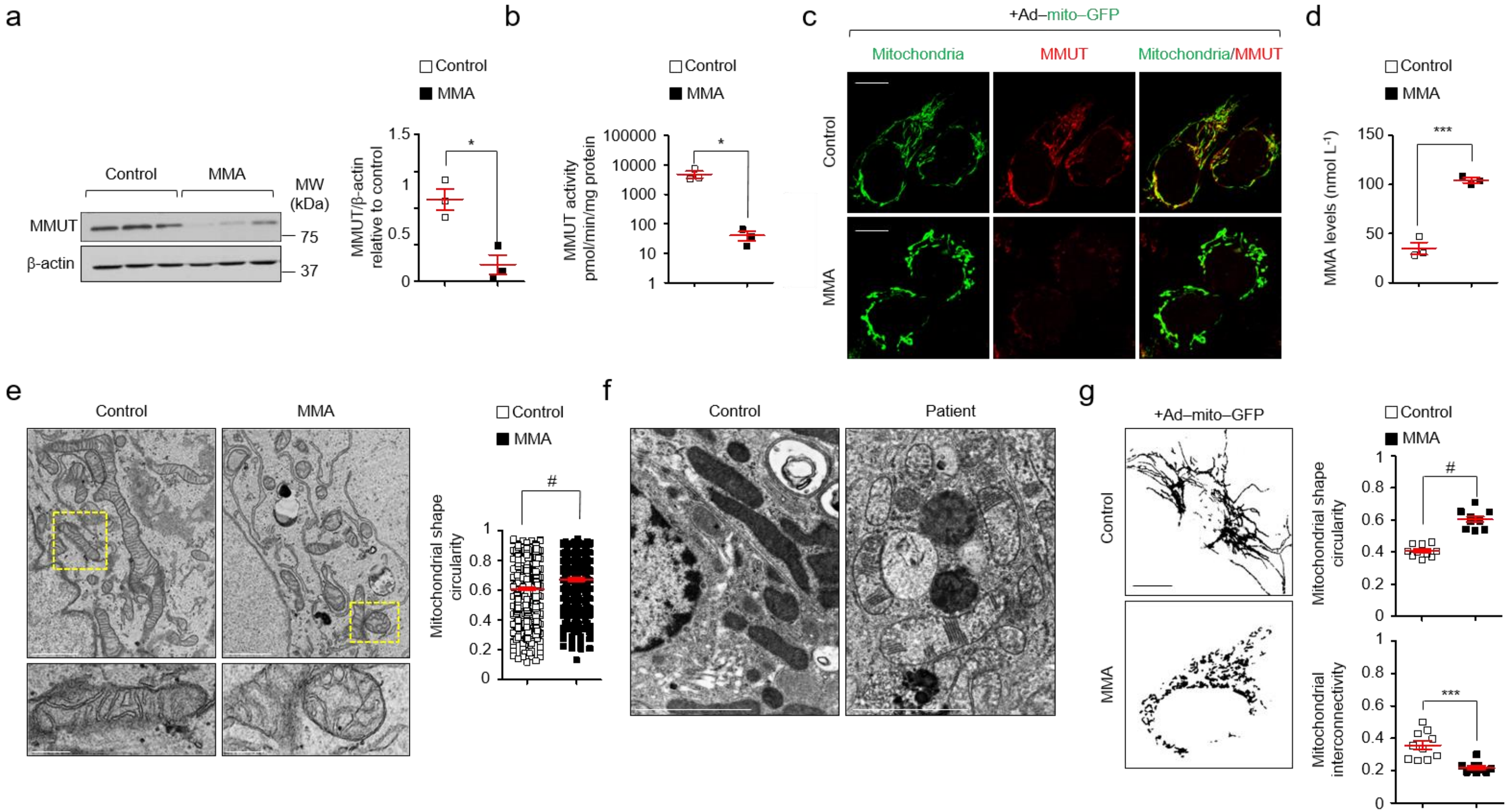

Figure 1 Abnormal mitochondrial network in MMA kidney cells. (**a**) Immunoblotting and quantification of MMUT protein levels and (**b**) MMUT enzyme activity in control and MMA kidney cells, *n*=3 independent experiments. β–actin used as loading control. (**c** and **g**) Cells were transduced with adenoviral particles bearing the mitochondrially–targeted green fluorescent protein (Ad–mito–GFP, green). (**c**) After 24h post–transduction, the cells were immunostained for MMUT (red) and imaged by confocal fluorescence microscopy. Yellow indicates the colocalization. (**d**) Quantification of methylmalonic acid (MMA) levels by liquid chromatography tandem mass spectrometry (LC–MS/MS, *n*=3 independent experiments). (**e**) Representative electron micrographs and quantification of the shape (expressed as circularity) of the mitochondrial network in control and MMA kidney cells; *n*=527 mitochondria pooled from 24 control cells and *n*=310 mitochondria pooled from 20 MMA cells. The experiments were performed twice. Dotted yellow squares contain images at higher magnification. (**f**) Representative electron micrographs showing the mitochondrial network in kidney biopsies from an individual healthy control subject and a patient with MMA. (**g**) Representative inverted confocal micrographs (left) and quantification of shape (expressed as circularity, top right) or interconnectivity (bottom right) of the mitochondrial network in control and MMA kidney cells; each point representing the average values for circularity or interconnectivity in a cell, *n*=10 cells per each condition pooled from two independent experiments. Plots represent mean ± SEM. Two tailed Student's *t* test, **P*<0.05, ****P*<0.001 and $^{\#}$*P*<0.0001 relative to control cells. Scale bars are 10 μm in **c** and **g**, and 1μm (top panel) and 250nm (bottom panel) in **e** and 2 μm in **f.** Unprocessed scans of original blots are shown in Supplementary Fig. 13. Source data are provided as a Source Data file.

Figure 2

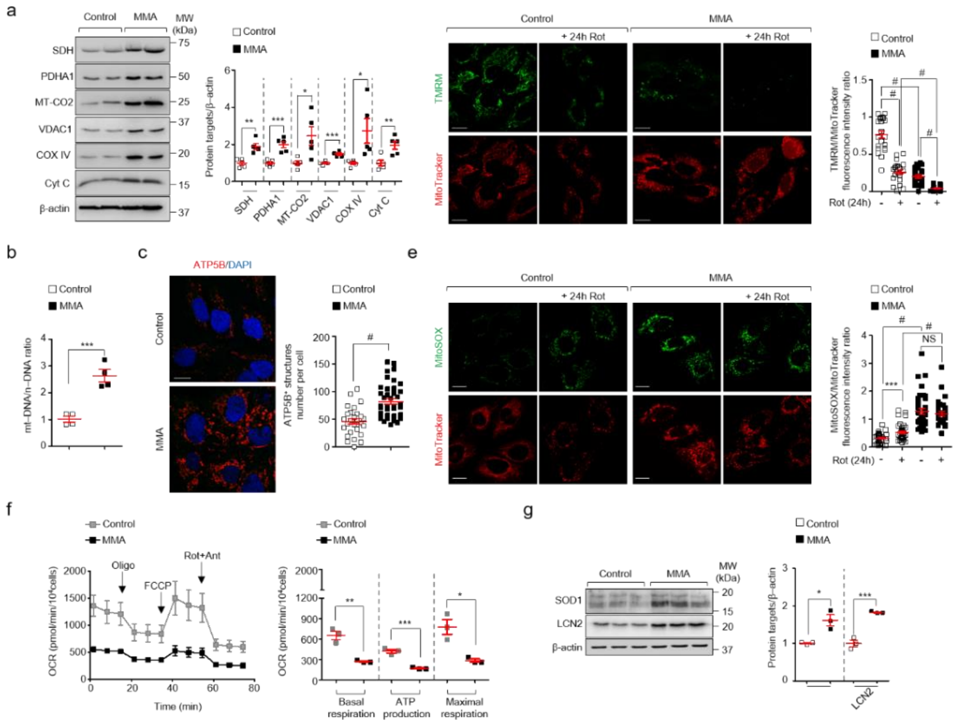

Figure 2. Mitochondrial dysfunctions in MMA kidney cells. (**a**) Representative immunoblotting and quantification of the indicated mitochondrial proteins; *n*=5 independent experiments. (**b**) The ratio between mitochondrial DNA (*ND1*) and nuclear DNA (*ACTB*) was analysed by quantitative PCR; *n*=4 independent experiments. (**c**) Cells were immunostained for ATP5B (red) and imaged by confocal microscopy. Representative confocal micrographs and quantification of numbers of ATP5B$^+$ structures per cell (each point representing the number of ATP5B$^+$ structures in a cell; *n*=27 control cells and *n*=40 MMA cells pooled from three independent experiments;). Nuclei counterstained with DAPI (blue). (**d–e**) Cells were exposed to mitochondrial complex I inhibitor Rotenone (Rot, 5 µM). After 24 h of treatment, the cells were loaded (**d**) with tetramethylrhodamine methyl ester (TMRM; green; mitochondrial membrane potential fluorescent probe, 50 nM for 30 min at 37°C) and MitoTracker (red; fluorescent probe that localizes to mitochondria; 1□M for 30 min at 37°C) or (**e**) with MitoSOX (green; mitochondrial ROS indicator, 2.5 µM for 25 min at 37°C) and MitoTracker (red), and analysed by confocal microscopy. Representative confocal micrographs and quantification of (**d**) membrane potential and (**e**) mitochondrial ROS (both calculated as ratios between TMRM and MitoTracker or MitoSOX and MitoTracker fluorescence intensities, with each point representing the average fluorescence intensity ratio in a cell). TMRM/MitoTracker: *n*=21 untreated and Rot–treated control cells, *n*=22 untreated MMA cells and *n*=18 Rot–treated MMA cells. MitoSOX/MitoTracker: *n*=31 untreated control cells and *n*= 40 Rot–treated control cells *n*=36 untreated MMA cells and *n*= 31 Rot–treated MMA cells. Data were pooled from three independent experiments. (**f**) Oxygen consumption rate (OCR) and individual parameters for basal respiration, ATP production and maximal respiration. OCRs were measured at baseline and upon the sequential addition of Oligomycin (Oligo, 1 µM), FCCP (0.5 µM) and Rotenone (Rot; 1 µM) + Antimycin A (Ant; 1 µM), *n*=3 independent experiments. (**g**) Immunoblotting and quantification of the indicated proteins; *n*=3 independent experiments. Plots represent mean ± SEM. Two tailed Student's *t* test, *$P<0.05$, **$P<0.01$, ***$P<0.001$ and $^{\#}P<0.0001$ relative to untreated control or to Rot–treated control cells or to untreated MMA cells. β–actin used as loading control in **a** and **b**. Scale bars, 10 µM. NS: non–significant. Source data are provided as a Source Data file.

Figure 3

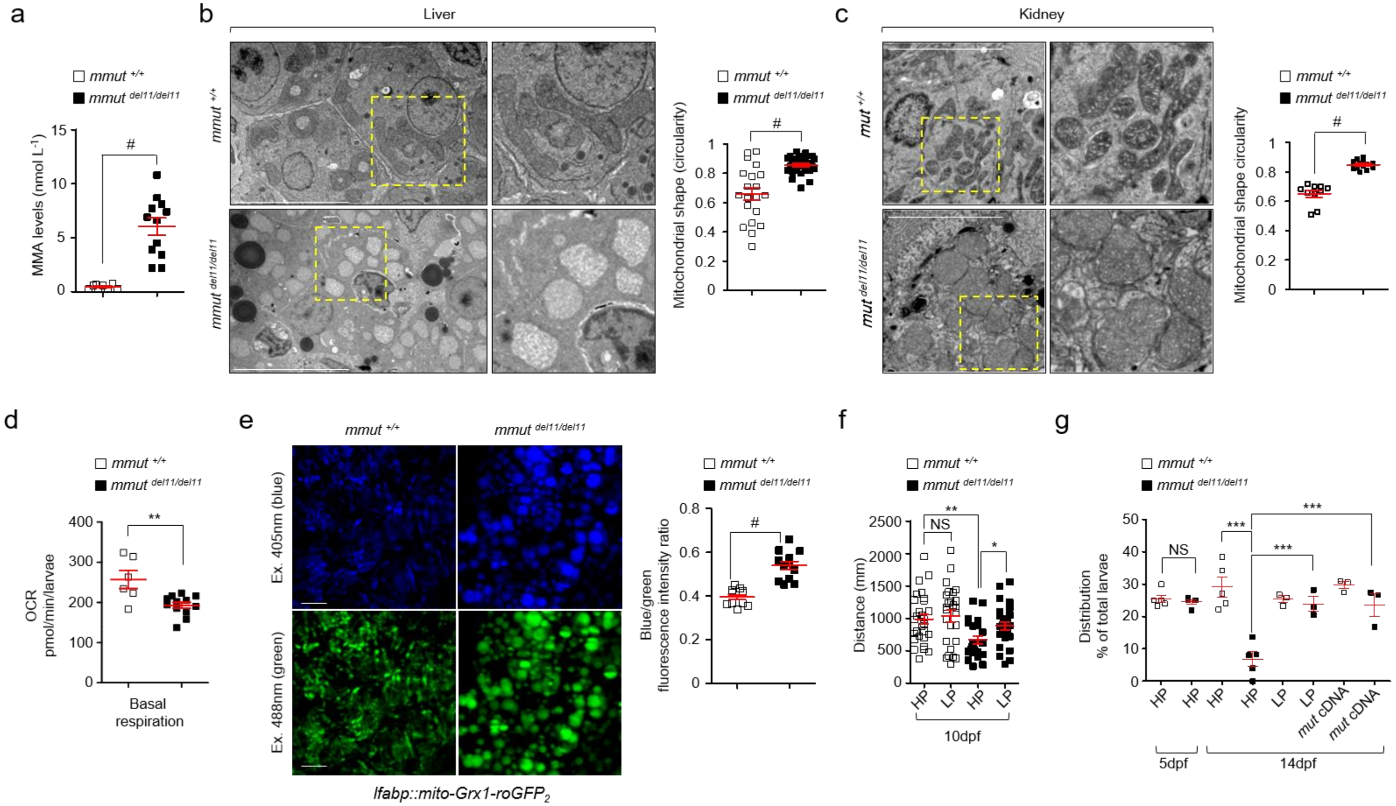

Figure 3. Mitochondrial abnormalities and phenotypic changes in *mmut*–deficient zebrafish. (**a**) Quantification of MMA levels by LC–MS/MS; *n*=8 *mmut*$^{+/+}$ and *n*=12 *mmut*$^{del11/del11}$ zebrafish. (**b–c**) Representative electron micrographs and quantification of the mitochondrial shape (expressed as circularity) in (**b**) livers and in (**c**) kidneys of 10–dpf–*mmut* zebrafish (*n*=9 and *n*=15 randomly selected fields of views pooled from three *mmut*$^{+/+}$ and *mmut*$^{del11/del11}$ zebrafish livers, respectively; *n*=10 and *n*=13 randomly selected fields of views pooled from three *mmut*$^{+/+}$ and *mmut*$^{del11/del11}$ zebrafish kidneys, respectively). Dotted yellow squares contain images at higher magnification. (**d**) Oxygen consumption rate (OCR) and individual parameters for basal respiration in 10–dpf–*mmut* zebrafish, *n*= 6 *mmut*$^{+/+}$ and 12 *mmut*$^{del11/del11}$ zebrafish. (**e**) Zebrafish expressing mito–Grx1–roGFP2 in the liver were outcrossed with *mmut* $^{+/del11}$ zebrafish. Quantification of ratios between 405 (blue) and 488 (green) fluorescence intensities, with each point representing the average fluorescence intensity ratio in a zebrafish liver; *n*=11 *mmut*$^{+/+}$ and *n*=12 *mmut*$^{del11/del11}$ zebrafish. (**f**) Tracking analyses of motor behavior in 10–dpf–*mmut* zebrafish fed with a high or low protein diet (HP or LP, respectively). Quantification of the covered distance, with each point representing the average distance covered by an individual zebrafish; *n*=28 HP–fed *mmut*$^{+/+}$, *n*=26 LP–fed *mmut*$^{+/+}$, *n*=23 HP–fed *mmut*$^{del11/del11}$ and *n*=27 LP–fed *mmut*$^{del11/del11}$ zebrafish. (**g**) Distribution of *mmut* zebrafish (calculated as percentage of the total larvae) in HP or LP–fed at 5 and 14–dpf or in *mmut* zebrafish stably expressing *mmut* in the liver; *n*≥3 independent experiments, with each containing ~100 *mmut* zebrafish larvae. Plots represent mean ± SEM. Two tailed Student's *t* test, **P*<0.05, ***P*<0.01 and $^{\#}P$<0.0001 relative to *mmut*$^{+/+}$ or HP-*mmut*$^{del11/del11}$ in a, b, c, d and e. One–way ANOVA followed by Bonferroni's *post hoc* test, ****P*<0.001 relative to *mmut*$^{+/+}$ or 14–dpf–HP–fed *mmut*$^{+/+}$ or *mmut*$^{del11/del11}$ zebrafish. Scale bars are 5 µm in **b** and in **c,** and 100□m in **e**. NS: non–significant. Source data are provided as a Source Data file.

Figure 4

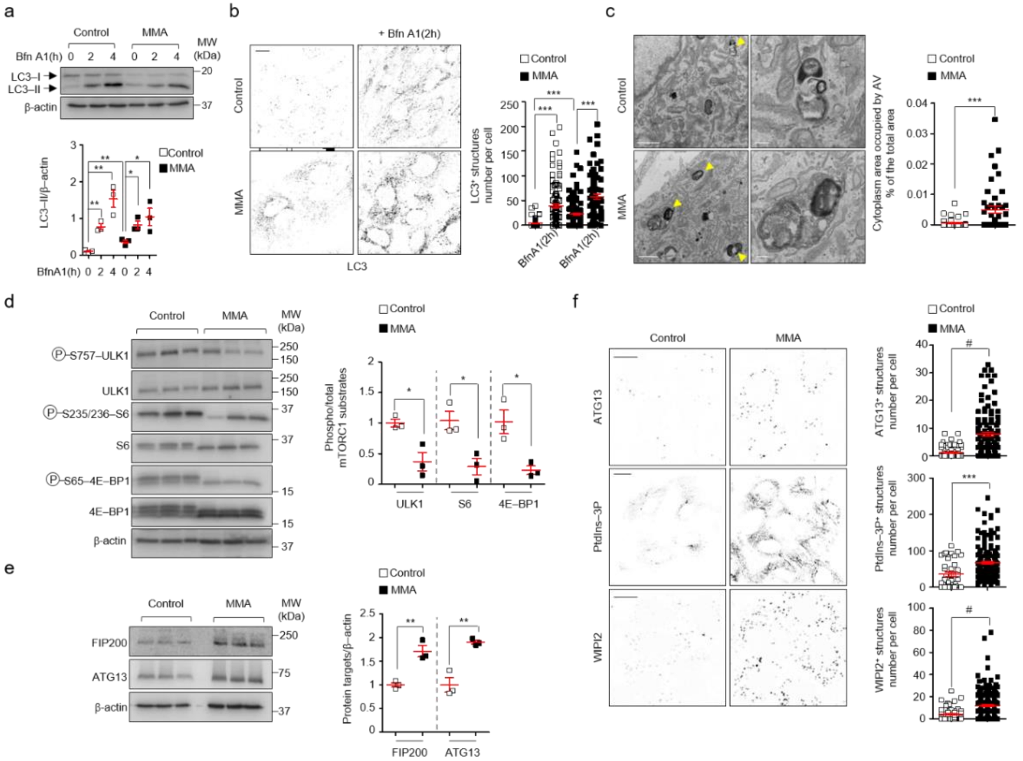

Figure 4. *MMUT* deficiency stimulates autophagy in MMA cells. (**a–b**) Cultured cells were exposed to lysosome–based proteolysis inhibitor Bafilomycin A1 (Bfn A1, 250 nM for the indicated time). Representative immunoblotting and quantification of LC3–II protein levels; *n*=3 independent experiments. Two tailed Student's *t* test, **P*<0.05 and ***P*<0.01 relative to untreated control or MMA cells. (**b**) Representative inverted confocal micrographs and quantification of numbers of punctate LC3$^+$ structures, with each point representing the average number of LC3$^+$ structures in a cell; *n*= 122 untreated control cells, *n*= 127 Bfn A1–treated control cells, *n*= 127 untreated MMA kidney cells and n=77 Bfn A1–treated MMA kidney cells. Data were pooled from three independent experiments. One–way ANOVA followed by Bonferroni's *post hoc* test, ****P*<0.001 relative to untreated control or MMA cells. (**c**) Representative electron micrographs and quantification of cytoplasm area occupied by autophagy vacuoles (AV; expressed as percentage of the total area); *n*=43 control cells and *n*=45 MMA cells. Data were pooled from two independent experiments. Arrowheads indicate EM–compatible AV. (**d–e**) Immunoblotting and quantification of (**d**) phosphorylated and total forms of mTORC1 substrates and (**e**) of FIP200 and ATG13 protein levels, *n*=3 independent experiments. (**f**) Representative inverted confocal micrographs and quantification of numbers of ATG13$^+$ (top panel) or PtdIns–3P$^+$ (middle panel) or WIPI2$^+$ (bottom panel) structures, with each point representing the average number of positive structure in a cell. Number of ATG13$^+$ structures: *n*= 86 control cells and *n*=118 MMA cells. Number of PtdIn–3P$^+$ structures: *n*= 41 control cells and *n*=141 MMA cells. Number of WIPI2$^+$ structures: *n*=71 control cells and *n*=253 MMA cells. Data were pooled from three independent experiments. Plots represent mean ± SEM. Two tailed Student's *t* test, **P*<0.05, ***P*<0.01, ****P*<0.001 and $^{\#}$*P*<0.0001 relative to control cells in **c**, **d**, **e** and **f**. β–actin was used as loading control in **a**, **d** and **e**. Scale bars are 10μm in **b** and **f**, and 1μm and 250nm in **c** (left and right panel, respectively). NS: non–significant. Source data are provided as a Source Data file.

Figure 5

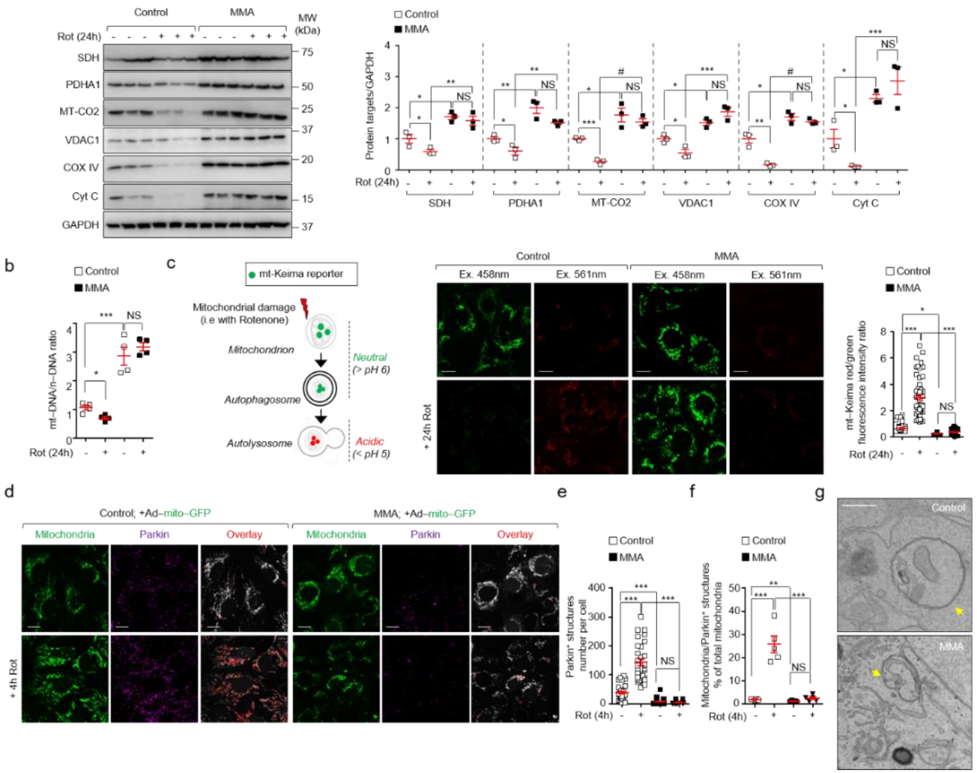

Figure 5. Impaired mitophagy–mediated degradation of MMA diseased mitochondria. (**a–f**) Cells were exposed to Rotenone (5 µM) for the indicated time. (**a**) Immunoblotting and quantification of indicated mitochondrial proteins; *n*=3 independent experiments. GAPDH used as loading control. (**b**) The ratio between mitochondrial (*ND1*) and nuclear DNA (*ACTB*) was determined by qPCR; *n*= 4 independent experiments. (**c**) Workflow of the strategy used to monitor the cellular delivery of damaged mitochondria to lysosomal compartments. Cells were transduced for 24h with adenoviral particles bearing the mitochondrially–targeted form of Keima (mt–Keima). Representative confocal micrographs and quantification of ratios of red/green fluorescence signal, with each point representing the average red/green fluorescence intensity ratio in a cell; *n*=46 untreated control cells and *n*=52 Rotenone–treated control cells, and *n*=51 untreated MMA cells and *n*=53 Rotenone–treated MMA cells. (**d–f**) Cells were transduced with adenoviral particles bearing the mitochondrially–targeted green fluorescent protein (Ad–mito–GFP). After 24h post–transduction, the cells were exposed to Rotenone for 4h, immunostained for with Parkin (magenta) and analyzed by confocal microscopy. (**d**) Representative confocal micrographs and quantification of numbers of (**e**) Parkin$^+$ and (**f**) GFP/Parkin$^+$ structures. Number of Parkin$^+$ structures, with each point representing the number of positive structures in a cell: *n*=30 untreated and Rotenone–treated control cells, *n*=39 untreated MMA cells and *n*=52 Rotenone–treated MMA cells. Number of GFP/Parkin$^+$ structures (expressed as percentage of total mitochondria): *n*=5 randomly selected fields of views per condition, with each containing ~10 cells. (**g**) Representative electron micrographs (EM) showing the engulfment of mitochondria within EM–compatible, double membrane–autophagic vacuoles in control but not in MMA kidney cells. Data were pooled from three independent experiment in **c**, **e** and **f**. Plots represent mean ± SEM. Two tailed Student's *t* test, *$P<0.05$, **$P<0.01$ and ***$P<0.001$ relative to untreated control cells or to Rotenone–treated control cells in **a**, **b** and in **f.** One–way ANOVA followed by Bonferroni's *post hoc* test, *$P<0.05$ and ***$P<0.001$ relative to untreated control cells or to Rotenone–treated control cells in **c** and **e**. Scale bars are 10 µm in **c** and in **d**, and 250nm in **g**. NS, non–significant. Source data are provided as a Source Data file.

Figure 6

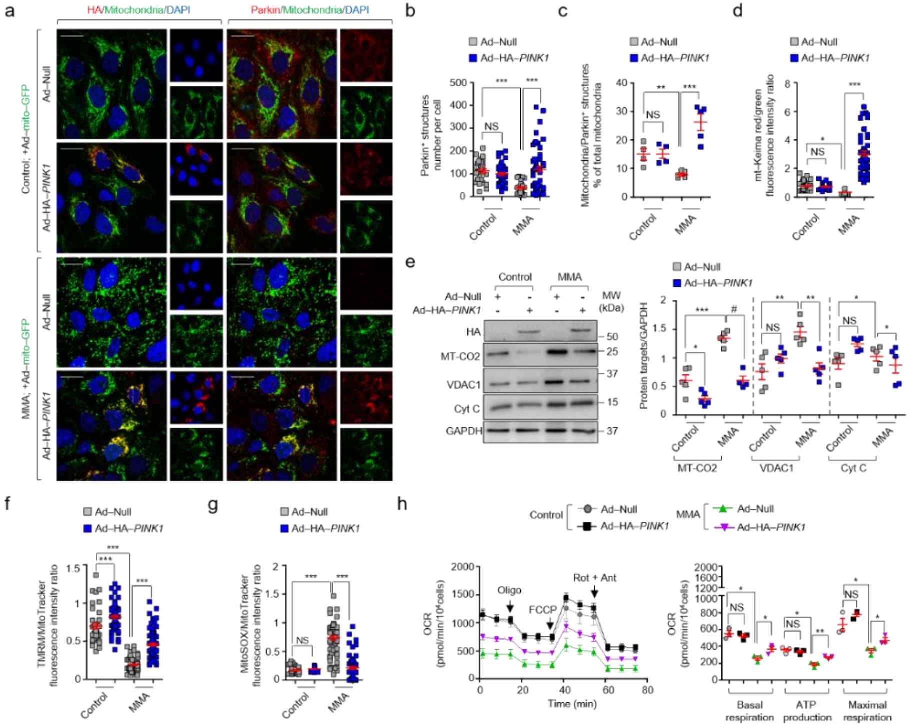

Figure 6. Rescue of mitochondrial function and homeostasis by re–expressing PINK1 in MMA kidney cells. (**a–c**) Cells were transduced with adenovirus expressing mitochondrially–targeted GFP (green) and subsequently with adenovirus bearing Null (Ad–Null) or HA–*PINK1* (red). (**a**) Representative confocal micrographs and (**b**) quantification of numbers of Parkin$^+$ structures in a cell. Numbers of control cells transduced with Ad–Null (*n*= 25) or Ad–*PINK1* (*n*=39) and of MMA cells transduced with Ad–Null (*n*= 57) or HA–*PINK1* (*n*=55). (**c**) Quantification of mito–GFP/Parkin$^+$ structures (expressed as percentage of total mitochondria); *n*≥4 fields of views for control and MMA cells. Nuclei counterstained with DAPI (blue). (**d–e**) Null and HA–*PINK1* expressing cells were transduced with adenovirus particles bearing mt–Keima and analysed by confocal microscopy. (**d**) Quantification of red/green fluorescence intensity ratio in a cell. Numbers of control cells transduced with Ad–Null (*n*=46) or HA–*PINK1* (*n*=38) and of MMA cells transduced with Ad–Null (*n*=51) or HA–*PINK1* (*n*=54). (**e**) Representative immunoblotting and quantification of the indicated mitochondrial proteins; *n*=5 independent experiments. (**f–g**) Cells were loaded with (**f**) TMRM (green) or (**g**) MitoSOX (green) and MitoTracker (red), and analysed by confocal microscopy. Quantification of TMRM/MitoTracker or MitoSOX/MitoTracker fluorescence intensity ratio in a cell. Numbers of control cells transduced with Ad–Null (*n*=43) or HA–*PINK1* (*n*=62) and of MMA cells transduced with Ad–Null (*n*=83) or HA–*PINK1* (*n*=84) for TMRM/MitoTracker. Numbers of control cells transduced with Ad–Null (*n*=38) or HA–*PINK1* (*n*=56) and of MMA cells transduced with Ad–Null (*n*=59) or HA–*PINK1* (*n*=64) for MitoSOX/MitoTracker. (**h**) Oxygen consumption rate (OCR) and individual parameters for basal respiration, ATP production and maximal respiration. OCRs were measured at baseline and upon the sequential addition of Oligomycin (Oligo, 1μM), FCCP (0.5 μM) and Rotenone (Rot; 1μM) + Antimycin A (ANT; 1μM). Data in **a**–**h** were pooled from three independent experiments. Plots represent mean ± SEM. One–way ANOVA followed by Bonferroni's *post hoc* test, **P*<0.05 and ****P*<0.001 relative to control or MMA cells transduced with Ad–Null in **b**, **d, f** and **g**. Two tailed Student's *t* test, **P*<0.05, ***P*<0.01, ****P*<0.001 and $^{\#}$*P*<0.0001 relative to control and MMA cells transduced with Ad–Null in **c**, **e**, and **h**. Scale bars,10μm. NS: non–significant. Source data are provided as a Source Data file.

Figure 7

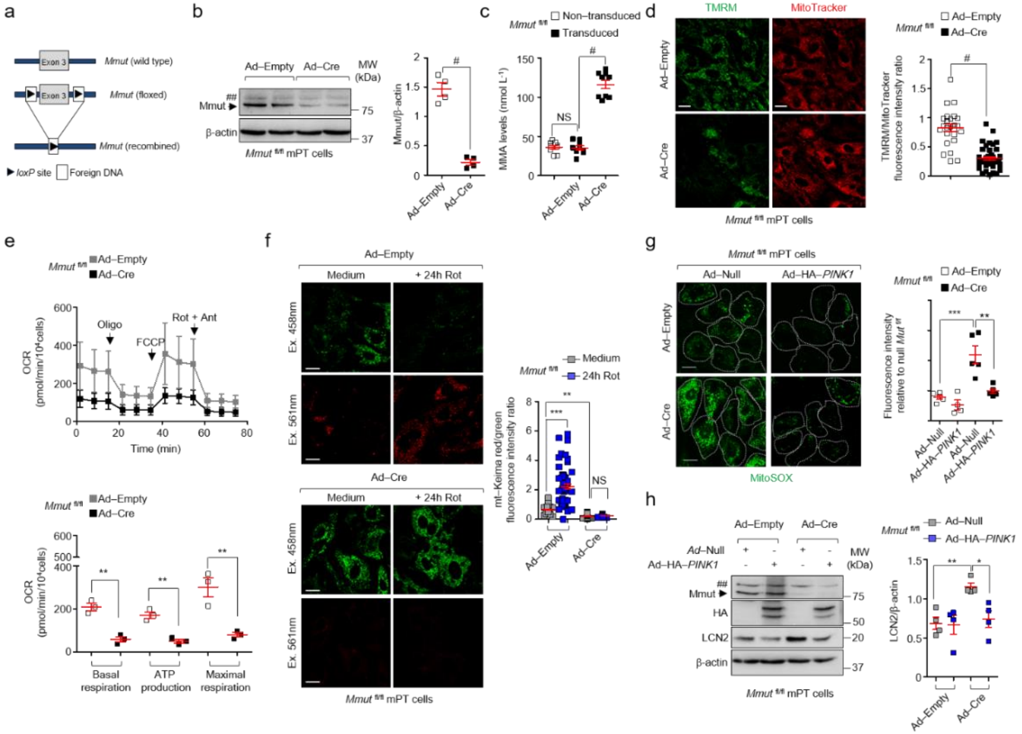

Figure 7. *MMUT* deletion damages mitochondria and blunts PINK1–directed mitophagy triggering epithelial stress in kidney cells. (**a–i**) mPT cells from floxed *Mmut* kidneys transduced with adenovirus bearing Empty (Ad–Empty) or Cre recombinase (Ad–Cre) for 5 days. (**a**) Workflow of strategy used to generate the floxed *Mmut* alleles. (**b**–**c**) Validation of *Mmut* deletion by (**b**) immunoblotting (*n*=4 independent experiments) and (**c**) by LC–MS/MS analysis of MMA levels, *n*=9 samples pooled from three independent experiments. (**d**) Cells were loaded with TMRM (green) and MitoTracker (red) and analysed by confocal microscopy. Quantification of fluorescence intensity ratio in a cell. Numbers of cells transduced with Ad–Empty (*n*=25) or Ad–Cre (*n*=45). (**e**) Oxygen consumption rate (OCR) and individual parameters for basal respiration, ATP production and maximal respiration. OCRs were measured at baseline and upon the sequential addition of Oligomycin (Oligo), FCCP and Rotenone (Rot) + Antimycin A (Ant); *n*=3 independent experiments. (**f**) *Mmut* cells were transduced for 24h with an adenovirus expressing mitochondrially–targeted form of Keima (mt–Keima) and exposed to Rotenone (Rot, 5 µM for 24h). Representative confocal micrographs and quantification of red/green fluorescence intensity ratio in a cell. Numbers of untreated (*n*=68) and Rot–treated (*n*=57) control cells, and of untreated (*n*=51) and Rot–treated (*n*=58) *Mmut* deleted cells. (**g–h**) Control and *Mmut*–deleted cells were transduced with an adenovirus expressing Null or HA–*PINK1* for 24 h. (**g**) Cells were loaded with MitoSOX (green) and analysed by confocal microscopy. Representative confocal micrographs and quantification of MitoSOX fluorescence intensity, $n \geq 4$ randomly selected fields of views, with each containing ~ 10cells. (**h**) Representative immunoblotting and quantification of LCN2 levels, *n*=4 independent experiments. β–actin used as loading control. Data in **d**, **f** and **g** were pooled from three independent experiments Plots represent mean±SEM. Asterisks denote non–specific bands in **b** and **h**. Two tailed Student's *t* test, *$P<0.05$, **$P<0.01$, ***$P<0.01$ and $^{\#}P<0.0001$ relative to control cells in **b**, **c**, **d** and **e** or relative to control or *Mmut*–deleted cells transduced with Ad–Null in **h .** One–way ANOVA followed by Bonferroni's *post hoc* test, **$P<0.01$and ***$P<0.001$ relative to untreated control cellsor relative to control or *Mmut*–deleted cells transduced with Ad–Null in **f** and **g**. Scale bars,10µm. NS: non–significant. Source data are provided as a Source Data file.

Figure 8

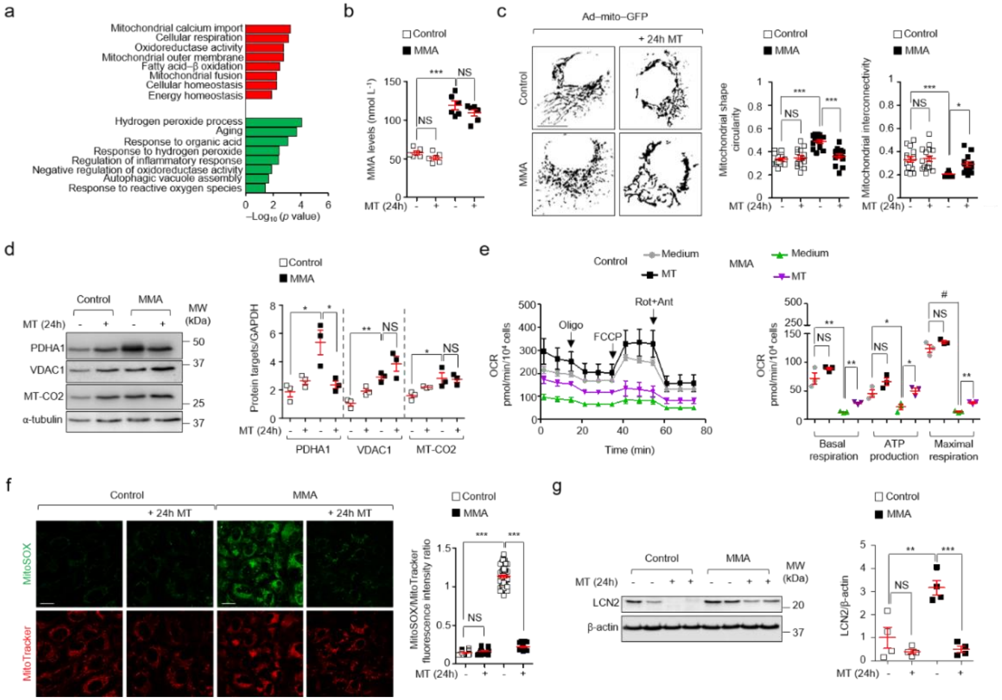

Figure 8. Mitochondrially–targeted ROS scavenger mito–TEMPO repairs mitochondrial functions in MMA cells. (**a**) Gene ontology (GO) annotations significantly upregulated (red) and downregulated (green) by the *in silico*–prioritized hits according to Drug Set Enrichment Analysis (DSEA). (**b–g**) Cells were treated with mito–TEMPO (MT; 10μm for 24h). (**b**) Quantification of MMA levels by LC–MS/MS; *n*=6 samples pooled from three independent experiments. One–way ANOVA followed by Bonferroni's *post hoc* test, ****P*<0.001 relative to untreated control or MMA cells (**c**) Cells were transduced with adenovirus bearing the mitochondrially–targeted GFP (green). After 24h post–transduction, the cells were treated with MT, and analysed by confocal microscopy. Representative inverted confocal micrographs and quantification of circularity (expressed as circularity) and interconnectivity of the mitochondrial network. Circularity: *n*= 15 cells per each condition. Interconnectivity: *n*=15 untreated and MT–treated control cells, *n*=15 untreated MMA cells and *n*=13 MT–treated MMA cells. Data were pooled from three independent experiments. One–way ANOVA followed by Bonferroni's *post hoc* test, **P*<0.05 and ****P*<0.001 relative to untreated control or MMA cells. (**d**) Representative immunoblotting and quantification of the indicated mitochondrial proteins, *n*=3 independent experiments. α–tubulin used as loading control. (**e**) Oxygen consumption rate (OCR) and individual parameters for basal respiration, ATP production and maximal respiration. OCRs were measured at baseline and upon the sequential addition of Oligomycin (Oligo), FCCP and Rotenone (Rot) + Antimycin A (Ant), *n*=3 independent experiments. (**f**) Cells were loaded with MitoSOX (2.5 μM for 25 min at 37°C and MitoTracker (red; 1μM for 25 min at 37°C), and analysed by confocal microscopy. Representative confocal micrographs and quantification of mitochondrial ROS (calculated as ratio between MitoSOX and MitoTracker fluorescence intensities; each point representing the average fluorescence intensity ratio in a cell. Numbers of untreated (*n*=36) or MT–treated (*n*=28) control cells and of untreated (*n*=51) or MT–treated (*n*=28) MMA cells. Data were pooled from three independent experiments. One–way ANOVA followed by Bonferroni's *post hoc* test, ****P*<0.001 relative to untreated control or MMA cells. (**g**) Representative immunoblotting and quantification of LCN2 levels, *n*=4 independent experiments. β–actin used as loading control Plots represent mean ± SEM. Two tailed Student's *t* test, **P*<0.05, ***P*<0.01 and ****P*<0.001 relative to untreated control or MMA cells in**d**, **e** and **g**. Scale bars are 10μm. NS: non–significant. Source data are provided as a Source Data file.

Figure 9

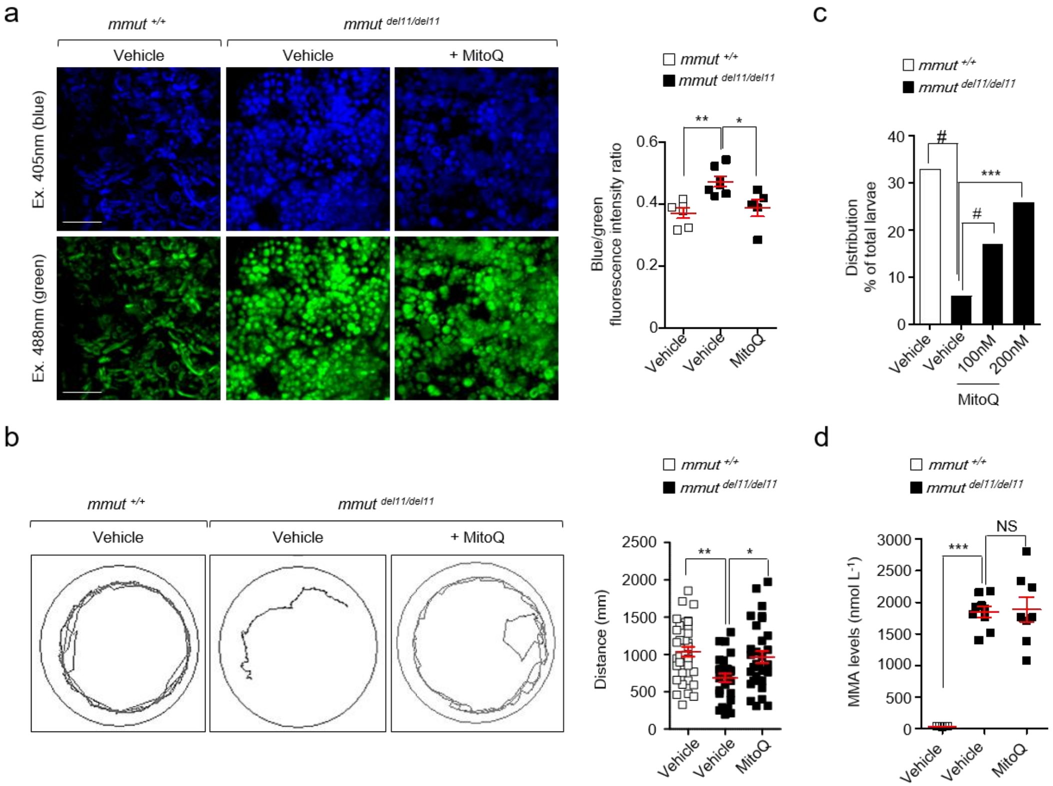

Figure 9. Mitochondrially–targeted ROS scavenger MitoQ rescues the MMA–associated phenotypes in *mmut*–deficient zebrafish. (**a**–**d**) Zebrafish were treated with vehicle or with the mitochondria–targeted ROS scavenger MitoQ (200 nM for 24h). (**a**) Representative confocal micrographs and quantification of ratios between 405 (blue) and 488 (green) fluorescence intensities in *mmut* zebrafish expressing mito–Grx1–roGFP2 in the liver. Each point represents the average fluorescence intensity ratio in a zebrafish liver; *n*= 6 untreated *mmut*$^{+/+}$ zebrafish and *n*=7 untreated *mmut*$^{\mathrm{del11/del11}}$ zebrafish, and *n*=5 MitoQ–treated *mmut*$^{\mathrm{del11/del11}}$ zebrafish. Kruskal–Wallis followed by Dunn's multiple comparison test, **P*<0.05 and ***P*<0.01 relative to vehicle–treated *mmut*$^{+/+}$ or *mmut*$^{\mathrm{del11/del11}}$ zebrafish. (**b**) Tracking analyses of motor behavior in 10–dpf *mmut* zebrafish. Quantification of covered distance, with each point representing the average distance covered by an individual zebrafish; *n*=28 vehicle–treated *mmut*$^{+/+}$ and *n*=27 vehicle–treated *mmut*$^{\mathrm{del11/del11}}$ and *n*=31 MitoQ–treated *mmut*$^{\mathrm{del11/del11}}$. One–way ANOVA followed by Bonferroni's *post hoc* test, **P*<0.05 and ***P*<0.01 relative to vehicle–treated *mmut*$^{+/+}$ or to *mmut*$^{\mathrm{del11/del11}}$ zebrafish. (**c**) Distribution of *mmut* zebrafish (calculated as percentage of total larvae) after treatment with vehicle or MitoQ. Chi–square goodness of fit test, ****P*<0.001 and $^{\#}$*P*<0.0001 relative to vehicle–treated *mmut*$^{+/+}$ or *mmut*$^{\mathrm{del11/del11}}$ zebrafish. Data derived from one experiment (*n*≥77*mmut* zebrafish per each group). (**d**) Quantification of MMA levels by LC–MS/MS; *n*= 5 vehicle–treated *mmut*$^{+/+}$ zebrafish and *n*=9 vehicle–treated *mmut*$^{\mathrm{del11/del11}}$ zebrafish and *n*=8 MitoQ–treated *mmut*$^{\mathrm{del11/del11}}$ zebrafish. Plots represent mean ± SEM. Kruskal–Wallis followed by Dunn's multiple comparison test, ***P*<0.01 relative to vehicle–treated *mmut*$^{+/+}$ or *mmut*$^{\mathrm{del11/del11}}$ zebrafish. Scale bars, 100 µm. NS: non–significant. Source data are provided as a Source Data file.

Figure 10

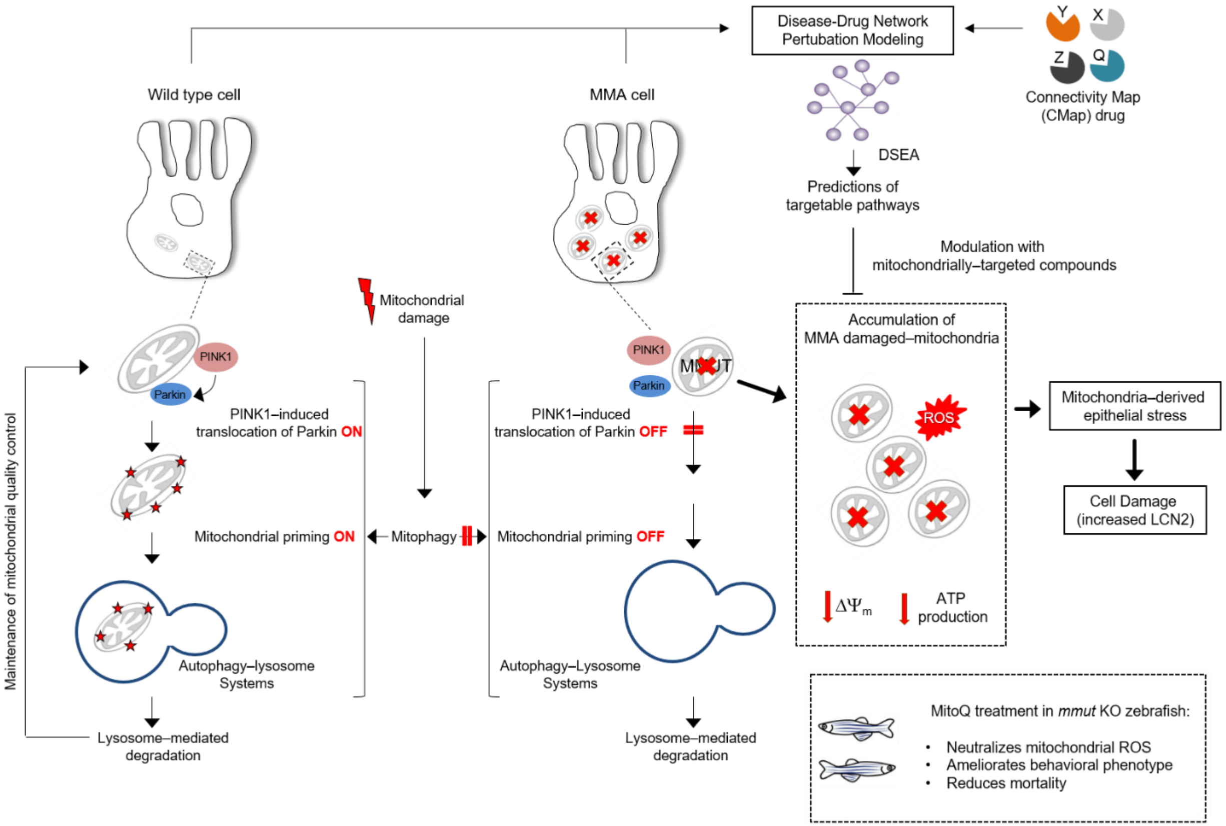

Figure 10. Proposed model depicting the link between mitochondrial dysfunction and epithelial stress in MMA. In wild type kidney cells (left), mitochondrial stress (*e.g.* treatment with Rotenone) stimulates PINK1–induced translocation of Parkin to damaged mitochondria. This triggers the activation of mitophagy and the subsequent disposal of dysfunctional mitochondria through autophagy–lysosome degradation systems, hence safeguarding the homeostasis and function of the mitochondrial network. By contrast, in MMA–affected kidney cells (right), the impaired PINK/Parkin–mediated mitophagy impedes the delivery of damaged mitochondria and their degradation by autophagy–lysosome systems. This leads to the accumulation of diseased mitochondria and exacerbates the mitochondrial alterations induced by *MMUT* deficiency, including accumulation of toxic metabolites, collapsed mitochondrial membrane potential ($\Delta\psi_m$), and abnormal energetic profiling and increased mitochondrial ROS. These mitochondrial defects trigger epithelial stress, causing ultimately cell damage (*e.g.* LCN2 overproduction). Drug–disease network perturbation modeling, based on gene expression profiles from MMA patient–derived kidney cells against a large compendium of gene expression signatures derived from 1309 small bioactive drug compounds, identifies targetable disease–relevant biological pathways. The modulation of the identified targets (*e.g.* treatment with mitochondria–targeted ROS scavengers MT or MitoQ) repairs mitochondrial dysfunctions, neutralizes epithelial stress and cell damage in MMA cells, and improves disease–relevant phenotypes in *mmut*–deficient zebrafish.

Impaired Mitophagy Links Mitochondrial Disease to Epithelial Stress in Methylmalonyl–CoA Mutase Deficiency

Alessandro Luciani[1,*], Anke Schumann[1,2,*], Marine Berquez[1,*], Zhiyong Chen[1,11], Daniela Nieri[1], Mario Failli[3], Huguette Debaix[1], Beatrice Paola Festa[1], Natsuko Tokonami[1], Andrea Raimondi[4], Alessio Cremonesi[5], Diego Carrella[6], Patrick Forny[2], Stefan Kölker[7], Francesca Diomedi Camassei[8], Francisca Diaz[9], Carlos T. Moraes[9], Diego Di Bernardo[6], Matthias R. Baumgartner[2] and Olivier Devuyst[1,10]

[1]Institute of Physiology and NCCR Kidney.CH, University of Zurich, 8057 Zurich, Switzerland
[2]Division of Metabolism and Children's Research Center, University Children's Hospital, 8032 Zurich, Switzerland
[3]Department of Biomedicine, University of Eastern Finland, Kuopio 70211, Finland
[4] San Raffaele Scientific Institute, Experimental Imaging Center, 20132 Milan, Italy;
[5]Division of Clinical Chemistry and Biochemistry, University Children's Hospital Zurich, 8032 Zurich, Switzerland
[6]Telethon Institute of Genetics and Medicine, Pozzuoli, 80078 Naples, Italy
[7]Division of Inherited Metabolic Diseases, University Children's Hospital Heidelberg, 69120 Heidelberg, Germany
[8]Department of Laboratories–Pathology Unit, Bambino Gesù Children's Hospital, 00165 Rome, Italy
[9]Department of Neurology, University of Miami Miller School of Medicine, 33136 Miami, USA
[10]Division of Nephrology, Cliniques Universitaires Saint–Luc, 1040 Brussels, Belgium;
[*]These authors contributed equally

Correspondence: alessandro.luciani@uzh.ch (A.L.) or olivier.devuyst@uzh.ch (O.D.)

Supplementary Information

Supplementary Figure 1–13
Supplementary Table 1–4

Description of Additional Supplementary Files

Supplementary Data 1

Supplementary Figure 1

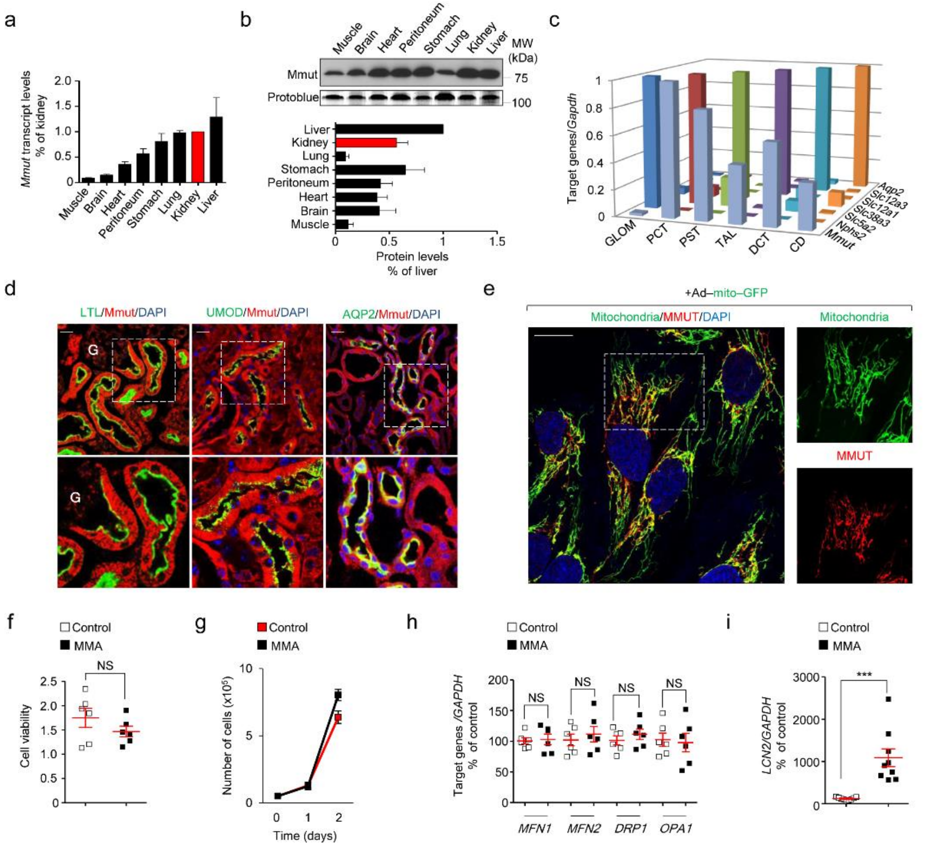

Supplementary Figure 1. Tissue, nephron–segment and intracellular compartmentalization of the enzyme MMUT, and characterization of MMA patient–derived cells. (**a**) Transcript and (**b**) protein expression of the enzyme Mmut in mouse tissues were determined by reverse transcription– quantitative PCR (RT–qPCR; *n*=3 mice) and by immunoblotting (*n*=4 mice), respectively. Protoblue was used as loading control. (**c**) Transcript levels of *Mmut* in nephron specific segments were measured by RT−qPCR. The abundance of each segment–related gene (GLOM=*Nphs2*; PCT=*Scl5a2*; PST=*Slc38a3*; TAL=*Slc12a1*; DCT=*Slc12a3* and CD=*Aqp2*) defines the purity of each segment fraction. Quantification of all segment specific marker genes was performed in comparison with *Gapdh* as an endogenous control (*n*=3 mice). (**d**) Representative images showing the segment–specific compartmentalization of Mmut (red) in LTL+ (green, left) proximal tubules or in UMOD+ (green, middle) thick ascending limb tubules or in AQP2+ (green, right) collecting duct. G denotes glomerulus. (**e**) Cells were transduced with adenoviral particles expressing the mitochondrially–targeted green fluorescent protein (Ad–mito–GFP). After 24h post–transduction, the cells were immunostained for MMUT (red) and imaged by confocal microscopy. Yellow indicates the colocalization. Dotted white squares represent regions of the respective panels magnified. (**f**) Cell viability was assessed by Cell Counting Kit–8 (CCK–8) assay; *n*=6 replicates pooled from three biologically independent experiments. (**g**) Growth curves in control and MMA kidney cells, *n*=3 biologically independent experiments. (**h–i**) Transcript levels of (**h**) *MFN1*, *MFN2*, *DRP1* and *OPA1* or (**i**) *LCN2* were measured by RT−qPCR; *n*=6 replicates in **h** and *n*=9 replicates in **i**. Values in **h** and **i** are pooled of three biologically independent experiments. Plots represent mean ± SEM. Two tailed Student's *t* test, ****P*<0.001 relative to control cells. Nuclei counterstained with DAPI (blue) in **d** and **e**. Dotted white squares represent regions of the respective panels magnified in **d** and **e**. Scale bars are 30μm in **d** and 10μm in **e**. GLOM, glomerulus; PCT, proximal convoluted tubule; PST, proximal straight tubule; TAL, thick ascending limb tubule; DCT, distal convoluted tubule and CD, collecting duct; NS: non–significant.

Supplementary Figure 2

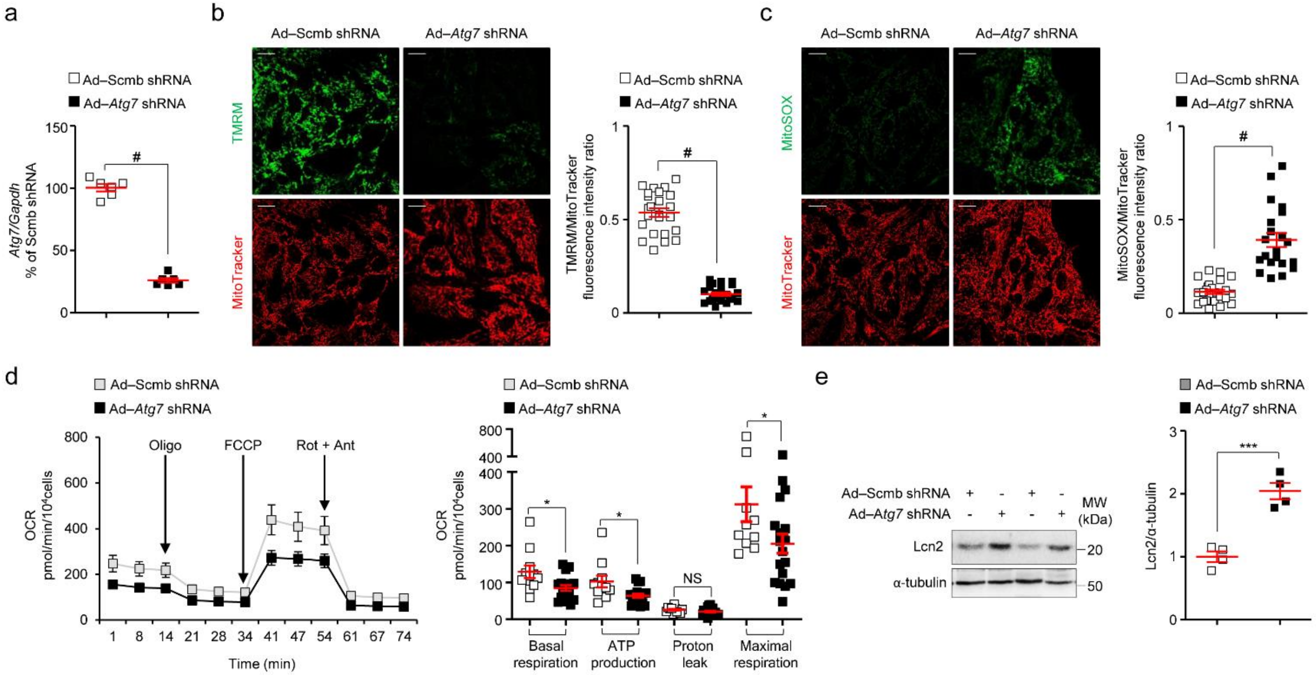

Supplementary Figure 2. Autophagy deficiency leads to mitochondrial dysfunctions in kidney tubule cells. (**a–e**) Primary cultures of proximal tubule cells derived from mouse kidneys were transduced with adenovirus particles carrying scrambled or *Atg7* short hairpin RNA (shRNA) for 5 days. (**a**) Transcript levels of *Atg7* and *Gapdh* were measured by RT–qPCR; *n*=6 replicates pooled from three biologically independent experiments. (**b–c**) Cultured cells were loaded with (**b**) tetramethylrhodamine methyl ester (TMRM, green; mitochondrial membrane potential fluorescent probe, 50 nM for 30 min at 37°C) and MitoTracker (red; fluorescent probe that localizes to mitochondria, 1 µM for 30 min at 37°C) or with (**c**) MitoSOX (green; mitochondrial ROS indicator, 2.5 µM for 30 min at 37°C) and MitoTracker (red), and analyzed by confocal microscopy. Representative images and quantification of (**b**) membrane potential and (**c**) mitochondrial ROS production (both calculated as ratio between TMRM and MitoTracker or MitoSOX and MitoTracker fluorescence intensities, with each point representing the average fluorescence intensity ratio in a cell). TMRM/MitoTracker: *n*=24 control cells and *n*=23 *Atg7*-deleted cells. MitoSOX/MitoTracker: *n*=24 control cells and *n*=21 *Atg7*-deleted cells. Values are pooled from three biologically independent experiments. (**d**) Oxygen consumption rate (OCR) and individual parameters for basal respiration, ATP production, proton leak and maximal respiration. OCRs were measured at baseline and after the sequential addition of Oligomycin (Oligo, 1□M), FCCP (0.5□M) and Rotenone (Rot; 1µM) + Antimycin A (Ant; 1□M); *n*=11 replicates pooled from four biologically independent experiments (for cells transduced with Ad−Scmb shRNA) and *n*=18 replicates pooled from six biologically independent experiments (for cells transduced with Ad−*Atg7* shRNA). (**e**) Immunoblotting and quantification of Lcn2, *n*=4 biologically independent experiments. α–tubulin was used as loading control. Plots represent mean ±SEM. Two tailed Student's *t* test, **P*<0.05, ****P*<0.001 and #*P*<0.0001 relative to cells transduced with Scmb shRNA. Scale bars, 10µm. NS: non–significant.

Supplementary Figure 3

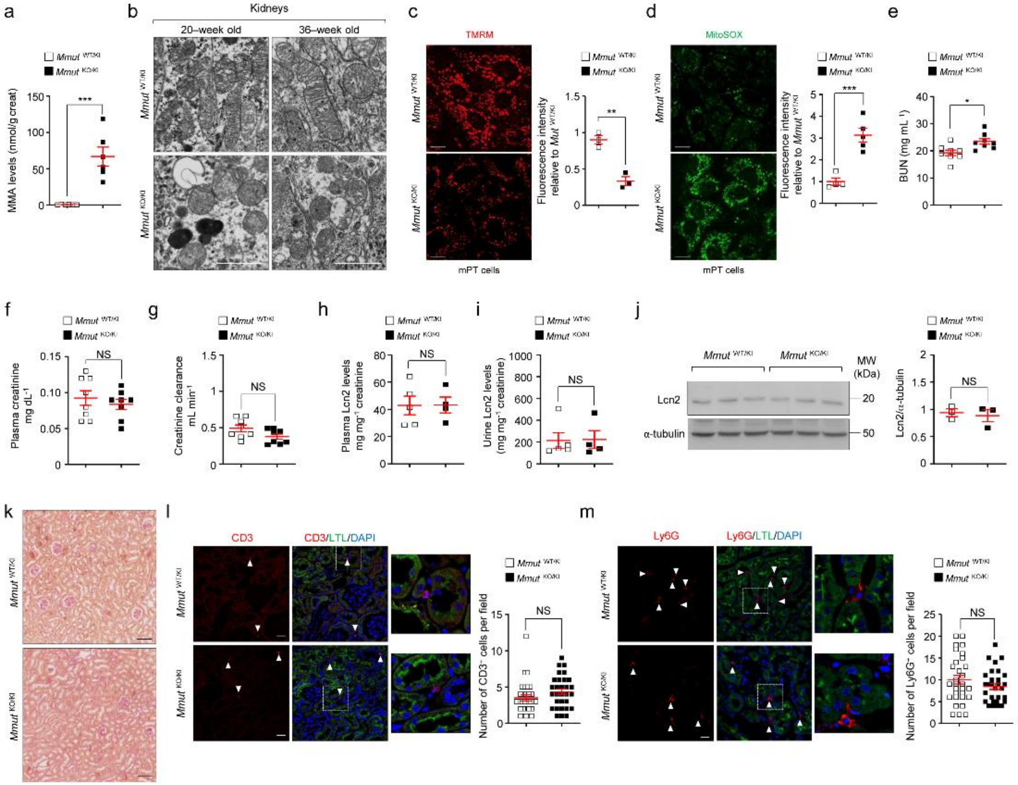

Supplementary Figure 3. Mitochondrial and kidney phenotypes in *Mmut*$^{KO/KI}$ mice. (**a**) Quantification of MMA levels in the urines of 32–36– week–old *Mmut*$^{WT/KI}$ and *Mmut*$^{KO/KI}$ using LC–MS/MS; n=6 animals per each group. (**b**) Representative electron micrographs showing the mitochondrial network in 20–week–or 36–week–old kidney tubules of *Mmut*$^{WT/KI}$ and *Mmut*$^{KO/KI}$ mice. (**c–d**) Primary cultures of proximal tubule cells derived from 20 week–old kidneys of *Mmut* $^{WT/KI}$ and *Mmut* $^{KO/KI}$ mice were loaded (**c**) with tetramethylrhodamine methyl ester (TMRM; green; mitochondrial membrane potential fluorescent probe, 50 nM for 30 min at 37°C) and MitoTracker (red; fluorescent probe that localizes to mitochondria; 1 μM for 30 min at 37°C) or with (**d**) MitoSOX (green; mitochondrial ROS indicator, 2.5 μM for 25 min at 37°C) and MitoTracker (red), and analyzed by live confocal fluorescence microscopy. Representative confocal micrographs and quantification of TMRM or MitoSOX fluorescence intensities; n=3 randomly selected fields of views, with each containing ~10 cells (for TMRM) and n4 randomly selected fields of views, with each containing ~10 cells (for MitoSOX). Data are pooled from three independent experiments. (**e–f**) Quantifications of (**e**) urea and (**f**) creatinine, and measurements of (**g**) creatinine clearance in 32–36 –week–old *Mmut* mice, n=8 animals per group. (**h–i**) Levels of Lcn2 (**h**) in plasma or (**i**) urine harvested from 32–36– week–old *Mmut* mice were measured by ELISA, n= 5 *Mmut*$^{WT/KI}$ and n= 4 *Mmut*$^{KO/KI}$. (**j**) Immunoblotting and quantification of Lcn2 protein levels in whole–tissue lysates harvested from kidneys of 32–36 –week–old *Mmut* mice (n=3 mice per each group). α–tubulin used as loading control. (**k**) Representative micrographs and detection of collagen deposition by Picro Sirius Red staining in kidneys of 32–36 –week–old *Mmut* mice. (**l–m**) Representative confocal micrographs and quantification of numbers of (**l**) CD3^{+} cells (marker of T cells; red) or (**m**) Ly6G^{+} (marker of granulocytes, monocytes and neutrophils; red) in kidneys of 32–36– week–old *Mmut* mice. Proximal tubules labelled by Lotus Tetragonolobus Lectin (LTL; green); n=30 randomly selected fields of views. Data are pooled from three mice. Dotted yellow squares contain images at higher magnification. Arrowheads indicate the CD3 or Ly6G positive cells. Plots represent mean ± SEM. Two tailed Student's t test, *$P<0.05$, **$P<0.01$ and ***$P<0.001$ relative to *Mmut*$^{WT/KI}$. Nuclei counterstained with DAPI (blue). Scale bars are 1μm in **b**, 10 μm in **c** and **d**, 1mm in **k** and 20μm in **l** and **m**. NS: non–significant.

Supplementary Figure 4

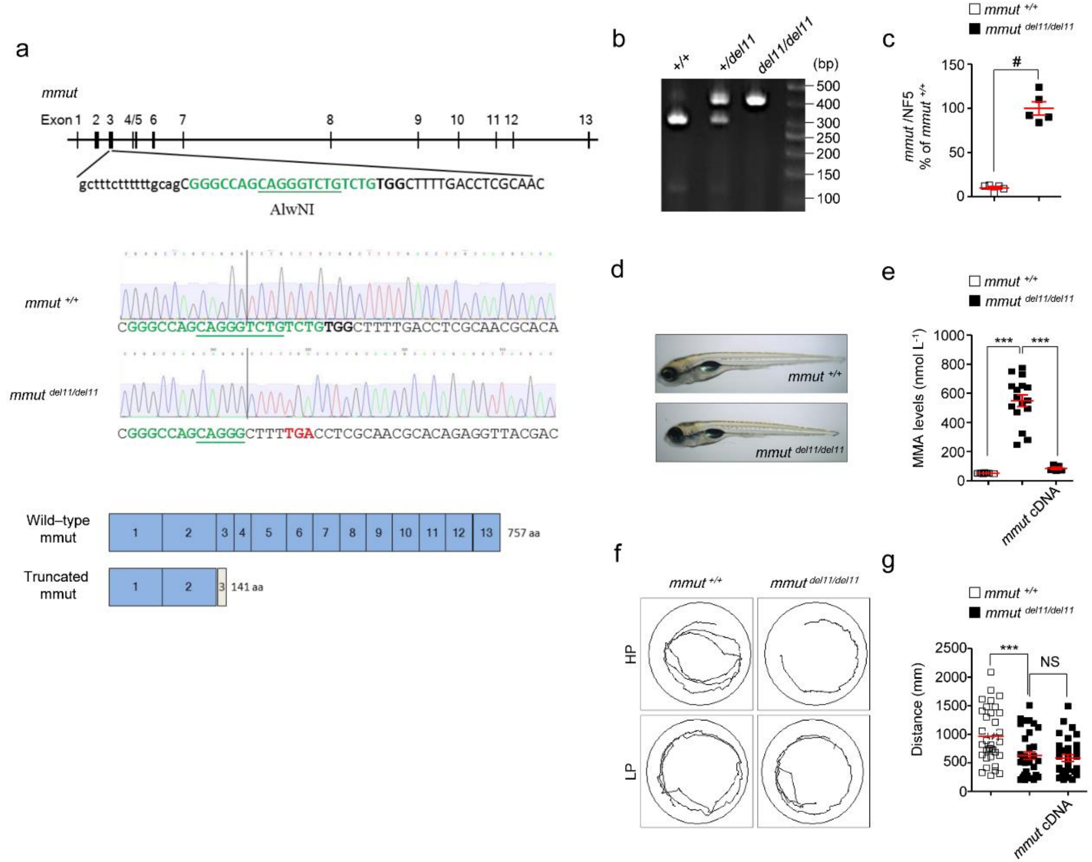

Supplementary Figure 4. Generation, validation and characterization of *mmut* knockout zebrafish model. (**a**) CRISPR–Cas9–induced deletion (green) generates a frameshift of the open reading frame, resulting in a premature stop codon (TGA) within the exon 3 of *mmut* gene (middle panel) that produces a truncated protein of 141 amino acids. The underlined sequence represents the AlwNI site used for the detection of the deletion. (**b**) AlwNI digestion of PCR products after the amplification of the CRISPR–Cas9 targeting region using genomic DNA extracted from caudal of wild–type (+/+), heterozygous (+/del11) and homozygous (del11/del11) zebrafish. Wild type allele: two lower bands 333bp + 120bp correspond to PCR products cut by AlwNI. Mutant allele: upper band 453bp, resistant to AlwNI digestion. (**c**) Transcript levels of *mmut* in zebrafish kidneys was determined by RT–qPCR; *n*=5 animal per each group. (**d**) Representative images of *mmut*$^{+/+}$and *mmut*$^{\mathrm{del11/del11}}$zebrafish embryos at 5–dpf. (**e**) Quantification of MMA levels in *mmut* zebrafish by LC–MS/MS; *n*=8 *mmut*$^{+/+}$ zebrafish and *n*=16 *mmut*$^{\mathrm{del11/del11}}$ zebrafish and *n*=5 *mmut*$^{\mathrm{del11/del11}}$ zebrafish expressing *mmut* in the liver. (**f**) Tracking analyses of motor behavior in 10–dpf–*mmut* zebrafish larvae fed high or low protein diet. (**g**) Quantification of mean covered distance, with each point representing the mean distance covered by an individual zebrafish; *n*=36 *mmut*$^{+/+}$ zebrafish and *n*=34 *mmut*$^{\mathrm{del11/del11}}$ zebrafish and *n*=33 *mmut*$^{\mathrm{del11/del11}}$ zebrafish expressing *mmut* cDNA in the liver. Plots represent mean ± SEM. Two tailed Student's *t* test, #$P<0.0001$ relative to *mmut* $^{+/+}$ in **c**. One–way ANOVA followed by Bonferroni's *post hoc* test, ***$P<0.001$ relative to *mmut* $^{+/+}$ or relative to *mmut*$^{\mathrm{del11/del11}}$ zebrafish in **e** and **g**. NS: non–significant.

Supplementary Figure 5

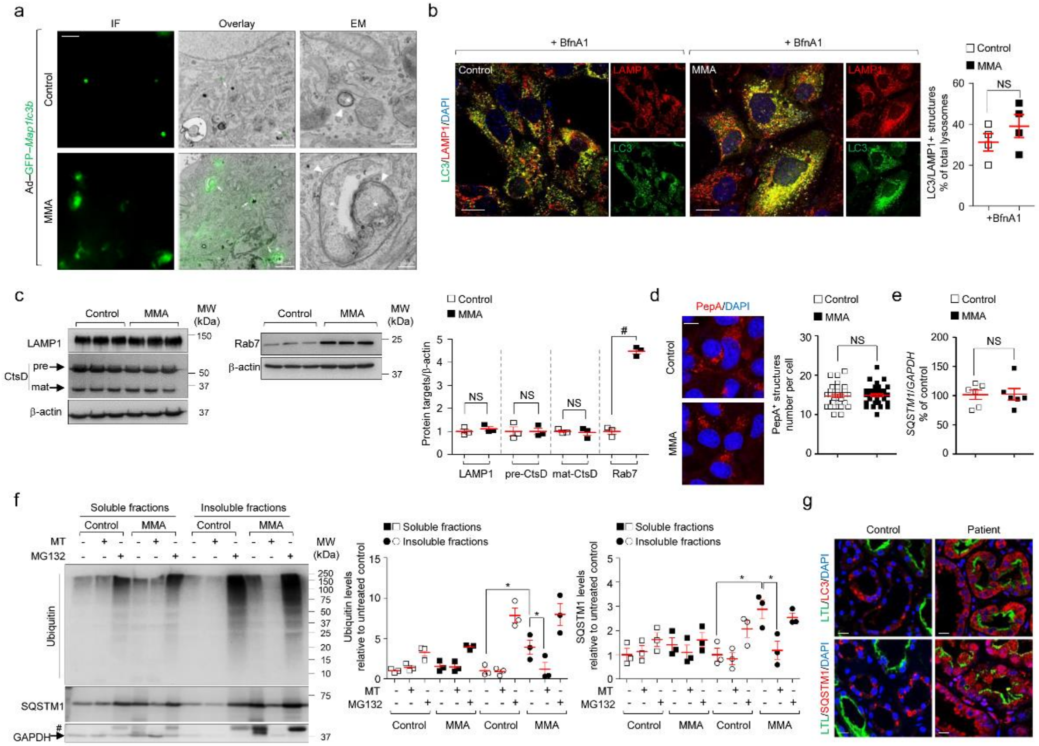

Supplementary Figure 5. Dysregulation of autophagy in MMA kidney cells. (**a**) Cells were transduced with GFP–tagged *Map1lc3b* (Ad–GFP–*Map1lc3b*) bearing adenoviral particles for 24h. The punctate GFP–LC3$^+$ structures were imaged by live confocal fluorescence microscopy. Selected cells were further processed, and serial sections were analyzed by electron microscopy. (**b**) Cells were cultured in presence or in absence of Bafilomycin A1 (Bfn A1, 250 nM for 4h). Representative confocal micrographs and quantification of numbers of LC3/LAMP1$^+$ structures (expressed as percentage of total lysosomes; *n*= 4 randomly selected fields per condition, with each containing ~10 cells. Data are pooled from two independent experiments. Yellow indicates colocalization. (**c**) Immunoblotting and quantification of LAMP1, Cathepsin D (CtsD) and RAB7 protein levels; β–actin used as loading control. Two tailed Student's *t*–test, $^{\#}P<0.0001$ relative to control cells, *n*=3 independent experiments. (**d**) Cells were loaded Bodipy–FL–Pep A (1 μM, for 1h at 37°C), fixed and analysed by confocal microscopy. Quantification of numbers of Pep A$^+$ structures, with each point representing the number of Pep A$^+$ structures in a cell; *n*= 30 cells pooled from three independent experiments. (**e**) Transcript levels of *SQSTM1* and *GAPDH* in control and in MMA cells were measured by RT–qPCR; *n*=6 pooled from three independent experiments. (**f**) Control and MMA kidney cells were treated with the mitochondrially–targeted ROS scavenger mito–TEMPO (MT, 10 μm for 24h) or with the proteasome inhibitor MG132 (50 μm for 16h). Representative immunoblotting and quantification of ubiquitin, SQSTM1 and GAPDH protein levels in the soluble and insoluble fractions obtained from control and MMA cells. Two tailed Student's *t*–test, $^*P<0.05$ relative to untreated control or MMA kidney cells, *n*=3 independent experiments. Asterisk denotes the presence of non–specific bands. (**g**) Representative confocal micrographs of LC3 (top panel, red) and of SQSTM1 (bottom panel, red) in kidney biopsy samples from an individual healthy control subject and patient with MMA. Kidney proximal tubules labelled by LTL (green). Nuclei counterstained with DAPI. Scale bars are 10μm (left panel) and 2μm (middle panel) and 250nm (right panel) in **a,** 10μm in **b** and **d,** and 30μm in **g**. NS: non–significant.

Supplementary Figure 6

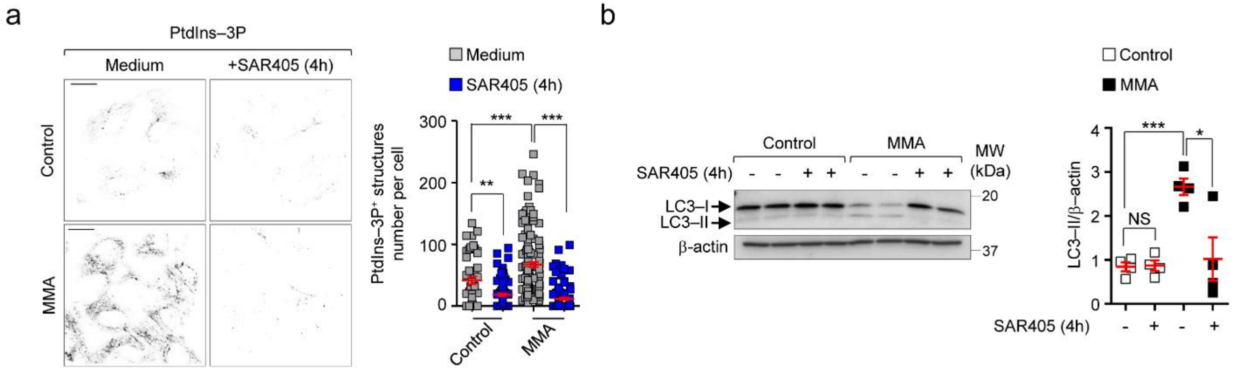

Supplementary Figure 6. Inhibition of Vps34–induced PtdIns–3P production blocks autophagosome biogenesis. (a–b**)** Cells were exposed to the highly selective Vps34 inhibitor SAR405 (5 μM for 4h). (**a**) Representative inverted confocal micrographs and quantification of numbers of PdtIns–3P^{+} structures, with each point representing the average number of PdtIns–3P^{+} structures in a cell; n=45 untreated control cells, *n*= 93 SAR405–treated control cells, n=141 untreated MMA cells and n=114 SAR405–treated MMA cells. Data are pooled from three independent experiments. One–way ANOVA followed by Bonferroni's *post hoc* test, ***P*<0.01 and ****P*<0.001 relative to untreated control or MMA cells. (**b**) Representative immunoblotting and quantification of LC3 protein levels, *n*=4 independent experiments. β–actin used as a loading control. Two tailed Student's *t* test, **P*<0.05 and ****P*<0.001 relative to untreated control or MMA cells. NS: non–significant.

Supplementary Figure 7

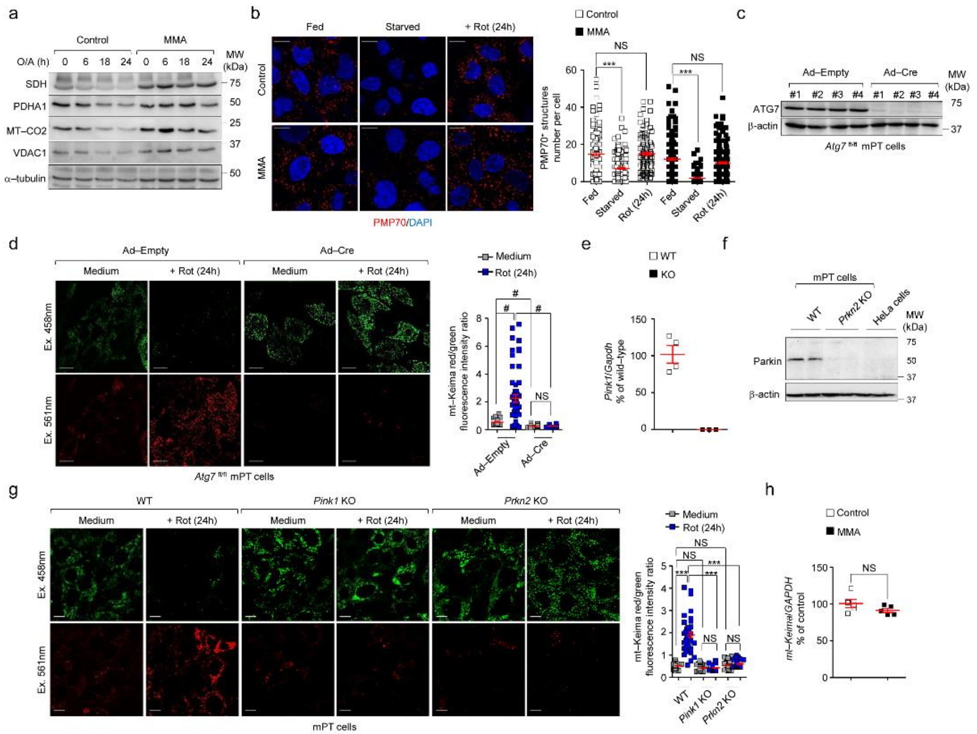

Supplementary Figure 7. Mitophagy in MMA cells or in proximal tubule cells derived from floxed *Atg7* or from *Pink1* or *Prkn2* knockout mice. (**a**) Cells were exposed to Oligomycin (4 µM) and Antimycin (0.8 µM) for the indicated times. Immunoblotting of the indicated mitochondrial proteins, *n*=2 independent experiments. (**b**) Cells were cultured under normal growth (fed) or nutrient–deprived (starve) conditions or exposed to Rotenone (Rot, 5 µm for 24h) and immunostained for PMP70 (red), and analysed by confocal microscopy. Representative confocal micrographs and quantification of PMP70^{+} structures per cell, with each point representing the number of PMP70^{+} structures in a cell; *n*= 142 fed control cells, *n*=181 starved control cells and *n*= Rot–treated control cells, *n*=189 fed MMA cells, *n*=196 starved MMA cells and *n*=212 Rot–treated MMA cells. Data are pooled from three independent experiments. One–way ANOVA followed by Bonferroni's *post hoc* test, ****P*<0.001 relative to fed control or MMA cells. Nuclei counterstained with DAPI (blue). (**c–d**) Primary cultures of proximal tubule cells derived from kidneys of floxed *Atg7* mice were transduced with Empty (Ad–Empty) or Cre recombinase (Ad–Cre) bearing adenoviral particles for 5 days. (**c**) Validation of the deletion of *Atg7* by immunoblotting, *n*=4 independent experiments. (**d**) Control and *Atg7*–deleted cells were transduced for 24h with adenoviral particles bearing mitochondrially–targeted form of Keima (mt–Keima), and exposed to Rot. Representative confocal micrographs and quantification of ratios of red/green fluorescence signal, with each point representing the average red/green fluorescence intensity ratio in a cell; *n*=54 untreated control cells, *n*=55 Rot–treated control cells, *n*=46 untreated *Atg7* deleted cells and *n*=44 Rot–treated *Atg7* deleted cells. Two tailed Student's *t* test, $^{\#}P$<0.001 relative to untreated or Rot–treated control cells. (**e**) Transcript levels of *Pink1* and *Gapdh* were assessed by RT–qPCR in 12–week–old brain of *Pink1* WT and KO mice; *n*=4 WT brains and *n*=3 KO brains. (f) Immunoblotting of Parkin in *Prkn2* WT and KO kidneys or in HeLa cells. (**g**) WT, *Pink1* and *Prkn2* KO cells were transduced for 24h with adenoviral particles bearing mitochondrially–targeted form of Keima (mt–Keima). After 24h post–transduction, the mt–Keima expressing cells were exposed to Rotenone for 24h and analysed by confocal microscopy. Representative confocal micrographs and quantification of ratios of red/green fluorescence signal, with each point representing the average red/green fluorescence intensity ratio in a cell; *n*=50 untreated control cells and *n*=41 Rot–treated control cells, *n*=82 untreated *Pink1* KO cells and *n*=79 Rot–treated *Pink1* KO cells, and *n*=55 untreated *Prkn2* KO cells and *n*=44 Rot–treated *Prkn2* KO cells. One–way ANOVA followed by Bonferroni's *post hoc* test, ****P*<0.001 relative to untreated WT cells or to Rotenone–treated WT cells. (**h**) Transcript levels of *mt–Keima* and *GAPDH* in control and MMA kidney cells were measured by RT–qPCR; *n*=5 independent experiments. α–tubulin or β–actin was used as loading control. Plots represent mean ± SEM. Scale bars are 10µm. NS: non–significant

Supplementary Figure 8

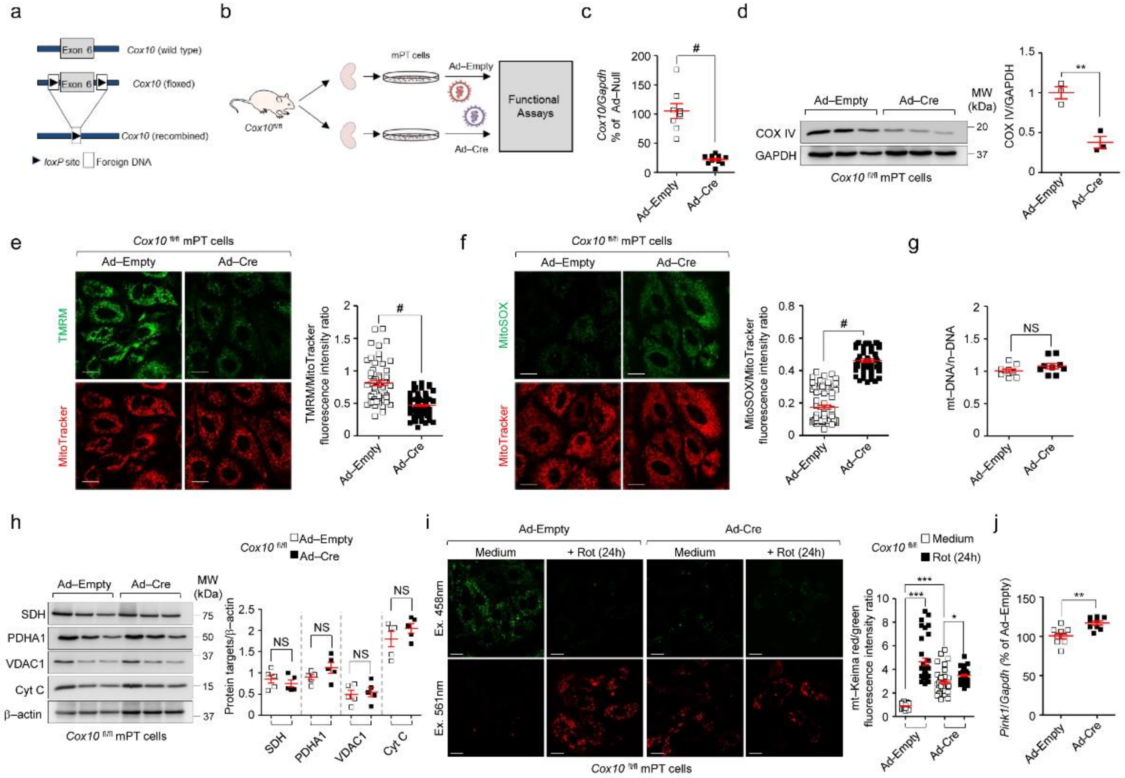

Supplementary Figure 8. Mitochondrial abnormalities in *Cox10*–deficient kidney cells are not linked to deficient mitophagy. (**a**–**j**) Primary cultures of proximal tubule cells derived from kidneys of floxed *Cox10* mice were transduced with Empty (Ad–Empty) or Cre recombinase (Ad–Cre) bearing adenoviral particles for 5 days. (**a**–**b**) Workflow of strategy used (**a**) to generate floxed *Cox10* alleles and (**b**) to delete *Cox10* gene *in vitro* in primary cultures of proximal tubule cells derived from floxed *Cox10* kidneys. (**c**–**d**) Validation of *Cox10* deletion (**c**) by RT–qPCR (*n*≥ 8 pooled from four independent experiments) and (**d**) by immunoblotting, *n*=3 independent experiments. (**e**–**f**) Cultured cells were loaded (**e**) with tetramethylrhodamine methyl ester (TMRM; green; mitochondrial membrane potential fluorescent probe, 50 nM for 30 min at 37°C) and MitoTracker (red; fluorescent probe that localizes to mitochondria; 1μM for 30 min at 37°C) or (**f**) with MitoSOX (green; mitochondrial ROS indicator, 2.5 μM for 25 min at 37°C) and MitoTracker (red), and analysed by live confocal fluorescence microscopy. Representative confocal micrographs and quantification of (**e**) membrane potential and (**f**) mitochondrial ROS production (both calculated as ratios between TMRM and MitoTracker or MitoSOX and MitoTracker fluorescence intensities, with each point representing the fluorescence intensity ratio in a cell). TMRM/MitoTracker: *n*=60 cells transduced with Ad–Empty and *n*=95 cells transduced with Ad–Cre. MitoSOX/MitoTracker: *n*=74 cells transduced with Ad–Empty and n=56 cells transduced with Ad–Cre. Data are from three independent experiments. (**g**) Ratio between mitochondrial DNA (*Nd1*) and nuclear DNA (*Hbb*) was determined by quantitative PCR; *n*=9 pooled from 3 independent experiments. (**h**) Immunoblotting and quantification of the indicated mitochondrial proteins; *n*=5 independent experiments. (**i**) Control and *Cox10* deleted cells were transduced for 24h with adenoviral particles bearing mt–Keima and exposed to Rotenone (5μM for 24h). Representative confocal micrographs and quantification of ratios of red/green fluorescence signal, with each point representing the average red/green fluorescence intensity ratio in a cell; *n*=39 untreated control cells and *n*=35 Rot–treated control cells, and *n*=40 untreated *Cox10* deleted cells and *n*=45 Rot–treated *Cox10* deleted cells. One–way ANOVA followed by Bonferroni's *post hoc* test, **P*<0.05 and ****P*<0.001 relative to untreated control cells or *Cox10*–deleted cells. (**i**) Transcript levels of *Pink1* and *Gapdh* in *Cox10* cells were determined by RT–qPCR, *n*= 9 pooled from three independent experiments. Two tailed Student's *t*–test, ***P*<0.01 and $^{\#}P$<0.0001 relative to cells transduced with Ad–Empty in **c**, **d**, **e**, **f**, **g**, **h** and **j**. Plots represent mean ± SEM. Scale bars are 10μm. NS: non–significant.

Supplementary Figure 9

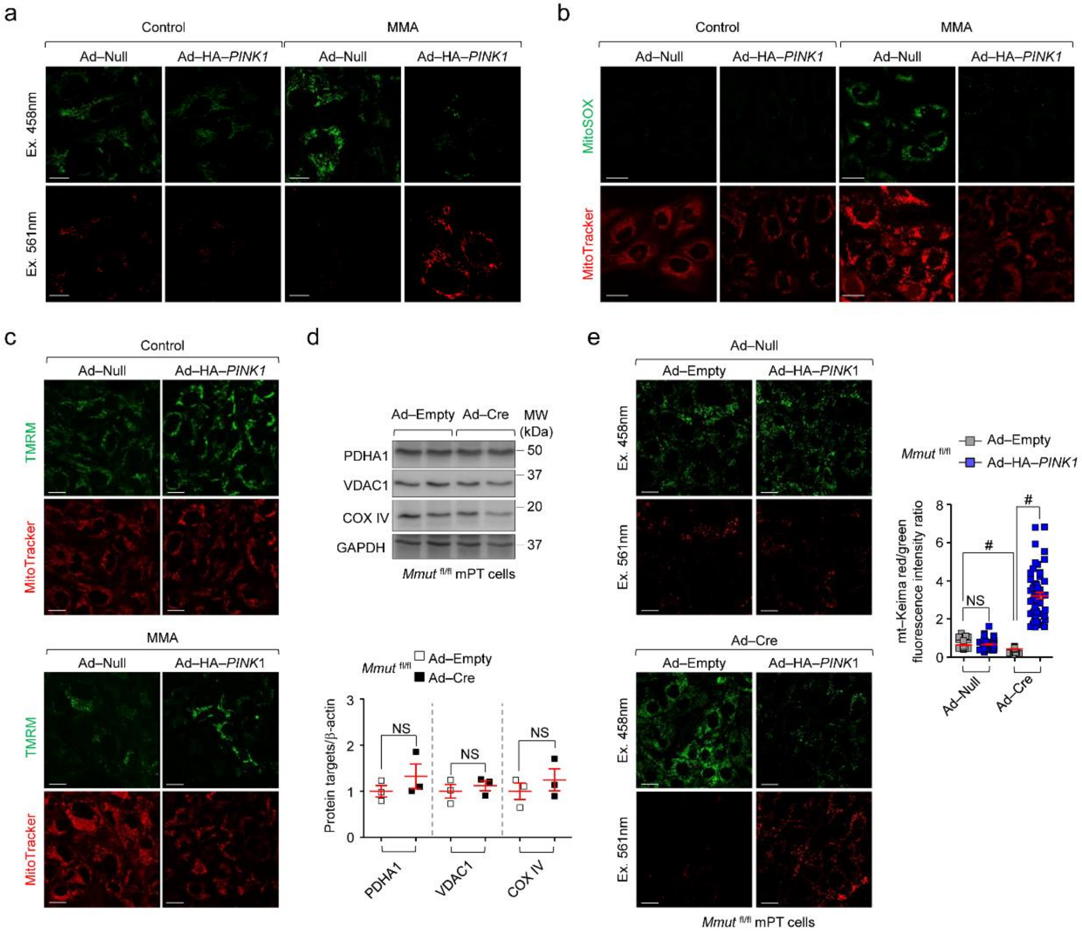

Supplementary Figure 9. Re– expression of PINK1 restores mitophagy in patient–derived and *Mmut* deleted kidney tubular cells. (**a–c**) Representative micrographs of experiments plotted in figure 6**d**, 6**f** and 6**g**. (**d**) Immunoblotting and quantification of the indicated mitochondrial proteins; *n*=3 independent experiments.(**e**) Control and *Mmut* deleted cells expressing Ad–Null or Ad–HA–*PINK1* were subsequently transduced for 24h with adenoviral particles bearing matrix mitochondrially–targeted form of Keima (mt–Keima), and analyzed by live confocal microscopy. Representative confocal micrographs and quantification of ratios of red/green fluorescence signal, with each point representing the average red/green fluorescence intensity ratio in a cell; *n*= 57 control cells transduced with Ad–Null and *n*= 65 control cells transduced with Ad–HA–*PINK1*, and *n*= 55 *Mmut* deleted cells transduced with Ad–Null; *n*= 59 *Mmut* deleted cells transduced with Ad–HA–*PINK1*. Two tailed Student's *t*–test, $^{\#}P<0.001$ relative to control cells transduced with control cells transduced with Ad–Empty or to *Mmut* deleted cells transduced with Ad–Empty. Plots represent mean ± SEM. Scale bars are 10 µm.

Supplementary Figure 10

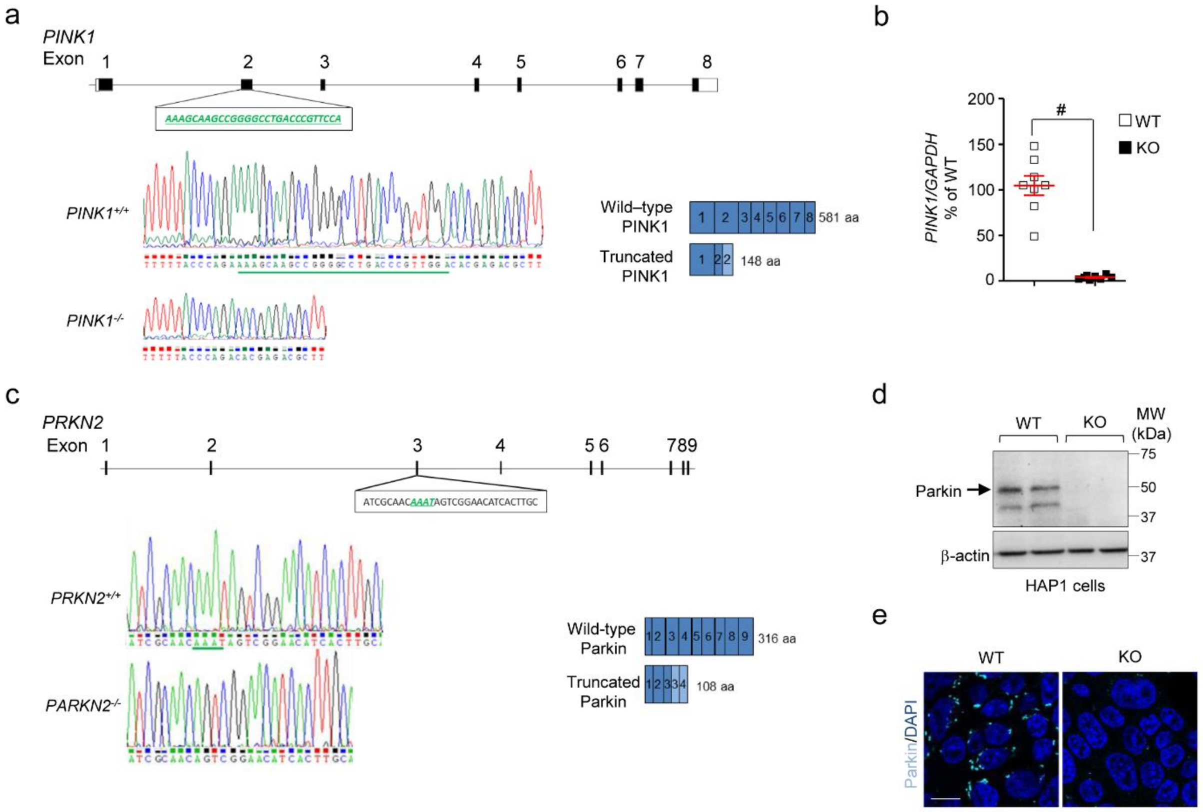

Supplementary Figure 10. Generation and validation of *PINK1* or *PRKN2* knockout HAP–1 cells. (**a**) CRISPR–Cas9–induced deletion (green) generates a frameshift of the open reading frame, resulting in premature stop codon (TGA) within the exon 2 of *PINK1* gene, which ultimately produces a truncated protein of 148 amino acids. (**b**) Validation of the *PINK1* deletion by RT–qPCR, *n*=8 pooled from 4 independent experiments. Plots represent mean ± SEM. Two tailed Student's *t*–test, $^{\#}P<0.0001$ relative to WT cells. (**c**) CRISPR–Cas9–induced deletion (green) generates a frameshift of the open reading frame, resulting in premature stop codon (TGA) within the exon 3 of *PRKN2* gene, which ultimately produces a truncated protein of 108 amino acids. (**d–e**) Validation of the gene deletion by (**d**) immunoblotting and (**e**) confocal microscopy assays. Arrowhead indicates the predicted molecular weight of Parkin. Nuclei counterstained with DAPI (blue). Scale bars are 10μm.

Supplementary Figure 11

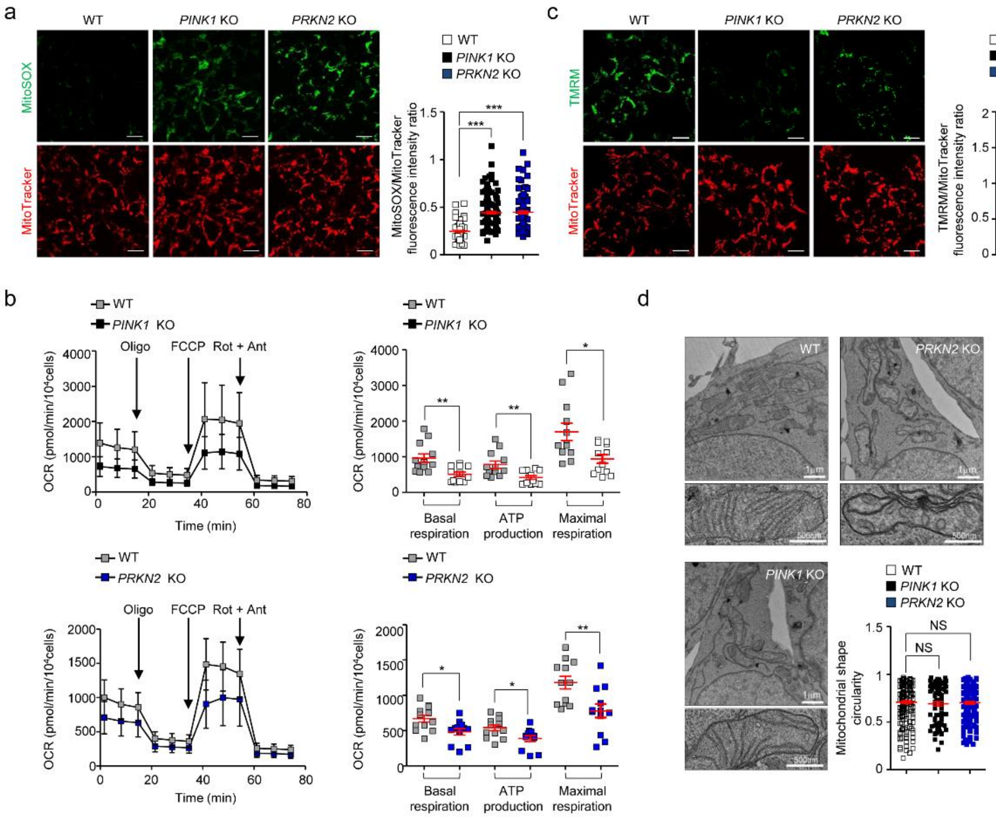

Supplementary Figure 11. Deficiency of *PINK1* or *PRKN2* leads to mitochondrial alterations in HAP–1 cells. (**a** and **c**) Cultured cells were loaded (**a**) with MitoSOX (green; mitochondrial ROS indicator, 2.5 µM for 25 min at 37°C) and MitoTracker (red; fluorescent probe that localizes to mitochondria; 1µM for 30 min at 37°C) or with tetramethylrhodamine methyl ester (TMRM; green; mitochondrial membrane potential fluorescent probe, 50 nM for 30 min at 37°C) and MitoTracker (red), and analysed by live confocal fluorescence microscopy. Representative confocal micrographs and quantification of (**a**) mitochondrial ROS production and (**c**) membrane potential (both calculated as ratios between TMRM and MitoTracker or MitoSOX and MitoTracker fluorescence intensities, with each point representing the fluorescence intensity ratio in a cell). MitoSOX/MitoTracker: n=93 WT cells, n=143 *Pink1* KO cells and n=113 *Prkn2* KO cells in **a**; TMRM/MitoTracker: n=114 WT cells, n=141 *Pink1* KO cells and n=147 *Prkn2* KO cells in **c.** Data are pooled from four independent experiments. One–way ANOVA followed by Dunnett's *post hoc* test, ***$P<0.001$ relative to WT cells in **a** and **c**. (**b**) Oxygen consumption rates (OCR) and individual parameters for basal respiration ATP production, proton leak and maximal respiration. OCRs were measured under basal level and after the sequential addition of Oligomycin (Oligo, 1µM), FCCP (0.5µM) and Rotenone (Rot; 1µM) + Antimycin A (Ant; 1µM). Two tailed Student's *t*–test *$P<0.05$ and **$P<0.001$ relative to WT cells, n=12 pooled from four independent experiments. (**d**) Representative electron micrographs and quantification of the shape (expressed as circularity) of the mitochondrial network; n=173 mitochondria pooled from 21 WT cells and n=77 mitochondria pooled from 10 *PINK1* KO cells and n=158 mitochondria pooled from 16 *PRKN2* KO cells. The electron microscopy data are representative of two independent experiments. Plots represent mean ± SEM. Scale bars are 10µm. NS: non–significant.

Supplementary Figure 12

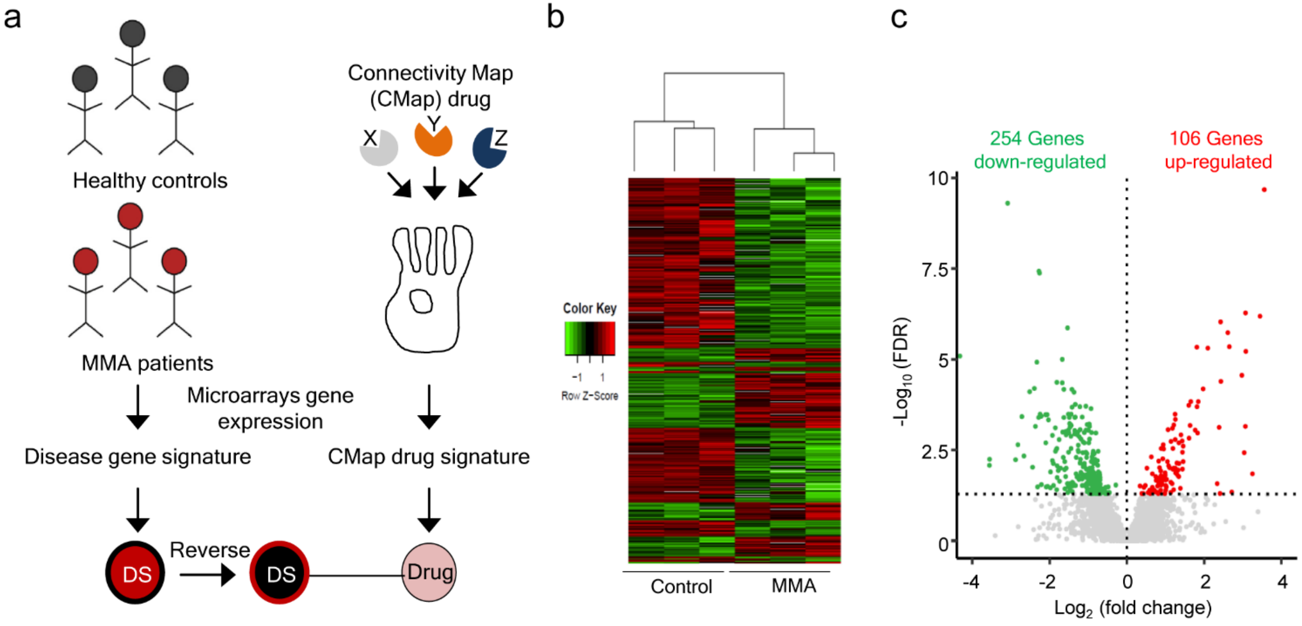

Supplementary Figure 12. Transcriptome profiling of control and MMA kidney cells. (**a**) The MANTRA 2.0 tool concept. The connectivity map, which includes transcriptional profiles following treatment of 1309 small molecules across five different cell lines, is compared against the disease gene signature obtained from the comparison of gene expression profiles between control and MMA cells. This analysis enables to capture compounds transcriptionally closer to the inverse MMA gene signature in order to identify potential drug compound–targeted biological pathway candidates. (**b**) Hierarchical–clustering and heat map: representation of the 360 genes identified as differentially expressed between control and MMA kidney cells, *n*=3 per each group. Expression levels are color–coded and indicate the fold change in pairwise comparisons; upregulated and downregulated genes are shown in red and green, respectively. (**c**) Volcano plot of transcriptome–wide analyses between control and MMA kidney cells. Transcripts significantly changing [$P \leq 0.05$, log2 |fold change| $\geq \pm 1.5$] are represented by green (downregulated genes) and red (upregulated genes) dots, respectively.

Supplementary Table 1. Disease–causing mutations and MMUT enzyme activity in kidney cells derived from patients with MMA

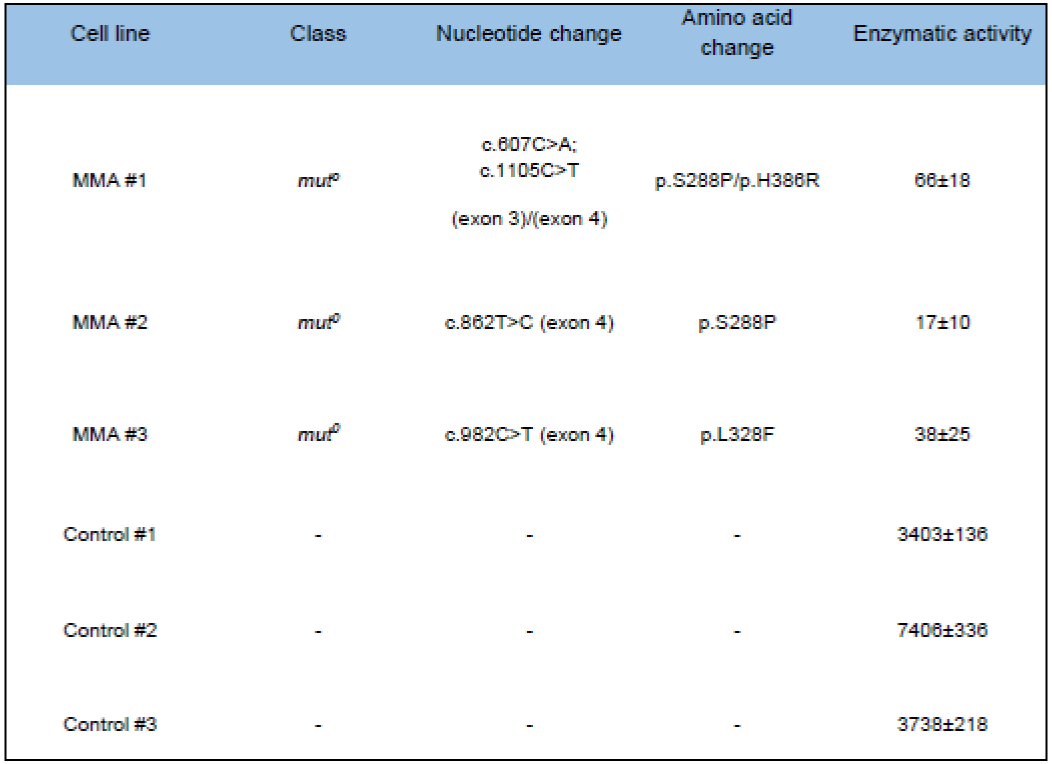

Cell line	Class	Nucleotide change	Amino acid change	Enzymatic activity
MMA #1	*mut*^{0}	c.607C>A; c.1105C>T (exon 3)/(exon 4)	p.S288P/p.H386R	66±18
MMA #2	*mut*^{0}	c.862T>C (exon 4)	p.S288P	17±10
MMA #3	*mut*^{0}	c.982C>T (exon 4)	p.L328F	38±25
Control #1	-	-	-	3403±136
Control #2	-	-	-	7406±336
Control #3	-	-	-	3738±218

mut$_0$, complete deficiency;

Enzymatic activity expressed as pmol× min$_{-1}$×mg$_{-1}$ of MMUT protein; the numbers represent the mean ± SEM of three independent experiments

Supplementary Table 2. Mouse primer pairs used for the gene expression analysis

Gene name	Forward primer (5'-3')	Reverse primer (5'-3')	PCR products (bps)	Efficiency
Gapdh	TGCACCACCAACTGCTTAGC	GGATGCAGGGATGATGTTCT	176	1.04 ± 0.03
Npsh2	GTCTAGCCCATGTGTCCAAA	CCACTTTGATGCCCCAAATA	162	1.03 ± 0.03
Slc12a3	CATGGTCTCCTTTGCCAACT	TGCCAAAGAAGCTACCATCA	148	1.01 ± 0.03
Slc12a1	CCGTGGCCTACATAGGTGTT	GGCTCGTGTTGACATCTTGA	154	0.99 ± 0.04
Aqp2	TCACTGGGTCTTCTGGATCG	CGTTCCTCCCAGTCAGTGT	147	1.03 ± 0.04
Slc5a2	TTGGGCATCACCATGATTTA	GCTCCCAGGTATTTGTCGAA	164	1.01 ± 0.03
Slc38a3	GTTATCTTCGCCCCCAACAT	TGGGCATGATTCGGAAGTAG	109	0.99 ± 0.02
Mmut	CAATGGCAGCAGTATTTGGA	GATCAGCCACTTTGGGAATC	150	0.99 ± 0.03
Pink	ATATGCTGCCCCCACACTAC	CAACTGCAAGGTCATCATGG	149	1.02 ± 0.02
Atg7	AGCTTGGCTGCTACTTCTGC	CTGCAGGACAGAGACCATCA	149	0.98 ± 0.03
Lcn2	ATGTCACCTCCATCCTGGT	GTGGCCACTTGCACATTGT	148	0.97 ± 0.03
Cox10	GGCAGATAAGCCCATTGCTA	TGACCCTCTTCAGTGGTGTG	156	1.02 ± 0.03

Supplementary Table 3. Human primer pairs used for the gene expression analysis

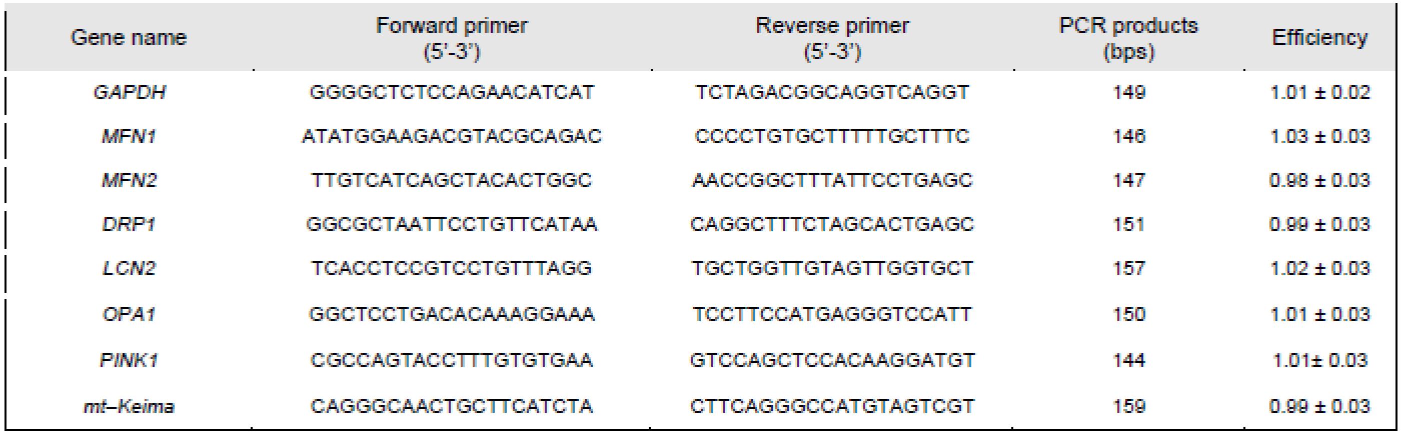

Gene name	Forward primer (5'-3')	Reverse primer (5'-3')	PCR products (bps)	Efficiency
GAPDH	GGGGCTCTCCAGAACATCAT	TCTAGACGGCAGGTCAGGT	149	1.01 ± 0.02
MFN1	ATATGGAAGACGTACGCAGAC	CCCCTGTGCTTTTTGCTTTC	146	1.03 ± 0.03
MFN2	TTGTCATCAGCTACACTGGC	AACCGGCTTTATTCCTGAGC	147	0.98 ± 0.03
DRP1	GGCGCTAATTCCTGTTCATAA	CAGGCTTTCTAGCACTGAGC	151	0.99 ± 0.03
LCN2	TCACCTCCGTCCTGTTTAGG	TGCTGGTTGTAGTTGGTGCT	157	1.02 ± 0.03
OPA1	GGCTCCTGACACAAAGGAAA	TCCTTCCATGAGGGTCCATT	150	1.01 ± 0.03
PINK1	CGCCAGTACCTTTGTGTGAA	GTCCAGCTCCACAAGGATGT	144	1.01± 0.03
mt–Keima	CAGGGCAACTGCTTCATCTA	CTTCAGGGCCATGTAGTCGT	159	0.99 ± 0.03

Supplementary Table 4. Zebrafish primer pairs used for the gene expression analysis

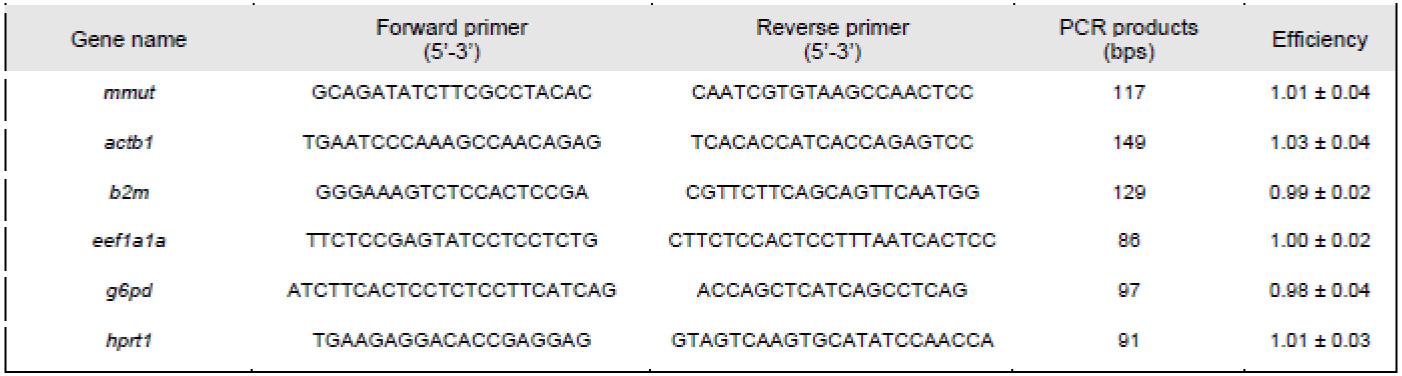

Gene name	Forward primer (5'-3')	Reverse primer (5'-3')	PCR products (bps)	Efficiency
mmut	GCAGATATCTTCGCCTACAC	CAATCGTGTAAGCCAACTCC	117	1.01 ± 0.04
actb1	TGAATCCCAAAGCCAACAGAG	TCACACCATCACCAGAGTCC	149	1.03 ± 0.04
b2m	GGGAAAGTCTCCACTCCGA	CGTTCTTCAGCAGTTCAATGG	129	0.99 ± 0.02
eef1a1a	TTCTCCGAGTATCCTCCTCTG	CTTCTCCACTCCTTTAATCACTCC	86	1.00 ± 0.02
g6pd	ATCTTCACTCCTCTCCTTCATCAG	ACCAGCTCATCAGCCTCAG	97	0.98 ± 0.04
hprt1	TGAAGAGGACACCGAGGAG	GTAGTCAAGTGCATATCCAACCA	91	1.01 ± 0.03

IV. Discussion and perspectives

Rare kidney diseases represent a group of at least 150 different disorders, with an overall prevalence of about 60–80 cases per 100 000 in Europe and in the USA. Inherited kidney disease is one of the cause of kidney transplantation for 10% of the adults and for almost all children and it is the fifth most common cause of end-stage-kidneys disease after diabetes, hypertension, glomerulonephritis, and pyelonephritis. The progress in kidney transplantation is improving the survival of these patients; however, they often have compromised health linked to a poor quality of life. Patients with inherited kidney diseases have multisystem complications as the kidney is involved in the regulation of essential homoeostatic processes (Devuyst et al. 2014). Mechanistic studies in different models and cells systems, as performed in this thesis, have allowed better characterization of pathways involved in rare diseases and offer novel therapeutic perspectives.

New mechanistic insights and therapeutic approaches for Lowe syndrome and Dent disease

The generation and characterization of a new OCRL-deficient mouse model for Lowe syndrome/Dent disease 2 allowed us to investigate the renal and extra-renal manifestations encountered in patients affected by these diseases. The loss of *Ocrl* in mouse kidney induces PT dysfunction characterized by LMW proteinuria and albuminuria and muscular defect associated with dysfunctional locomotricity and reduced growth, as observed in patients carrying a mutation in *OCRL*. The impairment of PT function observed in this mouse model is reflected by defective receptor-mediated endocytosis caused by the reduced expression of the apical endocytic receptor megalin. This mouse model did not show glycosuria, phosphaturia nor calciuria, mimicking the partial renal Fanconi syndrome observed in patients with Lowe syndrome/Dent disease 2.

The lack of models available for Lowe syndrome/Dent disease was one of the major restrictions to assess the cellular and molecular mechanism of OCRL in kidney cells. The first developed *Ocrl* KO mice did not exhibit kidney, eye or brain phenotype due to to the compensatory role of INPP5B, the closest paralogue of OCRL in mice and humans (Jänne et al. 1998). The conditional double *Ocrl* and *Innp5b* KO mouse model (Inoue et al. 2017) showed a generalized kidney PT dysfunction reflecting the renal phenotype observed in patients. However, this mouse model does not allow the discrimination between the individual role of OCRL and INPP5B in the pathophysiology of the disease. To overcome this concern, we used here a novel humanized mouse model expressing human *INPP5B* in *Ocrl*$^{Y/+}$; *Inpp5b*$^{-/-}$ or in *Ocrl*$^{Y/-}$; Inpp5b$^{-/-}$ background (hereinafter referred to as *Ocrl*$^{Y/+}$ *or Ocrl*$^{Y/-}$ respectively). The genetic architecture of this humanized mouse line allowed us to investigate directly the functional consequences associated with the single loss of OCRL activity. The reinsertion of the human INPP5B in the *Ocrl*$^{Y/+}$; *Inpp5b*$^{-/-}$ background was fundamental for survival (Bothwell et al. 2011; Festa et al. 2019). The differences between the humanized *Ocrl*$^{Y/-}$ mice and the conditional double *Ocrl* and *Innp5b* KO (Inoue et al. 2017) were evident when comparing the defective tubular endocytic phenotypes. In fact, the single lack of *Ocrl* in the transgenic mice results in a selective dysfunction of the clathrin receptor-mediated endocytosis, as evidenced by the specific defective uptake of the low-molecular-weight protein β-lactoglobulin and the unchanged internalization of dextran, a fluid phase marker (Festa et al. 2018). By contrast, the conditional deletion of *Ocrl* and *Inpp5b* resulted in an unspecific impairment of both clathrin-dependent and clathrin-independent endocytosis, as showed by a decreased of β-lactoglobulin and dextran uptake (Inoue et al. 2017).

We were able to reconstitute critical aspects of the disease *in vitro* by establishing differentiated and polarized proximal tubular cell cultures (mPT cells) from *Ocrl*$^{Y/-}$ mouse kidneys. OCRL coordinates the progression of internalized endocytosis cargo along the endosomal pathway by maintaining the PI(4,5)P_2 homeostasis. The deficient degradation of PI(4,5)P_2 by the 5 phosphatase OCRL in early endosomes triggers an aberrant F-actin polymerization. The abnormal actin dynamics impairs consequently the trafficking of various classes of receptors, including those that pass through the early endosomes to be rapidly recycled back to the plasma membrane such as the endocytic receptors cubilin and megalin. The trapping of megalin in early endosomes, and hence its defective endosomal trafficking, might partly link the OCRL deficiency to kidney tubule dysfunction associated with Lowe syndrome. These defects in receptors recycling appear as a potential therapeutic target for rescuing the PT dysfunction associated with the disease. Altogether, these findings provide new insights into the mechanisms of endocytosis as well as into the molecular pathogenesis of Dent disease/Lowe syndrome.

Recent exciting discoveries demonstrated that the defective endocytic uptake caused by OCRL deficiency is rescued by targeting the actin machinery with latrunculin B, an inhibitors of actin polymerization, or with the selective depletion of PI(4,5)P_2 (Vicinanza et al. 2011). Other studies showed that actin polymerization is arising not only from PI(4,5)P_2 but also from other phosphoinositide lipids. For example, it has been shown that PI(3)P acts in conjunction with PI(4,5)P_2 in a curved vesicles and triggers actin polymerization (Gallop et al. 2013). PI(3)P is produced by the phosphorylation of PI via Vps34 - a class III PI3K- and it is enriched in endosomes, where it is essential for their function (Figure 10) (Gillooly et al. 2000). In an OCRL-deficient retinal pigmented epithelial (RPE) cell line, inhibition of PI(3)P production by treatment with PI3K inhibitors wortmannin and Vps34-IN1 reduces the actin comet (Daste et al. 2017). All these data suggested that PI3K inhibitors might be a therapeutic strategy in Lowe syndrome/Dent disease 2. Additionally, PI3K inhibitors that have been developed for cancer therapy, are approved for clinical use, and are thus available for drug repurposing (Yang et al. 2019). For instance, Alpelisib, a PI3K inhibitor which target p110α, has shown clinical benefit in children with PROS/CLOVES syndrome (Venot et al. 2018), a rare overgrowth syndrome resulting from the activation PIK3CA gene.

We showed that alpelisib treatment on PT cells derived from *Ocrl* mice alleviates the aberrant actin polymerization at endosome by reducing levels of PI(4,5)P_2 and PI3P. These changes were paralleled by an improvement of the endocytic machinery and absorptive capacity in both cellular and mouse model for Lowe syndrome/Dent disease 2. These results confirmed the link between phosphoinositide lipids homeostasis, actin polymerization and endocytic trafficking in the pathophysiology of Lowe syndrome. Alpelisib might be a promising candidate for drug repurposing in the context of this disorder, as there is currently no treatment.

Loss of LMWP in urine is the main feature observed in patients with Lowe syndrome/Dent disease 2. These proteins, which are quantified and detected more consistently and earlier than the other solutes such as glucose, phosphate and amino acids, offer faithful biomarkers of defective receptor-mediated endocytosis in PT (De Matteis et al. 2017). In our studies, we showed that alpelisib, a class IA PI3K inhibitor, restores megalin expression at the plasma membrane and consequently rescues the apical endocytic uptake capacity of PT cells *in vitro* and *in vivo.* This effect is reflected by the decrease of CC16 and albumin loss in *Ocrl*$^{Y/-}$ mice treated with the PI3K inhibitor. Mice treated with alpelisib did not show major toxic effects, except glycosuria. This effect is in line with alpelisib administration being known to interfere with insulin pathway and induce an increase of glucose in the blood, and could be considered as a biomarker for drug dosing. However, mice in both groups (vehicle and treated) gained body weight, suggesting that the drug does not affect their development.

The rescue of endocytosis by alpelisib is explained by its action on the actin machinery. Alpelisib rebalances the levels of PI(4,5)P_2 and PI(3)P, which results in a decreased of actin polymerization in endosome compartment and improvement of the endocytic flux. Moreover, this treatment improves the absorptive capacity of PT cells by restoring the level of megalin at the plasma membrane. Our data indicates a bispecific effect of alpelisib on phosphoinositide production: on the production of PI(3,4,5)P_3 and its conversion to PI(3)P, and on production of PI(4,5)P_2. PI3K is involved in many cellular pathways including cell growth, survival, metabolism and autophagy. Therefore we cannot exclude that the improvement of the endocytic capacity is due to effects on PI(3,4,5)P_3 directly and the combined effect on other pathways modulated by this kinase.

This study focused on the PT function as it is first affected in paediatric patients with Lowe syndrome/Dent disease 2, and because progressive kidney disease is the primary cause of morbidity and mortality in these individuals. In fact, the study of urinary solutes is easily accessible and quantify, while the measurement of muscular or behavioural defect requires more complex investigations, sometimes invasive. Therefore, more work is needed to evaluate the potentially beneficial effects of alpelisib on other organs involved in the disease such as muscle and eyes.

Alpelisib may be particularly suitable for long-term use in patients, as it does not completely block PI3K activity and thus maintains functions of the signalling pathway. The hyperglycaemia induced by alpelisib, observed in mouse and in patients, may be manageable by dietary changes. Proximal tubule dysfunction is the first manifestation of kidney disease in Lowe syndrome/Dent disease 2 patients; alpelisib intervention in early stage might slow down the onset and progression of chronic kidney disease and therefore have a significant impact on lifespan and quality of life. Collectively, these data highlight the importance of drug repurposing for treating PT dysfunction in Lowe syndrome/Dent disease 2.

Deciphering the pathogenic cascade from MMUT deficiency to mitochondrial alterations and cell damage offers promising therapeutic avenues

The development of kidney tubular cells derived from the urine of patients with MMA and the establishment of a new zebrafish mutant line lacking for *mmut* enabled us to study the link between MMUT deficiency and epithelial cell dysfunction. The loss of MMUT induces an accumulation of damaged and dysfunctional mitochondria, which results in the production of a large amount of ROS, generating epithelia stress and cell damage. In particular, MMUT deficiency impairs the PINK/Parkin-mediated mitophagy, leading to an accumulation of altered mitochondria that trigger cellular stress. We used an unbiased drug–disease network modeling approach as a prioritization tool to identify plausible druggable targets. Our *in silico* analyses strongly suggest that mitochondria–targeted strategies to correct imbalances in redox homeostasis might reverse disease-relevant pathways in MMA.

The epithelial cells from the kidney tubules are enriched in mitochondria to sustain their specialized transport functions. Impairment of mitochondrial homeostasis or assembly might lead to kidney tubule dysfunction in various types of diseases (e.g. mutations in genes encoding for electron carriers proteins or assembly factors) (Emma et al. 2016). The presence of fragmented mitochondria and an increase of mitochondria DNA in MMA patient-derived kidney cells suggest that MMUT deficiency alters mitochondria network. Furthermore, energetic study showed a reduction of mitochondrial membrane potential as well as a reduction of baseline respiration, total respiration capacity and ATP turnover in MMA cells. These altered and dysfunctional mitochondria trigger the production of ROS, associated with an increase of Lipocalin 2 (LCN2), a marker of cellular damage. The abnormal mitochondria are also observed in mouse kidney tubule cells conditionally inactivated for the floxed *Mmut* alleles *in vitro* and in the kidney of mice carrying a mutant *Mmut* allele (p.Met698Lys, corresponding to the patient mutation p.Met700Lys) and a knock-out *Mmut* allele (hereafter referred to as *Mmut*$^{KI/KO}$ mice), confirming the importance of MMUT to maintain the mitochondria homeostasis and function. Despite the elevated levels of MMA metabolite and mitochondria abnormalities, these mutant mice showed no significant alterations in kidney function, neither structural damage nor interstitial inflammation in the kidneys compared to the control mice, thus failing to recapitulate the kidney disease associated with MMA.

To overcome this difficulty, we developed the first *mut* knock-out zebrafish model using CRISPR/Cas9 genome editing. The zebrafish has become a significant model system for studying kidney disease as the patterning of the kidney tubule is well conserved in zebrafish pronephros, with the expression of junctional complexes, endolysosomal apparatus, and receptors and transporters that are required for performing their absorptive functions. The modifications of mitochondria morphology and function described in *Mmut* $^{KO/KI}$ and patient-derived kidney cells were observed in the zebrafish model. Moreover, in contrast to the mouse model, the mutant zebrafish show a more complete disease-relevant phenotype, including liver mitochondriopathy, behavioural abnormalities and an excess of mortality. Interesting, these features are rescued when the fish are feeding with a low protein diet, a strategy currently used in MMA patients to prevent the accumulation of methylmalonic acid. These results demonstrate the key role of MMUT in preserving the mitochondrial network and homeostasis and the probable involvement of mitochondria quality control system in the disease.

Autophagy is an evolutionarily conserved process that degrades malfunctioning cellular constituents within a double-membrane structure called an autophagosome (Choi, Ryter, and Levine 2013). This quality control pathway is essential to maintain cellular homeostasis and function. Using a comprehensive series of autophagy–based assays, we were able to describe the downstream consequences of the *MUT* deletion on autophagy. Surprisingly, we observed an increase of autophagic vesicles due to the stimulation of autophagosome biogenesis. Furthermore, upstream signalling cascades involved in the regulation of autophagy biogenesis, such as mTORC1 and ULK1 complexes, were downregulated and upregulated respectively. Collectively, these data suggest that MUT deficiency stimulates autophagy by regulating, at least in part, upstream signalling cascades involved in autophagosome biogenesis.

It is known that the selective degradation of damaged and/or dysfunctional mitochondria occurs via a process called mitophagy (Palikaras, Lionaki, and Tavernarakis 2018). This process is selectively induced by the recruitment and activation of the mitochondrial serine/threonine protein kinase PINK1 and E3-ubiquitin-protein ligase Parkin to the outer mitochondrial membrane. This pathway drives mitochondria to be sequestered within autophagosomes and delivered to the endolysosome for degradation. Here, we used different pharmacological and genetics approaches to investigate the consequence of the loss of MMUT function on the selective degradation of damaged mitochondria. Rotenone treatment on control and MMA cells damages the mitochondria and triggers their selectively degradation by mitophagy. Parkin, which translocates to damaged mitochondria in physiology condition, was reduced in MMA cells in both normal and mitophagy induced conditions. The consequence of the defective PINK1-PRKN mechanism is the impairment of the mutant cells to deliver the dysfunctional mitochondria to the autophagy-lysosome degradation systems. This observation was monitored with mt-Keima, a ratiometric pH-sensitive probe used to measure the delivery of damaged mitochondria (which were labelled by the mitochondrial targeted form of a fluorescent Keima protein, mt-Keima) to the lysosomes (Katayama et al. 2011). These cellular defects compromise the clearance of mitochondria; trigger accumulation of mitochondria as shown by a marked increase of mitochondrial proteins and DNA. Expression of PINK1 in mutant cells activates mitophagy-mediated degradation of damaged mitochondria, improves the function of the mitochondrial network and homeostasis, and thereby averting mitochondria-derived epithelial distress and cell damage.

We used MANTRA, an *in silico* tool, to identify plausible druggable targets in the MMA context (Carrella et al. 2014). These *in silico* analyses suggested that targeting mitochondrial function and homeostasis might reverse disease phenotypes associated with MMUT deficiency. Taking in account the MANTRA predictions, we used compounds targeting mitochondria, such as mito–TEMPO (MT) and MitoQ and tested their potential benefits *in vitro* and *in vivo*. Consistent with *in silico* predictions, MT rescues the morphology and homeostasis of the mitochondrial network and improves its function, neutralizing thereby mitochondria–derived oxidative stress and cell damage in MMA kidney cells. We applied this strategy in *mut*–deficient zebrafish model: treatment with a low, non–toxic dose of MitoQ alleviated the mitochondrial oxidative stress and improved the behavioural phenotype of the fish model. The *in silico* predictions were validated by exposing MMA cells to either merbromin or lycorine, the two top drug candidate compounds that obtained a similar transcriptional responses but have distinct structure. This treatment of MMA cells improved the morphological abnormalities of the mitochondrial network (*e.g.* circularity and mitochondrial interconnectivity) as well as its functioning (*e.g.* membrane mitochondrial potential and production of mitochondrial ROS). On the other hand, merbromin and lycorine did not modify the levels of methylmalonic acid in MMA cells, supporting the concept that mitochondrial targeting acts independently from the elevation of toxic MMA metabolites. These results support the concept that targeting mitochondria, in order to improve their function and homeostasis, might represent a valid therapeutic perspective in MMA.

Taking all together, the studies reported in this thesis support the importance to develop new models, *in vivo* and v*itro*, to decipher the cellular and molecular pathway involve in rare genetic diseases. The development of news tools, such as *in silico* analysis, are essential to improve the identification of a candidate molecule for drug repurposing.

V. References

André, F. *et al.* Alpelisib for PIK3CA-Mutated, Hormone Receptor–Positive Advanced Breast Cancer. *N. Engl. J. Med.* (2019).

Ballabio, A. & Bonifacino, J. S. Lysosomes as dynamic regulators of cell and organismal homeostasis. *Nat. Rev. Mol. Cell Biol.* **21**, 101–118 (2020).

Banasik, J.L. “Renal function.” Pathology and Laboratory Medicine (2016) https://basicmedicalkey.com/renal-function/

Barness, L. A. The metabolic and molecular bases of inherited disease, 7th ed. C.R. Scriver, A.L. Beaudet, W.S. Sly, D. Valle, Vol. 3, McGraw Hill, New York, 1995, pp. 4605. *Am. J. Med. Genet.* **66**, 87–87 (1996).

Baumgartner, M. R. *et al.* Proposed guidelines for the diagnosis and management of methylmalonic and propionic acidemia. *Orphanet J. Rare Dis.* **9**, (2014).

Bedin, M. *et al.* Human C-terminal *CUBN* variants associate with chronic proteinuria and normal renal function. *J. Clin. Invest.* **130**, 335–344 (2020).

Bernard, D. J. & Nussbaum, R. L. X-inactivation analysis of embryonic lethality in Ocrlwt/−;Inpp5b−/− mice. *Mamm. Genome* **21**, 186–194 (2010).

Bilanges, B., Posor, Y. & Vanhaesebroeck, B. PI3K isoforms in cell signalling and vesicle trafficking. *Nat. Rev. Mol. Cell Biol.* **20**, 515–534 (2019).

Blanchard, A. *et al.* Observations of a large Dent disease cohort. *Kidney Int.* **90**, 430–439 (2016).

Bökenkamp, A. *et al.* Dent-2 disease: a mild variant of Lowe syndrome. *J. Pediatr.* **155**, 94–99 (2009).

Bothwell, S. P. *et al.* Mouse Model for Lowe Syndrome/Dent Disease 2 Renal Tubulopathy. *J. Am. Soc. Nephrol.* **22**, 443–448 (2011).

Boya, P., Codogno, P. & Rodriguez-Muela, N. Autophagy in stem cells: repair, remodelling and metabolic reprogramming. *Development* **145**, dev146506 (2018).

Burke, J. E. Structural Basis for Regulation of Phosphoinositide Kinases and Their Involvement in Human Disease. *Mol. Cell* **71**, 653–673 (2018).

Carlsson, S.R. and Simonsen A. Membrane dynamics in autophagosomebiogenesis.” Journal of Cell Science. (2015).

Carrella, D. *et al.* Mantra 2.0: an online collaborative resource for drug mode of action and repurposing by network analysis. *Bioinformatics* **30**, 1787–1788 (2014).

Chace, D. H., DiPerna, J. C., Kalas, T. A., Johnson, R. W. & Naylor, E. W. Rapid diagnosis of methylmalonic and propionic acidemias: quantitative tandem mass spectrometric analysis of propionylcarnitine in filter-paper blood specimens obtained from newborns. *Clin. Chem.* **47**, 2040–2044 (2001).

Chen, Y. & Klionsky, D. J. The regulation of autophagy – unanswered questions. *J Cell Sci* **124**, 161–170 (2011).

Cherqui, S. & Courtoy, P. J. The renal Fanconi syndrome in cystinosis: pathogenic insights and therapeutic perspectives. *Nat. Rev. Nephrol.* **13**, 115–131 (2017).

Choi, A. M. K., Ryter, S. W. & Levine, B. Autophagy in Human Health and Disease. *N. Engl. J. Med.* **368**, 651–662 (2013).

Christensen, E. I., Birn, H., Storm, T., Weyer, K. & Nielsen, R. Endocytic Receptors in the Renal Proximal Tubule. *Physiology* **27**, 223–236 (2012).

Christensen, E. I. *et al.* Loss of chloride channel ClC-5 impairs endocytosis by defective trafficking of megalin and cubilin in kidney proximal tubules. *Proc. Natl. Acad. Sci.* **100**, 8472–8477 (2003).

Christensen, E. I. & Gburek, J. Protein reabsorption in renal proximal tubule—function and dysfunction in kidney pathophysiology. *Pediatr. Nephrol.* **19**, 714–721 (2004).

Christensen, E. I. & Birn, H. Megalin and cubilin: multifunctional endocytic receptors. *Nat. Rev. Mol. Cell Biol.* **3**, 258–267 (2002).

Christensen, E. I., Wagner, C. A. & Kaissling, B. Uriniferous Tubule: Structural and Functional Organization. in *Comprehensive Physiology* 805–861 (American Cancer Society, 2012). doi:10.1002/cphy.c100073.

Cudkowicz, M. E. *et al.* Safety and efficacy of ceftriaxone for amyotrophic lateral sclerosis: a multi-stage, randomised, double-blind, placebo-controlled trial. *Lancet Neurol.* **13**, 1083–1091 (2014).

Cullen, P. J. & Steinberg, F. To degrade or not to degrade: mechanisms and significance of endocytic recycling. *Nat. Rev. Mol. Cell Biol.* **19**, 679–696 (2018).

Curthoys, N. P. & Moe, O. W. Proximal Tubule Function and Response to Acidosis. *Clin. J. Am. Soc. Nephrol.* **9**, 1627–1638 (2014).

Daste, F. *et al.* Control of actin polymerization via the coincidence of phosphoinositides and high membrane curvature. *J Cell Biol* jcb.201704061 (2017) doi:10.1083/jcb.201704061.

De Leo, M. G. *et al.* Autophagosome-lysosome fusion triggers a lysosomal response mediated by TLR9 and controlled by OCRL. *Nat. Cell Biol.* **18**, 839–850 (2016).

De Matteis, M. A., Staiano, L., Emma, F. & Devuyst, O. The 5-phosphatase OCRL in Lowe syndrome and Dent disease 2 | Nature Reviews Nephrology. *Nat. Rev. Nephrol.* **13**, 455–470 (2017).

Devuyst, O. & Igarashi, T. Chapter 41 - Renal Fanconi Syndrome, Dent Disease, and Bartter Syndrome. in *Genetics of Bone Biology and Skeletal Disease (Second Edition)* (eds. Thakker, R. V., Whyte, M. P., Eisman, J. A. & Igarashi, T.) 783–799 (Academic Press, 2018). doi:10.1016/B978-0-12-804182-6.00041-1.

Devuyst, O., Knoers, N. V. A. M., Remuzzi, G. & Schaefer, F. Rare inherited kidney diseases: challenges, opportunities, and perspectives. *The Lancet* **383**, 1844–1859 (2014).

Devuyst, O. & Luciani, A. Chloride transporters and receptor-mediated endocytosis in the renal proximal tubule. *J. Physiol.* **593**, 4151–4164 (2015).

Di Paolo, G. & De Camilli, P. Phosphoinositides in cell regulation and membrane dynamics. *Nature* **443**, 651–657 (2006).

Dickson, L. E., Wagner, M. C., Sandoval, R. M. & Molitoris, B. A. The Proximal Tubule and Albuminuria: Really! *J. Am. Soc. Nephrol.* **25**, 443–453 (2014).

Doherty, G. J. & McMahon, H. T. Mechanisms of Endocytosis. *Annu. Rev. Biochem.* **78**, 857–902 (2009).

Dusso, A. S. Kidney disease and vitamin D levels: 25-hydroxyvitamin D, 1,25-dihydroxyvitamin D, and VDR activation. *Kidney Int. Suppl.* **1**, 136–141 (2011).

Dvela-Levitt, M. *et al.* Small Molecule Targets TMED9 and Promotes Lysosomal Degradation to Reverse Proteinopathy. *Cell* **178**, 521-535.e23 (2019).

Ebner, M., Koch, P. A. & Haucke, V. Phosphoinositides in the control of lysosome function and homeostasis. *Biochem. Soc. Trans.* **47**, 1173–1185 (2019).

Eckardt, K.-U. *et al.* Evolving importance of kidney disease: from subspecialty to global health burden. *The Lancet* **382**, 158–169 (2013).

Emma, F., Montini, G., Parikh, S. M. & Salviati, L. Mitochondrial dysfunction in inherited renal disease and acute kidney injury. *Nat. Rev. Nephrol.* **12**, 267–280 (2016).

Erdmann, K. S. *et al.* A Role of the Lowe Syndrome Protein OCRL in Early Steps of the Endocytic Pathway. *Dev. Cell* **13**, 377–390 (2007).

Eshbach, M. L. & Weisz, O. A. Receptor-Mediated Endocytosis in the Proximal Tubule. *Annu. Rev. Physiol.* **79**, 425–448 (2017).

Festa, B. P. *et al.* OCRL deficiency impairs endolysosomal function in a humanized mouse model for Lowe syndrome and Dent disease. *Hum. Mol. Genet.*

Festa, B.P.,Berquez M., Nieri D. and Luciani A. Endolysosomal disorders affecting the proximal tubule of the kidney: New mechanistic insights and therapeutics. *Reviews of Physiology, Biochemistry and Pharmacology* (2020).

Fetro, C. & Scherman, D. Drug repurposing in rare diseases: Myths and reality. *Therapies* **75**, 157–160 (2020).

Foreman, J. W. Fanconi Syndrome. *Pediatr. Clin. North Am.* **66**, 159–167 (2019).

Forny, P. *et al.* Novel Mouse Models of Methylmalonic Aciduria Recapitulate Phenotypic Traits with a Genetic Dosage Effect. *J. Biol. Chem.* **291**, 20563–20573 (2016).

Fowler B., Leonard J. V. and Baumgartner M. R. 2008. “Causes of and diagnostic approach to methylmalonic acidurias.” Journal of Inherited Metabolic Disease 31 (3):350. https://doi.org/10.1007/s10545-008-0839-4

Fruman, D. A. *et al.* The PI3K Pathway in Human Disease. *Cell* **170**, 605–635 (2017).
Majerus, P. W. & York, J. D. Phosphoinositide phosphatases and disease. *J. Lipid Res.* **50**, S249–S254 (2009).

Fyfe, J. C. *et al.* The functional cobalamin (vitamin B12)-intrinsic factor receptor is a novel complex of cubilin and amnionless. *Blood* **103**, 1573–1579 (2004).

Gailly, P. *et al.* A novel renal carbonic anhydrase type III plays a role in proximal tubule dysfunction. *Kidney Int.* **74**, 52–61 (2008).

Gallop, J. L., Walrant, A., Cantley, L. C. & Kirschner, M. W. Phosphoinositides and membrane curvature switch the mode of actin polymerization via selective recruitment of toca-1 and Snx9. *Proc. Natl. Acad. Sci.* **110**, 7193–7198 (2013).

Gillooly, D. J. *et al.* Localization of phosphatidylinositol 3-phosphate in yeast and mammalian cells. *EMBO J.* **19**, 4577–4588 (2000).

Haarmann, A. *et al.* Renal involvement in a patient with cobalamin A type (cblA) methylmalonic aciduria: a 42-year follow-up. *Mol. Genet. Metab.* **110**, 472–476 (2013).

Hamacher-Brady, A. & Brady, N. R. Mitophagy programs: mechanisms and physiological implications of mitochondrial targeting by autophagy. *Cell. Mol. Life Sci.* **73**, 775–795 (2016).

Hegde, R. N. *et al.* Unravelling druggable signalling networks that control F508del-CFTR proteostasis. *eLife* **4**, e10365 (2015).

Hörster, F. *et al.* Long-term outcome in methylmalonic acidurias is influenced by the underlying defect (mut0, mut-, cblA, cblB). *Pediatr. Res.* **62**, 225–230 (2007).

Hryciw, D. H. *et al.* Cofilin Interacts with ClC-5 and Regulates Albumin Uptake in Proximal Tubule Cell Lines. *J. Biol. Chem.* **278**, 40169–40176 (2003).

Hsu, F. & Mao, Y. The structure of phosphoinositide phosphatases: Insights into substrate specificity and catalysis. *Biochim. Biophys. Acta* **1851**, 698–710 (2015).

Hurle, M. R. *et al.* Computational Drug Repositioning: From Data to Therapeutics. *Clin. Pharmacol. Ther.* **93**, 335–341 (2013).

Inoue, K. *et al.* Kidney Tubular Ablation of Ocrl/Inpp5b Phenocopies Lowe Syndrome Tubulopathy. *J. Am. Soc. Nephrol.* **28**, 1399–1407 (2017).

Iorio, F. *et al.* Discovery of drug mode of action and drug repositioning from transcriptional responses. *Proc. Natl. Acad. Sci.* **107**, 14621–14626 (2010).

Jänne, P. A. *et al.* Functional overlap between murine Inpp5b and Ocrl1 may explain why deficiency of the murine ortholog for OCRL1 does not cause Lowe syndrome in mice. *J. Clin. Invest.* **101**, 2042–2053 (1998).

Jean, S. & Kiger, A. A. Coordination between RAB GTPase and phosphoinositide regulation and functions. *Nat. Rev. Mol. Cell Biol.* **13**, 463–470 (2012).

Juric, D. *et al.* Phosphatidylinositol 3-Kinase α–Selective Inhibition With Alpelisib (BYL719) in PIK3CA-Altered Solid Tumors: Results From the First-in-Human Study. *J. Clin. Oncol.* **36**, 1291–1299 (2018).

Kaksonen, M., and Roux A. Mechanisms of Clathrin-Mediated Endocytosis. *Nature Reviews Molecular Cell Biology* 19 (5): 313–26 (2018).

Karatzas, A. *et al.* Fanconi syndrome in the adulthood. The role of early diagnosis and treatment. *J. Musculoskelet. Neuronal Interact.* **17**, 303–306 (2017).

Karoui, K. E. *et al.* Endoplasmic reticulum stress drives proteinuria-induced kidney lesions via Lipocalin 2. *Nat. Commun.* **7**, 10330 (2016).

Katayama, H., Kogure, T., Mizushima, N., Yoshimori, T. & Miyawaki, A. A Sensitive and Quantitative Technique for Detecting Autophagic Events Based on Lysosomal Delivery. *Chem. Biol.* **18**, 1042–1052 (2011).

Kaufmann, P., Pariser, A. R. & Austin, C. From scientific discovery to treatments for rare diseases – the view from the National Center for Advancing Translational Sciences – Office of Rare Diseases Research. *Orphanet J. Rare Dis.* **13**, 196 (2018).

Kawakami, T. *et al.* Deficient Autophagy Results in Mitochondrial Dysfunction and FSGS. *J. Am. Soc. Nephrol. JASN* **26**, 1040–1052 (2015).

Klootwijk, E. D. *et al.* Renal Fanconi syndrome: taking a proximal look at the nephron. *Nephrol. Dial. Transplant.* **30**, 1456–1460 (2015).

Lamb, J. *et al.* The Connectivity Map: Using Gene-Expression Signatures to Connect Small Molecules, Genes, and Disease. *Science* **313**, 1929–1935 (2006).

Leheste, J.-R. *et al.* Megalin Knockout Mice as an Animal Model of Low Molecular Weight Proteinuria. *Am. J. Pathol.* **155**, 1361–1370 (1999).

Levine, B. & Kroemer, G. Biological Functions of Autophagy Genes: A Disease Perspective. *Cell* **176**, 11–42 (2019).

Lloyd, S. E. *et al.* A common molecular basis for three inherited kidney stone diseases. *Nature* **379**, 445–449 (1996).

Luciani, A. *et al.* Impaired mitophagy links mitochondrial disease to epithelial stress in methylmalonyl-CoA mutase deficiency. *Nat. Commun.* **11**, 1–21 (2020).

Luciani, A. *et al.* Impaired Lysosomal Function Underlies Monoclonal Light Chain–Associated Renal Fanconi Syndrome. *J. Am. Soc. Nephrol.* ASN.2015050581 (2015) doi:10.1681/ASN.2015050581.

Luzio, J. P., Parkinson, M. D. J., Gray, S. R. & Bright, N. A. The delivery of endocytosed cargo to lysosomes. *Biochem. Soc. Trans.* **37**, 1019–1021 (2009).

Luzio, J. P., Pryor, P. R. & Bright, N. A. Lysosomes: fusion and function. *Nat. Rev. Mol. Cell Biol.* **8**, 622–632 (2007).

Mahadevappa, R., Nielsen, R., Christensen, E. I. & Birn, H. Megalin in acute kidney injury: foe and friend. *Am. J. Physiol.-Ren. Physiol.* **306**, F147–F154 (2013).

Majerus, P.W., and York J.D. Phosphoinositide Phosphatases and Disease. *Journal of Lipid Research* 50: S249–54 (2009).

Malcomson, B. *et al.* Connectivity mapping (ssCMap) to predict A20-inducing drugs and their antiinflammatory action in cystic fibrosis. *Proc. Natl. Acad. Sci.* **113**, E3725–E3734 (2016).

Manoli, I. *et al.* Targeting proximal tubule mitochondrial dysfunction attenuates the renal disease of methylmalonic acidemia. *Proc. Natl. Acad. Sci.* **110**, 13552–13557 (2013).

Matteis, M. A. D. & Godi, A. PI-loting membrane traffic. *Nat. Cell Biol.* **6**, 487–492 (2004).

McMahon, H. T. & Boucrot, E. Molecular mechanism and physiological functions of clathrin-mediated endocytosis. *Nat. Rev. Mol. Cell Biol.* **12**, 517–533 (2011).

Menzies, F. M. *et al.* Autophagy and Neurodegeneration: Pathogenic Mechanisms and Therapeutic Opportunities. *Neuron* **93**, 1015–1034 (2017).

Mizushima, N. & Levine, B. Autophagy in Human Diseases. *N. Engl. J. Med.* (2020)

Nachury, M. V. *et al.* A Core Complex of BBS Proteins Cooperates with the GTPase Rab8 to Promote Ciliary

Membrane Biogenesis. *Cell* **129**, 1201–1213 (2007).

Nakada-Tsukui, K., Watanabe, N., Maehama, T. & Nozaki, T. Phosphatidylinositol Kinases and Phosphatases in

Entamoeba histolytica. *Front. Cell. Infect. Microbiol.* **9**, (2019).

Nguyen, T. N., Padman, B. S. & Lazarou, M. Deciphering the Molecular Signals of PINK1/Parkin Mitophagy. *Trends Cell Biol.* **26**, 733–744 (2016).

Nielsen, R., Christensen, E. I. & Birn, H. Megalin and cubilin in proximal tubule protein reabsorption: from experimental models to human disease. *Kidney Int.* **89**, 58–67 (2016).

Noort, V. van *et al.* Novel Drug Candidates for the Treatment of Metastatic Colorectal Cancer through Global Inverse Gene-Expression Profiling. *Cancer Res.* **74**, 5690–5699 (2014).

Novarino, G., Weinert, S., Rickheit, G. & Jentsch, T. J. Endosomal chloride-proton exchange rather than chloride conductance is crucial for renal endocytosis. *Science* **328**, 1398–1401 (2010).

Oberholzer, V. G., Levin, B., Burgess, E. A. & Young, W. F. Methylmalonic aciduria. An inborn error of metabolism leading to chronic metabolic acidosis. *Arch. Dis. Child.* **42**, 492–504 (1967).

Palikaras, K., Lionaki, E. & Tavernarakis, N. Mechanisms of mitophagy in cellular homeostasis, physiology and pathology. *Nat. Cell Biol.* **20**, 1013–1022 (2018).

Paranjpe, M. D., Taubes, A. & Sirota, M. Insights into Computational Drug Repurposing for Neurodegenerative Disease. *Trends Pharmacol. Sci.* **40**, 565–576 (2019).

Park, E. *et al.* Muscle involvement in Dent disease 2. *Pediatr. Nephrol. Berl. Ger.* **29**, 2127–2132 (2014).

Phan, T. K. *et al.* Phosphoinositides: multipurpose cellular lipids with emerging roles in cell death. *Cell Death Differ.* **26**, 781–793 (2019).

Pierzynowska, K., Kamińska, T. & Węgrzyn, G. One drug to treat many diseases: unlocking the economic trap of rare diseases. *Metab. Brain Dis.* **35**, 1237–1240 (2020).

Polesel, M. & Hall, A. M. Axial differences in endocytosis along the kidney proximal tubule. *Am. J. Physiol.-Ren. Physiol.* **317**, F1526–F1530 (2019).

Pushpakom, S. *et al.* Drug repurposing: progress, challenges and recommendations. *Nat. Rev. Drug Discov.* **18**, 41–58 (2019).

Saftig, P. & Klumperman, J. Lysosome biogenesis and lysosomal membrane proteins: trafficking meets function. *Nat. Rev. Mol. Cell Biol.* **10**, 623–635 (2009).

Sarpatwari, A. & Kesselheim, A. S. Reforming the Orphan Drug Act for the 21st Century. *N. Engl. J. Med.* **381**, 106–108 (2019).

Schröder, B. A., Wrocklage, C., Hasilik, A. & Saftig, P. The proteome of lysosomes. *Proteomics* **10**, 4053–4076 (2010).

Schuh, C. D. *et al.* Combined Structural and Functional Imaging of the Kidney Reveals Major Axial Differences in Proximal Tubule Endocytosis. *J. Am. Soc. Nephrol.* **29**, 2696–2712 (2018).

van der Sluijs, P. *et al.* The small GTP-binding protein rab4 controls an early sorting event on the endocytic pathway. *Cell* **70**, 729–740 (1992).

Sun, W., Zheng, W. & Simeonov, A. Drug discovery and development for rare genetic disorders. *Am. J. Med. Genet. A.* **173**, 2307–2322 (2017).

Suzuki, C., Tanida, I., Oliva Trejo, J. A., Kakuta, S. & Uchiyama, Y. Autophagy Deficiency in Renal Proximal Tubular Cells Leads to an Increase in Cellular Injury and Apoptosis under Normal Fed Conditions. *Int. J. Mol. Sci.* **21**, (2019).

Tambuyzer, E. *et al.* Therapies for rare diseases: therapeutic modalities, progress and challenges ahead. *Nat. Rev. Drug Discov.* **19**, 93–111 (2020).

Tang, C., Livingston, M. J., Liu, Z. & Dong, Z. Autophagy in kidney homeostasis and disease. *Nat. Rev. Nephrol.* **16**, 489–508 (2020).

Venot, Q. *et al.* Targeted therapy in patients with PIK3CA-related overgrowth syndrome. *Nature* **558**, 540–546 (2018).

Verdon, Q. *et al.* SNAT7 is the primary lysosomal glutamine exporter required for extracellular protein-dependent growth of cancer cells. *Proc. Natl. Acad. Sci. U. S. A.* **114**, E3602–E3611 (2017).

Vicinanza, M. *et al.* OCRL controls trafficking through early endosomes via PtdIns4,5P2-dependent regulation of endosomal actin. *EMBO J.* **30**, 4970–4985 (2011).

Vicinanza, M., D'Angelo G., Di Campli A. and De Matteis M.A. Function and dysfunction of the PI system in membrane trafficking. *EMBO J.* 27: 2457–70(2008).

Volpatti, J. R. *et al.* Identification of drug modifiers for RYR1-related myopathy using a multi-species discovery pipeline. *eLife* **9**, e52946 (2020).

Volpatti, J. R. *et al.* The expanding spectrum of neurological disorders of phosphoinositide metabolism. *Dis. Model. Mech.* **12**, (2019).

Wallroth, A. & Haucke, V. Phosphoinositide conversion in endocytosis and the endolysosomal system. *J. Biol. Chem.* **293**, 1526–1535 (2018).

Wang, H., Lo, W.-T. & Haucke, V. Phosphoinositide switches in endocytosis and in the endolysosomal system. *Curr. Opin. Cell Biol.* **59**, 50–57 (2019).

Welling, P. A. & Weisz, O. A. Sorting It Out in Endosomes: An Emerging Concept in Renal Epithelial Cell Transport Regulation. *Physiology* **25**, 280–292 (2010).

van der Wijst, J., Belge, H., Bindels, R. J. M. & Devuyst, O. Learning Physiology from Inherited Kidney Disorders. *Physiol. Rev.* **99**, 1575–1653 (2019).

Yang, J. *et al.* Targeting PI3K in cancer: mechanisms and advances in clinical trials. *Mol. Cancer* **18**, 26 (2019).

Yin, Z., Pascual, C. & Klionsky, D. J. Autophagy: machinery and regulation. *Microb. Cell* **3**, 588–596 (2016).

Zhang, S.-D. & Gant, T. W. sscMap: An extensible Java application for connecting small-molecule drugs using gene-expression signatures. *BMC Bioinformatics* **10**, 236 (2009).

Zhen, Y. & Stenmark, H. Cellular functions of Rab GTPases at a glance. *J. Cell Sci.* **128**, 3171–3176 (2015).

Zhuo, J. L. & Li, X. C. Proximal Nephron. *Compr. Physiol.* **3**, 1079–1123 (2013).

Zoja, C., Abbate, M. & Remuzzi, G. Progression of renal injury toward interstitial inflammation and glomerular sclerosis is dependent on abnormal protein filtration. *Nephrol. Dial. Transplant.* gfu261 (2014) doi:10.1093/ndt/gfu261.

Zoncu, R. *et al.* A Phosphoinositide Switch Controls the Maturation and Signaling Properties of APPL Endosomes. *Cell* **136**, 1110–1121 (2009).

VI. Acknowledgements

I would like to express my sincere gratitude to Prof. Devuyst for giving me the opportunity to do my PhD in his lab. His guidance, experience, knowledge and feedback helped me in all the time of research. Without his support since my first day, this work would not have been possible.

I would like to express my gratitude to the members of my thesis committee, Prof. Baumgartner, Prof. Hall, Prof. Huynh-Do and Dr Luciani for their insightful comments, encouragement and their support during those years.

Every word written and every result described in this thesis would not be present without the continuous support of the MIKADO team. I would like to thank Alessandro for his advices, encouragement and for the discussions we had every morning around a coffee for the past five years. I thank Nadine, Huguette and Marianne for their technical help and guidance during the PhD. I am thankful to my fellow labmates for the good times we had together, especially to Jennifer, Marta, Daniela, Patrick and Guglielmo for the laugh, the parties and all the chocolates we shared together. My sincere gratitude goes to the former members of the lab, Alkaly, Eric and Paola, for their support and advice since the first day, and the long nights we spent in the lab and outside the lab. Many thanks to Paola for your trust, your friendship, your advice and your training during these years. I will remember all the good time we spent together behind the microscope or during our winter dinners. A special thanks to all the French speakers, who let me speak French during the stressful moment and who supported me behind my computer.

I would like to express my gratitude to Elizabetha, Merel, Luisa and Amalia, for all the days and evenings we spent together, for the hiking and the skiing, for their support, their encouragement and their friendship.

I am also very thankful for my old friends; Justine, for your open ears, your calm and our shopping days; and Aurore for your trust in me since we were teenagers.

Finally, I would like to dedicate this thesis to my loving parents, who always follow their daughters everywhere they go, for their love and their trust. My little sister for reading this thesis, for her encouragement and support. Merci pour tout.

VII. Curriculum vitae

BERQUEZ Marine
15 March 1991
Schaffhauserstrasse 403, 8050 Zürich, Switzerland
Tel: 0766816951
E-mail: marine.berquez@uzh.ch

Education:

2016/2020 – PhD student in Cell Biology, Institute of Physiology, University of Zurich, Switzerland
Thesis Supervisor: Prof. Dr. med. Olivier Devuyst.
Project title: Mechanistic Insights and New Therapeuthics For Rare Kidney Disorders

2017/2020 – Diploma of Advance Study in Translational Nephrology, University of Berne, Switzerland

2013/2015 – Master Science degree in Biology and Health, specialization in Host-Graft Interaction**,** University of François Rabelais- Tours, FRANCE

2010/2013 – Bachelor in Life Sciences and Health, specialization in Cellular Biology and Physiology, University of Limoges- Limoges, FRANCE

2006/2009 – Baccalauréat in Science, Lycée Jean Giraudoux**,** Châteauroux, France

Research training:

2016-2020 – PhD student, Study the endolysosomal pathway in the proximal tubule
Institute of Physiology - Prof. Dr. Med. Olivier DEVUYST «Mechanisms of inherited kidney disorders » – Zurich, Switzerland

01-06/2015 – Master thesis, Investigation of the regulation of the humoral immune response after hepatic gene transfer of a MHC class I molecule
INSERM UMR 1064, University of Nantes - Prof. Dr. Med. Ignacio ANEGON « Center of research in transplantation and immunology » – Nantes, France

04-06/2014 – Intern, Study of the signalization pathway of interleukin 10 in human dendritic cells
EA 4245, University of François Rabelais - Dr. Florence VELGE-ROUSEL « Dendritic cell, immunomodulation and graft» – Tours, France

05-07/2013 – Intern, Generation of a vector allowing the expression of an immunoglobulin from patient with Randall syndrome
CNRS UMR 7276, University of Limoges - Prof. Dr. Med. Michel COGNE «Control of the immune B response and lymphoproliferation » – Limoges, France

Technical skills:

Animal experimentation:
- LTK module 1
- Intraperitoneal injection in the mouse,
- Sample of kidney, spleen, liver and lymph node
- Metabolic cages

Cell culture:

- Culture of human cell lines
- Primary culture of microdissected proximal tubules from kidney

Molecular biology techniques:

- Construction of a vector
- Western Blot
- PCR
- Quantitative PCR
- Sequencing

Immunology techniques:

- Flow cytometry
- ELISA
- Immunohistochemical-staining on tissue
- Confocal microscopy

Teaching experience:

2016-2017 – Teaching assistant in physiology practical laboratory, Faculty of Medicine, UZH
1st and 2nd year medical students, 15 hours/year

Courses and Summer Schools:

2018 – Rare Disease Initiative Zurich (RADIZ) summer school, Warth, Switzerland
2016 – Course in laboratory animal science (mice/rats) FELASA Category B

Publications:

1. Festa BP., Berquez M., Nieri D., Luciani A. Endolysosomal disorders affecting the proximal tubule of the kidney: New mechanistic insights and therapeutics. ***Reviews of Physiology, Biochemistry and Pharmacology, 2020***

2. Chen Z., Berquez M. & Luciani A. Mitochondria, mitophagy, and metabolic disease: towards assembling the puzzle***. Cell Stress 6: 147-150, 2020***

3. Berquez M.*, Gadsby JR.*, Festa BP.*, Butler R., Jackson SP., Berno V., Luciani A., Devuyst O. & Gallop JL. *Those authors contributed equally. Phosphoinositide 3-kinase inhibitor alpelisib restores actin organization and improves proximal tubule dysfunction in Lowe syndrome and Dent disease. ***Kidney international 98: 883-896, 2020.*** Highlighted by an Commentary

4. De Leo E., Elmonem MA. , Berlingerio SP., Berquez M., Festa BP., Raso R., Bellomo F., Starborg T., Janssen MJ., Abbaszadeh Z., Cairoli S., Goffredo BM., Masereeuw R., Devuyst O., Lowe M., Levtchenko E., Luciani A., Emma F., Rega LR. Cell-Based Phenotypic Drug Screening Identifies Luteolin as Candidate Therapeutic for Nephropathic Cystinosis. ***Journal of the American Society of Nephrology 37: 1522-1537, 2020***

5. Luciani A.*,Schumann A.*, Berquez M.*, Chen Z.*, Nieri D., Failli M., Debaix H., Festa BP., Tokonami N., Raimondi A., Cremonesi A., Carrella D., Forny P., Kölker S., Camassei FC., Diaz F., Moraes CT, Di Bernardo D., Baumgartner MR. & Devuyst O. *Those authors contributed equally. Impaired Mitophagy Links Mitochondrial Disease to Epithelial Stress in Methylmalonyl-CoA Mutase Deficiency. ***Nature Communications 970, 2020***

6. Festa BP.*, Berquez M.*, Gassama A., Amrein I. , Ismail H., Samardzija M., Staiano L., Luciani A., Grimm C., Nussbaum RL., De Matteis MA., Dorchies O., Scapozza L., Wolfer DP. & Devuyst O. *Those authors contributed equally. OCRL deficiency impairs endolysosomal function in a humanized mouse model for Lowe syndrome and Dent disease. ***Human Molecular Genetics 28: 1931-1946, 2018***

7. Festa BP., Chen Z., Berquez M., Debaix H., Prange JA., Van de Hoek G., Alessio C., Raimondi A., Nevo N., Giles RH., Devuyst O. & Luciani A. Impaired autophagy bridges lysosomal storage disease and epithelial dysfunction in the kidney. ***Nature Communications 161, 2018***

Awards:

2018 – Best poster award, Rare Disease Initiative Zurich (RADIZ) summer school, Warth, Switzerland

Oral Communication/Poster:

2020 – **CRF International Cystinosis Research Symposium**, New Port Beach, USA
Poster: “Zebrafish model of nephropathic cystinosis”

2018 – **RADIZ (Rare Disease Initiative Zurich) summer school**, Warth, Switzerland
Poster and Oral presentation: “Impaired Mitophagy Bridges Mitochondrial Disorders and Epithelial Damage in the Kidney”

2018 – **Rare Disease Initiative Zurich (RADIZ) internal seminar**, Zurich, Switzerland.
Oral presentation: “Characterization of a mouse model for Lowe syndrome and Dent disease 2”

2018 – **LS^2 (Life Science Switzerland) Annual Meeting**. Lausanne, Switzerland
Poster: “Impaired Mitophagy Bridges Mitochondrial Disorders and Epithelial Damage in the Kidney”